Inorganic Tin Halide Perovskites for Planar Photovoltaic Devices

A thesis submitted for the degree of

Doctor of Philosophy

The University of Warwick

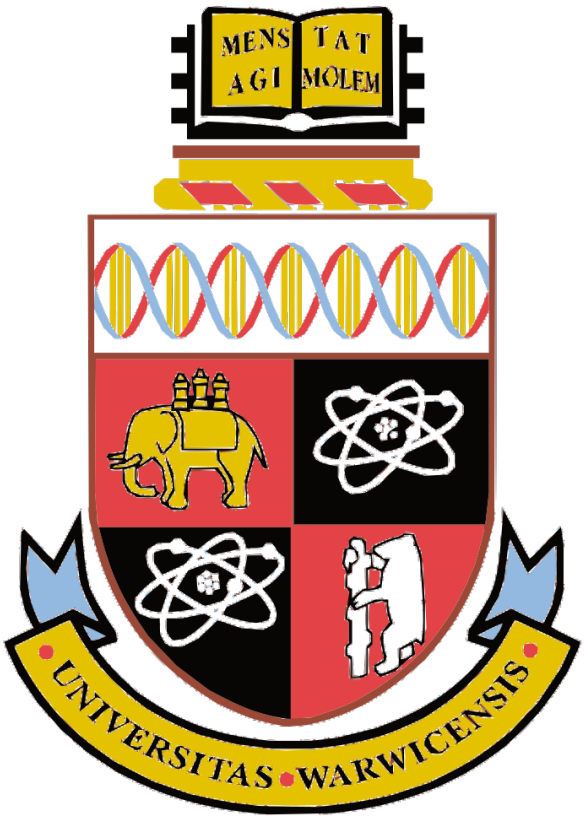

Supervised by Dr. Ross Hatton and Professor Richard Walton

Department of Chemistry

Kenneth Marshall

August 2017

Abstract

The research presented in this thesis focuses on the use of B-γ $CsSnI_3$ perovskite as the light harvesting semiconductor in discrete layer photovoltaic (PV) devices. Chapters 1 and 2 give a brief introduction with relevant theory, and experimental techniques respectively. Chapter 3 describes the use of B-γ $CsSnI_3$ in PV devices based on a CuI| $CsSnI_3$| fullerene architecture, showing how device V_{oc} is strongly dependent on the energetics at the perovskite| fullerene interface, and that using excess SnI_2 in $CsSnI_3$ preparation greatly improves device stability. Chapter 4 describes the effect that different tin halides have on stabilising films of B-γ $CsSnI_3$ and on the performance of PV devices. $SnCl_2$ was found to be the most beneficial source of excess Sn, with the champion device achieving a power conversion efficiency of over 3.5% combined with remarkable stability. Spontaneous n-type doping of the fullerene layer by $SnCl_2$ is shown to be the reason for high device efficiency. In Chapter 5 the effect of different substrate electrodes on the stability of PV devices based on $CsSnI_3$:$SnCl_2$ films is described. It is shown that the stability of thin films of B-γ $CsSnI_3$ perovskite towards oxidation in air depends strongly on the choice of substrate electrode and that unencapsulated devices using ITO or semi-transparent Au as the hole-extracting electrode, without an HTL, are more stable than those using an HTL. PV devices using ITO only as the hole-extracting electrode exhibit the highest stability, with a 30% reduction in efficiency only after $\sim$ 20 hours testing in air for the champion device. Chapter 6 describes an investigation of A and B site substitution in $CsSnI_3$, with particular focus on Rb partial A-site substitution. It was found that increasing the Rb content reduced film stability, but significantly increased device V_{oc} due to an increase in the perovskite ionisation potential.

Contents

Declaration

The work presented in this thesis has been conducted at the Department of Chemistry at The University of Warwick except for the X-ray photoelectron spectroscopy, Ultra-violet photoelectron spectroscopy, scanning electron microscopy, and Panalytical X'Pert Pro MRD X-ray diffraction measurements, which were carried out in the Department of Physics. XPS/UPS data collection and analysis assistance was provided by Dr Marc Walker. Assistance with X-ray diffraction data collection on Panalytical X'Pert Pro MRD was provided by Dr David Walker. All data collection was performed by me apart from that mentioned above. Parts of the work have been published in scientific journals and presented at the conferences MC12 (July 2015), and the Organic and Perovskite Solar Cells Conference (October 2016).

Acknowledgements

I would like to thank my supervisors Dr Ross Hatton and Professor Richard Walton for their guidance and support throughout my PhD.

I would also like to thank members of the Hatton and Walton Groups for their help and fun; Oliver Hutter, Martin Tyler, David "The Great Dave" Burnett, Daniel Cook, Luke Daniels, Dinesha Dabera, Jessica Pareira, Jaemin Lee, Silvia Varagnolo, and Philip Bellchambers.

I would also like to thank Professor Tim Jones, Professor Julie Macpherson and Patrick Unwin for allowing me to access equipment, Dr Marc for providing photoelectron spectroscopy measurements, Dr David Walker for assistance with Panalytical X-ray diffraction, and Dr Stephen York for assistance with scanning electron microscopy.

List of Publications

- "Tin Perovskite/ fullerene planar layer photovoltaics: improving the efficiency and stability of lead-free devices", K. P. Marshall, R. I. Walton, and R. A. Hatton, *J. Mater. Chem. A*, 2015, **3**, 11631-11640.

- "Enhanced stability and efficiency in hole-transport-layer-free $CsSnI_3$ perovskite photovoltaics", K. P. Marshall, M. Walker, R. I. Walton and R. A. Hatton, *Nat. Energy*, 2016, **1**, 16178.

- "Elucidating the role of the hole-extracting electrode on the efficiency and stability of $CsSnI_3$ / C_{60} perovskite photovoltaics", K. P. Marshall, M. Walker, R. I. Walton, R. A. Hatton, in press, *J. Mater. Chem A*.

List of Abbreviations

ETL	Electron transport layer
HTL	Hole transport layer
PV	Photovoltaic
PPV	Perovskite photovoltaic
OPV	Organic photovoltaic
APTMS	3-Aminopropyltrimethoxysilane
BCP	Bathocuproine
DMF	*N,N*-dimethylformamide
DMSO	Dimethylsulfoxide
ICBA	Indene-C_{60}-bis adduct
ITO	Indium tin oxide
MPTMS	3-Mercaptopropyltrimethoxysilane
$PC_{61}BM$, PCBM	Phenyl-C_{61}-butyric acid methylester
$PC_{70}BM$	Phenyl-C_{70}-butyric acid methylester
PEDOT:PSS	Poly(3,4-ethylenedioxythiophene): polystyrene sulfonate
P3HT	Poly(3-hexylthiophene)
Spiro-OMeTAD	2,2',7,7'-Tetrakis[N,N-di(4-methoxyphenyl)amino] -9,9'-spirobifluorene
AFM	Atomic force microscopy/ microscope
EQE	External quantum efficiency
SEM	Scanning electron microscopy/ microscope
UPS	Ultraviolet photoelectron spectroscopy
XPS	X-ray photoelectron spectroscopy

XRD	X-ray diffraction
SD	Standard deviation
0D	Zero-dimensional
1D	One-dimensional
2D	Two-dimensional
3D	Three-dimensional
NREL	National Renewable Energy Laboratory
CIF	Crystallographic information file
UV	Ultraviolet
vis	Visible light
IR	Infra-red
NIR	Near infra-red
CB	Conduction band
E_{f}	Fermi level
E_{g}	Band-gap
HOMO	Highest unoccupied molecular orbital
LUMO	Lowest unoccupied molecular orbital
VL	Vacuum level
VB	Valence band
n	Number of data points in set
I_p	Ionisation potential
ϕ	Work function
J_{sc}	Short-circuit current density
V_{oc}	Open-circuit voltage
FF	Fill factor

η	Power conversion efficiency
$B(\nu, T)$	Spectral radiance as function of ν and T
c	Speed of light in a vacuum
E_B	Binding energy
E_k	Kinetic energy
h	Planck's constant
$\hbar$	Reduced Planck's constant
k_{B}	Boltzmann's constant
P	Power density
q_e	Charge of an electron
T	Absolute temperature
λ	Wavelength
ν	Frequency
β, IMFP	Inelastic mean free path
ϵ_0	Permittivity of free space
ϵ_r	Relative permittivity

Chapter 1

Introduction

1.1 Context

Both the per capita energy demand and the world population have been increasing exponentially since the start of the industrial revolution, with global population expected to reach ~ 9.7 billion by 2050.[1] After 2050 there is some disagreement as to whether the population will continue increasing up to ~ 13.3 billion or plateau and then start decreasing to a lower estimate of 9.5 billion by 2100. Per capita energy demand increased by a factor of 1.56 between 1965 and 2009 (from 47.3 to 73.8 GJ/capita),[2, 3] and as developing nations become wealthier, they too will have higher per capita energy demands. To meet the increase in demand for energy, expansion of the use of renewable resources will be necessary, since continued reliance on fossil fuels will result in dangerous anthropogenic climate change and because of increasing scarcity of fossil fuels, especially oil, with current oil reserves expected to last only about 65 years. Renewable sources of energy also have the advantage of providing increased energy independence, compared to fossil fuels, because the latter are often concentrated in a few locations.

Global warming leading to climate change is caused by absorbance of black body radiation emitted from the Earth's surface by secondary greenhouse gases, the most prolific of which

being carbon dioxide, which accounts for more than 60% of the effects of anthropogenic global warming,[4] although per molecule it is not the most powerful greenhouse gas. CO_2 absorbs long-wavelength IR radiation, at 641 $cm^{-}1$ = 15.6 µm, near to the peak of the Earth's black body emission spectrum as a bending vibrational mode, and is long-lived in Earth's atmosphere.

Of the renewable energy technologies, solar power is one of the most promising for large scale electricty generation, because the energy in the sunlight incident on the Earth's total surface in 1 hour is sufficient to meet annual global energy demands. Indeed, global solar power consumption increased 72 fold between 2004 and 2014 (an average annual increase of 53%), increasing 38% from 2013 to 2014, making it the second most widely used source of renewable energy, after electricity generation from wind.[5]

Renewable energy technologies all have drawbacks and so a mix of different technologies is needed to provide a reliable electricity supply. For example, solar power does not generate electricity when it is dark, and the output is dependent on the season and cloud coverage. For this reason efficient means of energy storage are needed, such as using the solar energy collected during the day to generate H_2 by water splitting, or to pump water from a low reservoir to a high reservoir for hydroelectric.

1.2 The Solar Resource

Photovoltaic (PV) devices convert near infra-red, visible and some ultraviolet light from the Sun directly into electricity.

The temperature of the surface of the Sun is $\sim$ 5780 K, and the radiation spectrum it emits can be modelled as black body radiation which is calculated using Planck's law (Equation 1.1):

$$B(\nu, T) = \frac{2h\nu^3}{c^2} \frac{1}{e^{\frac{h\nu}{k_B T}} - 1} \tag{1.1}$$

where $B(\nu, T)$ is the spectral radiance as a function of frequency and temperature, which is the emitted power per unit area of the emitting surface per unit frequency per unit solid angle, h is the plank constant, ν is the frequency of light, c is the speed of light in a vacuum, k_{B} is the Boltzmann constant, and T is absolute temperature of the body.

The solar spectrum on the Earth's surface is shown in Figure 1.1. The spectrum at the Earth's surface differs from that in space due to light absorbance and scattering by atmospheric gases, water droplets, and dust particles.

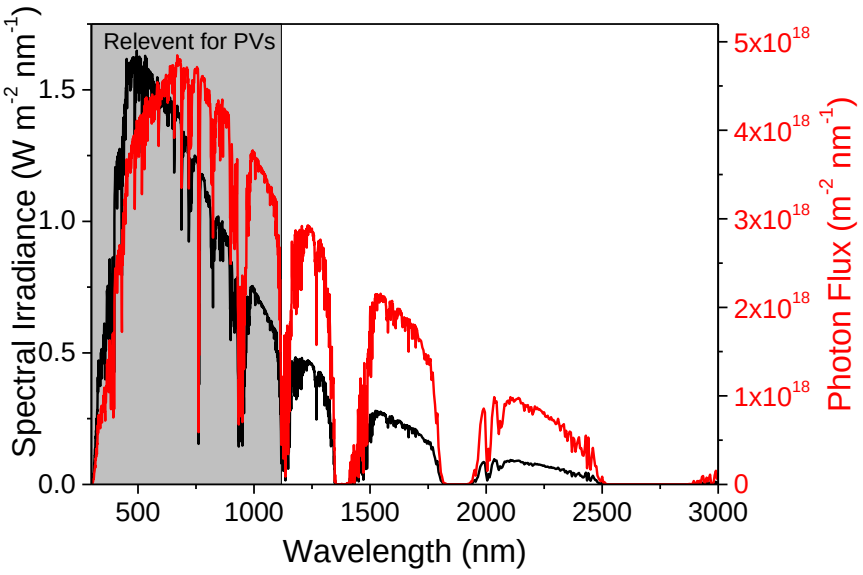

Figure 1.1: Solar spectrum at the surface of the Earth, AM 1.5G.

Solar simulators are typically characterised in terms of shape and power density. Air mass (AM) is a measure of the amount of atmosphere that light is travelling through (or simulated to travel through); AM 1.5G represents the solar spectrum for sunlight travelling through a thickness of 1.5 atmospheres, i.e. coming in at an angle of 48.2° from the direction normal to the Earth's surface, G refers to 'global' which includes the effects of diffuse radiation incident on the surface, as opposed to 'direct' (D), which only refers direct solar radiation which is partially blocked by the atmosphere. For solar simulators AM refers to the shape of the spectrum, and they are typically calibrated with a power density of 100 mW/cm^2, unless used in conjunction

with solar concentrator.

Single-junction PVs typically absorb light with onset wavelengths of ~ 1100 nm or lower.

1.3 Semiconductors

The heart of a photovoltaic device is a semiconductor which enables light absorption and sufficient time for the photogenerated electron hole pair to be separated before recombination.

1.3.1 Orbitals

Pure semiconductors are materials which have low electrical conductivity at low temperatures and light intensities (depending on the band-gap), but can be made to conduct by illuminating with intense light, applying an electric field, doping with impurities, or by heating.

Atoms hold electrons in atomic orbitals with quantised energies. Two atomic orbitals on neighbouring atoms in a molecule or in an extended solid can combine to form a bonding and anti-bonding orbital, and the strength of the coupling interaction determines the energy difference between them. In a 3-dimensional lattice, atomic orbitals can combine to form bands of closely spaced energy levels which are effectively a continuum of states when the difference in energy between them is < 25 meV (the thermal energy at room temperature (25 °C)). There are also energy ranges in which density of states is zero, called band gaps. The density of states in a band and the size of the band gap are determined by the strength of atomic orbital interaction, i.e. the greater the interaction of atomic orbitals, the greater the band gap.

1.3.2 Fermi Level

All materials have a Fermi level (E_f), which is defined as the energy at which the probability of electron occupancy is 0.5, although there does not need to be an available state at the E_f.

Materials with a finite density of states at the E_f are metals. Metals have a partially filled band which allows electrons to move freely through the material under the influence of an electric field. The probability of state occupancy at temperature, T, is given by the Fermi-Dirac distribution function (Equation 1.2 and Figure 1.2). The energy difference between the E_f and the vacuum level (VL) is called the work function (ϕ), and is the sum of the chemical potential and surface potential, the former refers to potential difference between an electron at the E_f of a material and the vacuum level in the absence of an electric field, and the latter of which results from the existence of a dipolar layer at the surface of all solids. The vacuum level is a place just outside the surface of a material where the electron is at rest, i.e. the change in potential energy of an electron with respect to position is 0 ($\frac{\mathrm{d}E}{\mathrm{d}x} = 0$) (Figure 1.3).

$$p(E,T) = \frac{1}{e^{(E-E_\mathrm{f})/(k_\mathrm{B}T)} + 1} \tag{1.2}$$

where E is potential energy, T is absolute temperature, and k_B is the Boltzmann constant.

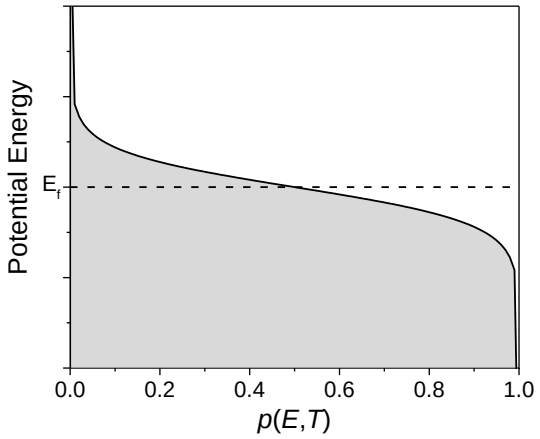

Figure 1.2: Plot of a Fermi-Dirac distribution function at $T > 0$

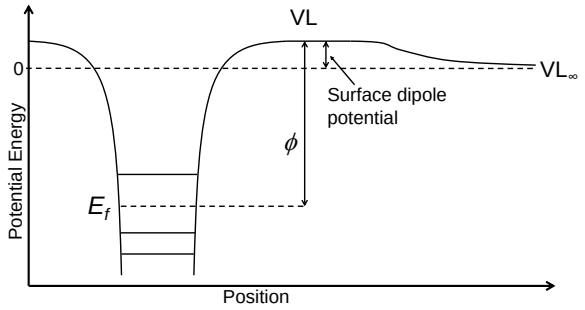

Figure 1.3: Energy level diagram depicting the potential well of a solid material.

1.3.3 Semiconductor Definition

Semiconductors are typically characterised as electronic materials with a band gap which is less than ~ 3 eV. Materials with band gaps > 3 eV are generally considered insulators (although this cut-off is in fact rather arbitrary). Semi-metals have a band gap of 0 eV; a partially filled band in which the density of states at the E_{f} is close to zero, of which graphite is the best known example. These are summarised in Figure 1.4.

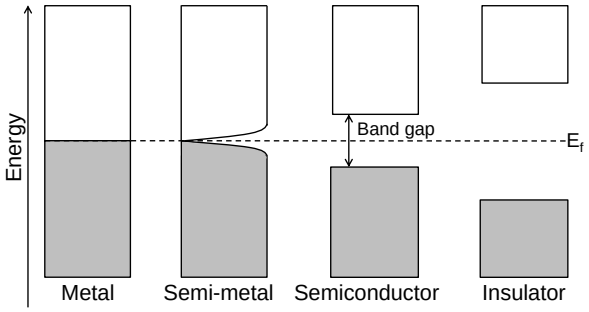

Figure 1.4: Electronic band diagrams of a metal, semimetal, semiconductor and insulator. Grey shade indicates filled states, unshaded indicates unfilled states.

In metals and semi-metals at $T > 0$ K there is a distribution of energy state occupancy near the Fermi level due to the thermal energy distribution of electrons. At 0 K there is an abrupt cut off between occupied and unoccupied energy states called the Fermi energy, above which $p(E) = 0$, below the Fermi energy, $p(E) = 1$. In a semiconductor without impurity atoms or

defect states in the band gap (intrinsic), at room temperature, i.e. a semiconductor in which there are no energy states in the band gap, the Fermi level is half way between the valence band edge and the conduction band edge. The valence band is almost completely occupied and the conduction band is almost completely unoccupied, because the thermal energy of an electron at room temperature (~ 25 meV) is typically much smaller than the band gap, and so the probability of occupying a state in the conduction band is very low.

1.3.4 Semiconductor Doping

Semiconductors can be doped with impurities (atoms) or with defect/vacancy sites in the band-gap in two ways; n-type or p-type. n-Type doping involves creating occupied energy states which are close to the conduction band edge, which moves the E_{f} towards the conduction band edge with increasing concentrations of n-type dopants. Conversely p-type doping requires unoccupied energy states close to the valence band edge, which has the effect of moving the E_{f} closer to the valence band edge.

1.3.5 Metal-Semiconductor Interfaces

When two materials come into contact, charge transfer will take place causing the E_{f} of the materials to come into alignment because the electrons will move towards lower potential; i.e. the material with the higher lying E_{f} will transfer electron density to the material with the lower E_{f}. At the interface of the materials there is a depletion region where all of the charge is concentrated. The charge transfer interaction causes an abrupt VL shift at the interface; this is known a Schottky barrier (Figure 1.5).[6, 7]

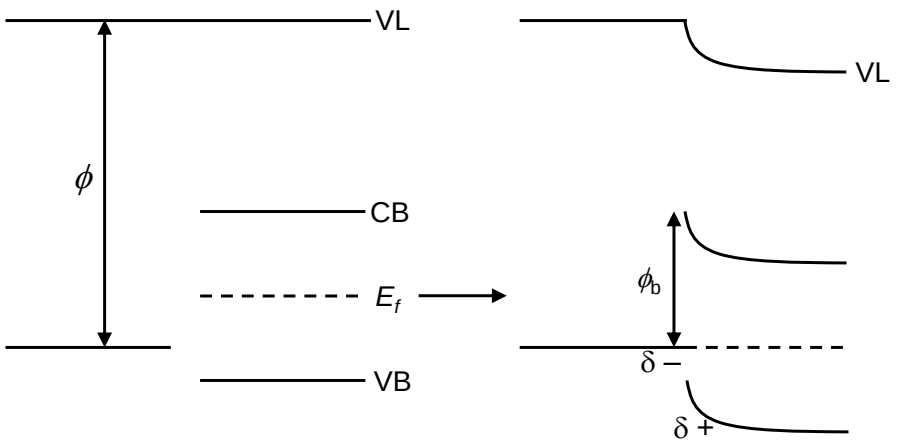

Figure 1.5: Diagram of a metal-semiconductor interface before and after contact, forming a Schottky barrier. ϕ_b is the Schottky barrier height.

The shape of the band bending is described by the Poisson equation which calculates electrostatic potential for a given charge distribution:

$$\frac{\mathrm{d}^2V}{\mathrm{d}x^2} = \frac{\rho}{\epsilon} \tag{1.3}$$

where V is the electric potential, ρ is the charge distribution, and ϵ is the dielectric constant of the material.

Alternatively, an Ohmic contact, which has little or no rectifying behaviour, may form when the E_f of the metal is lower in energy than the VB edge or higher in energy than the CB edge of the semiconductor, or a tunnelling contact may form in the case of a heavily doped semiconductors which can hold high charge densities at the interface, leading to a narrow depletion region capable of allowing tunnelling electrons through.

1.4 Current Photovoltaic Technologies

Currently first generation single crystal silicon dominates the PV market. Silicon PVs have numerous advantages over other existing technologies; (i) they are well understood, having

been very widely studied since 1954 when the first practical solar cell was fabricated at Bell Laboratories [8]; (ii) silicon photovoltaics can be very efficient - the record efficiency for single crystal silicon photovoltaics is now over 25% (Figure 1.6); and (iii) they are very stable with lifetimes now guaranteed at $>$ 25 years[9].

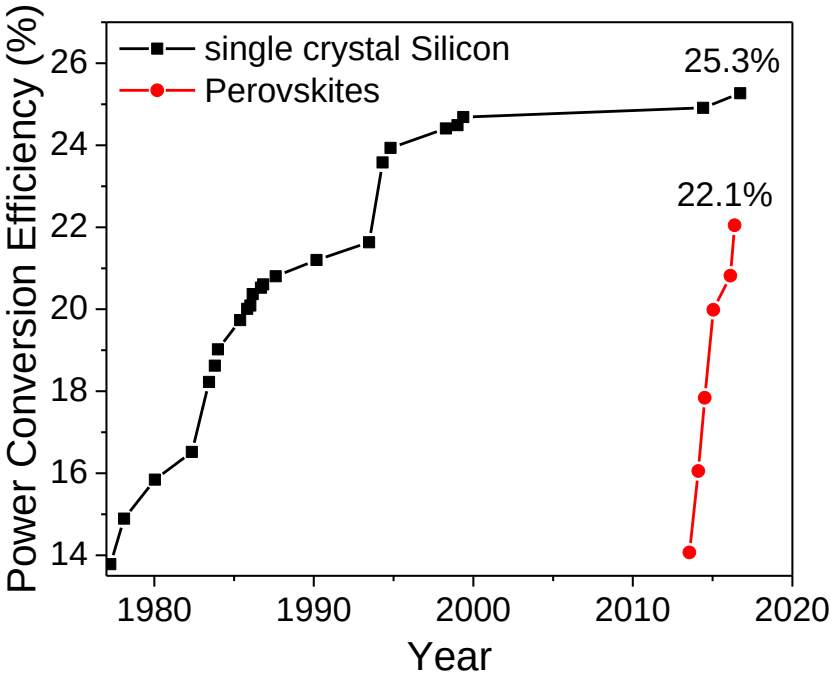

Figure 1.6: National Renewable Energy Laboratory (NREL) chart of record photovoltaic power conversion efficiency by technology over time for devices under 1 sun illumination.[10] Measured by independent recognised test labs; e.g. NREL, National Institute of Advanced Industrial Science and Technology, and Fraunhofer Institute for Solar Energy Systems.

However, there are drawbacks to silicon PV technology; (i) highly purity silicon is required, which is relatively expensive to produce; (ii) very high temperatures are required to process silicon because single crystal ingots are grown from melted silicon, thus leading to high energy production and long energy payback times; (iii) by comparison with other single junction PVs, silicon requires very thick layers (100 - 300 µm) in order to achieve optimal efficiency due to its weak light absorption for long wavelength light. In a single crystal silicon PV device, p-doped

Si is placed in a homojunction with n-doped Si, forming a p-n junction. When the n- and p-doped parts of the material come into Fermi level alignment, a built in field is created at the interface; the depletion region, where all of the extractable, photo-generated electron-hole pairs charge are generated (photons absorbed outside of the depletion region generate electron-hole pairs where there is little electric field to separate the charges, and so they are likely to recombine).

Second generation PVs include amorphous and polycrystalline silicon, as well as some materials which are isovalent to silicon, the most widely used of which are CdTe, GaAs and $CuIn_xGa_{1-x}Se_2$. These are all thin-film technologies which require much less material than single crystal silicon PVs (photoactive layer typically 100s nm - several µm).

Third generation PV technologies are are based on unconventional semiconductors, including organic semiconductors, organic and organometallic dyes, quantum dots and, most recently, 3D halide perovskites. Emerging PV technologies using these semiconductors as the photoactive part have the advantage of being much cheaper to fabricate due to lower processing temperatures, the requirement for less semiconductor material, and not requiring high purity materials. As such the projected energy payback time (i.e. the time required to generate the energy required to fabricate itself) for emerging PVs is projected to be much lower than that of silicon PVs; 180 days has been reported for organic PVs (OPVs)[11] compared with an average of 1.7 years estimated for crystalline silicon PVs[12].

According to the Shockley-Queisser limit, the maximum theoretical efficiency of a single p-n junction photovoltaic is limited to $\sim 30.3\%$.[13] This absolute limit is due to unavoidable energy losses in a PV system; radiative recombination, hot electrons (electrons promoted above the conduction band edge losing energy as they relax to the band edge), black body radiation (radiation emitted by the material due to its thermal energy), impedance (resistive and capacitative losses), and spectral losses (photons lower in energy than the band gap which cannot

be harvested). The ideal band-gap predicted for a *p*-*n* junction is 1.1 - 1.5 eV,[13] which limits the wavelength range that can be harvested to $\lambda < 1125$ nm.

Multi-junction photovoltaics are a class of PVs capable of breaking the theoretical efficiency limit because they are based on the use of multiple light harvesting layers of different band-gaps, and so can efficiently harvest a larger portion of the solar spectrum (generating a smaller proportion of 'hot-electrons'). Fabricating multi-junction device architectures does, however, increase the cost due to requiring additional layers in the devices, but is useful in applications such as satellites where large power generation from a small cell area is required. Putting a second, solution processable junction on top of a conventional silicon PV is a way to improve the performance and price per watt of a PV device. Tandem PV devices are currently an area of interest for incorporating lead halide perovskite into Si PVs.[14]

1.5 Principles of Operation

PVs of all types operate using a narrow band gap light harvesting semiconductor. Light passes through a transparent electrode; usually the wide band gap metal oxide, indium tin oxide (ITO); indium oxide degenerately doped with tin, or fluorine doped tin oxide (FTO). The light harvesting semiconductor absorbs photons of light which excite electrons from its valence band to its conduction band - giving an electron-hole pair, which is then separated into free charge carriers. In a thin film PV device, an HTL and an ETL are used to facilitate the extraction of charge carriers to the external circuit by enabling selective transport of one carrier type to each electrode; this charge selection is due to the large energy barrier between the band edges of the light harvester and those of the charge transport layers, i.e. the CB edge of the HTL is higher in energy than that of the light harvester, thereby blocking electrons, and the VB edge of the ETL is lower than that of the light harvester, thereby blocking holes. When electron-hole

pairs are generated they can exist as free carriers or as bound electron-hole pairs; excitons. If the exciton binding energy of a material is greater than thermal energy ($k_{\mathrm{B}}T \sim 25$ meV at room temperature) excitons will be the primary charge carrier, which is the case in organic photovoltaic donor materials which have exciton binding energies of over 100 meV.[15] If the exciton binding energy is lower than thermal energy there will be more free charge carriers. In a PPV the electron and hole are not bound to each other due to the low exciton binding energy of the perovskite (< 25 meV). When a charge carriers reach their corresponding transport layer, a small abrupt potential energy gradient ensures efficient charge transfer and minimises reverse charge transfer i.e. the conduction band of the electron transport layer is below that of the conduction band edge of the light harvester, and the valence band edge of the hole transport material is above that of the light harvester (Figure 1.7*). The separated charge carriers then move from their respective transport layers to the electrodes, either due to diffusion or a built-in electric field and potential gradient which can form under short circuit conditions in the absence of mobile ions which would screen the charges of the electrodes, and then travel through the circuit (Figure 1.7).

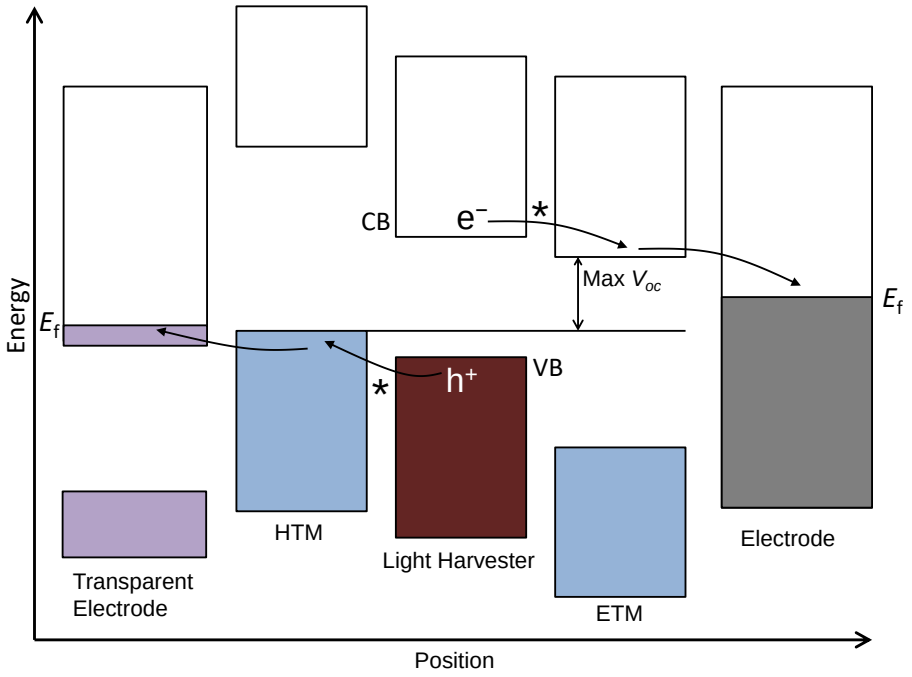

Figure 1.7: Zero-field flat band energy level diagram of a thin film photovoltaic, depicting the conduction bands and valence bands in each material, and the Fermi level in both electrodes.

1.6 Technical Characterisation

There are four figures of merit for calculating PV performance. Short-circuit current density (J_{sc}), open-circuit voltage (V_{oc}), fill factor (FF), and power conversion efficiency (η). J_{sc} is the current density generated under no external bias or load, V_{oc} is the voltage generated under an infinitely large load (i.e. when no current is flowing), FF is the ratio between the maximum power density output of the device and the product of J_{sc} and V_{oc}. η is proportional to all three parameters and calculated using the equation:

$$\eta = \frac{P_{out}}{P_{in}} = \frac{J_{\mathrm{sc}} \times V_{\mathrm{oc}} \times FF}{P_{in}} \tag{1.4}$$

$$FF = \frac{J_{mpp} \times V_{mpp}}{J_{\mathrm{sc}} \times V_{\mathrm{oc}}} \tag{1.5}$$

where J_{mpp} and V_{mpp} are the current density (J) and voltage (V), respectively, at the maximum power point; the point on the JV curve at which the product of J and V is maximised.

1.7 Perovskites

Perovskites are a class of inorganic material with the formula ABX_3, where A is a cation, B is a metal and X is an anionic species such as an oxide or a halide. The structure consists of corner sharing BX_6 octahedra and A-site cations surrounded by 8 octahedra (and each octahedron is surrounded by 8 A-site cations) (Figure 1.8). They share the structure of $CaTiO_3$, the first perovskite mineral discovered.

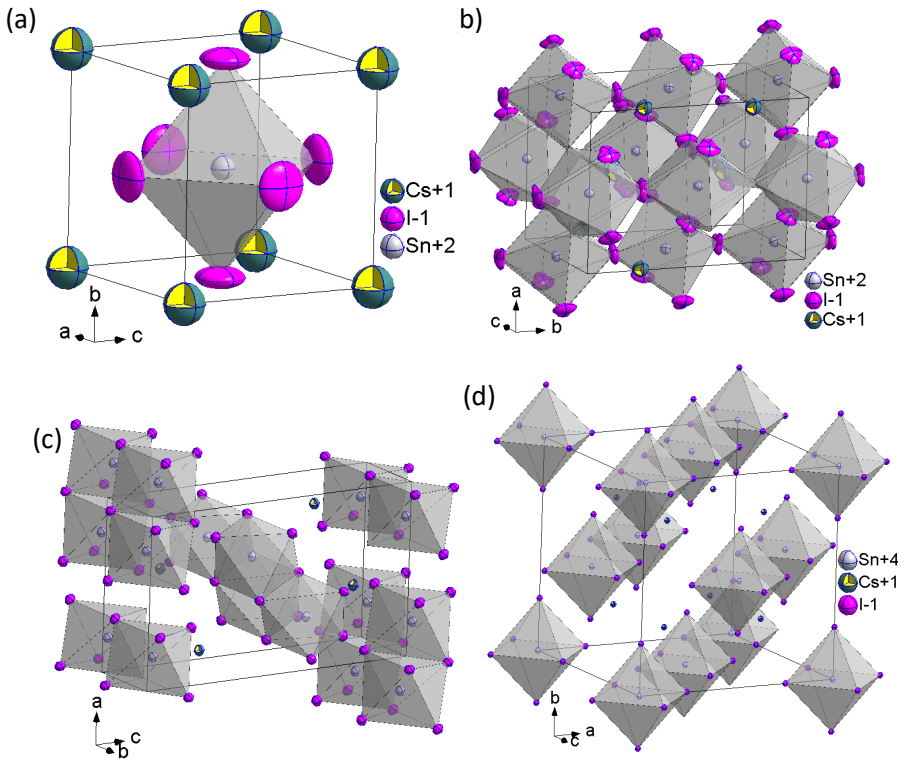

Figure 1.8: Crystal structures of perovskites **(a)** B-α $CsSnI_3$, **(b)** B-γ $CsSnI_3$, and non-perovskites **(c)** Y-$CsSnI_3$ and **(d)** Cs_2SnI_6.[16–18]

A halide perovskite structure can be predicted to be possible if it fits the tolerance factor

criterion:[19]

$$t = \frac{r_A + r_X}{(r_B + r_X)\sqrt{2}},\ 0.85 < t < 1.107 \tag{1.6}$$

where r is the ionic radius of the subscripted species. Another condition specific to halide perovskites is that the octahedral factor, μ, must be satisfied:

$$\mu = \frac{r_B}{r_X} > 0.414 \tag{1.7}$$

although there are a small number of outliers to both of these constraints, such as $CsBeF_3$ ($t = 1.275$, $\mu = 0.338$), and a few perovskites with $0.813 \leq t < 0.85$.[20]

Of particular relevence to the research presented in this thesis is the perovskite $CsSnI_3$ which has multiple phases: These are three 3D perovskite black polymorphs; B-α (Figure 1.8 (a)), B-β, and B-γ (Figure 1.8 (b)), where the latter two phases are similar to the B-α phase but with different degrees of octahedral tilting. These phases exist at different temperatures, with the cubic B-α $CsSnI_3$ existing at over 150 °C, and the orthorhombic B-γ $CsSnI_3$ existing below 89 °C, consequently the B-γ pase is of the most relevance for PV applications. In addition to this there is a non-perovskite, 1-dimensional, yellow (Y) phase (Figure 1.8 (c)). $CsSnI_3$ eventually converts to the 0-dimensional Cs_2SnI_6 in air (Figure 1.8 (d)).[16, 17]

1.8 Perovskite Photovoltaics (PPVs)

Perovskites have been widely studied for decades for their various properties, such as magnetic and electronic properties, although it was not until 2009 that they were first investigated for PV applications. Methylammonium lead iodide ($CH_3NH_3PbI_3$ or $MAPbI_3$) (Figure 1.9) and methylammonium lead bromide ($CH_3NH_3PbBr_3$ or $MAPbBr_3$), first reported in 1978[21], were used as a light harvesters in dye-sensitised solar cells in 2009, achieving over 3% power conversion efficiency (η).[22] Since then, the popularity of the newly emerged field of PPVs has

increased dramatically, becoming the fastest developing area of PV research, with a current record η of 22.1% (collaboration between the Korean Research Institute of Chemical Technoloty and the Ulsan National Institute of Science and Technology, South Korea) (Figure 1.6).[23] Tin perovskites have also been investigated due to their similar optoelectronic properties, although they have received only a fraction of the attention, and so have not achieved comparable performances to lead PPVs.[24–26]

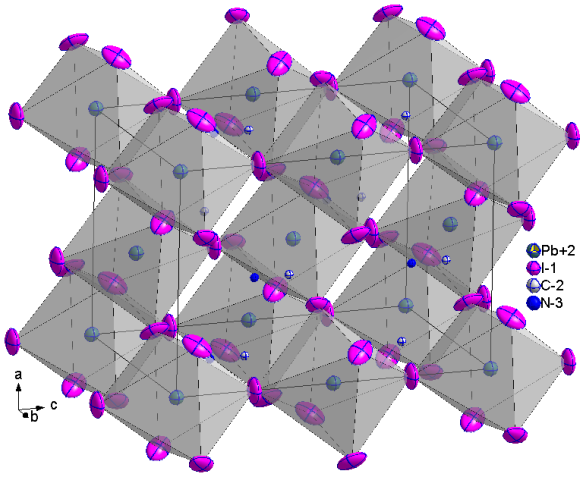

Figure 1.9: Unit cell of β-$CH_3NH_3PbI_3$.[17]

Lead and tin halide perovskites are attractive for PV applications because of their near ideal band gaps (1.5 - 1.6 eV for lead perovskites and 1.27 - 1.3 eV for tin perovskites), near the ideal according to the Shockley-Queisser limit, with the tin perovskite being in the ideal range, and lead just outside, broad and strong light absorption, small exciton binding energy ($<$ 25 meV), high charge carrier mobilities, and long carrier diffusion lengths ($>$ 100 nm).[16, 27–29] The exciton binding energy, which is the coulombic force of attraction between photogenerated electrons and hole, in the halide perovskites is lower than the thermal energy of particles at room temperature; 25 meV, and so photogenerated electrons and holes are effectively free charge carriers. Consequently they have high mobility and, in the absence of recombination centres, large diffusion lengths. Computational studies predict that the valence band is a weakly

antibonding band composed mostly of I 5p character, with some Pb 6s or Sn 5s character. The conduction band is an antibonding band with mostly Pb 6p or Sn 5p character, and some I 5p character (Figure 1.10).[30, 31]

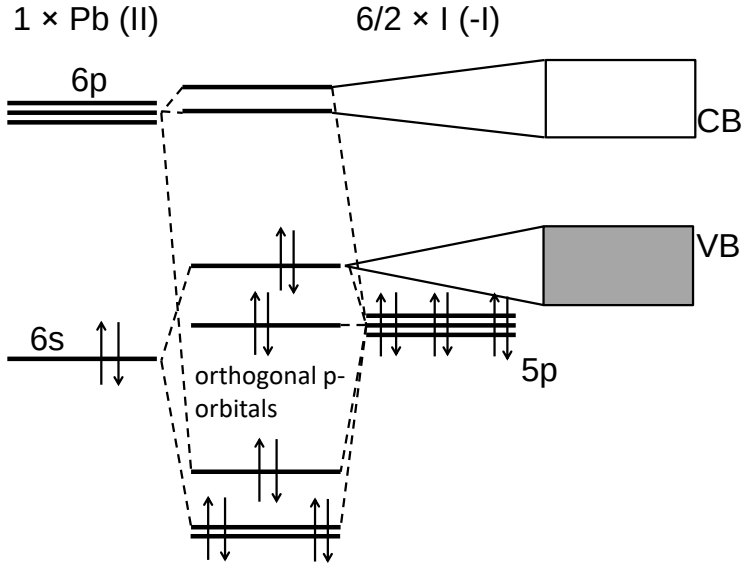

Figure 1.10: Molecular orbital diagram depicting origin of bands in lead halide perovskite

The reason for the lower band-gap in tin halide perovskites compared with their lead analogues is not obvious because, as discussed previously, in general stronger (shorter) bonds typically result in larger band gaps, and Pb-I bonds are longer than Sn-I bonds. The difference in band gap is due to relativistic contraction of Pb atomic orbitals caused by the high charge of the Pb nucleus.[31] This causes electrons, particularly *s* shell electrons, to move fast enough to significantly increase their mass (Equation 1.8), thereby reducing the Bohr radius of the orbitals (Equation 1.9). Because the B-site *s* orbitals contribute to the valence band, while the *p* orbitals contribute to the conduction band, the valence band is lowered in energy more than the conduction band, leading to an increase in band gap.[31]

$$m = \frac{m_0}{\sqrt{1 - \frac{v^2}{c^2}}} \tag{1.8}$$

where m is relativistic mass, m_0 is rest mass, v is velocity, and c is the speed of light.

$$a_0 = \frac{4\pi\epsilon_0\hbar^2}{m_e q_e^2} \tag{1.9}$$

where a_0 is the Bohr radius, ϵ_0 is the permittivity of free space, $\hbar$ is the reduced Planck's constant ($\frac{h}{2\pi}$), m_e is the mass of an electron, and q_e is the charge of an electron.

For $CsSnI_3$, $r_A = 1.88$ Å, $r_B = 1.10$ Å, and $r_X = 2.2$ Å, and so $t = 0.874$, and $\mu = 0.5$,[20, 32] which leaves some scope for changing the A- and X-sites whilst maintaining the 3D perovskite structure. Changing these constituents offers a means of tuning the optical and electronic properties, e.g. increasing the size of the A-site cation reduces the band-gap, and reducing the size of the X-site anion increases the band-gap. In the case of $CsSnI_3$, increasing the size of the A-site cation reduces octahedral tilting and makes the perovskite adopt a more cubic structure, thereby increasing the Sn-I-Sn bond angle (bringing it closer to the 180° angle of a cubic perovskite), thereby reducing electronic repulsion, and increasing the orbital overlap within the lattice. This effect is also observed for Pb perovskites, by changing the A-site of $APbI_3$ from Cs^+ to the larger organic cation methylammonium, $CH_3NH_3^+$ (MA^+), to the even larger formamidinium, $(NH_2)HC{=}(NH_2)^+$ (FA), the band gap decreases from 1.73 eV to 1.55 eV to 1.47 eV, and in Sn perovskites from 1.3 eV to 1.27 eV from Cs^+ to $CH_3NH_3^+$, whilst using $CH(NH_2)_2^+$ cation raises the band gap to 1.41 eV.[33] The increase in band gap caused by changing the A-site from Cs or CH_3NH_3 to $HC(NH_2)_2$ in Sn perovskites is caused by increased strain due to the smaller B-site, which causes the tolerance factor to become larger than 1 (1 being the optimal for cubic perovskite) (i.e. the A-B mismatch becomes too large).

Like other emerging technologies, the biggest advantage PPVs have over current commercial PVs is that they are potentially much cheaper to fabricate because they require much lower processing temperatures and much thinner semiconductor films than silicon PVs. PPVs can also be fabricated directly on flexible substrates[34, 35], which means they are amenable to

mass production using continuous roll-to-roll processing, which uses techniques such as screen printing and thermal evaporation. Because of this PPVs have been predicted to be capable of an energy payback time of less than 100 days.[36]

Another possible application of PPVs is to use them as part of a tandem PV with silicon. Silicon has low conversion of high energy photons to electrical power due to; (i) hot-electrons, and (ii) the disparity in absorption coefficients between high and low energy light for silicon, which leads to a situation in which high energy light is mostly absorbed before reaching the depletion region, and therefore has a high rate of radiative recombination. Perovskite semiconductors could potentially offer a cheap addition to a silicon device with higher power conversion efficiency for high energy light.[14, 37]

1.8.1 PPV device structures

PPVs can be fabricated with several different architectures, and it is not yet clear as to which will prove to be the most useful for practical applications. Reported structures include the dye-sensitised PV device structure,[22] the mesoporous pillared structure,[38] the meso-superstructure,[39, 40] the oxide electron transport layer planar heterojunction,[41] and the inverted planar heterojunction[42] (Figure 1.11).[43] By convention, devices in which electrons flow towards the substrate electrode (Figures 1.11 (a) - (d)) are considered to be conventional or 'standard' architectures, and devices in which electrons flow towards the top electrode (Figure 1.11 (e)) are described as inverted architecture. All of these architectures consist of a hole-extracting electrode, a hole transport layer (HTL) (e.g. 2,2',7,7'-Tetrakis[N,N-di(4-methoxyphenyl)amino]-9,9'-spirobifluorene (Spiro-OMeTAD)), light harvesting perovskite, an electron transport layer (ETL) (e.g. TiO_2) and an electron extracting electrode.

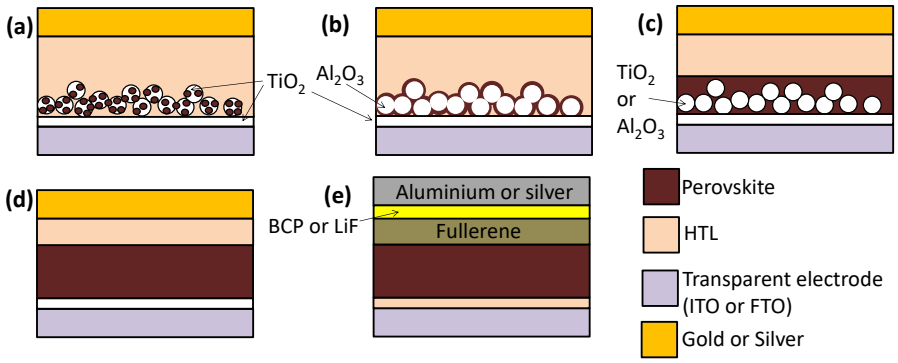

Figure 1.11: Schematics of different PPV architectures. **(a)** Dye-sensitised, **(b)** meso-superstructured, **(c)** pillared, **(d)** planar heterojunction with oxide electron transport layer, and **(e)** organic-type planar heterojunction.

In devices which use mesoporous TiO_2 or Al_2O_3, the use of a mesoporous layer gives the advantage of providing a high surface area scaffold on which light harvesting perovskite films can be grown[44], gives a large interface area between the perovskite and the ETL (which enables efficient electron extraction), and allows more light to be absorbed by the perovskite due to scattering (which increasing light path length in the device),[45, 46] but also adds complexity to the device in fabricating and annealing the nanoparticles. TiO_2 is a commonly used ETL because it has high thermal stability and is prepared using cheap materials, but it has a drawback of requiring high processing temperatures ($\sim$ 500 °C), and is also sensitive to UV light which can lead to degradation in PPV devices[40]. The high processing temperature is a problem because it can severely limit the choice of substrate to those that can withstand high temperatures.

Planar architectures are attractive because they are simple to fabricate. The organic planar structure has an advantage of a using low work function top electrode such as aluminium, which is cheaper than the high work function metals such as gold, which is often used in the standard architectures. Additionally films of organic semiconductors are processed at low temperature, which makes them compatible with low cost flexible plastic substrates. However

some organic semiconductors are expensive to produce, for example the HTL, Spiro-OMeTAD, which requires a long multi-step synthesis, and C_{60} and its derivatives, the architypal ETL, uses a lot of energy in production and is low yielding to synthesise.[47] These properties make many organic semiconductors expensive, and so there is a motivation to minimise the number of different organic semiconductor layers used.[48] In the context of the research presented in this thesis the inverted discrete layer structure is the architecture of choice because of its ease of fabrication, and the tunability of LUMO position in C_{60} derivatives.

Organic semiconductors all have a system of conjugated π bonds, which results in a relatively narrow HOMO-LUMO gap between the π and π^* orbitals. An important advantage of organic semiconductors in general is that there is considerable scope for engineering optical and electronic properties by changing functional groups on the periphery and in the conjugated core of the molecule. This property makes organic semiconductors attractive for use with with perovskites due to the ability to tune orbital positions to match those of the perovskite, in order to minimise electrical losses that occur when extracting charges to the external circuit.

The majority of PPV devices reported to date use the perovskite in a distributed heterojunction device architecture, in which *n*-type meso-porous TiO_2 serves as the ETL and a p-type organic semiconductor is used as the HTL. There are also a smaller number of reports of planar-heterojunction PPVs based on a *p-i-n* structure, including those in which TiO_2 is replaced with organic semiconductors such as fullerenes, which have achieved $\eta > 20\%$.[23, 49, 50] Planar device architectures using organic charge transport layers may also offer the best prospects for accommodating the very large thermal expansion exhibited by some metal halide perovskites.[16] There is also interest in identifying low cost organic and inorganic HTLs such as the Cu(I) compounds CuI and CuSCN, which can be processed from solution at low temperature.[51–54]

1.8.2 The Development of Perovskite Thin Film Fabrication Techniques

In the first publication reporting the use of perovskite as a light harvesting material in a PV device in 2009 by Kojima *et al.*, $CH_3NH_3PbI_3$ was deposited from 8 wt% γ-butyrolactone (GBL) solution onto a mesoporous TiO_2 film, and allowed to dry, which produced isolated perovskite nanocrystals decorating the surface of the TiO_2 in a dye-sensitised architecture with a liquid hole-transporting electrolyte similar to that depicted in Figure 1.11 (a), an η of 3.8% was reported.[22] This structure was improved upon in 2012 by Kim *et al.*, who replaced the liquid electrolyte with a solid hole transporter; spiro-OMeTAD, and increased the concentration of the precursor to 20 wt%, leading to a $\eta > 9\%$.[55]

The next major advance occurred in November 2012 when Lee *et al.* reported on the use of Al_2O_3 as a scaffold layer for fabricating high coverage perovskite films, in the structure depicted in Figure 1.11 (b).[39] In that work a 20 wt% precursor solution containing 3:1 ratio of CH_3NH_3I and $PbCl_2$ in DMF was used, and the film was annealed at 100 °C. The use of $PbCl_2$ instead of PbI_2 has since been shown to improve the morphology and interfacial charge transport, while chloride is not incorporated in the bulk of the perovskite, and most coming off as CH_3NH_3Cl during the annealing step.[56] The very high charge carrier mobility of the perovskite ensured that the photogenerated charges could be transported directly to the compact TiO_2 layer, since Al_2O_3 is an insulator, and doesn't accept any charges from the perovskite. Whereas, in the case of using a mesoporous TiO_2, which has lower charge carrier mobilities than the perovskite, the TiO_2 would have to carry the electrons a longer distance to the electrode, thereby increasing series resistance and the chance of recombination. The champion device had $\eta > 10\%$.

The use of mixed methylammonium (MA) - formamidinium (FA) cation perovskite was first reported in 2014 by Pellet *et al.*, and has become commonly used since then.[57] In that

paper the authors found that the ideal ratio of CH_3NH_3:$HNCHNH_3$ was 3:2. The inclusion of $HNCH_3NH_3$ reduced the band-gap of the perovskite and led to a higher device J_{sc} with a similar V_{oc} and *FF* compared with the reference MA lead perovskite. Whilst pure $FAPbI_3$ is more stable in a hexagonal phase known as δ-$FAPbI_3$ or the "yellow phase" (which is a different structure from the orthorhombic yellow phases of $CsSnI_3$ and $CsPbI_3$)[58]. In 2016 Jacobsson *et al.* systematically tested lead perovskites with varying ratios of MA and FA cations, and I and Br anions.[59] They found that the perovskite which made devices with the highest η was $(CH_3NH_3)_{1/3}(HNCHNH_3)_{2/3}PbI_{2.5}Br_{0.5}$, achieving an η of 20.7%. Saliba *et al.* reported on the use of Pb perovskite containing three cations; Cs, MA and FA, resulting in a champion device with an η of 21.1%, as well as excellent stability.[23] In that work a pillared structure with Li-doped mesoporous TiO_2 ETL, and spiro-OMeTAD HTL with a Au top electrode.

A big advance in planar heterojunction (PHJ) PPVs occurred in 2013 when Liu *et al.* demonstrated the use of dual source evaporation as a means to produce thick, highly uniform perovskite films for use in PHJ PPVs (Figure 1.12), such as that depicted in Figure 1.11 (d).[41] The optimised ratio of precursor deposition rates for the co-evaporation was determined to be approximately 4:1 CH_3NH_3I: $PbCl_2$, and found an optimal thickness of 330 nm. The champion device had $\eta > 15\%$, with $J_{sc} > 20$ mA/cm^2 and $V_{oc} > 1$ V.

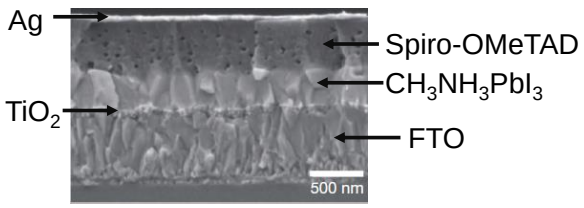

Figure 1.12: Cross-sectional SEM of a device in which the perovskite was prepared using dual-source evaporation. Taken from ref. [41].

Another advance in the fabrication of high quality perovskite films was the introduction of a two step deposition method: In 2013, Burschka *et al.* reported PPV devices in which the perovskite had much higher coverage on mesoporous TiO_2 than in earlier dye-sensitised type architectures, leading to the pillared structure (Figure 1.11 (c)).[38] This was achieved by first spin-coating PbI_2 onto the mesoporous TiO_2 from high concentration, 33 wt% solution, which resulted in a high loading onto the mesoporous layer. The PbI_2 coated TiO_2 film was then dipped into a solution of CH_3NH_3I. The film was then rinsed and dried at 70 °C, forming $CH_3NH_3PbI_3$. A champion device η of 15% was achieved. In 2014, Jeon *et al.* reported another novel technique of anti-solvent precipitation.[60] The group used a perovskite precusor solution with mixed solvent γ-butyrolactone (GBL) and dimethylsulfoxide (DMSO). This solution was spin-cast onto a mesoporous TiO_2 layer, forming an intermediate phase where the materials were fully mixed and coordinated with DMSO on the slide. Toluene was then dropped onto the film while the substrate was spinning, causing the precipitation of a dense uniform perovskite film $>$ 300 nm thick - thicker than the mesoporous TiO_2 layer. The champion device had an $\eta > 16\%$.[60]

The inverted planar architecture (Figure 1.11 (e)) was first reported in 2013, when Jeng *et al.* used C_{60}, $PC_{61}BM$ and ICBA as ETLs for $CH_3NH_3PbI_3$ based PPV, achieving an η of 3.9%.[42] In that work, a very thin film of perovskite, $<$ 30 nm, was used, and so the efficiency was limited by the low thickness, poor film uniformity and crystallite size of the photoactive layer.[42] In 2014, Kim *et al.* improved upon this by using mixed DMF and GBL to improve the morphology, and reported a device $\eta > 6\%$.[61] In 2016 Shao *et al.* reported a device with $\eta > 19\%$, using a $CH_3NH_3PbI_3$ film over 500 nm thick,[62] prepared using a method taken from the literature. First PbI_2 was spin-cast onto a PEDOT:PSS HTL and dried at 70 °C. The CH_3NH_3I was then spin-cast on top, and the film was annealed at 100 °C.[63] During the annealing step, the slides were placed in a glass Petri dish, alongside a small amount of

DMF,[64] which resulted in crystals 100s of nm across (Figure 1.13). Shao *et al.* improved upon this reported procedure by adding a solvent annealing step after deposition of $PC_{61}BM$ using dichlorobenzene while also thermally annealing at 100 °C.[62] This ordered the fullerene molecules, reducing the trap state density and increasing the potential difference between the perovskite VB edge and the $PC_{61}BM$ LUMO position, leading to a significant increase in V_{oc}, reporting a maximum of 1.13 V.

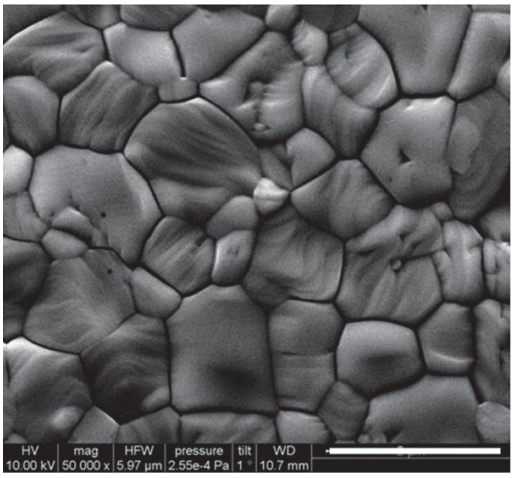

Figure 1.13: SEM of a perovskite film prepared using solvent annealing technique, scale bar is 2 µm. Taken from ref. [64].

1.8.3 Potential Problems with Perovskite Photovoltaics

Stability

Stabilising halide perovskites so that they are suitable for applications is one of the main challenges to be addressed in PPV research, and is also connected to environmental problems associated with tin and lead halide perovskites because of the toxicity of the degradation products. For outdoor, long-term applications, it is inevitable that the photoactive materials will be exposed to air and moisture even with encapsulation given sufficient time. Therefore the device must have a minimum inherent stability without encapsulation. $CH_3NH_3PbI_3$ degrades

in the presence of water in the manner:[65]

$$CH_3NH_3PbI_3 \xrightarrow{H_2O} CH_3NH_2 + HI + PbI_2$$

There is also some evidence that the organic component of $CH_3NH_3PbI_3$ is unstable towards oxygen under illumination, degrading by a photocatalysed deprotonation of the methylammonium cation:[66]

$$CH_3NH_3PbI_3 \xrightarrow{\text{Light}} CH_3NH_3PbI_3^*$$

$$O_2 + CH_3NH_3PbI_3^* \longrightarrow O_2^{\bullet -} + CH_3NH_3PbI_3^+$$

$$CH_3NH_3PbI_3 + O_2^{\bullet -} \longrightarrow CH_3NH_2 + PbI_2 + \tfrac{1}{2}I_2 + H_2O$$

There has been a lot of progress towards developing more stable PPVs in recent years.[67] Mei *et al.* reported a device in 2014 based on mesoporous TiO_2 and ZrO_2 with a porous carbon top electrode with an η of 12.8% that was stable for over 1000 hours in air under illumination.[68] The drawbacks to this were its complicated structure and use of a carbon electrode which would have too high a sheet resistance for large scale use. There have also been reports of the use of a layer of Al_2O_3 to protect the perovskite from oxidation with considerable success.[65, 69] Nui *et al.* first showed modest improvement in stability under warm humid conditions over the course of 18 hours,[65] Guarnera *et al.* then showed a device that was highly stable for 350 hours under illumination[69].

Toxicity

Lead and lead compounds are well known to be toxic towards the nervous system,[70] and the most common exposure to lead in humans comes from food because lead can transmit up the food chain.[71] Consequently leeching of lead into soil is a major concern,[72] and there are concerns as to whether lead perovskites will be suitable for commercial applications, given their

instability towards water which results in the production of partially water soluble lead compound PbI_2[65, 73]. There is some evidence that tin perovskites may also be unsuitable for PV applications due to the formation of HI acid as Sn(II) oxidises in water to Sn(IV), which could be dangerous to aquatic life, which is often sensitive to pH changes.[74] However, the overall potential impact of decomposition products of Sn perovskites is not as well understood.[75]

Although lead PPVs have achieved the highest η and stability to date, there are concerns over its toxicity, which has been widely documented.[76, 77] While it is still uncertain whether halide PPVs of any kind will be environmentally viable,[74, 78] tin halide perovskite may still be able to offer a less toxic potential alternative to lead perovskite.

However, it is still uncertain to what extent the toxicity of lead will be a problem; the small amount of perovskite required to make the 100s of nm thick films in PV devices could make the environmental impact of the lead of low significance.[78, 79]

Hysteresis

PPVs have been shown to exhibit hysteretic behaviour, that is different performance when scanning forward and reverse JV sweeps, which can cause an inflation of reported η in devices, making it difficult to predict the true performance for applications. Several explanations have been given for this behaviour, including the roles of surface trap states, ferroelectric effects caused by alignment of methylammonium ions, and iodide ion migration.[80] Currently the most favoured theory is iodide migration causing charge accumulation, possibly in combination with trap states.[81] For this reason it is always important to measure hysteresis when reporting on PVs of any kind, but particularly in the context of PPV research. The extent of hysteresis is dependent on the scan speed of a JV measurement; the faster the scan the less hysteresis is observed.[80] For example, a scan speed of 0.3 V/s may cause hysteresis to be hidden, and so slower scan speeds should be used.

1.8.4 Tin Perovskite Photovoltaics

Tin perovskites are a potential substitute for lead perovskites due to their having similar electrical properties and the advantage of a lower band gap than analogous lead perovskites which are closer to the ideal predicted by Shockley-Queisser limit for single-junction PV devices. The tin perovskite, $CH_3NH_3SnI_3$ has been shown to be effective in conjunction with mesoporous TiO_2 and has been reported to have a record η of 6%.[82] $CH_3NH_3SnI_{(3-x)}Br_x$[26, 82], $CsSnI_{(3-x)}Br_x$[83–85] and $CH(NH_2)_2SnI_{(3-x)}Br_x$[86, 87], where x is between 0 and 3, have all been reported for use in PVs.

Part of the reason for the low efficiency of tin PPVs compared with their lead analogues is due to their susceptibility to forming tin vacancy defects,[83, 88] which behave as p-type dopants, leading to high recombination losses; thereby reducing the fill factor (FF) and open-circuit voltage (V_{oc}) in devices. These vacacny defects may be charge balanced by Sn(IV) ions in the crystals or by an excess of Sn crystal-terminating groups. Additionally, tin perovskites crystallise much more rapidly after solution processing than their lead analogues; for example the black phase $CsSnI_3$ forms immediately on spin-spin casting from DMF solution.[89] Very fast crystallisation results in the formation of smaller crystals with low uniformity, lowering charge transport, and increasing the density of surface defects because of the high surface to volume ratio. Another problem which has limited research in tin perovskites is their susceptibility towards oxidation in air because Sn is more stable in the 4+ oxidation state than the 2+ state. Conversely, lead is more stable in the 2+ state due to relativistic contraction of the orbitals, due to the high charge of the Pb nucleus, which causes the electrons to move faster than in Sn (at speeds close enough to c to cause significant change in mass (Equation 1.8)), which reduces the Bohr radius of the electrons (Equation 1.9). This relativistic effect stabilises the s orbitals more than p orbitals, making the s electrons more strongly bound to the nucleus, and so less

able to participate in bonding interactions, or to be removed from the Pb atom. This is known as the "inert pair effect".[31, 90] Whilst this effect is present for tin, and is responsible for the meta-stability of the 2+ oxidation state, it is less pronounced. Consequently the black phase of $CsSnI_3$ eventually irreversibly converts to Cs_2SnI_6 upon air exposure, in which Sn is in its more stable 4+ oxidation state. $CsSnI_3$ has another stable phase; the 1-dimensional yellow phase (Y-$CsSnI_3$), which can form in the presence of moisture or other solvents.[16, 17]

At room temperature, in the absence of air, $CsSnI_3$ adopts a 3D orthorhombic perovskite structure which is known as the black phase. The E_g of this semiconductor is near optimal for PV applications ($\sim$ 1.3 eV [16]),[13] which combined with its high optical absorption coefficient ($\sim 10^4$ cm^{-1} in the visible region)[91] and low exciton binding energy ($\sim$ 18 meV),[27] makes $CsSnI_3$ attractive as a light harvesting semiconductor in PPVs because photoexcitation results in free carrier generation for light with wavelengths as long as $\sim$ 950 nm.[16] However, the material is prone to the formation of a high density of Sn cation vacancy defects, which serve as p-type dopants and recombination centres.[16, 88]

In practice the ingress of oxygen and moisture into PV devices is inevitable and so an important challenge in the area of lead-free PPV research is to develop strategies that can be used in conjunction with encapsulation to slow the rate of oxidation of Sn-perovskites enough for applications to be possible. There have been only a handful of literature reports relating to the use of Sn perovskites in PPVs which clearly demonstrate the potential to achieve high η [24–26, 82–84], although there are little quantitative data showing how device performance changes upon exposure to air.

Due to the propensity fo the *p*-type self-doping, $CsSnI_3$ was first used by Chung *et al.* as an HTL in PPVs in which a Ru complex dye, N719, was the primary light harvesting material.[24] In that work $CsSnI_3$ was synthesised using a vacuum melt process at 450 °C, and devices without N719 performed very badly with $\eta \sim 0.2\%$. That pioneering work was

quickly followed by Chen *et al.*,[25] who demonstrated a Schottky contact type PPV based on a vacuum evaporated layer of $CsSnI_3$ formed by sequential deposition of alternating layers of CsI and $SnCl_2$ followed by annealing at 175 °C to form the perovskite. Although the device fill factor (FF) was very low (~ 0.22) due to a very low shunt resistance and high series resistance. That was the first work in which $CsSnI_3$ served as the light harvester. Concurrently to this Zhou *et al.*[92] reported that $CsSnI_3$ could be synthesised at room temperature from a mixed solution of CsI and SnI_2, although, in that work, films formed using that that method were not tested for their optoelectronic properties or applications. In 2014, Noel *et al.* reported the highest η to date for a Sn PPV; $\sim 6\%$, achieved using $MASnI_3$ as the light harvesting semiconductor.[82] However those devices were also shown to exhibit a very large variation in performance and poor stability, with deeply coloured devices becoming completely transparent minutes upon exposure to air.[82] That work was published a few days before a report by Hao *et al.*[26] who showed that η close to 6% could be achieved using $CH_3NH_3SnIBr_2$ and that the V_{oc} could be tuned by varying the ratio of iodide to bromide as a result of a change in E_g. In 2016, Wang *et al.* reported the use of high quality films of $CsSnI_3$ in PV devices.[85] The $CsSnI_3$ was synthesised using a vacuum melt, and then transferred to a nitrogen filled glove-box, where it was dissolved in a mixture of DMF, acetonitrile and methyoxyacetonitrile at 20 wt%, and spin cast to form thin films. The spin cast films were annealed at 150 °C, which caused the crystal size to increase from $\sim$ 50 nm to $\sim$ 350 nm, allowing the authors to achieve devices with $\eta > 3\%$ using PCBM ETL. In 2017, Song *et al.* reported on the use of $CsSnI_3$ based PPVs using large excess of SnI_2 (1:2.5 ratio of CsI:SnI_2) in conjunction with a reducing atmosphere made by placing a hydrazine solution in the spin coater chamber, and using mesoporous TiO_2 ETL and achieved an $\eta > 4.8\%$.[93]

In 2015, Koh *et al.* reported on the use of $FASnI_3$ in conjunction with mesoporous TiO_2.[86] The authors achieved a champion η of 2.1% with a $J_{sc} > 20$ mA/cm^2 using a 20 mol% SnF_2

additive. The material has an E_g of 1.41 eV. In 2016, Lee *et al.* used $FASnI_3$ with 20 mol% added SnF_2 and 10 mol% added pyrazine prepared from DMSO solution, to form uniform layers on mesoporous TiO_2.[94] They achieved an η of 4.8% with much better *FF* (0.63) and V_{oc} (0.32) than the earlier paper by Koh *et al.* Also in 2016 Zhang *et al.* reported the use of $FASnI_2Br$ with an E_g of 1.68 eV, in planar architecture with vacuum evaporated C_{60} ETL. They achieved an η of 1.72%.[87] Later Liao *et al.* reported the use of $FASnI_3$ in planar architecture with $\eta > 6\%$ with C_{60} ETL, using a 10 mol% SnF_2 additive in the precursor solution, DMSO solvent and crystallising the perovskite with diethylether anti-solvent to form highly uniform films with large crystals.[95]

In 2017 there were demonstrations of PPVs with $\eta > 8\%$, and one of $\eta > 9\%$. The former, by Zhao *et al.*, used a mixed MA:FA A-site cation system using DMSO perovskite solution with chlorobenzene washing and 100 °C annealing in the inverted structure in conjunction with C_{60} ETL.[96] Shao *et al.* then reported on the use of partial substitution of FA with a large cation; phenylethylamonium (PEA), in their $FASnI_3$ percursor solutions, to form a phase separated 2D/3D perovskite, with the 2D separated to the bottom of the film acting as a template for the 3D perovskite, giving large ($\sim$ 1 µm), orientated crystals.[97] They reported $\eta > 9\%$ in the inverted structure in conjunction with C_{60} ETL.

Tin has also been used in mixed Sn-Pb perovskites; $CH_3NH_3Sn_xPb_{1-x}I_3$. By changing the ratio of lead to tin the band gap can be altered from $\sim$ 1.55 eV to $\sim$ 1.17 eV by altering the composition from $x = 0$ to 0.7; extending the absorption out to 1060 nm,[98] although functional devices using 100% Sn perovskite were not achieved. Zuo *et al.* later reported the use of mixed B-site perovskite made using $PbCl_2$ to improve morphology, and a 15 mol% substitution of Pb for Sn in a planar structure using $PC_{61}BM$ ETL and achieved an $\eta > 10\%$, which was an improvement over their 100% Pb control material.[99] Hao *et al.* also reported a series of mixed Sn-Pb halide perovskites in this range, displaying an anomolous trend in the

band gaps, with the onset for IPCE of $CH_3NH_3SnI_3$ being in between that of $CH_3NH_3PbI_3$ and that of $CH_3NH_3Pb_{0.25}Sn_{0.75}I_3$.[100] However, their highest reported device η was using the $CH_3NH_3PbI_3$, with $\eta > 8\%$, but did achieve $J_{sc} > 20$ mA/cm^2 and $\eta > 7\%$ for 50 mol% substitution of Pb for Sn.

1.8.5 Reduced Dimensional Perovskites

One approach for improving the stability of PPVs has been to use layered perovskites, which incorporate a large spacing cation (L) between layers which is hydrophobic to reduce water ingress. These have a general formula: $L_2A_{n-1}Pb_nI_{3n+1}$, where n is the thickness (in octahedra units) of the layers (so in the limit of $n \to \infty$, the material approaches standard perovskite $APbI_3$). While this has been shown to improve stability, by reducing the dimensionality the band gap of the perovskite increases due to quantum confinement (Figure 1.14), and the conductivity may also be expected to decrease in the direction normal to the planes of octahedra, both of which operate to reduce the short-circuit current density (J_{sc}) in devices compared with 3D lead perovskite.

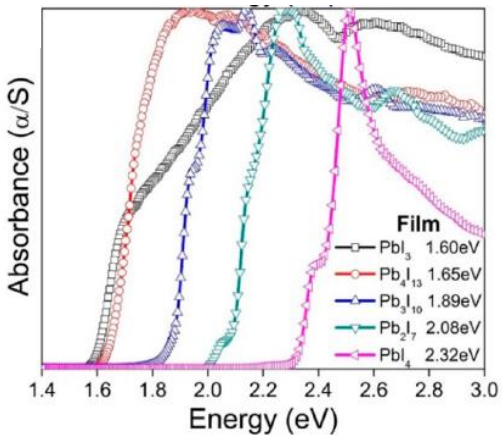

Figure 1.14: UV/vis/NIR absorbance spectra of films of $CH_3NH_3PbI_3$ and $(BA)_2(MA)_{n-1}Pb_nI_{3n+1}$, where $n = 1$, 2, 3 or 4. Taken from ref. [101]

Smith *et al.* reported on the use of $C_6H_5(CH_2)_2NH_2^+$ (PEA) as a spacing group to make $(PEA)_2(MA)_2Pb_3I_{10}$ (i.e. $n = 3$), leading to an $\eta > 4\%$, with a $V_{oc} > 1$ V.[102] Additionally they found that the XRD pattern of the $(PEA)_2(MA)_2Pb_3I_{10}$ was unchanged after 46 days in 52% humid air, whereas the $MAPbI_3$ films had significantly degraded after 20 days. Cao *et al.* later extended this work, using n-butylammonium (BA) instead of PEA as the spacing group, with more characterisation and different n values, using $n = 1$, 2, 3, 4 or ∞.[101] In this series the band gap goes from 2.24 eV for $n = 1$ to 1.60 ev for $n = 4$ and 1.52 eV for $n = \infty$ for the bulk materials. They also found that a film of the material $(BA)_2(MA)_2Pb_3I_{10}$ was visibly unchanged and had little change in its XRD pattern after 2 months in $\sim 40\%$ humid air, whereas the $MAPbI_3$ had degraded after a short time. For device performance, similar results were found to Smith *et al.* in that $\eta > 4\%$ was achieved for the best layered perovskite, where $n = 3$.

In 2016, Tsai *et al.* reported 2D perovskites in PVs which achieved $\eta > 12\%$ for $(BA)_2(MA)_{n-1}Pb_nI_{3n+1}$.[1
By spin casting the perovskite from heated solution (110 °C) which improved the crystallinity of the films, as evidenced by reduction in the full-width-at-half-maximum of peaks in the XRD patterns of the films. The best performing perovskite in devices was for $n = 4$.

1.8.6 Other Metal Halide Materials

In addition to substitution of lead for tin, there have been other attempts at exploring the potential of lead-free halide perovskites for PV applications. Hexagonal structured bismuth (III) halide materials, with the composition $A_3Bi_2I_9$, are probably the most widely studied mixed metal halide materials for use as light harvesters for PPVs after the Group 4 halide perovskites. The Bi materials have the advantage of being more stable towards humidity and oxygen than tin and lead halide perovskites. However, the best device η of Bi halide based PVs to date is $< 2\%$ (using $Cs_3Bi_2I_9$), largely due to low J_{sc} which results from the 0D structure

and relatively large band gap (> 2 eV) of these materials.[37, 104]

Körbel *et al.* reported a large computational screening of different perovskites containing elements from all across the Periodic Table (apart from radioactive elements, noble gases and lanthanides), to find materials appropriate for PV applications; i.e. materials with narrow direct band gaps and high charge carrier mobilities and small exciton binding energy.[105] Over 32000 possible combinations were tested, and 199 stable perovskites were found, but only two materials besides lead, tin and germanium halide perovskites were found to have appropriate band gaps; $BaPbO_3$ and $BaZrSe_3$. In that study the calculated band gaps were considerably underestimated from the experimental, e.g. a band gap of 0.85 eV was predicted for $CsSnI_3$ whereas the experimental values are at 1.3 eV [16, 17], which may limit the value of this study.

1.9 Context for this Project

When this project began in 2013, the field of PPVs was beginning to become very popular; and devices with $\eta > 10\%$ had been reported using $CH_3NH_3PbI_{3-x}Cl_x$ based PPV devices in 2012,[39] and in 2013 two papers were published, separately reporting lead PPV devices with $\eta \sim 15\%$ using different methods.[38, 41] However, there were concerns which still persist about whether lead halide perovskite would be suitable for use in commercial PV devices due to the well known toxicity of lead. $CsSnI_3$ had been used as an HTL in dye-sensitised solar cells with $\eta > 10\%$,[24] and was a promising choice for a lead-free perovskite light harvester due to its narrow band gap and high charge carrier mobilities.[16] However, there were known challenges associated with the instability towards oxygen and water, and its tendency to form *p*-type dopant states. At that time there had been no significant publications on the use of tin halide perovskite for use as a light harvester in photovoltaics.

References

[1] J. Melorose, R. Perroy, and S. Careas, "World population prospects: The 2015 revision summary and key findings," Tech. Rep., 2015.

[2] V. Smil, *Energy transitions: History, requirements, prospects*. Santa Barbara: Praeger/ABC CLIO, 2010.

[3] J. Bolt and J. L. van Zanden, "The Maddison Project: Collaborative research on historical national accounts," *Econ. Hist. Rev.*, vol. 67, pp. 627–651, 2014.

[4] P. Forster, V. Ramaswamy, P. Araxo, T. Bernsten, R. Betts, D. W. Fahey, J. Haywood, J. Lean, D. C. Lowe, G. Myhre, J. Nganga, R. Prinn, G. Raga, M. Schulz, and R. V. Dorland, "Changes in atmospheric constituents and in radiative forcing," in *Climate Change 2007: The Physical Science Basis*, 22, vol. 30, 2007, pp. 129–234.

[5] "BP statistical review of world energy," Tech. Rep., 2015.

[6] H. Ishii, K. Sugiyama, E. Ito, and K. Seki, "Energy level alignment and interfacial electronic structures at organic metal and organic organic interfaces," *Adv. Mater.*, vol. 11, pp. 605–625, 1999.

[7] R. T. Tung, "The physics and chemistry of the Schottky barrier height," *Appl. Phys. Rev.*, vol. 1, p. 011 304, 2014.

[8] D. M. Chapin, C. S. Fuller, and G. L. Pearson, "A new silicon p-n junction photocell for converting solar radiation into electrical power," *J. Appl. Phys.*, vol. 25, pp. 676–677, 1954.

[9] D. C. Jordan and S. R. Kurtz, "Photovoltaic degradation rates - an analytical Review," *Prog. Photovoltaics Res. Appl.*, vol. 21, pp. 12–29, 2013.

[10] *NREL chart*, 2016.

[11] F. C. Krebs, N. Espinosa, M. Hösel, R. R. Søndergaard, and M. Jørgensen, "25th anniversary article: Rise to power - OPV-based solar parks," *Adv. Mater.*, vol. 26, pp. 29–39, 2014.

[12] V. Fthenakis, "How long does it take for photovoltaics to produce the energy used?" *PE Mag.*, pp. 16–17, 2012.

[13] W. Shockley and H. J. Queisser, "Detailed balance limit of efficiency of p-n junction solar cells," *J. Appl. Phys.*, vol. 32, pp. 510–519, 1961.

[14] J. Werner, L. Barraud, A. Walter, M. Bräuninger, F. Sahli, D. Sacchetto, N. Tétreault, B. Paviet-Salomon, S.-J. Moon, C. Allebé, M. Despeisse, S. Nicolay, S. D. Wolf, B. Niesen, and C. Ballif, "Efficient near-infrared-transparent perovskite solar cells enabling direct comparison of 4 -terminal and monolithic perovskite/silicon tandem cells," *ACS energy Lett.*, vol. 1, pp. 474–480, 2016.

[15] V. I. Arkhipov and H. Bässler, "Exciton dissociation and charge photogeneration in pristine and doped conjugated polymers," *Phys. Status Solidi Appl. Res.*, vol. 201, pp. 1152–1187, 2004.

[16] I. Chung, J.-H. Song, J. Im, J. Androulakis, C. D. Malliakas, H. Li, A. J. Freeman, J. T. Kenney, and M. G. Kanatzidis, "$CsSnI_3$: Semiconductor or metal? High electrical conductivity and strong near-infrared photoluminescence from a single material. High hole mobility and phase-transitions.," *J. Am. Chem. Soc.*, vol. 134, pp. 8579–8587, 2012.

[17] C. C. Stoumpos, C. D. Malliakas, and M. G. Kanatzidis, "Semiconducting tin and lead iodide perovskites with organic cations: phase transitions, high mobilities, and near-infrared photoluminescent properties.," *Inorg. Chem.*, vol. 52, pp. 9019–9038, 2013.

[18] W. Werker, "Die kristallstruktur des Rb_2SnI_6 und Cs_2SnI_6," *Recl. des Trav. Chim. des Pays-Bas*, vol. 58, pp. 257–258, 1939.

[19] V. M. Goldschmidt, "Die gesetze der krystallochemie," *Naturwissenschaften*, vol. 14, pp. 477–485, 1927.

[20] C. Li, X. Lu, W. Ding, L. Feng, Y. Gao, and Z. Guo, "Formability of ABX_3 (X = F, Cl, Br, I) halide perovskites.," *Acta Crystallogr. B.*, vol. 64, pp. 702–707, 2008.

[21] D. Weber, "$CH_3NH_3PbX_3$, a Pb(II)-System with cubic perovskite structure," *Zeitschrift für Naturforsch.*, vol. 33b, pp. 1443–1445, 1978.

[22] A. Kojima, K. Teshima, Y. Shirai, and T. Miyasaka, "Organometal halide perovskites as visible-light sensitizers for photovoltaic cells.," *J. Am. Chem. Soc.*, vol. 131, pp. 6050–6051, 2009.

[23] M. Saliba, T. Matsui, J.-Y. Seo, K. Domanski, J.-P. Correa-Baena, N. Mohammad K., S. M. Zakeeruddin, W. Tress, A. Abate, A. Hagfeldt, and M. Grätzel, "Cesium-containing triple cation perovskite solar cells: Improved stability, reproducibility and high efficiency," *Energy Environ. Sci.*, vol. 9, pp. 1989–1997, 2016.

[24] I. Chung, B. Lee, J. He, R. P. H. Chang, and M. G. Kanatzidis, "All-solid-state dye-sensitized solar cells with high efficiency.," *Nature*, vol. 485, pp. 486–489, 2012.

[25] Z. Chen, J. J. Wang, Y. Ren, C. Yu, and K. Shum, "Schottky solar cells based on $CsSnI_3$ thin-films," *Appl. Phys. Lett.*, vol. 101, p. 093 901, 2012.

[26] F. Hao, C. C. Stoumpos, D. H. Cao, R. P. H. Chang, and M. G. Kanatzidis, "Lead-free solid-state organic–inorganic halide perovskite solar cells," *Nat. Photonics*, vol. 8, pp. 489–494, 2014.

[27] Z. Chen, C. Yu, K. Shum, J. J. Wang, W. Pfenninger, N. Vockic, J. Midgley, and J. T. Kenney, "Photoluminescence study of polycrystalline $CsSnI_3$ thin films: Determination of exciton binding energy," *J. Lumin.*, vol. 132, pp. 345–349, 2012.

[28] S. D. Stranks, G. E. Eperon, G. Grancini, C. Menelaou, M. J. P. Alcocer, T. Leijtens, L. M. Herz, A. Petrozza, and H. J. Snaith, "Electron-hole diffusion lengths exceeding 1 micrometer in an organometal trihalide perovskite absorber.," *Science*, vol. 342, pp. 341–344, 2013.

[29] G. Xing, N. Mathews, S. Sun, S. S. Lim, Y. M. Lam, M. Grätzel, S. Mhaisalkar, and T. C. Sum, "Long-range balanced electron- and hole-transport lengths in organic-inorganic $CH_3NH_3PbI_3$.," *Science*, vol. 342, pp. 344–347, 2013.

[30] L.-Y. Huang and W. R. L. Lambrecht, "Electronic band structure, phonons, and exciton binding energies of halide perovskites $CsSnCl_3$, $CsSnBr_3$, and $CsSnI_3$," *Phys. Rev. B*, vol. 88, p. 165 203, 2013.

[31] P. Umari, E. Mosconi, and F. De Angelis, "Relativistic GW calculations on $CH_3NH_3PbI_3$ and $CH_3NH_3SnI_3$ perovskites for solar cell applications.," *Sci. Rep.*, vol. 4, p. 4467, 2014.

[32] R. D. Shannon, "Revised effective ionic radii and systematic studies of interatomic distances in halides and chalcogenides," *Acta Crystallogr. Sect. A Found. Adv.*, vol. A32, pp. 751–767, 1976.

[33] P. P. Boix, S. Agarwala, T. M. Koh, N. Mathews, and S. G. Mhaisalkar, "Perovskite solar cells: Beyond methylammonium lead iodide," *J. Phys. Chem. Lett.*, vol. 6, pp. 898–907, 2015.

[34] P. Docampo, J. M. Ball, M. Darwich, G. E. Eperon, and H. J. Snaith, "Efficient organometal trihalide perovskite planar-heterojunction solar cells on flexible polymer substrates.," *Nat. Commun.*, vol. 4, p. 2761, 2013.

[35] Y. Zhang, X. Hu, L. Chen, Z. Huang, Q. Fu, Y. Liu, L. Zhang, and Y. Chen, "Flexible, hole transporting layer-free and stable $CH_3NH_3PbI_3$/ $PC_{61}BM$ planar heterojunction perovskite solar cells," *Org. Electron.*, vol. 30, pp. 281–288, 2016.

[36] J. Gong, S. Darling, and F. You, "Perovskite photovoltaics: Life-cycle assessment of energy and environmental impacts," *Energy Environ. Sci.*, vol. 8, pp. 1953–1968, 2015.

[37] S. Yang, W. Fu, Z. Zhang, H. Chen, and C.-Z. Li, "Recent advances in perovskite solar cells: Efficiency, stability and lead-free perovskite," *J. Mater. Chem. A*, vol. 5, pp. 11 462–11 482, 2017.

[38] J. Burschka, N. Pellet, S.-J. Moon, R. Humphry-Baker, P. Gao, M. K. Nazeeruddin, and M. Grätzel, "Sequential deposition as a route to high-performance perovskite-sensitized solar cells.," *Nature*, vol. 499, pp. 316–319, 2013.

[39] M. M. Lee, J. Teuscher, T. Miyasaka, T. N. Murakami, and H. J. Snaith, "Efficient hybrid solar cells based on meso-superstructured organometal halide perovskites.," *Science*, vol. 338, pp. 643–647, 2012.

[40] T. Leijtens, G. E. Eperon, S. Pathak, A. Abate, M. M. Lee, and H. J. Snaith, "Overcoming ultraviolet light instability of sensitized TiO_2 with meso-superstructured organometal tri-halide perovskite solar cells.," *Nat. Commun.*, vol. 4, p. 2885, 2013.

[41] M. Liu, M. B. Johnston, and H. J. Snaith, "Efficient planar heterojunction perovskite solar cells by vapour deposition.," *Nature*, vol. 501, pp. 395–398, 2013.

[42] J.-Y. Jeng, Y.-F. Chiang, M.-H. Lee, S.-R. Peng, T.-F. Guo, P. Chen, and T.-C. Wen, "$CH_3NH_3PbI_3$ perovskite/fullerene planar-heterojunction hybrid solar cells.," *Adv. Mater.*, vol. 25, pp. 3727–3732, 2013.

[43] H.-S. Kim, S. H. Im, and N.-G. Park, "Organolead halide perovskite: new horizons in solar cell research," *J. Phys. Chem. C*, vol. 118, pp. 5615–5625, 2014.

[44] D. Ramirez, M. A. M. Escobar, J. F. Montoya, and F. Jaramillo, "Understanding the role of the mesoporous layer in the thermal crystallization of a meso-superstructured perovskite solar cell," *J. Phys. Chem. C*, vol. 120, pp. 8559–8567, 2016.

[45] W. R. Erwin, H. F. Zarick, E. M. Talbert, and R. Bardhan, "Light trapping in mesoporous solar cells with plasmonic nanostructures," *Energy Environ. Sci.*, vol. 9, pp. 1577–1601, 2016.

[46] C. J. C. Barbe, F. Arendse, P. Comte, M. Jirousek, F. Lenzmann, V. Shklover, M. Gra, and M. Gratzel, "Nanocrystalline Titanium Oxide Electrodes for Photovoltaic Applications," *J. Am. Ceram. Soc.*, vol. 80, pp. 3157–3171, 1997.

[47] M. Mojica, J. A. Alonso, and F. Méndez, "Synthesis of fullerenes," *J. Phys. Org. Chem.*, vol. 26, pp. 526–539, 2013.

[48] T. Salim, S. Sun, Y. Abe, A. Krishna, A. C. Grimsdale, and Y. M. Lam, "Perovskite-based solar cells: impact of morphology and device architecture on device performance," *J. Mater. Chem. A*, vol. 3, pp. 8943–8969, 2015.

[49] N. K. Elumalai, M. A. Mahmud, D. Wang, and A. Uddin, "Perovskite solar cells: Progress and advancements," *Energies*, vol. 9, p. 861, 2016.

[50] W. Nie, H. Tsai, R. Asadpour, A. J. Neukirch, G. Gupta, J. J. Crochet, M. Chhowalla, S. Tretiak, M. A. Alam, and H.-l. Wang, "High-efficiency solution-processed perovskite solar cells with millimeter-scale grains," *Science*, vol. 347, pp. 522–525, 2015.

[51] J. A. Christians, R. C. M. Fung, and P. V. Kamat, "An inorganic hole conductor for organo-lead halide perovskite solar cells. Improved hole conductivity with copper iodide.," *J. Am. Chem. Soc.*, vol. 136, pp. 758–764, 2014.

[52] N. J. Jeon, J. Lee, J. H. Noh, M. K. Nazeeruddin, M. Grätzel, and S. I. Seok, "Efficient inorganic-organic hybrid perovskite solar cells based on pyrene arylamine derivatives as hole-transporting materials.," *J. Am. Chem. Soc.*, vol. 135, pp. 19 087–19 090, 2013.

[53] J. Wang, S. Wang, X. Li, L. Zhu, Q. Meng, Y. Xiao, and D. Li, "Novel hole transporting materials with a linear π-conjugated structure for highly efficient perovskite solar cells.," *Chem. Commun. (Camb).*, vol. 50, pp. 5829–32, 2014.

[54] A. S. Subbiah, A. Halder, S. Ghosh, N. Mahuli, G. Hodes, and S. K. Sarkar, "Inorganic hole conducting layers for perovskite-based solar cells," *J. Phys. Chem. Lett.*, vol. 5, pp. 1748–1753, 2014.

[55] H.-S. Kim, C.-R. Lee, J.-H. Im, K.-B. Lee, T. Moehl, A. Marchioro, S.-J. Moon, R. Humphry-Baker, J.-H. Yum, J. E. Moser, M. Grätzel, and N.-G. Park, "Lead iodide perovskite sensitized all-solid-state submicron thin film mesoscopic solar cell with efficiency exceeding 9%.," *Sci. Rep.*, vol. 2, p. 591, 2012.

[56] Q. Chen, H. Zhou, Y. Fang, A. Z. Stieg, T.-B. Song, H.-H. Wang, X. Xu, Y. Liu, S. Lu, J. You, P. Sun, J. McKay, M. S. Goorsky, and Y. Yang, "The optoelectronic role of chlorine in $CH_3NH_3PbI_3$(Cl)-based perovskite solar cells," *Nat. Commun.*, vol. 6, pp. 1–9, 2015.

[57] N. Pellet, P. Gao, G. Gregori, T.-Y. Yang, M. K. Nazeeruddin, J. Maier, and M. Grätzel, "Mixed-organic-cation perovskite photovoltaics for enhanced solar-light harvesting.," *Angew. Chem. Int. Ed. Engl.*, vol. 53, pp. 3151–3157, 2014.

[58] C. Yi, J. Luo, S. Meloni, A. Boziki, N. Ashari-Astani, C. Grätzel, S. M. Zakeeruddin, U. Röthlisberger, and M. Grätzel, "Entropic stabilization of mixed A-cation ABX_3 metal halide perovskites for high performance perovskite solar cells," *Energy Environ. Sci.*, vol. 9, pp. 656–662, 2016.

[59] T. Jesper Jacobsson, J.-P. Correa-Baena, M. Pazoki, M. Saliba, K. Schenk, M. Grätzel, and A. Hagfeldt, "Exploration of the compositional space for mixed lead halogen perovskites for high efficiency solar cells," *Energy Environ. Sci.*, vol. 9, pp. 1706–1724, 2016.

[60] N. J. Jeon, J. H. Noh, Y. C. Kim, W. S. Yang, S. Ryu, and S. I. Seok, "Solvent engineering for high-performance inorganic-organic hybrid perovskite solar cells.," *Nat. Mater.*, vol. 13, pp. 897–903, 2014.

[61] H.-B. Kim, H. Choi, J. Jeong, S. Kim, B. Walker, S. Song, and J. Y. Kim, "Mixed solvents for the optimization of morphology in solution-processed, inverted-type perovskite/fullerene hybrid solar cells.," *Nanoscale*, vol. 6, pp. 6679–6683, 2014.

[62] Y. Shao, Y. Yuan, and J. Huang, "Correlation of energy disorder and open-circuit voltage in hybrid perovskite solar cells," *Nat. Energy*, vol. 1, p. 15 001, 2016.

[63] Z. Xiao, C. Bi, Y. Shao, Q. Dong, Q. Wang, Y. Yuan, C. Wang, Y. Gao, and J. Huang, "Efficient, high yield perovskite photovoltaic devices grown by interdiffusion of solution-processed precursor stacking layers," *Energy Environ. Sci.*, vol. 7, p. 2619, 2014.

[64] Z. Xiao, Q. Dong, C. Bi, Y. Shao, Y. Yuan, and J. Huang, "Solvent annealing of perovskite-induced crystal growth for photovoltaic-device efficiency enhancement," *Adv. Mater.*, vol. 26, pp. 6503–6509, 2014.

[65] G. Niu, W. Li, F. Meng, L. Wang, H. Dong, and Y. Qiu, "Study on the stability of $CH_3NH_3PbI_3$ films and the effect of post-modification by aluminum oxide in all-solid-state hybrid solar cells," *J. Mater. Chem. A*, vol. 2, pp. 705–710, 2014.

[66] N. Aristidou, I. Sanchez-Molina, T. Chotchuangchutchaval, M. Brown, L. Martinez, T. Rath, and S. A. Haque, "The role of oxygen in the degradation of methylammonium lead trihalide perovskite photoactive layers," *Angew. Chemie Int. Ed.*, vol. 54, pp. 8208–8212, 2015.

[67] T. A. Berhe, W.-N. Su, C.-H. Chen, C.-J. Pan, J.-H. Cheng, H.-M. Chen, M.-C. Tsai, L.-Y. Chen, A. A. Dubale, and B.-J. Hwang, "Organometal halide perovskite solar cells: degradation and stability," *Energy Environ. Sci.*, vol. 9, pp. 323–356, 2016.

[68] A. Mei, X. Li, L. Liu, Z. Ku, T. Liu, Y. Rong, M. Xu, M. Hu, J. Chen, Y. Yang, M. Grätzel, and H. Han, "A hole-conductor–free, fully printable mesoscopic perovskite solar cell with high stability," *Science*, vol. 345, pp. 295–298, 2014.

[69] S. Guarnera, A. Abate, W. Zhang, J. M. Foster, G. Richardson, A. Petrozza, and H. J. Snaith, "Improving the long-term stability of perovskite solar cells with a porous Al_2O_3 buffer layer," *J. Phys. Chem. Lett.*, vol. 6, pp. 432–437, 2015.

[70] G. Flora, D. Gupta, and A. Tiwari, "Toxicity of lead: a review with recent updates," *Interdiscip. Toxicol.*, vol. 5, pp. 47–58, 2012.

[71] M. Wierzbicka and D. Antosiewicz, "How lead can easily enter the food chain - a study of plant roots," *Sci. Total Environ.*, vol. 134, pp. 423–429, 1993.

[72] European Food Safety Authority, "Scientific opinion on lead in food," *EFSA J.*, vol. 8, p. 1570, 2010.

[73] H. L. Clever and F. J. Johnston, "The solubility of some sparingly soluble lead salts: An evaluation of the solubility in water and aqueous electrolyte solution," *J. Phys. Chem. Ref. Data*, vol. 9, pp. 751–784, 1980.

[74] A. Babayigit, A. Ethirajan, M. Muller, and B. Conings, "Toxicity of organometal halide perovskite solar cells," *Nat. Mater.*, vol. 15, pp. 247–251, 2016.

[75] A. Babayigit, D. Duy Thanh, A. Ethirajan, J. Manca, M. Muller, H.-G. Boyen, and B. Conings, "Assessing the toxicity of Pb- and Sn-based perovskite solar cells in model organism Danio rerio," *Sci. Rep.*, vol. 6, p. 18 721, 2016.

[76] F. Bischoff, L. C. Maxwell, R. D. Evans, and F. R. Nuzum, "Studies on the toxicity of various lead compounds given intravenously," *J. Pharmacol. Exp. Ther.*, vol. 34, pp. 85–109, 1928.

[77] O. Tarragó, "Lead toxicity," *Agency Toxic Subst. Dis. Regist.*, 2010.

[78] L. Serrano-Lujan, N. Espinosa, T. T. Larsen-Olsen, J. Abad, A. Urbina, and F. C. Krebs, "Tin- and lead-based perovskite solar cells under scrutiny: An environmental perspective," *Adv. Energy Mater.*, vol. 5, p. 1 501 119, 2015.

[79] J. Zhang, X. Gao, Y. Deng, Y. Zha, and C. Yuan, "Comparison of life cycle environmental impacts of different perovskite solar cell systems," *Sol. Energy Mater. Sol. Cells*, vol. 166, pp. 9–17, 2017.

[80] H. J. Snaith, A. Abate, J. M. Ball, G. E. Eperon, T. Leijtens, N. K. Noel, S. D. Stranks, J. T.-W. Wang, K. Wojciechowski, and W. Zhang, "Anomalous hysteresis in perovskite solar cells," *J. Phys. Chem. Lett.*, vol. 5, pp. 1511–1515, 2014.

[81] S. V. Reenen, M. Kemerink, and H. J. Snaith, "Modeling anomalous hysteresis in perovskite solar cells," *J. Phys. Chem. Lett.*, vol. 6, pp. 3808–3814, 2015.

[82] N. K. Noel, S. D. Stranks, A. Abate, C. Wehrenfennig, S. Guarnera, A.-A. Haghighirad, A. Sadhanala, G. E. Eperon, S. K. Pathak, M. B. Johnston, A. Petrozza, L. M. Herz, and H. J. Snaith, "Lead-free organic-inorganic tin halide perovskites for photovoltaic applications," *Energy Environ. Sci.*, vol. 7, pp. 3061–3068, 2014.

[83] M. H. Kumar, S. Dharani, W. L. Leong, P. P. Boix, R. R. Prabhakar, T. Baikie, C. Shi, H. Ding, R. Ramesh, M. Asta, M. Graetzel, S. G. Mhaisalkar, and N. Mathews, "Lead-free halide perovskite solar cells with high photocurrents realized through vacancy modulation," *Adv. Mater.*, vol. 26, pp. 7122–7127, 2014.

[84] D. Sabba, H. K. Mulmudi, R. R. Prabhakar, T. Krishnamoorthy, T. Baikie, P. P. Boix, S. Mhainsalkar, and N. Mathews, "Impact of anionic Br^- substitution on open circuit voltage in lead free perovskite ($CsSnI_{3-x}Br_x$) solar cells .," *J. Phys. Chem. C*, vol. 119, pp. 1763–1767, 2015.

[85] N. Wang, Y. Zhou, M. G. Ju, H. F. Garces, T. Ding, S. Pang, X. C. Zeng, N. P. Padture, and X. W. Sun, "Heterojunction-depleted lead-free perovskite solar cells with coarse-grained B-γ -$CsSnI_3$ thin films," *Adv. Energy Mater.*, vol. 6, p. 1 601 130, 2016.

[86] T. M. Koh, T. Krishnamoorthy, N. Yantara, C. Shi, W. L. Leong, P. P. Boix, A. C. Grimsdale, S. G. Mhaisalkar, and N. Mathews, "Formamidinium tin-based perovskite with low E_g for photovoltaic applications," *J. Mater. Chem. A*, vol. 3, pp. 14 996–15 000, 2015.

[87] M. Zhang, M. Lyu, J.-H. Yun, M. Noori, X. Zhou, N. A. Cooling, Q. Wang, H. Yu, P. C. Dastoor, and L. Wang, "Low-temperature processed solar cells with formamidinium tin halide perovskite/fullerene heterojunctions," *Nano Res.*, vol. 9, pp. 1570–1577, 2016.

[88] P. Xu, S. Chen, H.-J. Xiang, X.-G. Gong, and S.-H. Wei, "Influence of defects and synthesis conditions on the photovoltaic performance of perovskite semiconductor $CsSnI_3$," *Chem. Mater.*, vol. 26, pp. 6068–6072, 2014.

[89] F. Hao, C. C. Stoumpos, P. Guo, N. Zhou, T. J. Marks, R. P. H. Chang, and M. G. Kanatzidis, "Solvent-mediated crystallization of $CH_3NH_3SnI_3$ films for heterojunction depleted perovskite solar cells," *J. Am. Chem. Soc.*, vol. 137, pp. 11 445–11 452, 2015.

[90] P. Pyykkö, "Relativistic effects in structural chemistry," *Chem. Rev.*, vol. 88, pp. 563–594, 1988.

[91] K. Shum, Z. Chen, J. Qureshi, C. Yu, J. J. Wang, W. Pfenninger, N. Vockic, J. Midgley, and J. T. Kenney, "Synthesis and characterization of $CsSnI_3$ thin films," *Appl. Phys. Lett.*, vol. 96, p. 221 903, 2010.

[92] Y. Zhou, H. F. Garces, B. S. Senturk, A. L. Ortiz, and N. P. Padture, "Room temperature "one-pot" solution synthesis of nanoscale $CsSnI_3$ orthorhombic perovskite thin films and particles," *Mater. Lett.*, vol. 110, pp. 127–129, 2013.

[93] T.-B. Song, T. Yokoyama, S. Aramaki, and M. G. Kanatzidis, "Performance Enhancement of Lead-Free Tin-Based Perovskite Solar Cells with Reducing Atmosphere-Assisted Dispersible Additive," *ACS Energy Lett.*, vol. 2, pp. 897–903, 2017.

[94] S. J. Lee, S. S. Shin, Y. C. Kim, D. Kim, T. K. Ahn, J. H. Noh, J. Seo, and S. I. Seok, "Fabrication of efficient formamidinium tin iodide perovskite solar cells through SnF_2-pyrazine complex," *J. Am. Chem. Soc.*, vol. 138, pp. 3974–3977, 2016.

[95] W. Liao, D. Zhao, Y. Yu, C. R. Grice, C. Wang, A. J. Cimaroli, P. Schulz, W. Meng, K. Zhu, R. G. Xiong, and Y. Yan, "Lead-free inverted planar formamidinium tin triiodide perovskite solar cells achieving power conversion efficiencies up to 6.22%," *Adv. Mater.*, vol. 28, pp. 9333–9340, 2016.

[96] Z. Zhao, F. Gu, Y. Li, W. Sun, S. Ye, H. Rao, Z. Liu, Z. Bian, and C. Huang, "Mixed-Organic-Cation Tin Iodide for Lead-Free Perovskite Solar Cells with an Efficiency of 8.12%," *Adv. Sci.*, vol. 1700204, 2017.

[97] S. Shao, J. Liu, G. Portale, H.-H. Fang, G. R. Blake, G. H. ten Brink, L. J. A. Koster, and M. A. Loi, "Highly Reproducible Sn-Based Hybrid Perovskite Solar Cells with 9% Efficiency," *Adv. Energy Mater.*, vol. 1702019, p. 1 702 019, 2017.

[98] Y. Ogomi, A. Morita, S. Tsukamoto, T. Saitho, N. Fujikawa, Q. Shen, T. Toyoda, K. Yoshino, S. S. Pandey, and S. Hayase, "$CH_3NH_3Sn_xPb_{(1-x)}I_3$ perovskite solar cells covering up to 1060 nm," *J. Phys. Chem. Lett.*, vol. 5, pp. 1004–1011, 2014.

[99] F. Zuo, S. T. Williams, P. W. Liang, C. C. Chueh, C. Y. Liao, and A. K. Y. Jen, "Binary-metal perovskites toward high-performance planar-heterojunction hybrid solar sells," *Adv. Mater.*, vol. 26, pp. 6454–6460, 2014.

[100] F. Hao, C. C. Stoumpos, R. P. H. Chang, and M. G. Kanatzidis, "Anomalous band gap behavior in mixed Sn and Pb perovskites enables broadening of absorption spectrum in solar cells," *J. Am. Chem. Soc.*, vol. 136, pp. 8094–8099, 2014.

[101] D. H. Cao, C. C. Stoumpos, O. K. Farha, J. T. Hupp, and M. G. Kanatzidis, "Two-dimensional homologous perovskites as light absorbing materials for solar cell applications," *J. Am. Chem. Soc.*, vol. 2, pp. 7843–7850, 2015.

[102] I. C. Smith, E. T. Hoke, D. Solis-ibarra, M. D. Mcgehee, and H. I. Karunadasa, "A layered hybrid perovskite solar-cell absorber with enhanced moisture stability," *Angew. Chemie Int. Ed.*, vol. 126, pp. 11 414–11 417, 2014.

[103] H. Tsai, W. Nie, J.-C. Blancon, C. C. Stoumpos, R. Asadpour, B. Harutyunyan, A. J. Neukirch, R. Verduzco, J. J. Crochet, S. Tretiak, L. Pedesseau, J. Even, M. A. Alam, G. Gupta, J. Lou, P. M. Ajayan, M. J. Bedzyk, M. G. Kanatzidis, and A. D. Mohite, "High-efficiency two-dimensional Ruddlesden–Popper perovskite solar cells," *Nature*, vol. 536, pp. 312–316, 2016.

[104] B. W. Park, B. Philippe, X. Zhang, H. Rensmo, G. Boschloo, and E. M. J. Johansson, "Bismuth based hybrid perovskites $A_3Bi_2I_9$ (A: Methylammonium or cesium) for solar cell application," *Adv. Mater.*, vol. 27, pp. 6806–6813, 2015.

[105] S. M. Körbel, M. Marques, and S. Botti, "Stability and electronic properties of new inorganic perovskites from high-throughput ab initio calculations," *J. Mater. Chem. C*, vol. 4, pp. 3157–3167, 2016.

Chapter 2

Experimental Techniques

This chapter describes the experimental techniques and methods used in the research presented in this thesis.

2.1 Scanning Electron Microscopy

Scanning electron microscopy (SEM) is an imaging method in which, under high vacuum, a beam of electrons generated by an electron gun using a heated tungsten filament is accelerated by an electric field, and focused with a magnetic lens onto the sample, as schematically illustrated in Figure 2.1. The primary electron beam causes secondary electrons to be ejected from the sample which are collected by a detector which measures the secondary electron current as the primary electron beam is scanned in a raster pattern across the area of sample of interest. Electron microscopy is able to achieve much higher resolution than optical microscopy because the de Broglie wavelength of an electron is much smaller than that of visible light.

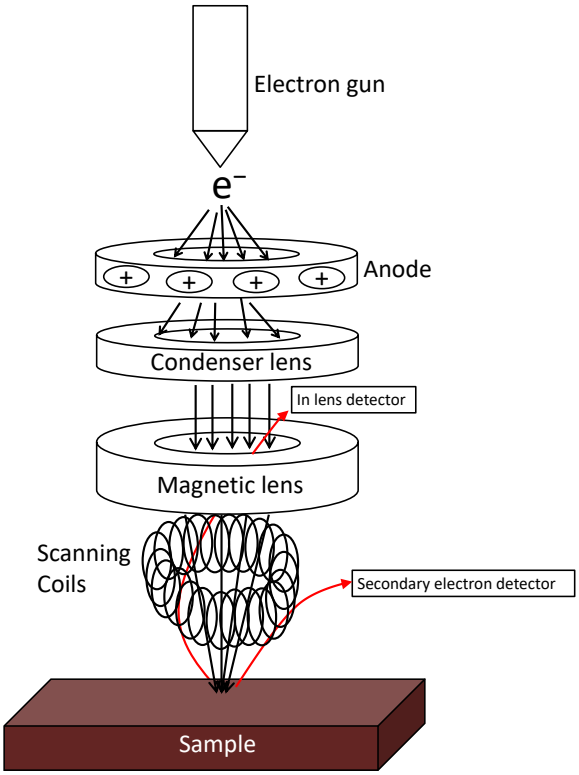

Figure 2.1: Schematic of the main components of an SEM.

The wavelength, λ, of matter is calculated using the de Broglie equation:

$$\lambda = \frac{h}{p} \tag{2.1}$$

where h is the Planck constant, and p is momentum. An electron accelerated through a 10 kV field would gain kinetic energy of 10 keV, which translates to a λ of 1.23×10^{-2} nm (Equations 2.2 - 2.4).

$$E_k = QV = 1.602 \times 10^{-19} \times 10000 \text{ J} = \sqrt{p^2c^2 + m_0^2c^4} \tag{2.2}$$

$$pc = \sqrt{E_k^2 + 2E_k m_0 c^2} \simeq \sqrt{2E_k m_0 c^2} = 1.620 \times 10^{-14} \text{ kg m}^2 \text{ s}^{-2} \tag{2.3}$$

$$\lambda \simeq \frac{hc}{1.62010^{-14}} = 1.23 \times 10^{-2} \text{ nm} \tag{2.4}$$

where E_k is kinetic energy, Q is charge on a particle, V is the accelerating voltage, m_0 is the particle (electron) rest mass, and c is the speed of light in vacuum.

However, in practice SEM is typically limited to a spatial resolution of approximately 5 nm, which is limited by the interaction volume and spot size of the electron beam before it approaches the diffraction limit. SEM requires conducting samples or samples which are deposited on conducting substrates otherwise sample charging occurs which distorts the image. In this thesis SEM imaging was performed using a Zeiss SUPRA 55VP FEGSEM. Crystal size analysis of images was performed using ImageJ software.[1]

2.2 Atomic Force Microscopy

Atomic force microscopy (AFM) in tapping mode was used in this thesis to measure surface topography and film thickness. This technique uses the non-covalent interactions between a sharp tip and the surface of the sample of interest to construct an image of surface topography. In tapping mode the tip is made to oscillate close to its resonance frequency using a piezo element in the canilever holder. The detector monitors small changes in the position of the tip by monitoring the position of a laser reflected off of the cantilever using a quadrant detector (Figure 2.2 (a)). The closer the tip is to the sample surface, the lower the amplitude of oscillation due to the increased damping interaction between the tip and surface (Figure 2.2 (b)). AFM is capable of resolving differences in Z-position (i.e. on the axis normal to the sample's surface) of ~ 0.1 nm. The force of interaction between the tip can be described by a van der Waals type Lennard-Jones potential, where the dipolar adhesion forces scale with an inverse d^6 relation and the repulsive electrostatic force scales with an inverse d^{12} relation, where d is the tip-substrate separation (Figure 2.2 (c)). The main determinant of the lateral resolution of an AFM is the radius of the tip of the probe, which means that features smaller than the tip radius will appear to be larger than they truly are (Figure 2.2 (d)). AFM measurements were performed using a Veeco Multimode using tapping mode. AFM images were analysed using the software

WSxM.[2]

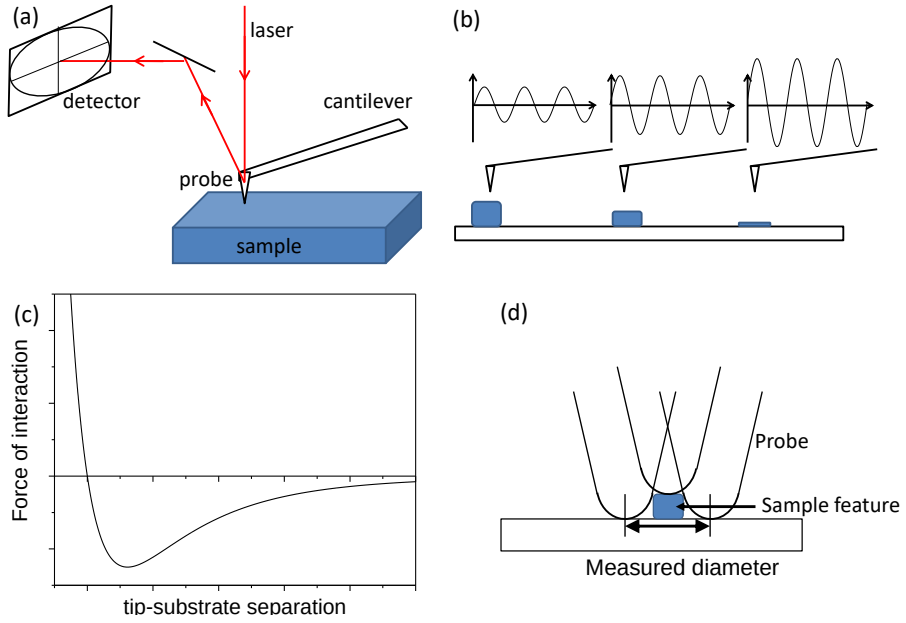

Figure 2.2: **(a)** Depiction of cantilever and detector of Atomic Force Microscope with laser being used to monitor changes in cantilever deflection, **(b)** diagram of tip amplitude of oscillation changes with respect to distance of tip from surface, **(c)** Lenard-Jones potential energy curve for an AFM tip interacting with a solid surface, **(d)** depiction of an AFM measuring a feature that is smaller than the tip radius.

2.3 X-ray Diffraction

Diffraction occurs when a plane wave is incident on narrow openings of similar size to the wavelength of the wave, such that as the wave passes through the openings it spreads out. If there are multiple openings the exiting waves interfere with one another either constructively or destructively (Figure 2.3), which leads to positions where the waves are observed, and positions where they are not (Figure 2.4); the simplest example of diffraction is the dual slit experiment. Constructive interference is only observed at certain angles, and the wave can be seen as bright spots. Conversely, when there is destructive interference, the wave can't be seen and there are

dark spots (Figure 2.4).

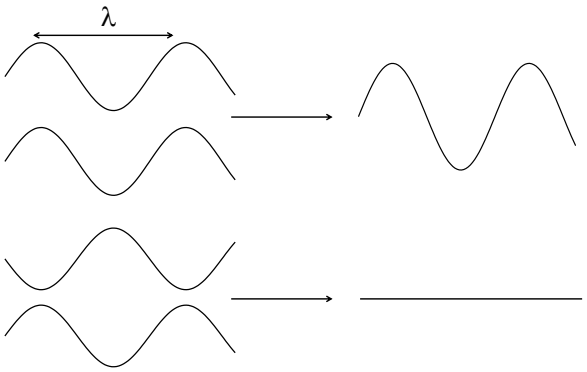

Figure 2.3: Two types of interference: Constructive (above) and destructive (below).

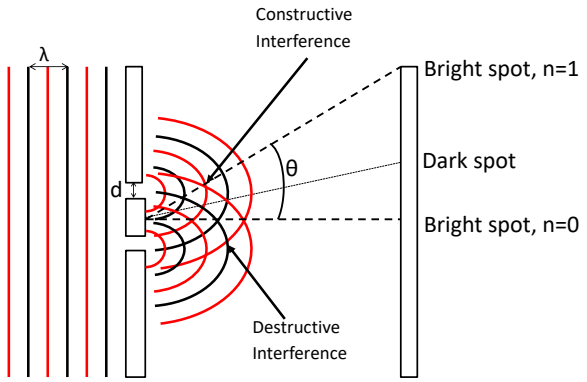

Figure 2.4: Dual slit diffraction

The wavelength of X-rays used for the X-ray diffraction measurement technique is of the same order as the distance between atoms in a crystal lattice. X-rays are directed towards a sample and are diffracted by planes of atoms – specifically the electrons. The intensity of the peaks is related to the density of atoms and the electron density associated with the atoms in the diffracting plane: the heavier the atom, the higher its scattering power. The angle at which peaks are observed in the diffraction pattern is related to the distance, d, between planes of atoms; the lower the d-spacing, the greater the angle of diffraction which is calculated using the Bragg equation;

$$n\lambda = 2d\sin(\theta) \tag{2.5}$$

where θ is the angle of incidence and of reflection of X-rays on the sample, $2d\sin(\theta)$ represents the difference in distance travelled by a photon reflecting off of one plane of atoms and by a photon reflecting off of an adjacent plane of atoms. When $2d\sin(\theta)$ is equal to an integer multiple of the wavelength of the X-rays, there will be constructive interference, leading to a peak in the X-ray pattern (Figure 2.5).

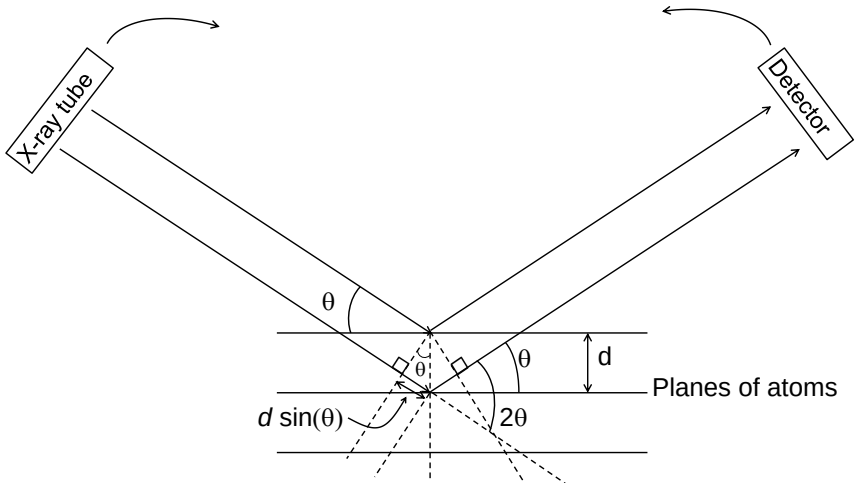

Figure 2.5: Diagram of X-ray Diffraction

In this work a Cu $K_{\alpha 1+2}$ X-ray source for which the average wavelength of the X-rays is 1.5418 Å. Thin films of the samples were deposited onto 11×11 mm^2 cut microscope slides, and XRD patterns were measured, usually under nitrogen, using a Bruker D8 diffractometer equipped with an Anton-Paar HTK900 gas chamber in θ-θ mode. The D8 does not have an adjustable z-stage position, and so when thin films on glass substrates were measured, there was an shift in peak positions from the predicted values to higher 2θ angles. A Panalytical X'Pert Pro MRD with an adjustable stage was also used for some experiments, usually under flow of nitrogen. Simulated powder patterns were calculated using the program Mercury with crystallographic information files (CIFs) from the inorganic crystallographic structure database

(ICSD).

Most samples investigated using XRD as part of the work presented in this thesis were thin films supported on glass substrates, so there is a variable peak displacement in all patterns stemming from the glass slides being taller than the sample holder, which causes peaks to be observed at slightly higher angles than they should, and reduces the intensity of peaks. This is because X-rays which reflect off of the surface of the sample must be incident at a lower angle than the centre of the beam, and so the effective θ angle is lower than the measured angle, and the focus of the beam is displaced so a smaller proportion of the beam reflects off of the surface to reach the detector (Figure 2.6).

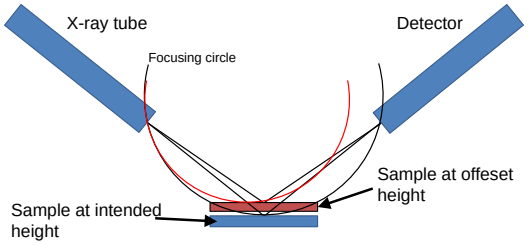

Figure 2.6: Diagram illustrating why there is a difference in observed 2θ when the sample position is different from the position of the sample holder.

Therefore the effect is a function of the ratio between the difference in position between the sample and the ideal sample location, the distance between the sample and the detector, and the θ angle. i.e. the greater the height offset, the smaller distance between the sample and the detector, and the smaller the θ angle, the greater the error on the position of peaks in the XRD pattern. This was corrected by changing the 2θ-axis offset of the pattern to match that of a simulated pattern.

2.4 Photovoltaic Device Testing

Device testing was performed in the same glove box as used for device fabrication unless otherwise stated. Current density-voltage (JV) curves were measured using a Keithley 2400 source-meter in the dark and under illumination from an ABET technologies Sun 2000 Solar Simulator which is based on a xenon short arc lamp with AM1.5G filters to simulate solar illumination at 100 mW/cm^2 (1 sun), calibrated using a silicon photodiode which generates a short circuit current of 45 mA/cm^2 under this condition. Devices were typically tested by sweeping a voltage across them from -1 V to $+1$ V in 0.01 V increments at a rate of 0.1 V/s, using a LabVIEW program to control the Keithley.[3] An equivalent circuit diagram of a photovoltaic is shown in Figure 2.7 (a), in a JV measurement the voltage is applied across the two terminals.

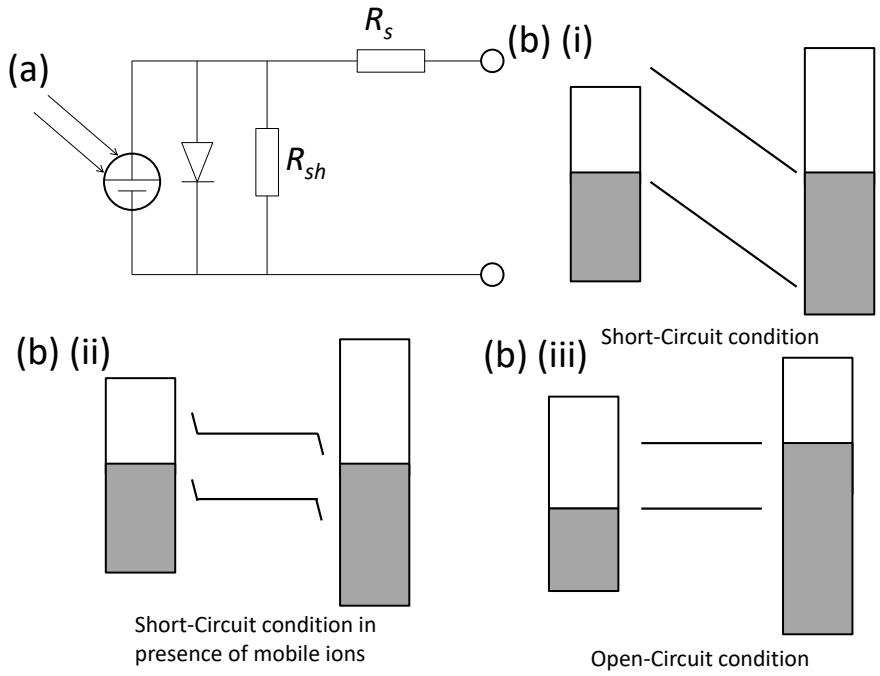

Figure 2.7: **(a)** Equivalent circuit diagram for a PV device, where R_{s} is series resistance and R_{sh} is shunt resistance. **(b)** Energy level diagrams of a simplified single layer PV device at the **(i)** short circuit condition in the absence of mobile ion vacancies, **(ii)** in the presence of mobile ion vacancies, and **(ii)** open circuit condition.

From the JV measurement the parameters J_{sc}, V_{oc}, FF, and η can be determined. The J_{sc} is the current density when the load resistance is zero, which corresponds to the condition when the E_{f} of the two electrodes are aligned and the built-in potential falling across the semiconductor is at a maximum (Figure 2.7 (b)(i)). However, in PPVs mobile ions in the crystal structure act to screen the electric field across the device (Figure 2.7 (b) (ii)).[4] V_{oc} is the voltage across a load that reduces the current to zero (Figure 2.7 (b)(iii)). The maximum V_{oc} is equal to the difference in energy between the LUMO of the electron transport layer and the valence band edge of the hole transport layer or light harvester. The FF is determined by the series (R_{s}) and shunt resistances (R_{sh}), where high series resistances and low shunt resistances will degrade the FF. The maximum achievable FF for p-n junctions (i.e. very low

R_s and very high R_{sh}) is dependent on the V_{oc} by the equation:[5]

$$FF = \frac{(q_e/k_B T)V_{oc} - \ln((q_e/k_B T)V_{oc} + 0.72)}{(q_e/k_B T)V_{oc}} \tag{2.6}$$

where q_e is the charge on an electron, k_B is the Boltzmann constant. e.g. the maximum FF for a V_{oc} of 1 V is 0.88.

Devices were made in sets of three slides, each with 6 pixels. In each experiment, typically 9 slides were used in one batch with three different fabrication methods – 3 slides per fabrication method. Data were analysed using Microsoft Excel and plotted in OriginPro.

2.5 External Quantum Efficiency

External quantum efficiency (EQE), also known as incident-photon-to-collected-electron efficiency (IPCE), is used to determine which parts of the solar spectrum generate the current in a photovoltaic device. A white light source is passed through a monochromator so that light of only one wavelength is incident on the device. The instrument uses two reference diodes to calibrate the measurement; one which is always kept in place, and another that measures the relative light intensity at the point of measurement compared with the permanent reference. The light is split so that both are measured simultaneously. The photocurrent at the J_{sc} condition is then measured and the EQE is calculated. EQE is defined by the ratio of electrons collected to the external circuit to the number of photons incident on the device, given by the equation:

$$\mathrm{EQE}(\lambda) = \frac{I(\lambda)}{q_e \phi(\lambda)} \tag{2.7}$$

where $I(\lambda)$ is current as a function of wavelength, q_e is electron charge, $\phi(\lambda)$ is photon flux as a function of wavelength.

EQE measurements were carried out using a Sciencetech SF150 xenon arc lamp and a PTI monochromator, with the monochromatic light intensity calibrated using a Si photodiode

(Newport 818-UV). The incoming monochromatic light was chopped at 180 Hz. For signal measurement a Stanford Research Systems SR 830 lock-in amplifier was used. The EQE instrument is controlled by custom software written with LabVIEW.[3]

2.6 Kelvin Probe

A Kelvin probe is an instrument that measures the contact potential difference between a vibrating gold electrode and the sample of interest, from which the work function of the sample can be determined using a suitable reference to calibrate the measured contact potential difference. The sample and the electrode must be electrically connected so that their Fermi levels align. The gold electrode is then placed within 1 mm of the sample and oscillated. The oscillation changes the capacitance of the system, inducing an alternating current in the wire connecting the electrode and sample. A voltage is then applied to null this induced oscillating current. The nulling voltage is equal in magnitude but opposite in polarity to the contact potential difference between the sample and the electrode. This value is compared to that for a freshly cleaved surface of a sample of highly orientated pyrolytic graphite (HOPG), which has a known work function of 4.475 eV.[6] The instrument is housed in a Faraday cage to minimise interference from2 stray capacitance.

The work function is the energy required to move an electron from the Fermi level of a material to the vacuum level and is a function of both the chemical potential and the surface potential. The surface potential arises from an electric dipolar layer at the surface due to the spilling of electron density into the vacuum.[7] Therefore the surface potential is dependent on the density and arrangement of atoms at the surface, and so different crystal faces have different surface potentials. The Kelvin probe that was used in this thesis has an error of ± 10 meV for individual measurements, although what is measured is the average workfunction of

the sample beneath the probe. In this thesis measurements were made on samples from three different places, and the average was taken as the value for that sample.

2.7 Photoelectron Spectroscopy

X-ray photoelectron spectroscopy (XPS) and ultraviolet photoelectron spectroscopy (UPS) are performed under high vacuum using a light source to probe core and valence electronic structure, respectively. In UPS, the light is generated using a gas discharge He 1 α source which generates photons of energy 21.22 eV. The X-ray source is a monochromated Al-K_α source which produces X-rays with energies of 1486.7 eV. The X-rays are generated by accelerating an electron beam towards an aluminium surface.

The sampling depth for UPS is $\sim$ 2 nm, and is $\sim$ 3 - 8 nm for XPS.[8] The sampling depth is defined as the depth from which 95% of photoelectrons are scattered before they reach the surface of the sample and can escape. The intensity of electrons from a given depth is given by the equation:

$$I_s = I_0 e^{-d/\beta} \tag{2.8}$$

where I_s is the intensity of photoelectrons at the surface of the sample, I_0 is the intensity of photoelectrons at the depth, d, of emission, and β is the inelastic mean free path (IMFP) of an electron. The IMFP is dependent on the energy of photoelectrons and the specific material; heavier elements generally have lower β values because the higher electron density is better at scattering photoelectrons. The IMFP for a given material at different electron kinetic energies follows a trend given by the equation:

$$\beta = \frac{A}{E^2} + BE^{1/2} \tag{2.9}$$

where E is the electron kinetic energy, and A and B are material specific quantities which depend on conduction band electron density, valence electron number, and atomic mass (Figure 2.8).[8]

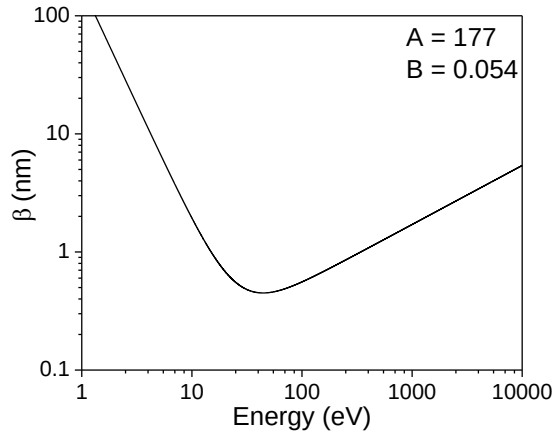

Figure 2.8: Variation of IMFP with electron energy for gold.

The sampling depth is the value for d at which

$$I_s = 0.05 I_0 \tag{2.10}$$

and so;

$$d = -\ln 0.05 \times \beta \approx 3\beta \tag{2.11}$$

In both UPS and XPS a bias is applied to the sample to ensure electrons which only just reach the vacuum level are collected by the detector, which measures the kinetic energy of the ejected electrons. This applied bias is then subtracted after the data are collected. The detector must be in thermodynamic equilibrium with the sample (i.e. Fermi level alignment), and measures the kinetic energy of photoelectrons using two hemispherical plates. Electrons enter through one side and reach the detector on the other side. The inner plate is positively charged and the outer plate is negatively charged. This allows only electrons of particular velocities to pass between the plates – too fast and the electron will collide with the outer

plate, and too slow and it will collide with the inner plate. By varying the voltage across the plates, the flux of electrons of different kinetic energies is measured.

In UPS valence electrons are ejected from a sample anywhere from a potential energy of 21.22 eV below the vacuum level up to the valence band edge. The kinetic energy of an ejected electron depends on the potential energy in the solid it is ejected from. Electrons from 21.22 eV below the vacuum level, and those which lose all of their kinetic to collisions on leaving the sample enter the analyser at a kinetic energy equal to the difference in work functions between the sample and detector (the contact potential) (Figure 2.9). The spectrum is then calibrated by adding the work function of the detector (ϕ_d), such that the low kinetic energy cut-off is equal to the work function of the sample (ϕ_s), and that 21.22 eV subtracted by the high kinetic energy cut-off is the E_f − VB edge difference.

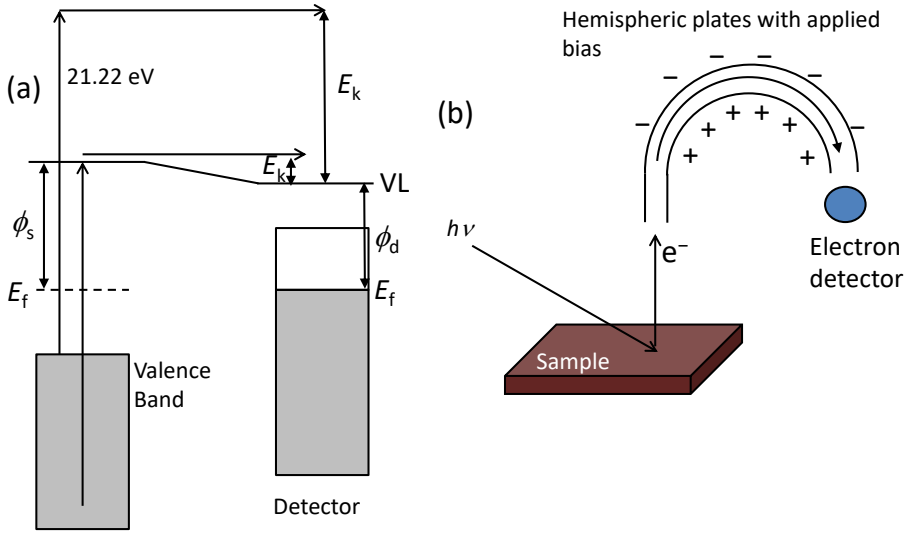

Figure 2.9: **(a)** Energy level diagram of UPS, and **(b)** diagram of photoelectron spectroscopy experiment. VL is the vacuum level.

XPS measures the binding energy of electrons ejected from in core atomic orbitals and so is a sensitive probe of elemental composition (Figure 2.10). The binding energies of photo-ejected electrons are dependent on the chemical environment (e.g. the oxidation state) because the valence electrons, which are involved in chemical bonding, affect the core level binding energy by determining the extent of screening of the ejected electrons from the attractive interaction with the nucleus. Gaussian-Lorentzian hybrid fits can be used to model experimental data to determine the intensity, binding energy, and number of chemical environments in which a specific element is, and comparison to references can give insight into the chemistry of a sample. The signal intensities and relative sensitivity factors (RSF) can be used to determine elemental ratios in a given sample. Depending on the orbital being probed, there are different degrees of peak splitting due to spin-orbit coupling. The s orbitals do not have peak splitting, p orbitals give rise to two peaks in a 1:2 area ratio, and d orbitals give rise to a two peaks in a 2:3 area ratio.

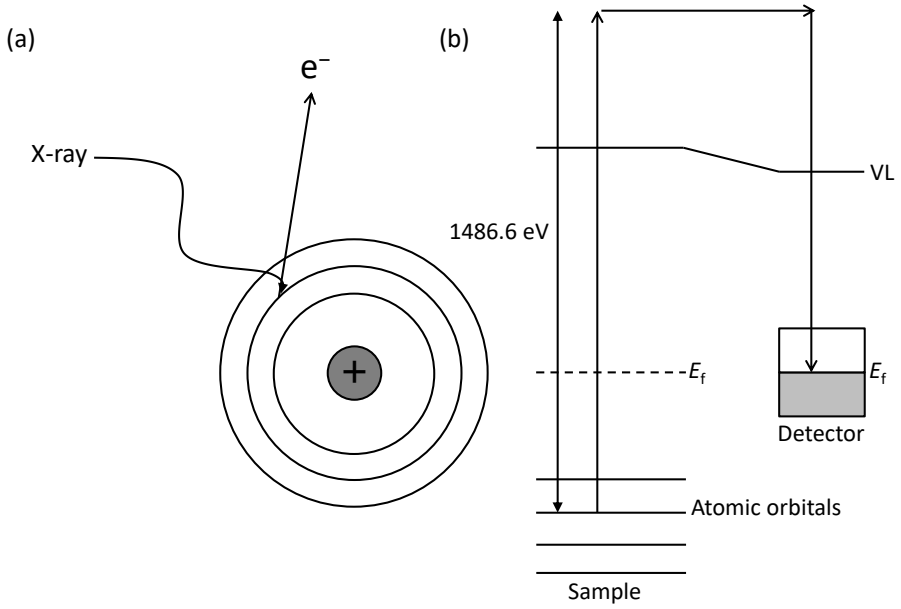

Figure 2.10: **(a)** XPS diagram of photon ejecting a core electron, and **(b)** Energy level diagram of an XPS experiment.

Photoelectron spectroscopy was performed using a Kratos AXIS Ultra DLD. Sputtering was carried out using a Minibeam ion gun (Kratos Analytical); a beam of 4 keV Ar^+ ions was incident on a 3×3 mm^2 area of surface sample. XPS peak fitting was performed using the software, CasaXPS[9].

2.8 Electronic Absorption Spectroscopy

Ultraviolet/visible/near-infrared (UV/vis/NIR) spectroscopy is a form of electronic spectroscopy in which a monochromated light source is passed through a sample and incident on a photodiode detector. The absorbance of the sample is then calculated using the formula;

$$A = \log\left(\frac{1}{T}\right) = \log\left(\frac{I_0}{I_t}\right) \tag{2.12}$$

where A is absorbance, T is transmittance, I_0 is intensity of the incident source, and I_t is the intensity of the transmitted light. In this thesis this technique was used to estimate the band gap and to monitor degradation of thin films in air in real time. Measurements were made using an Agilent Technologies Cary 60 spectrometer.

2.9 ITO Slide Cleaning

PV devices were fabricated on pre-patterned indium tin oxide (ITO) coated glass slides. Before fabrication of the devices the slides were cleaned using a eight stage cleaning process:

- Rinsing with acetone and drying with a stream of nitrogen.
- Ultrasonic agitation in an acetone 10 minutes.
- Drying with a stream of nitrogen.

- Ultrasonic agitation in water with a small amount of surfactant for 10 minutes.
- Ultrasonic agitation in water for 10 minutes.
- Rinsing with isopropanol.
- Ultrasonic agitation in isopropanol for 10 minutes.
- Holding the slides over boiling acetone vapour for 20 seconds, and then placing in a UV/O_3 environment for 15 minutes.

Ultrasonic agitation was carried out in a Fisherbrand FB11002 ultrasonic bath at 100% power. UV/O_3 treatment was carried out in a Nova-scan PSD-UVT ultraviolet surface decontamination system. ITO slides were from Thin Film Devices Inc. and have a sheet resistance of 15 ± 3 Ω/sq.

2.10 Spin Coating

Spin coating is a method of depositing thin films of materials onto substrates with thickness between a few nm and a few µm. There are two methods for applying the solution: (i) drop casting, in which the solution is covered over the substrate and then the substrate is spun; (ii) spin casting, in which the substrate is spun and while spinning the solution was dropped on top. High speed spinning causes the solution to spread evenly over the whole substrate in a very thin film as it is pushed outward by friction and capillary action forces (which push the solution in the direction perpendicular to radial direction) at a speed too great for the centripetal friction and intermolecular forces to keep the drop from expanding. As the solution dries, a solid film is formed. The thickness of films prepared by spin coating depends on the concentration of the solution used to make the film, the solvent evaporation rate, and is approximately inversely

proportional to the square root of the spin speed used.

$$t \propto \frac{1}{\sqrt{\omega}} \tag{2.13}$$

where t is film thickness and ω is spin speed. At low concentrations the film thickness is approximately linearly proportional to the concentration of solution. At higher concentrations a linear relation can no longer be assumed.

In the work presented in this thesis spin coating was performed in the glovebox (MBraun MB 20G LMF) using a SUSS MicroTec Delta 6RC spin coater. For spin coating outside of the glovebox a Chemat-Technologies Spin-Coater KW-4A was used.

2.11 Thermal Evaporation

Thermal evaporation under high vacuum is a method of depositing small organic semiconductors or metals onto substrates with a very high degree of control. The substrates onto which the material was to be deposited were placed in a holder above material sources, facing towards them with a shutter initially obscuring the substrates from the sources. The vacuum chamber was then evacuated to a pressure $\leq 1 \times 10^{-5}$ mbar. Once the desired vacuum pressure is achieved, the source was heated up until the material in the source began to evaporate, and then condenses on the substrate. The rate of evaporation and film thickness was measured using a quartz crystal microbalance. When the evaporation has reached the desired rate, the substrate shutter was opened. During evaporation the substrates were rotated in order to increase uniformity of the deposited films. In this work a CreaPhys evaporator with an MBraun evap bell-jar was used that was located inside of the glovebox.

2.12 Device Fabrication

After cleaning the ITO coated glass slides, the slides were transferred to a nitrogen filled glovebox. Materials were then deposited sequentially either by evaporation or by spin coating. A list of materials used in evaporation with rates and temperatures is shown in Table 2.1, and other materials are shown in Table 2.2. A list of solvents used is shown in Table 2.3. A diagram of a thin film device is shown in Figure 2.11. Top metal electrodes were evaporated through a shadow mask forming six 6 mm^2 electrodes on each slide.

Table 2.1: List of materials used in evaporation. Specific power is a measure of electrical power passing through a material source as a % of maximum power. e.g. at 10^{-5} mbar, Al evaporates at $\sim$ 880 °C.

Material	Rate (Å/s)	Typical thickness (nm)	Temperature (°C or specific power)	Supplier, purity
Aluminium	1	50-75	SP 12-20	Kurt J. Lesker, 99.999%
Bathocuproine	0.2-0.7	6	130	Alfa Aesar, 99.8%
Gold	1	8-20	SP 15	Kurt J. Lesker, 99.99%
MoO_3	0.3-0.5	5-10	SP 13	Sigma Aldrich, 99.99%
CuI	1	70	SP 8	Sigma Aldrich, 99.999%
CuPc	0.5	30-40	380	Sigma Aldrich, $>$ 99%

Table 2.2: List of materials used in solution processing or vacuum vapour deposition

Material	**Supplier**	**Purity**
CsI	Sigma Aldrich	99.9%
CsBr	Acros Organics	99.9%
CsCl	Fisher Scientific	99+%
RbI	Alfa Aesar	99.8%
SnI_2	Alfa Aesar	99.999%
$SnCl_2$	Sigma Aldrich	99.99%
SnF_2	Acros Organics	99%
SrI_2	Sigma Aldrich	99.99%
$SnBr_2$	Alfa Aesar	99.4%
CuSCN	Sigma Aldrich	99%
CH_3NH_2	Sigma Aldrich	33 wt% in ethanol
HI	Sigma Aldrich	57 wt% in H_2O
$PC_{61}BM$	Nano-c, Solenne	99%
$IC_{60}BA$	Ossila	99.5%
3-mercaptopropyltrimethoxysilane	Sigma Aldrich	95%
3-aminopropyltrimethoxysilane	Sigma Aldrich	97%
PEDOT:PSS	Ossila	1.3 - 1.7 wt% in H_2O

Table 2.3: List of solvents used

Solvent	**Supplier**	**Purity**
Acetone, GPR	Sigma Aldrich	99%
Isopropanol, HPLC	Sigma Aldrich	99.8%
Deionised water	Purite dispenser	>10 MΩ
N,N-dimethylformamide, anhydrous	VWR	99.8%
Chlorobenzene, anhydrous	Sigma Aldrich	99.8%
di-*n*-propylsulfide	VWR	98%
diethylsulfide	Sigma Aldrich	98%
1,2-dichlorobenzene, anhydrous	Sigma Aldrich	99.8%

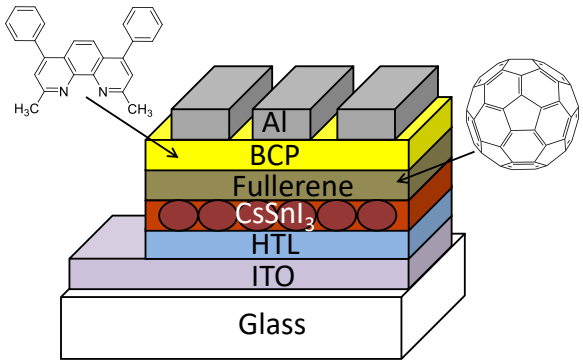

Figure 2.11: Diagram of a typical device fabricated in this work. HTL is hole transport layer, BCP is bathocuproine.

2.12.1 B-γ $CsSnI_3$ Deposition

B-γ $CsSnI_3$ (the primary light harvester used in this work) was deposited onto either ITO or onto a hole transport layer via spin coating. The solution was prepared from CsI, SnI_2, and tin(II) halide additive which were dissolved in *N,N*-dimethylformamide (DMF) typically in an 8 wt% solution for devices. Uniform films of 1 - 6.7 cm^2 in area were prepared either by spin casting or drop casting at 4000 rpm. AFM step-height analysis shows that this processing condition gives a film $\sim$ 50 nm thick on glass (Figure 2.12).

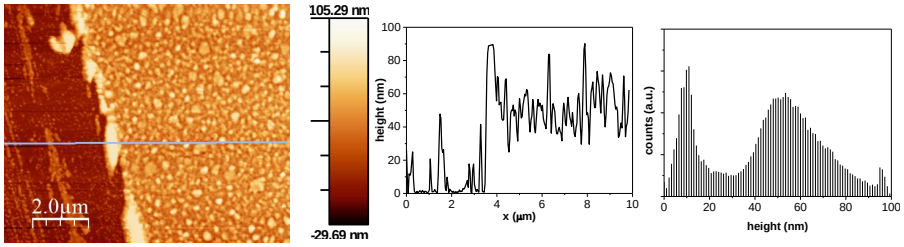

Figure 2.12: AFM stepheight image of film of $CsSnI_3$ drop cast from 8 wt% DMF solution at 4000 rpm onto a glass slide

2.12.2 ETL and HTL Spin Coating

CuI was spin coated from 50 mg/ml di-*n*-propylsulfide solution at 3000 rpm. CuSCN was spin coated from 50 mg/ml diethylsulfide solution at 3000 rpm. Phenyl-C_{61}-butyric acid methylester ($PC_{61}BM$) was typically deposited from 10 - 15 mg/ml chlorobenzene solution at 1000 or 1500 rpm. Indene-C_{60}-bis adduct ($IC_{60}BA$) was deposited from 5 - 10 mg/ml chlorobenzene solution at 1000 or 1500 rpm. PEDOT:PSS in 1.3 - 1.7 wt% aqueous solution was filtered through a 0.4 µm pore PTFE filter, and then drop cast at 5000 rpm in air, followed by drying on a hotplate at 120 °C for 20 minutes. This was then brought into the glovebox and dried for a further 5 minutes at 100 °C.

2.12.3 Thin Au film fabrication

Thin Au films were fabricated using mixed monolayers of 3-aminopropyltrimethoxysilane (APTMS) and 3-mercaptopropyltrimethoxysilane which were deposited onto glass slides by vapour deposition using vials containing the liquids under low pressure in a vacuum desiccator for 1 hour. Au was then thermally evaporated on top of this at a thickness of ≥ 8 nm.

2.13 Optical Simulations

Simulations of optical field intensity and of electronic absorbance spectra was performed using the program, The Essential MacLeod V9.7 by Thin Film Center Inc.[10] This software uses refractive index and extinction coefficient data obtained from the literature and an in-built MacLeod database for each material. This simulation package assumes the films are homogeneous slabs with smooth interfaces.

References

[1] C. A. Schneider, W. S. Rasband, and K. W. Eliceiri, "NIH image to ImageJ: 25 years of image analysis," *Nat. Methods*, vol. 9, pp. 671–675, 2012.

[2] I. Horcas, R. Fernández, J. M. Gómez-Rodríguez, J. Colchero, J. Gómez-Herrero, and A. M. Baro, "WSXM: A software for scanning probe microscopy and a tool for nanotechnology," *Rev. Sci. Instrum.*, vol. 78, p. 013 705, 2007.

[3] National Instruments Corporation, *LabVIEW*, 2012.

[4] A. Pockett, G. E. Eperon, N. Sakai, H. J. Snaith, L. M. Peter, and P. J. Cameron, "Microseconds, milliseconds and seconds: deconvoluting the dynamic behaviour of planar perovskite solar cells," *Phys. Chem. Chem. Phys.*, vol. 19, pp. 5959–5970, 2017.

[5] M. A. Green, "Solar cell fill factors: General graph and empirical expressions," *Solid State Electron.*, vol. 24, pp. 788–789, 1981.

[6] W. N. Hansen and G. J. Hansen, "Standard reference surfaces for work function measurements in air," *Surf. Sci.*, vol. 481, pp. 172–184, 2001.

[7] H. Ishii, K. Sugiyama, E. Ito, and K. Seki, "Energy level alignment and interfacial electronic structures at organic metal and organic organic interfaces," *Adv. Mater.*, vol. 11, pp. 605–625, 1999.

[8] M. Seah and W. Dench, "Quantitative electron spectroscopy of surfaces.," *Surf. Interface Anal.*, vol. 1, pp. 46–55, 1979.

[9] N. Fairley and Casa Software Ltd., *CasaXPS*, 2016.

[10] Thin Film Center Inc., *The Essential MacLeod V 9.7*, 2013.

Chapter 3

Inverted Planar $CsSnI_3$ Photovoltaics Using SnI_2 Additive

3.1 Background

One of the main factors limiting the performance of tin PPVs is the propensity for tin perovskites to form tin vacancy defects which act as *p*-type dopant states, trap states and recombination centres,[1, 2] which limit device J_{sc}, V_{oc} and *FF* by reducing device shunt resistance.[2, 3] One way to reduce the tin vacancy concentration is to synthesise the perovskite in a tin rich environment. Prior to the research described in this chapter, SnF_2 had been used as an additive to reduce the density of tin vacancy defects in $CsSnI_3$ so that it could be used both as a light harvester [1] and as a *p*-type HTL.[4, 5] The other major factor limiting tin PPV research is the propensity for Sn^{2+} to oxidise to Sn^{4+}, which can cause rapid degradation of tin PPV devices when exposed to oxygen and moisture.

3.1.1 $CsSnI_3$ PPV devices

Chung *et al.* reported the use of $CsSnI_3$ as an HTL in conjunction with mesoporous TiO_2 derivatised with a monolayer of the ruthenium organometallic dye N719, that served as the light harvester, and found that by substituting 5 mol% SnI_2 with SnF_2 and adding a further 5 mol% excess SnF_2 ($CsSnI_3$:SnF_2), the device η increased from 3.7% to 10.2%.[4] Those authors also found that devices without N719 exhibited a very low η of 0.2%, showing that the primary function of the $CsSnI_3$:SnF_2 was not as a light harvester, but as an HTL. Kumar *et al.* subsequently reported that $CsSnI_3$ processed from solutions stirred at 70 °C with 20 mol% SnF_2 additive and post deposition annealing at 70 °C could be used as the light absorber in a PPV device based on a distributed heterojunction with mesoporous TiO_2, achieving a very high J_{sc} of > 22 mA cm^{-2}.[1] Unfortunately device V_{oc} and FF was limited to ~ 240 mV and ~ 0.37 respectively, which limited η to 2.02%. Notably, devices fabricated without SnF_2 additive did not function at all, and whilst it was shown that fluoride was not incorporated into the $CsSnI_3$ lattice (by no significant change in lattice parameters from $CsSnI_3$ to $CsSnI_3$:SnF_2, or in XPS F 1s binding energy between SnF_2 and $CsSnI_3$:SnF_2), the possible optoelectronic functionality of the large quantity of SnF_2 additive present in the perovskite film was not discussed. In that work it was concluded that the V_{oc} in $CsSnI_3$ PPVs is, in general, severely limited by the high background free carrier density resulting from the high density of Sn-vacancy defects, even when prepared under Sn-rich conditions, and is not set by the difference between the conduction band minimum of the ETL and the valence band maximum, or highest occupied molecular orbital (HOMO) of the HTL, as is normally the case in a *p-i-n* PV structure. The same group went on to show that substitution of iodide with bromide in $CsSnI_3$ is an effective means of increasing the V_{oc}, achieving a V_{oc} of 0.41 V. However, the improvement in V_{oc} was at the expense of photocurrent due to the increase in E_g that resulted from the inclusion of Br

into the perovskite lattice.[6]

3.1.2 Results

This chapter describes research exploring the viability of using SnI_2 as the source of excess tin in $CsSnI_3$ instead of SnF_2, the rationale being that SnI_2 has higher solubility than SnF_2 in common solvents such as DMF, and using SnI_2 removes the complexity associated with the possibility of partial halide substitution because SnI_2 is already used as one of the precursors for $CsSnI_3$ synthesis. The first demonstration of orthorhombic $CsSnI_3$ (B-γ $CsSnI_3$) films prepared from solution at room temperature with defect densities low enough for use as the light harvesting semiconductor in PPV devices is documented. It is shown that addition of excess SnI_2 to perovskite precursor solutions is a very effective strategy for simultaneously improving both PPV device η and stability towards constant illumination and oxidation in air, and does not complicate the process of device fabrication. A combination of photoelectron spectroscopy, contact potential measurements and device studies using a model planar device architecture are used to elucidate the basis for this improvement and role of the excess SnI_2.

3.2 B-γ $CsSnI_3$ Thin Film Formation and Characterisation

3.2.1 Structural Characterisation of Thin Films

Dark red/brown $CsSnI_3$ thin films were prepared by one-step spin casting DMF solutions of CsI and SnI_2 onto glass slides or ITO glass at room temperature, without post-deposition annealing. Films of $CsSnI_3$ were typically made from an 8 wt% DMF solution, light translucent yellow in colour. The solution was spin cast at 4000 rpm for 60 s, and formed a film with a dark

brown/red colour within 30 s of starting the spinning. Figure 3.1 shows a SEM image and an AFM step-height cross-section which show that the $CsSnI_3$ films are made up of crystallites ~ 50 nm across and are ~ 50 nm thick.

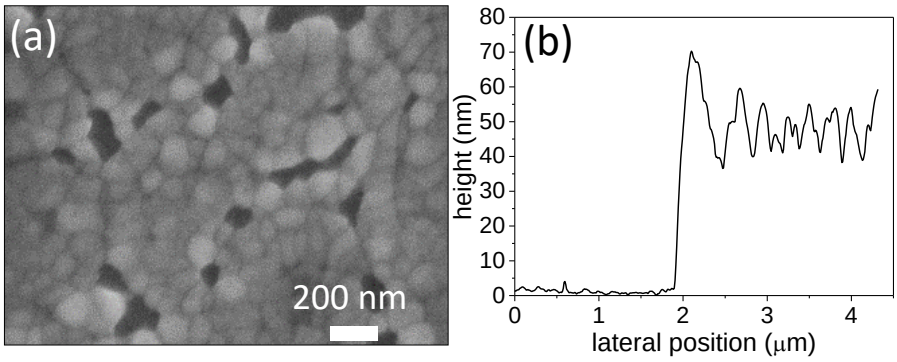

Figure 3.1: **(a)** SEM image of a film of $CsSnI_3$ with 10 mol% added SnI_2 deposited from 8 wt% DMF solution onto an ITO substrate with a 100 nm layer of CuI, **(b)** AFM stepheight cross section of a film of $CsSnI_3$ with 10 mol% added SnI_2 deposited from 8 wt% DMF solution onto a glass microscope slide.

XRD analysis (Figure 3.2 (a) and (b)) confirms that polycrystalline orthorhombic B-γ $CsSnI_3$ is formed spontaneously upon the solvent drying, which is remarkable given the speed of the spin coating and film drying process. It is evident from Figure 3.2 (e) that exposure of $CsSnI_3$ to ambient air causes the film to degrade into Cs_2SnI_6 and, most likely, amorphous SnO_2, although the latter is not evident in the XRD pattern, possibly because the SnO_2 crystallites are too small in diameter or the particles are amorphous. The XRD pattern of the film prepared using excess SnI_2 does not show any evidence for crystalline SnI_2, and so it is assumed to exist as an amorphous phase.

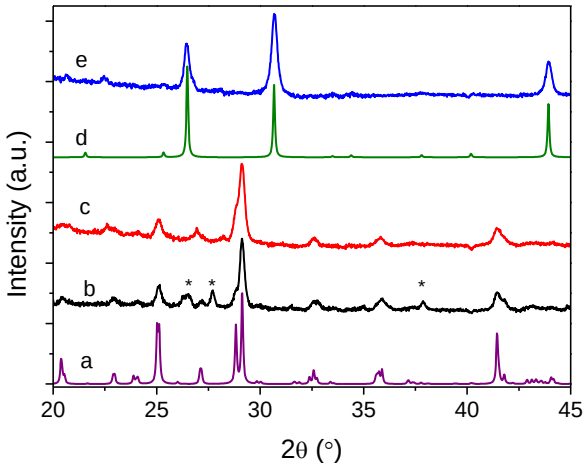

Figure 3.2: XRD patterns of **(a)** simulated $CsSnI_3$, thin films 16 wt% of **(b)** $CsSnI_3$, **(c)** $CsSnI_3$ + 10 mol% SnI_2, **(d)** simulated Cs_2SnI_6, and **(e)** a thin film of $CsSnI_3$ exposed to air for 16 hours. * Denotes background peaks. Simulated patterns calculated using CIFs from refs. [7] and [8].

XPS analysis of O 1s environment provides evidence of SnO_2 formation, as indicated by the increase in intensity of the peak at 530.7 eV (Figure 3.3).[9, 10] The peak at 531.9 eV in the oxidised film is assigned to physisorbed O_2 or H_2O.[11]

The peak fitting in Figure 3.4 (b) indicates that there is very little SnI_2 at the surface of the $CsSnI_3$ film because $\sim$ 95% of photoelectrons originate from the top $\sim$ 7 nm. However, the binding energy shoulders could equally well be fitted with peaks associated with SnI_4 and SnI_2 and so it is not possible to determine the extent to which the excess SnI_2 is at the $CsSnI_3$ surface based on the XPS analysis.

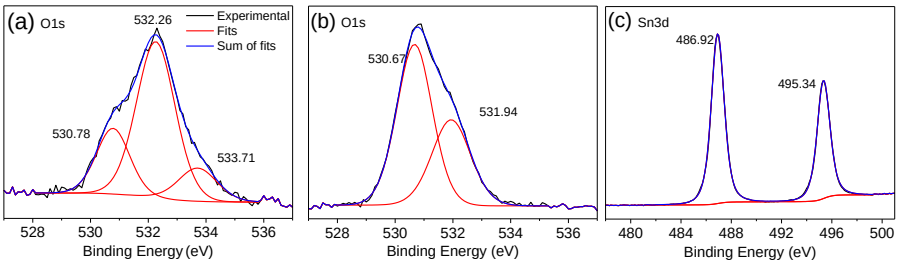

Figure 3.3: XPS spectra of **(a)** $CsSnI_3$ O1s, **(b)** $CsSnI_3$ exposed to air for 5 hours O1s, and **(c)** $CsSnI_3$ exposed to air for 5 hours Sn3d.

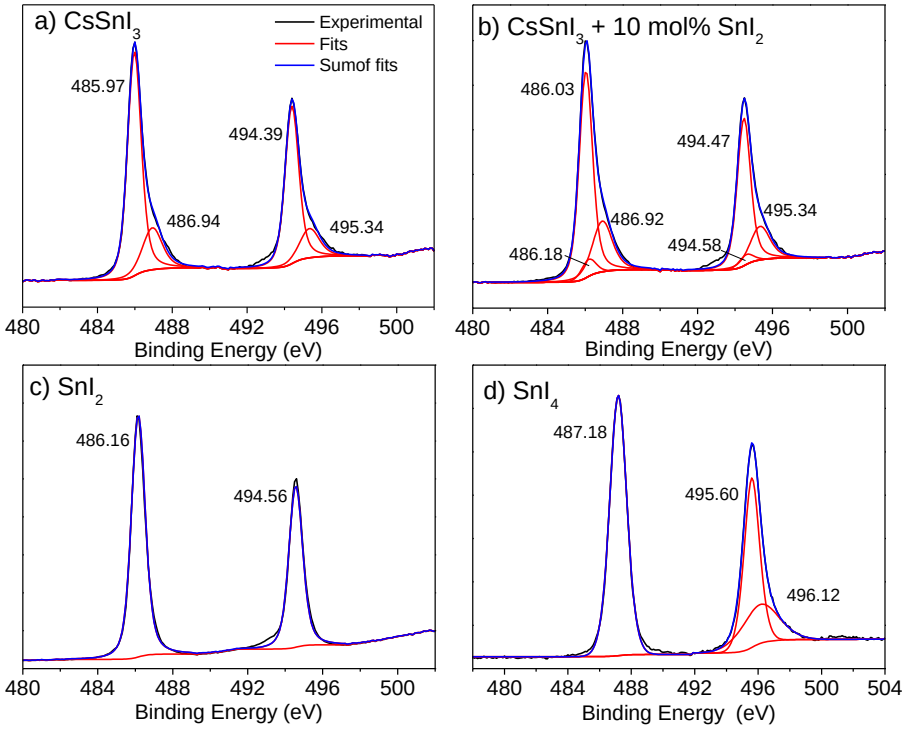

Figure 3.4: XPS spectra of Sn3d environments for **(a)** $CsSnI_3$, **(b)** $CsSnI_3$ + 10 mol% SnI_2, **(c)** SnI_2, and **(d)** SnI_4.

3.2.2 Electronic Characterisation of Thin Films

The UPS spectra shown in Figure 3.5 (a) and (b) show that adding SnI_2 to $CsSnI_3$ increases the difference between the valence band (VB) edge and the E_f from ~ 0.05 eV to ~ 0.37 eV, consistent with a reduction in the density of tin vacancy defects which are known to function as p-type dopant states in $CsSnI_3$.[2] Tin vacancies in the perovskite lattice gives rise to two holes

in the VB because two electrons must be supplied to satisfy the valency of the iodides. The fact that there is little change in the work function, ϕ; only 20 meV (Figure 3.5 (a)), indicates that the additional SnI_2 must reside at the $CsSnI_3$ crystallite surface, increasing the surface potential contribution to the ϕ, otherwise the shift in the E_f away from the VB edge would be expected to have resulted in a reduction in ϕ.

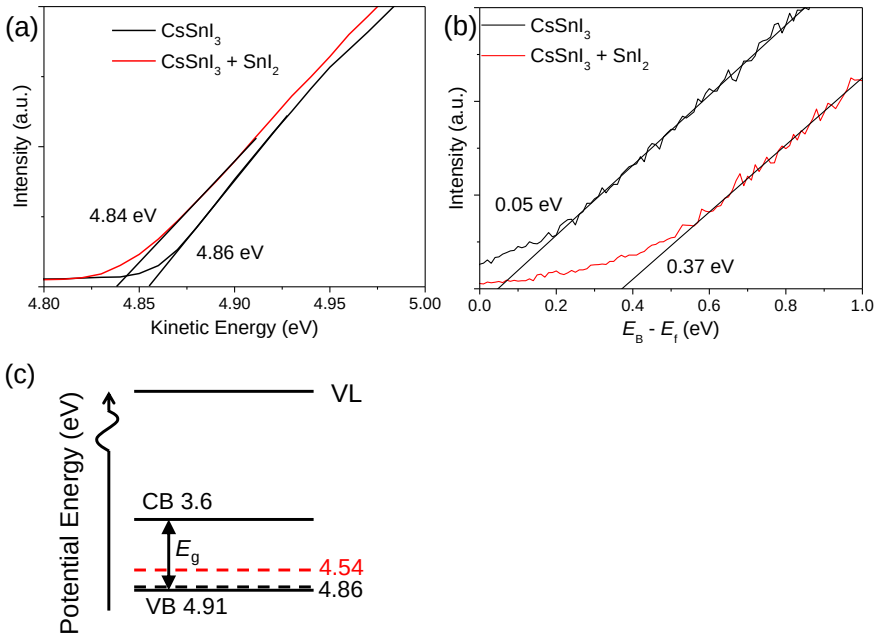

Figure 3.5: UPS of $CsSnI_3$ prepared with 10 mol% added SnI_2 (red) and with no added SnI_2 (black), showing **(a)** the low kinetic energy cut-off and **(b)** the high kinetic energy cut-off. **(c)** Energy level diagram informed by UPS and electronic absorbance measurements, showing VB edge and CB edge of $CsSnI_3$, and E_f levels for 0 mol% (black) and 10 mol% excess SnI_2. E_g value reported in the literature.[7, 12]

3.3 Device Studies

3.3.1 Rationale for PV Device Architecture

To test the utility of the B-γ $CsSnI_3$ films in PPV devices, model *p-i-n* PPVs were fabricated with the structure: indium tin oxide (ITO)| CuI or PEDOT:PSS| $CsSnI_3$| fullerene| bathocuproine (BCP)| Al, as schematically illustrated in Figure 3.6.

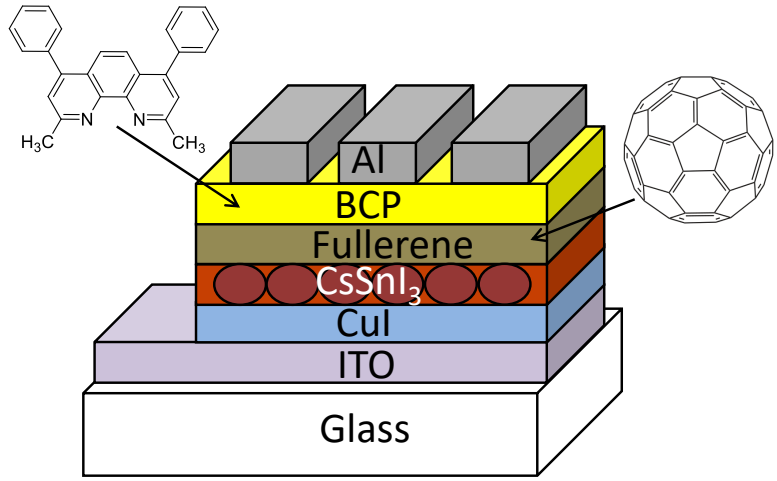

Figure 3.6: Model device architecture used in this chapter.

Whilst the majority of perovskite research pertains to *n-i-p* architecture, the reverse *p-i-n* structure has the advantage of lower processing temperatures because TiO_2 ETL is not used: As described in Chapter 1, TiO_2 requires a $\sim$ 500 °C annealing step to convert the $Ti(O^iPr)_4$ precursor to TiO_2 [13] and to improve the crystallinity of the film [14]. PEDOT:PSS was selected as the *p*-type material because it is already widely used in OPVs as a bottom contact HTL and has been used in lead-PPVs. CuI was also used as an HTL due to its proven effectiveness as a *p*-type seimiconductor in lead PPVs.[15] CuI also has the advantage that it can be processed by thermal evaporation and solution processing, which imparts flexibility in the fabrication method. However, in this study thermal evaporation of the CuI HTL was the deposition method of choice due to the high degree of control over film thickness and the low

roughness of films produced by this method.[16] However, it was later found that DMF solutions washed away underlying layers of solution processed CuI, and it is unknown whether or not the thermally evaporated layer was still intact. C_{60} was chosen as the ETL because it is the architypal organic ETL and is commercially available at very high purity. It is also amenable to thermal evaporation, and has variants with functional groups that can modify the electron affinity and improve the solubility in common solvents. C_{60}, BCP and their interface with Al are very well characterised in the field of OPVs.[17]

3.3.2 Selection of hole-transport-layer (HTL)

PPV devices with the structure ITO| HTL| $CsSnI_3$:SnI_2| C_{60}| BCP| Al were fabricated using PEDOT:PSS or CuI HTL, and it was found that devices made using CuI were superior due to higher J_{sc} and *FF*. Consequently CuI was the HTL of choice for the remainder of this study (Figure 3.7). Data shown in Table 3.1.

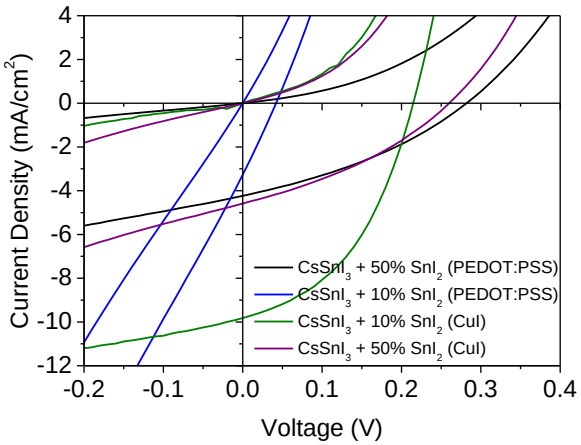

Figure 3.7: JV plots of the best devices in the structure ITO| PEDOT:PSS or CuI| $CsSnI_3$ + 10 or 50 mol% added SnI_2 (from 16 or 19 wt% DMF solution respectively)| C_{60}| BCP| Al.

Table 3.1: JV data of devices using either PEDOT:PSS or CuI as the HTL, and $CsSnI_3$ + 10 or 50 mol% excess SnI_2.

Device	n	J_{sc} (mA/cm^2)	V_{oc} (V)	*FF*	η (%)	Champion η (%)
PEDOT:PSS, $CsSnI_3$ + 50% SnI_2	17	3.59 ± 0.30	0.25 ± 0.03	0.34 ± 0.01	0.31 ± 0.05	0.40
CuI, $CsSnI_3$ + 10% SnI_2	15	8.53 ± 0.53	0.14 ± 0.04	0.33 ± 0.04	0.43 ± 0.16	0.71

CuSCN was also shown to work well as an HTL in devices with $PC_{61}BM$ ETL. This can be solution processed from diethyl sulfide. Representative JV curves are shown in Figure 3.8 and data are shown in Table 3.2. The data shows that the ordering of HTL effectiveness is; evaporated CuI > CuSCN > solution processed CuI ∼ no HTM (Table 3.3).

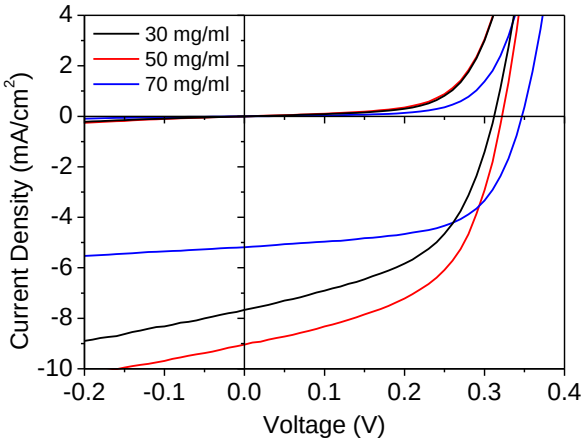

Figure 3.8: JV plots of representative devices made in the structure ITO| CuSCN| $CsSnI_3$:SnI_2| $PC_{61}BM$| BCP| Al using CuSCN from either 30, 50 or 70 mg/ml diethyl sulfide solution.

The external quantum efficiency (EQE) in Figure 3.9 shows that light is absorbed out to $\lambda = 930$ nm for devices with and without excess SnI_2, which coincides with the E_g of ∼ 1.3 eV for $CsSnI_3$ for $CsSnI_3$ reported in the literature.[7, 12] This confirms that $CsSnI_3$ is the primary light harvester, because none of the other semiconductors in the device can generate current

Table 3.2: JV data for devices made in the structure ITO| CuSCN| $CsSnI_3$| $PC_{61}BM$| BCP| Al using CuSCN from either 30, 50 or 70 mg/ml diethyl sulfide solution. n is data size.

Device	n	J_{sc} (mA/cm^2)	V_{oc} (V)	*FF*	η (%)	Champion η(%)
30 mg/ml	15	7.5 ± 1.0	0.32 ± 0.01	0.48 ± 0.04	1.15 ± 0.22	1.51
50 mg/ml	14	8.61 ± 0.79	0.33 ± 0.01	0.50 ± 0.04	1.41 ± 0.22	1.77
70 mg/ml	12	5.36 ± 1.15	0.35 ± 0.01	0.56 ± 0.05	1.07 ± 0.24	1.40

from such long wavelength light due to their much larger band-gaps. The two shoulders at low wavelengths are tentatively attributed to a contribution to the photocurrent by C_{60}. There is no significant difference in the shape of the IPCE between $CsSnI_3$ and $CsSnI_3$ with 10 mol% added SnI_2. The abrupt drop off in signal from $\lambda = 400$ nm to 300 nm is caused by the glass substrate blocking out the short wavelength light.

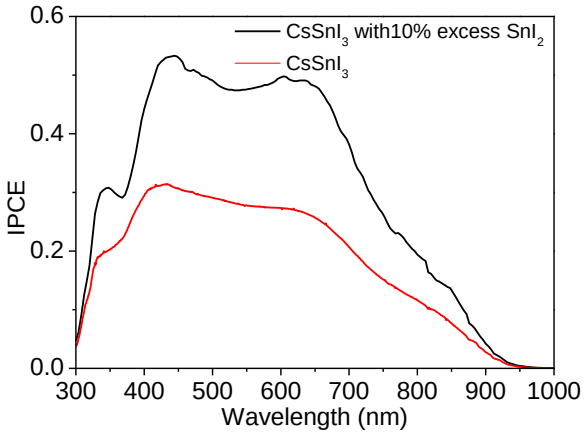

Figure 3.9: EQE of devices in the architecture ITO| CuI| $CsSnI_3$ with and without 10 mol% SnI_2| C_{60}| BCP| Al.

A flat-band energy level diagram of the materials used in the model architecture is shown in Figure 3.10. This was informed by UPS, Kelvin-probe, and electronic absorption data for ITO, CuI (Figure 3.11), SnI_2 (Figure 3.12), and $CsSnI_3$ (Figure 3.5); the $CsSnI_3$ band structure was determined using Kelvin probe and UPS to find the VB edge of $CsSnI_3$ without excess

SnI_2, the E_f was determined using the VB - E_f difference for $CsSnI_3$:SnI_2 from UPS. Literature values were used for the frontier orbital energies of the fullerenes[18, 19] and BCP,[17] and the workfunction of aluminium[20]. The data show that the VB edge of CuI is very low lying, and so a large energy barrier between $CsSnI_3$ and CuI might be expected, however, when the $CsSnI_3$ and CuI come into contact, there will be spontaneous electron transfer from the $CsSnI_3$ to defect states in the CuI due to the difference in E_f; UPS indicates that CuI is very strongly p-doped, and so is able to accept significant charge density. Consequently at the real interface the barrier to hole extraction would be much lower, and this would not impede the flow of holes very much due to the large number of defect states which can allow charge to pass through (discussed later).

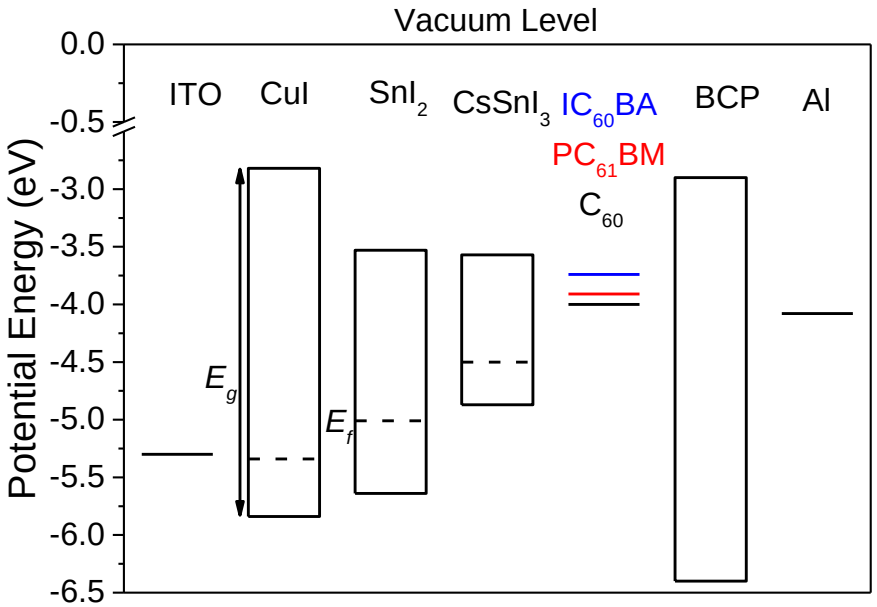

Figure 3.10: Flat band energy level diagram of materials used in devices. BCP values from ref. [17]. Al ϕ from ref. [20].

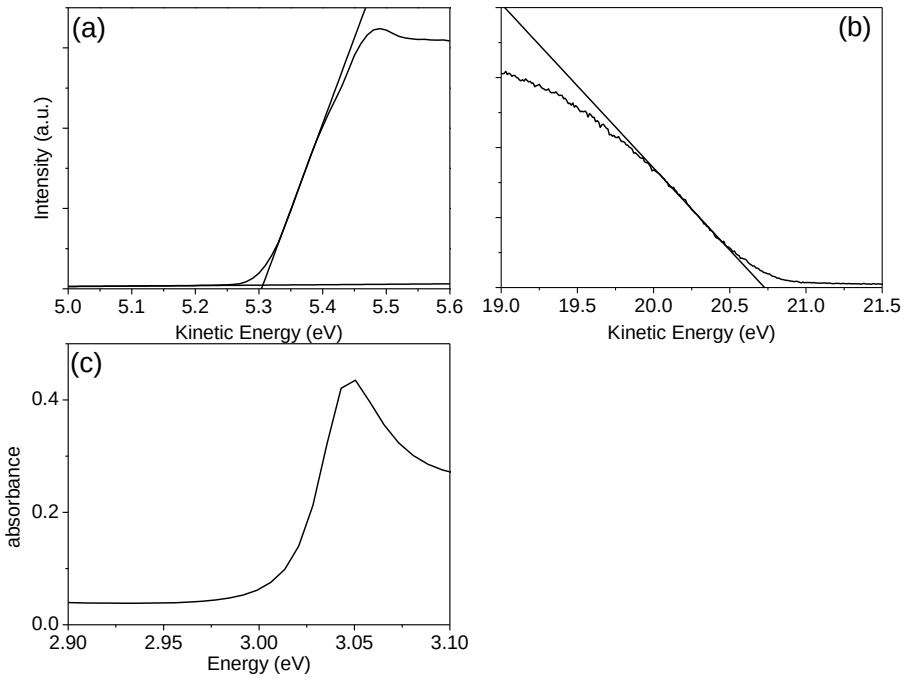

Figure 3.11: UPS of CuI showing **(a)** the low kinetic energy cut-off and **(b)** the high kinetic energy cut-off. **(c)** UV/vis spectrum of CuI.

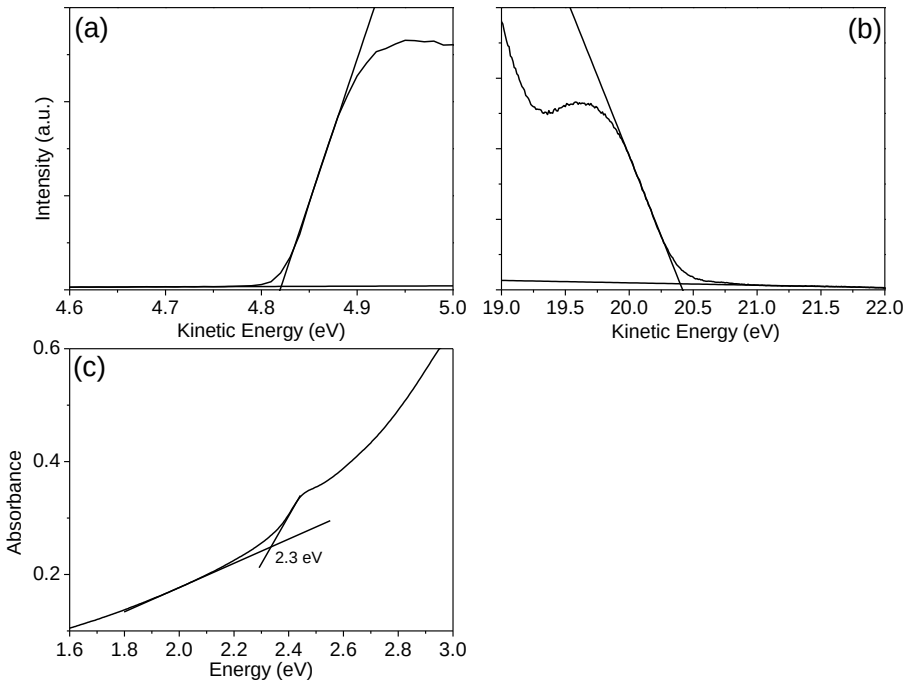

Figure 3.12: UPS of SnI_2 showing **(a)** the low kinetic energy cut-off and **(b)** the high kinetic energy cut-off. **(c)** UV/vis spectrum of SnI_2.

3.3.3 Hysteresis

Hysteresis has been a significant problem in PPVs because it can lead to overestimation and uncertainty in device η.[21, 22] It has been proposed that ion migration, resulting from iodide vacancy diffusion, leads to an accumulation of charges at interfaces during a linear sweep voltammetry measurment is the most likely cause of device hysteresis in PPVs. Computational studies have shown that iodine vacancies have the lowest energy of formation of the possible defects that could lead to hysteresis; 0.08 eV.[23, 24] However, $CsSnI_3$ devices from this study exhibited no significant hysteresis (Figure 3.13). Computational study has shown that the formation energy for iodine vacancies is much higher in $CsSnI_3$ than in $CH_3NH_3PbI_3$, which could explain the lack of hysteresis.[2] Other reports on tin PPVs have shown no significant hysteresis,[1, 25] and that PPV devices with $PC_{61}BM$ ETL tend to have less hysteresis than those using TiO_2 ETL.[26]

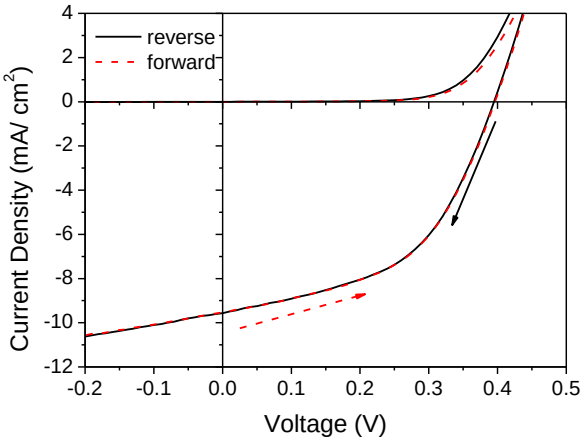

Figure 3.13: ITO| CuI| $CsSnI_3$:SnI_2| PCBM| BCP| Al device scanned in forward (-1 V to $+1$ V) and reverse ($+1$ V to -1 V) sweeps at a rate of 0.1 V/s showing negligible hysteresis.

3.3.4 Correlation Between PPV Device Performance and Excess SnI_2 loading

PPV devices were fabricated with the afforementioned model structure using $CsSnI_3$ prepared using different amounts of added SnI_2 from 8 wt% DMF solution, with 0, 5, 10 or 15 mol% excess SnI_2 and C_{60} ETL. Figure 3.14 summarises the key device performance parameters for 18 individual devices as a function of SnI_2 excess in the $CsSnI_3$ layer, from which it is evident that the optimal SnI_2 loading is 10 mol%.

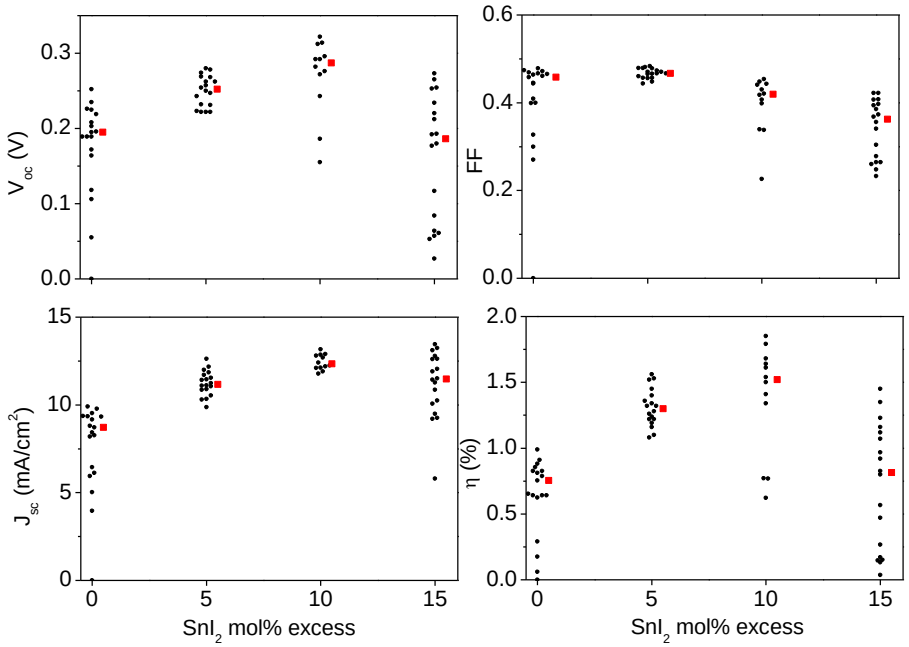

Figure 3.14: JV data for devices made in the model structure with using $CsSnI_3$ with different amounts of added SnI_2, and an evaporated C_{60} ETL. Red points represent mean values.

The improvement in device performance is due to a reduction in tin vacancy states in the $CsSnI_3$ as a result of synthesising in a tin rich environment, thereby reducing loses in J_{sc} and V_{oc} due to recombination. Figure 3.15 shows that adding too much SnI_2 leads a slight increase in series resistance, due to a greater barrier to charge extraction, and a reduction in shunt resistance (Figure 3.10).[1, 2]

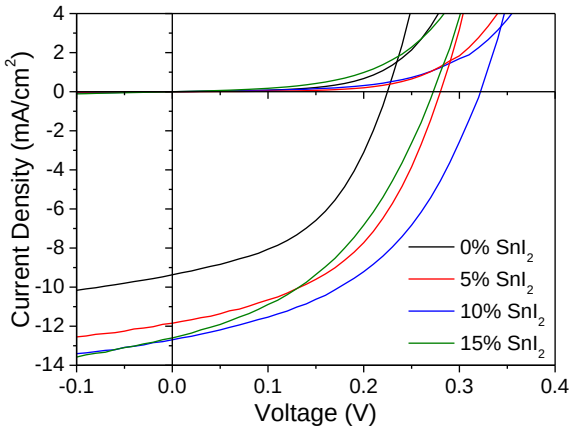

Figure 3.15: JV plots of champion devices in the architecture; ITO| CuI| $CsSnI_3$ + 10 or 15 mol% SnI_2| C_{60}| BCP| Al.

3.3.5 Effect of choice of ETL on PPV Device Performance

Using $CsSnI_3$ with 10 mol% SnI_2, devices were fabricated using different ETLs; C_{60}, $PC_{61}BM$, or $IC_{60}BA$, in conjunction with CuI HTL to investigate the extent to which V_{oc} was determined by the energetics of the $CsSnI_3$| fullerene interface. Champion JV characteristics of devices fabricated using different ETLs are shown in Figure 3.16. Data are summarised in Tables 3.3 and 3.4.

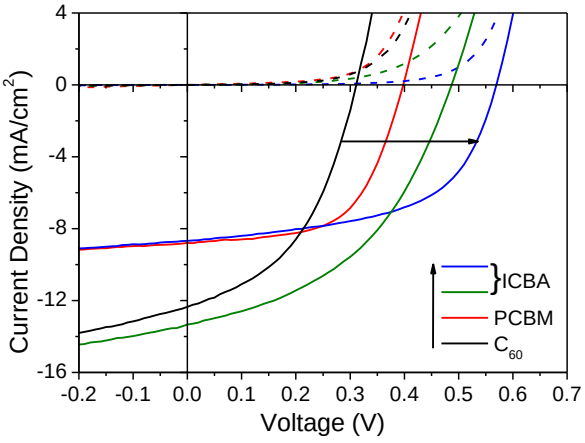

Figure 3.16: JV characteristics of champion devices in the model architecture using either C_{60}, $PC_{61}BM$ or ICBA (from 3 or 5 mg/ml solution) as the ETL.

Table 3.3: JV data for devices in the structure ITO| $CsSnI_3$:SnI_2| ETL| BCP| Al, where the ETL was C_{60}, $PC_{61}BM$, or ICBA.

Device	n	V_{oc} (V)	J_{sc} (mA/cm^2)	*FF*	η (%)	champion η (%)
C_{60} (40 nm)	17	0.26 ± 0.03	11.67 ± 0.50	0.38 ± 0.02	1.16 ± 0.18	1.40
$PC_{61}BM$ (15 mg/ml)	11	0.26 ± 0.04	8.6 ± 1.1	0.42 ± 0.07	1.02 ± 0.39	1.59
ICBA (7 mg/ml)	17	0.35 ± 0.03	10.7 ± 1.8	0.47 ± 0.08	1.79 ± 0.56	2.65

Table 3.4: JV data for devices in structure ITO| CuI| $CsSnI_3$:SnI_2| ETL| BCP| Al using different C_{60}, $PC_{61}BM$ or ICBA ETL, and either evaporated or solution processed CuI as the HTL.

Device	n	V_{oc} (V)	J_{sc} (mA/cm^2)	*FF*	η (%)	champion η (%)
C_{60} (40 nm), solution processed CuI	18	0.24 ± 0.02	11.43 ± 0.89	0.41 ± 0.03	1.16 ± 0.21	1.40
C_{60} (40 nm)	18	0.28 ± 0.03	11.6 ± 1.0	0.43 ± 0.03	1.42 ± 0.23	1.72
$PC_{61}BM$ (15 mg/ml)	16	0.36 ± 0.03	8.94 ± 0.27	0.54 ± 0.04	1.72 ± 0.26	2.07
ICBA (5 mg/ml)	16	0.49 ± 0.06	7.01 ± 0.68	0.50 ± 0.05	1.73 ± 0.44	2.60
ICBA (3 mg/ml)	14	0.43 ± 0.06	12.30 ± 0.48	0.40 ± 0.05	2.13 ± 0.53	2.76

As shown in Figure 3.16 and Table 3.3, changing the ETL from C_{60} to $PC_{61}BM$ to $IC_{60}BA$ resulted in an increase in V_{oc}, which is attributed to an improvment in interfacial energetics: raising the LUMO position of the ETL from $\sim$ 4.00 eV [18] to $\sim$ 3.91 eV [18, 19] to $\sim$ 3.74 eV [19] below the vacuum level, moves it closer to that of the $CsSnI_3$ CB edge, thereby reducing energy losses when transferring electrons from $CsSnI_3$ to the ETL. Although the exact magnitude of the electron affinity values in each of these materials is uncertain, the differences between them are well established.[18, 19] The systematic study of the effect of varying the ETL shows that the V_{oc} is not entirely limited by the defect density and recombination of the

$CsSnI_3$, as has been previously preposed,[1] and that there is actually considerable scope for improving device η through optimisation of the energetics at the $CsSnI_3$| ETL interface. Using a combination of $IC_{60}BA$ ETL and CuI HTL a champion η of 2.76% was achieved.

It is notable that the *FF* of devices using an evaporated fullerene layer are significantly lower than those using solution processed $PC_{61}BM$ or ICBA; 0.43 for C_{60}, 0.54 for $PC_{61}BM$ and 0.50 for ICBA. This is because C_{60} and $PC_{61}BM$ are deposited using different methods; C_{60} by thermal evaporation and $PC_{61}BM$ by spin coating, which leads to very different fullerene overlayer morphologies. Figure 3.17 shows that C_{60} films are much rougher and the morphology is very similar to the underlying perovskite layer, due to the even deposition of the material onto the underlying layer.

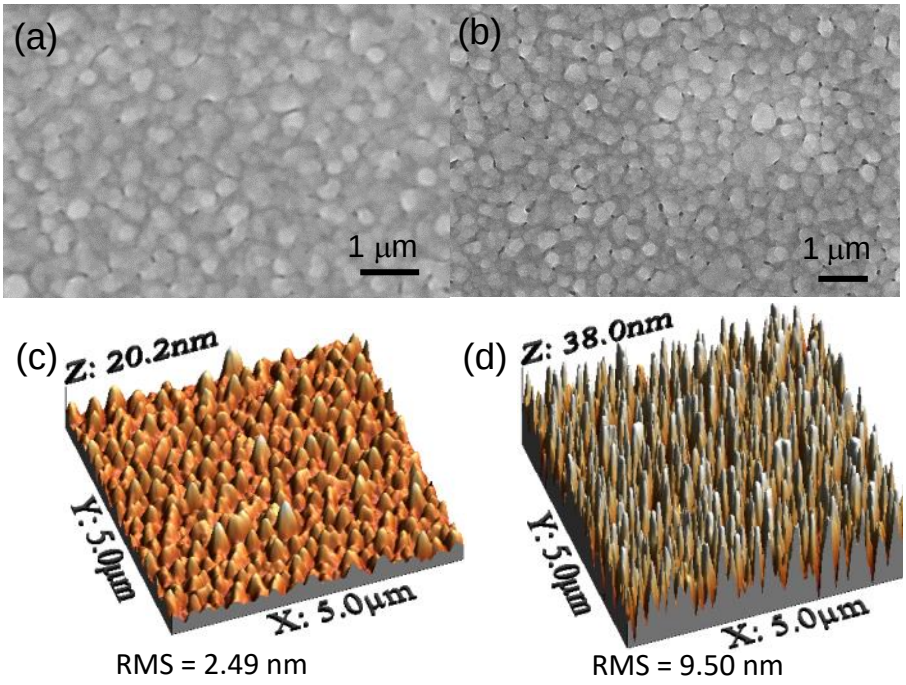

Figure 3.17: SEM images of **(a)** solution processed $PC_{61}BM$ and **(b)** evaporated C_{60} deposited on an ITO| $CsSnI_3$ substrate. And AFM images with root mean square (RMS) roughness values of **(c)** $PC_{61}BM$ and **(d)** C_{60} on a glass| $CsSnI_3$ substrate.

Conversely, $PC_{61}BM$ solution completely coats the slide before drying, which means that pores

in the film are more effectively filled due to capillary action, leading to a smoother, more continuous fullerene film. In terms of device performance, the rougher C_{60} film increases shunting current as the likelihood of filamentary short circuits is increased because there are more likely to be areas of the device with very thin C_{60} coverage.

3.4 Elucidating the Role of Excess SnI_2

3.4.1 Hole Transporting Properties

The charge transport properties of SnI_2 were investigated because the excess SnI_2 may have some degree of phase separation with respect to the $CsSnI_3$ in the film which would be expected to affect charge transport across one or both interfaces with the adjacent charge transport layers. Whilst it is evident that adding SnI_2 is beneficial to device performance, the reason is not fully understood because the possible optoelectronic role of the excess SnI_2 has not been considered; to a first approximation, a 10 mol% excess of SnI_2 is equivalent to a film of ~ 5 nm in thickness, which may be distributed throughout the film or phase separated to one or both interfaces with the charge extraction layers. The possibility that any excess of SnI_2 has not been considered because it was considered unlikely and there was a clear difference in device performance when SnI_2 was added, but elemental analysis of the films would be useful. Using a combination of JV measurements on unipolar diodes and by incorporating SnI_2 into organic planar heterojunction PV devices, it was determined that SnI_2 is capable of transporting holes, but not electrons because devices using SnI_2 as an HTL still function, but when used as an ETL, they do not (Figure 3.18). For device studies a 10 nm thickness of SnI_2 was used to ensure charges had to be transported through the SnI_2 film on the way to the electrode. Copper phthalocyanine (CuPc) and C_{60} was used in these devices because using evaporated over-layers ensured that the SnI_2 would not be dissolved by solvent.

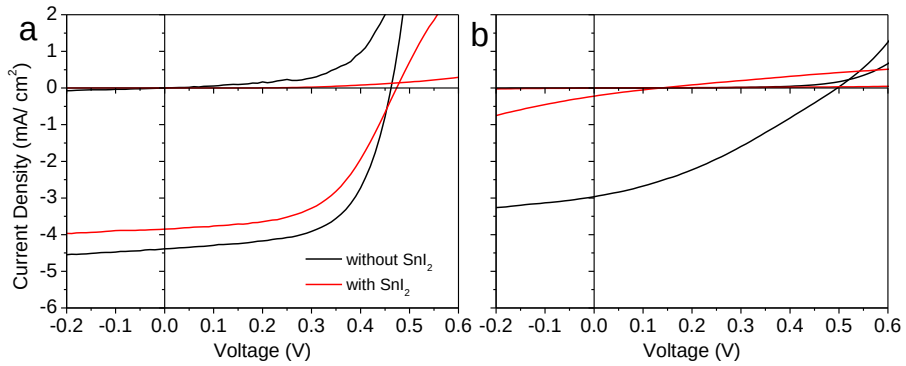

Figure 3.18: *JV* data for devices made with and without a 10 nm layer of SnI_2 in the structure **(a)** ITO| SnI_2| CuPc| C_{60}| BCP| Al, and **(b)** ITO| Al (0.8 nm)| SnI_2| C_{60}| CuPc| MoO_3| Al. Here CuPc is used as the light harvesting electron donor.

Data from unipolar diodes show that the hole mobility, μ_h of SnI_2 is of the order of 10^{-6} cm^2 V^{-1} s^{-1} (Figure 3.19). This was calculated using the Mott-Gurney law (Equation 3.1).[27]

$$\mu_h = \frac{8JL^3}{9\epsilon_0\epsilon_r V^2} \tag{3.1}$$

where J is current density, L is length or thickness, ϵ_0 is the permittivity of free space, ϵ_r is the relative permittivity of the probed material, and V is the applied voltage.

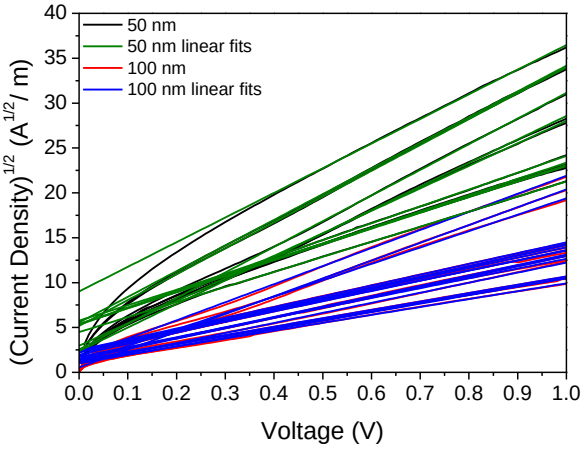

Figure 3.19: $J^{1/2}V$ data for unipolar diodes in the structure ITO| MoO_3| SnI_2 (50 or 100 nm)| MoO_3| Al.

It is therefore possible that SnI_2 does not impede the extraction of holes from $CsSnI_3$ to the CuI layer. To determine the accessibility of the SnI_2 valence band for hole transport we have measured the ionisation potential (I_p) of SnI_2 ($I_p = 5.64 \pm 0.05$ eV) and CuI films ($I_p = 5.84 \pm 0.05$ eV) were measured using UPS (Figures 3.11 and 3.12). The I_p of $CsSnI_3$ with added SnI_2 was measured to be 0.37 eV below E_f, with E_f measured to be 4.84 eV below the VL, giving and I_p of 5.21 eV, importantly the sample was transferred using an air tight arm to load the sample into the spectrometer which ensures that the $CsSnI_3$ film is not oxidised. The I_p and E_f values obtained from Kelvin probe and UPS are in close agreement with the values reported by Chung *et al.* using argon sputtered $CsSnI_3$ (who reported an I_p of 4.9 eV).[4] These energy levels along with the work function of each material measured using the Kelvin probe technique are given in Figure 3.10. The UPS measurements indicate heavy p-doping of CuI which helps to explain its hole transporting property (Figure 3.11). These acceptor states near the valence band edge may be manifested as either atom vacancy defects or as Cu(II) defects in the crystal structures. Without such p-doping, CuI would not be capable of extracting holes due to its low lying VB edge (Figure 3.10), which would present a large barrier to hole extraction from the $CsSnI_3$ VB into the ITO electrode. When thermodynamic equilibrium is established between the different materials in the device, as a result of electron transfer from $CsSnI_3$ (and SnI_2) into the CuI, the barrier to hole extraction is reduced (Figure 3.20), although is still significant. The in depth study given in Chapter 5 of this thesis clarifies the reason why the CuI HTL does not present a barrier to hole extraction. From the energy level diagram shown in Figure 3.10 it would be expected that there is a significant barrier to hole extraction from $CsSnI_3$ to SnI_2 (which is not heavily doped intrinsically) which is not consistent with JV characteristics observed in devices, even for those fabricated with $CsSnI_3$ using excesses of SnI_2 up to 15 mol%. It is therefore tentatively suggested that the excess SnI_2 is distributed over the whole $CsSnI_3$ crystallite surface, most likely as a discontinuous film. Further insight into this

important point is provided in chapters 4 and 5 of this thesis.

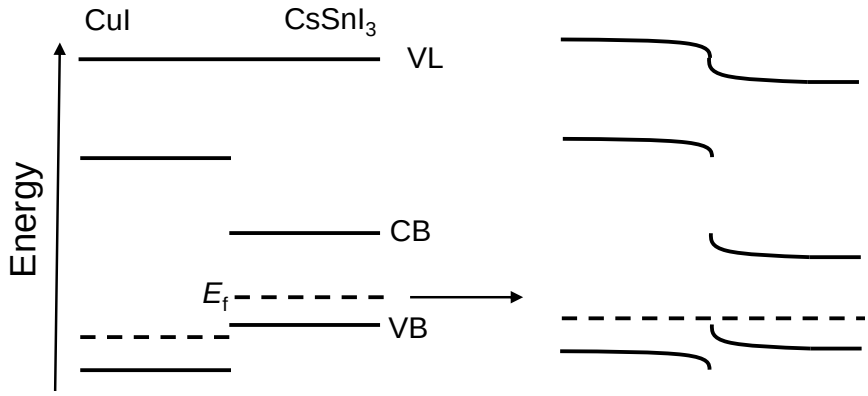

Figure 3.20: Energy level diagram depicting the CuI| $CsSnI_3$:SnI_2 interface, before and after electrical contact.

3.5 Probing the Energetics at the $CsSnI_3$| C_{60} Interface

The improvement in device performance when fabricated using excess SnI_2 in $CsSnI_3$ film formation can be attributed to a reduction in the Sn vacancy defect density, which reduces recombination losses. To investigate whether the energetics at the $CsSnI_3$| C_{60} interface may also play a role, the evolution of the energy difference between the Fermi level and vacuum level of $CsSnI_3$ upon increasing the thickness of C_{60} was measured using the Kelvin probe technique. This energy difference, ϵ_f^{vac}, corresponds to the work function of C_{60} when the film thickness is sufficient for the establishment of Fermi level alignment across the interface. If equilibrium is not achieved, ϵ_f^{vac} corresponds to the work function of the perovskite film with modified surface potential.[28, 29] From this, a positive vacuum level shift is observed at the interface between $CsSnI_3$ with 10 mol% added SnI_2 and C_{60}, which is not observed for $CsSnI_3$ with no excess SnI_2 (Figure 3.21). This difference is in qualitative agreement with the improvement in V_{oc} observed in devices when using $CsSnI_3$ with added SnI_2 over $CsSnI_3$ with no excess SnI_2.

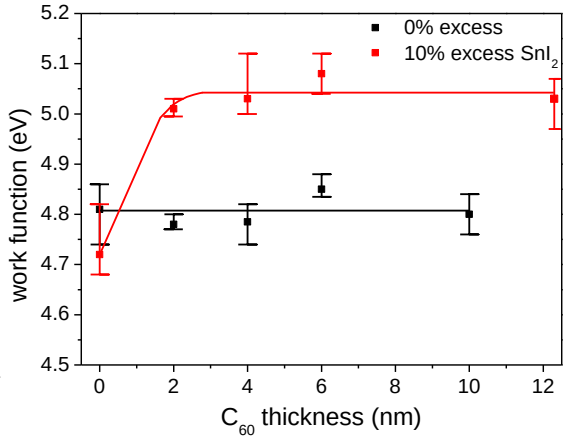

Figure 3.21: Kelvin-probe data of films of C_{60} of different thicknesses deposited on either $CsSnI_3$ or $CsSnI_3$ with 10 mol% added SnI_2.

The positive vacuum level shift reduces the energy loss that occurs when electrons are transferred from the $CsSnI_3$ to the C_{60} (as depicted in Figure 3.22). Such abrupt interfacial vacuum level shifts are well known to occur at the interface between different organic semiconductors and at the interface between organic semiconductors and metal electrodes.[28] It is tentatively suggested that the physical reason for the positive vacuum level shift is partial charge transfer between a thin layer of SnI_2 at the perovskite surface, since it is shown in Chapter 4 of this thesis that such a charge transfer interaction does occur between $SnCl_2$ and $PC_{61}BM$.

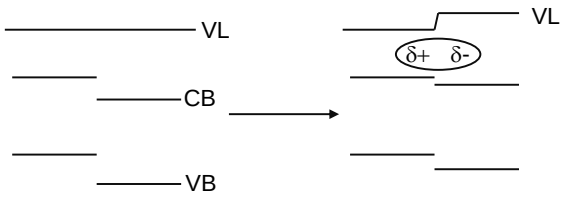

Figure 3.22: Flat band energy level diagram depicting abrupt vacuum level shift due to an interfacial dipole formation as a result of a charge transfer interaction between surface SnI_2 and C_{60}.

3.6 Effect of SnI_2 on Stability

The added SnI_2 was also found to impart improved stability to PV devices when stored in ambient air. Devices were taken into the air for periods of time and returned to the N_2 filled glovebox for JV analysis. Devices fabricated using $CsSnI_3$ with no excess SnI_2 degraded almost immediately in the air. However, champion devices made using $CsSnI_3$ with 10 mol% added SnI_2 still exhibited significant photovoltaic response (0.3% η) after 14 hours in air (Figure 3.23). $CsSnI_3$ + 10 mol% SnI_2 devices were also found to be more stable towards constant illumination under nitrogen (Figure 3.24). The degradation mechanisms under inert atmosphere are uncertain. However, degradation under illumination in inert atmosphere has been reported in organic PV.[30]

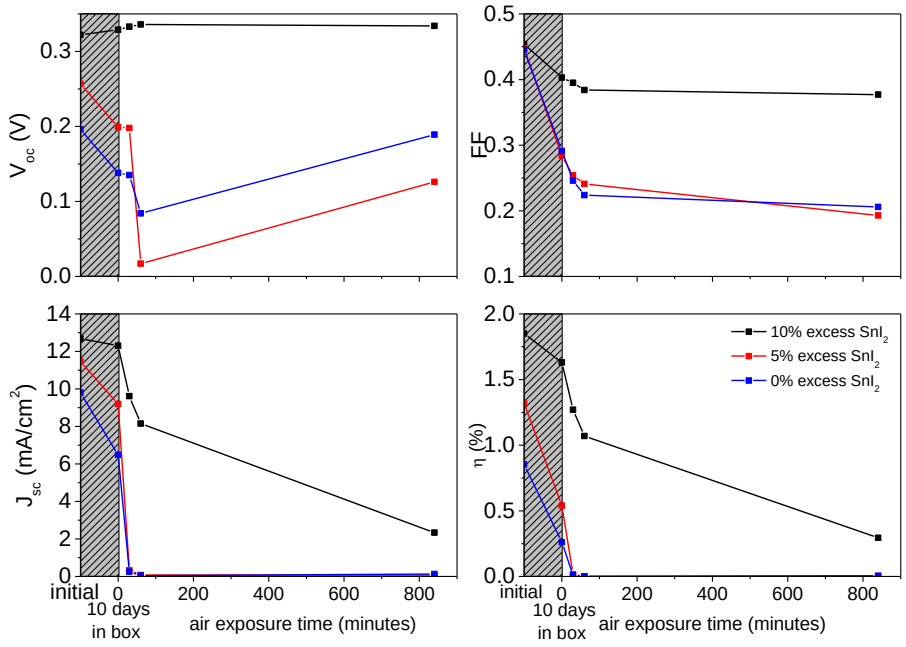

Figure 3.23: Key performance parameters of devices with the structure ITO| CuI| $CsSnI_3$ + 0, 5 or 10 mol% added SnI_2| C_{60}| BCP| Al as a function of ambient air exposure time. JV measurements were performed under nitrogen.

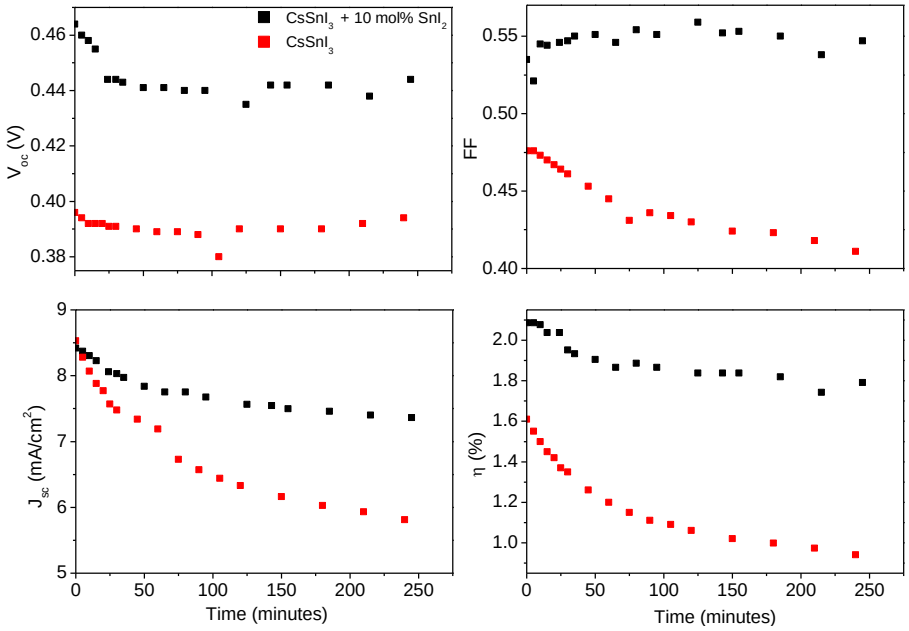

Figure 3.24: JV characteristics of devices in model architecture using $CsSnI_3$ with or without 10 mol% added SnI_2 under constant illumination under nitrogen.

Device deterioration due to air ingress is dependent on several parallel mechanisms, some of which may not be related to the perovskite layer such as aluminium electrode oxidation, C_{60} doping with oxygen,[31] and BCP crystallisation.[32] Therefore in order to determine the effect that $CsSnI_3$ degradation has on device performance, devices were fabricated in the structure shown in Figure 3.6 using $CsSnI_3$ with and without 10 mol% added SnI_2. The perovskite layer was exposed to air for 1 minute for some devices and compared to the devices that made without air exposure. The conversion of $CsSnI_3$ to Cs_2SnI_6 is likely to be a major contribution to reduction in J_{sc}, and because this conversion is expected to occur at the interface of the $CsSnI_3$ film, the change in energetics at the perovskite| C_{60} interface would be expected to cause an increase in series resistance therefore also affecting the *FF* of devices (Figure 3.25). The *JV* characteristics in Figure 3.26 are consistent with those of Figure 3.23 in terms of J_{sc}, V_{oc} and *FF*. Further insight into the degradation of inverted $CsSnI_3$ based PV devices is given in Chapters 4 and 5 of this thesis.

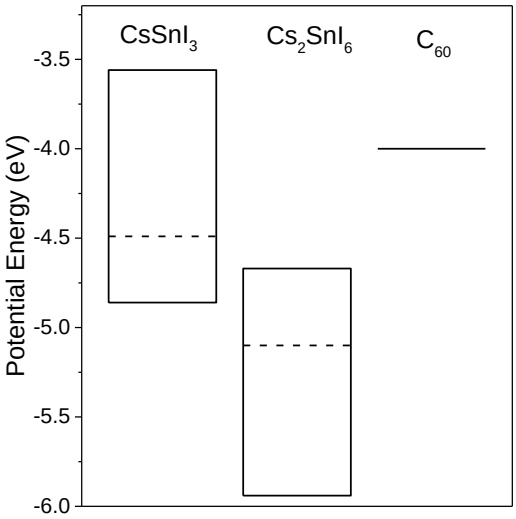

Figure 3.25: Energy level diagram depicting $CsSnI_3$, Cs_2SnI_6 and C_{60}.

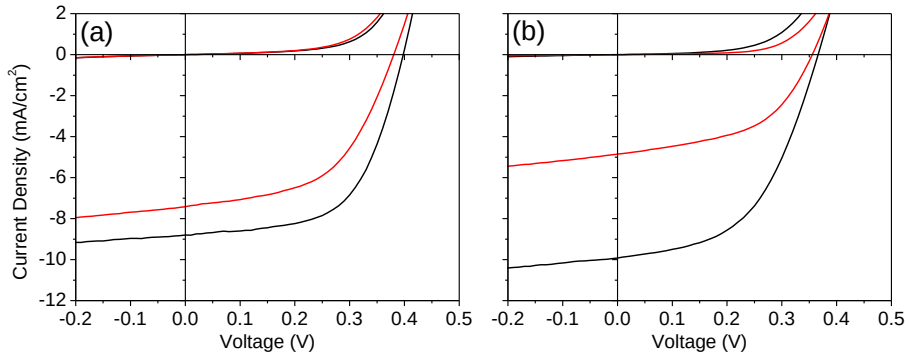

Figure 3.26: JV plots of devices made using **(a)** $CsSnI_3$ with 10 mol% added SnI_2 with and without 1 minute air exposure, and **(b)** $CsSnI_3$ with and without 1 minute air exposure.

3.7 Conclusions

In conclusion, the use of orthorhombic $CsSnI_3$ with defect densities low enough for use in photovoltaic devices based on a CuI| $CsSnI_3$| fullerene planar *p-i-n* structure was demonstrated. The V_{oc} can be approximately doubled from $\sim$ 0.28 V to $\sim$ 0.55 V by engineering the energetics at the perovskite| fullerene interface. To our knowledge, our devices had the highest V_{oc} and *FF* of any $CsSnI_3$ devices previously reported. A simple strategy for stabilising devices and used a combination of photoelectron spectroscopy, contact potential and device based measurements

for rationalising the reason for this was also demonstrated. Tin perovskite must be synthesised in a tin rich environment in order to be useful as a light harvester in photovoltaic devices in order to reduce the density of tin vacancy defects which lead to increased recombination. The charge transport properties of SnI_2 may also contribute towards improving the performance of $CsSnI_3$ devices.

References

[1] M. H. Kumar, S. Dharani, W. L. Leong, P. P. Boix, R. R. Prabhakar, T. Baikie, C. Shi, H. Ding, R. Ramesh, M. Asta, M. Graetzel, S. G. Mhaisalkar, and N. Mathews, "Lead-free halide perovskite solar cells with high photocurrents realized through vacancy modulation," *Adv. Mater.*, vol. 26, pp. 7122–7127, 2014.

[2] P. Xu, S. Chen, H.-J. Xiang, X.-G. Gong, and S.-H. Wei, "Influence of defects and synthesis conditions on the photovoltaic performance of perovskite semiconductor $CsSnI_3$," *Chem. Mater.*, vol. 26, pp. 6068–6072, 2014.

[3] W. Shockley and W. T. Read, "Statistics of the recombination of holes and electrons," *Phys. Rev.*, vol. 87, pp. 835–842, 1952.

[4] I. Chung, B. Lee, J. He, R. P. H. Chang, and M. G. Kanatzidis, "All-solid-state dye-sensitized solar cells with high efficiency.," *Nature*, vol. 485, pp. 486–489, 2012.

[5] L. Peedikakkandy and P. Bhargava, "Recrystallization and phase stability study of cesium tin iodide for application as a hole transporter in dye sensitized solar cells," *Mater. Sci. Semicond. Process.*, vol. 33, pp. 103–109, 2015.

[6] D. Sabba, H. K. Mulmudi, R. R. Prabhakar, T. Krishnamoorthy, T. Baikie, P. P. Boix, S. Mhainsalkar, and N. Mathews, "Impact of anionic Br^- substitution on open circuit voltage in lead free perovskite ($CsSnI_{3-x}Br_x$) solar cells .," *J. Phys. Chem. C*, vol. 119, pp. 1763–1767, 2015.

[7] I. Chung, J.-H. Song, J. Im, J. Androulakis, C. D. Malliakas, H. Li, A. J. Freeman, J. T. Kenney, and M. G. Kanatzidis, "$CsSnI_3$: Semiconductor or metal? High electrical conductivity and strong near-infrared photoluminescence from a single material. High hole mobility and phase-transitions.," *J. Am. Chem. Soc.*, vol. 134, pp. 8579–8587, 2012.

[8] W. Werker, "Die kristallstruktur des Rb_2SnI_6 und Cs_2SnI_6," *Recl. des Trav. Chim. des Pays-Bas*, vol. 58, pp. 257–258, 1939.

[9] P. R. Moses, L. M. Wier, J. C. Lennox, H. O. Finklea, J. R. Lenhard, and R. W. Murray, "X-ray photoelectron spectroscopy of alkylamine-silanes," *Anal. Chem.*, vol. 50, pp. 576–585, 1978.

[10] W.-K. Choi, "Chemical shifts and optical properties of tin oxide films grown by a reactive ion assisted deposition," *J. Vac. Sci. Technol. A Vacuum, Surfaces, Film.*, vol. 14, pp. 359–366, 1996.

[11] a. Pashutski, a. Hoffman, and M. Folman, "Low temperature XPS and AES studies of O2 adsorption on Al(100)," *Surf. Sci. Lett.*, vol. 208, pp. L91–L97, 1989.

[12] C. C. Stoumpos, C. D. Malliakas, and M. G. Kanatzidis, "Semiconducting tin and lead iodide perovskites with organic cations: phase transitions, high mobilities, and near-infrared photoluminescent properties.," *Inorg. Chem.*, vol. 52, pp. 9019–9038, 2013.

[13] E. Stathatos, P. Lianos, and C. Tsakiroglou, "Highly efficient nanocrystalline titania films made from organic/inorganic nanocomposite gels," *Microporous Mesoporous Mater.*, vol. 75, pp. 255–260, 2004.

[14] A. T. Raoufi and Davood, "The annealing temperature dependence of anatase TiO_2 thin films prepared by the electron-beam evaporation method," *Semicond. Sci. Technol.*, vol. 31, p. 125 012, 2016.

[15] J. A. Christians, R. C. M. Fung, and P. V. Kamat, "An inorganic hole conductor for organo-lead halide perovskite solar cells. Improved hole conductivity with copper iodide.," *J. Am. Chem. Soc.*, vol. 136, pp. 758–764, 2014.

[16] J. Eccher, W. Zajaczkowski, G. C. Faria, H. Bock, H. Von Seggern, W. Pisula, and I. H. Bechtold, "Thermal evaporation versus spin-coating: Electrical performance in columnar liquid crystal OLEDs," *ACS Appl. Mater. Interfaces*, vol. 7, pp. 16 374–16 381, 2015.

[17] T. Sakurai, S. Toyoshima, H. Kitazume, S. Masuda, H. Kato, and K. Akimoto, "Influence of gap states on electrical properties at interface between bathocuproine and various types of metals," *J. Appl. Phys.*, vol. 107, p. 043 707, 2010.

[18] B. W. Larson, J. B. Whitaker, X.-B. Wang, A. A. Popov, G. Rumbles, N. Kopidakis, S. H. Strauss, and O. V. Boltalina, "Electron affinity of phenyl-C_{61}-butyric acid methyl ester (PCBM)," *J. Phys. Chem. C*, vol. 117, pp. 14 958–14 964, 2013.

[19] Y. He, H. Y. Chen, J. Hou, and Y. Li, "Indene-C_{60} bisadduct: A new acceptor for high-performance polymer solar cells," *J. Am. Chem. Soc.*, vol. 132, pp. 1377–1382, 2010.

[20] P. A. Tipler and R. A. Llewellyn, *Modern Physics, 3rd Edition*. New York: W. H. Freeman and Company, 1999, p. 135.

[21] E. L. Unger, E. T. Hoke, C. D. Bailie, W. H. Nguyen, A. R. Bowring, T. Heumuller, M. G. Christoforo, and M. D. McGehee, "Hysteresis and transient behavior in current-voltage measurements of hybrid-perovskite absorber solar cells," *Energy Environ. Sci.*, pp. 3690–3698, 2014.

[22] H. J. Snaith, A. Abate, J. M. Ball, G. E. Eperon, T. Leijtens, N. K. Noel, S. D. Stranks, J. T.-W. Wang, K. Wojciechowski, and W. Zhang, "Anomalous hysteresis in perovskite solar cells," *J. Phys. Chem. Lett.*, vol. 5, pp. 1511–1515, 2014.

[23] S. V. Reenen, M. Kemerink, and H. J. Snaith, "Modeling anomalous hysteresis in perovskite solar cells," *J. Phys. Chem. Lett.*, vol. 6, pp. 3808–3814, 2015.

[24] B. Chen, M. Yang, S. Priya, and K. Zhu, "Origin of J-V hysteresis in perovskite solar cells," *J. Phys. Chem. Lett.*, vol. 7, pp. 905–917, 2016.

[25] F. Hao, C. C. Stoumpos, P. Guo, N. Zhou, T. J. Marks, R. P. H. Chang, and M. G. Kanatzidis, "Solvent-mediated crystallization of $CH_3NH_3SnI_3$ films for heterojunction depleted perovskite solar cells," *J. Am. Chem. Soc.*, vol. 137, pp. 11 445–11 452, 2015.

[26] Y. Shao, Z. Xiao, C. Bi, Y. Yuan, and J. Huang, "Origin and elimination of photocurrent hysteresis by fullerene passivation in $CH_3NH_3PbI_3$ planar heterojunction solar cells," *Nat. Commun.*, vol. 5, pp. 1–7, 2014.

[27] N. F. Mott and R. W. Gurney, *Electronic processes in ionic crystals*. New York: Oxford University Press, 1940.

[28] H. Ishii, K. Sugiyama, E. Ito, and K. Seki, "Energy level alignment and interfacial electronic structures at organic metal and organic organic interfaces," *Adv. Mater.*, vol. 11, pp. 605–625, 1999.

[29] S. R. Day, R. a. Hatton, M. a. Chesters, and M. R. Willis, "The use of charge transfer interlayers to control hole injection in molecular organic light emitting diodes," *Thin Solid Films*, vol. 410, pp. 159–166, 2002.

[30] M. O. Reese, A. J. Morfa, M. S. White, N. Kopidakis, S. E. Shaheen, G. Rumbles, and D. S. Ginley, "Pathways for the degradation of organic photovoltaic P3HT:PCBM based devices," *Sol. Energy Mater. Sol. Cells*, vol. 92, pp. 746–752, 2008.

[31] K. Norrman, N. B. Larsen, and F. C. Krebs, "Lifetimes of organic photovoltaics: Combining chemical and physical characterisation techniques to study degradation mechanisms," *Sol. Energy Mater. Sol. Cells*, vol. 90, pp. 2793–2814, 2006.

[32] P. Peumans, A. Yakimov, and S. R. Forrest, "Small molecular weight organic thin-film photodetectors and solar cells," *J. Appl. Phys.*, vol. 93, pp. 3693–3723, 2003.

Chapter 4

Enhancing the Properties of $CsSnI_3$ Films for Applications in Inverted PPVs Using Tin Halide Additives: A Systematic Study

4.1 Background

Building on the success of Chapter 3, SnF_2, $SnCl_2$, $SnBr_2$ and SnI_2 were systematically screened to identify the most effective as a source of excess Sn in $CsSnI_3$ film formation. These halides impart an additional degree of complexity due to the possibility of halide substitution into the perovskite lattice. Prior to this work only SnF_2 and SnI_2 had been tested as a source of excess tin in PPV devices.[1–3] However, PPV devices using SnF_2 exhibited poor performance, and it was not clear as to why SnF_2 was used given that it has poor solubility in the solvent most commonly used for the preparation of perovskite films; DMF.

4.2 Probing the Stability of Thin $CsSnI_3$:SnX_2 Films (X = F, Cl, Br, and I)

It is known that B-γ $CsSnI_3$ degrades to Cs_2SnI_6 in ambient air and that the absorption coefficient of Cs_2SnI_6 in the visible spectrum is a factor of 10 times smaller than that of B-γ $CsSnI_3$.[4] Consequently, it is possible to monitor the oxidation of thin films of $CsSnI_3$ in air by measuring the evolution of the electronic absorption spectrum with time, as shown in Figures 4.1 (a) and (b).

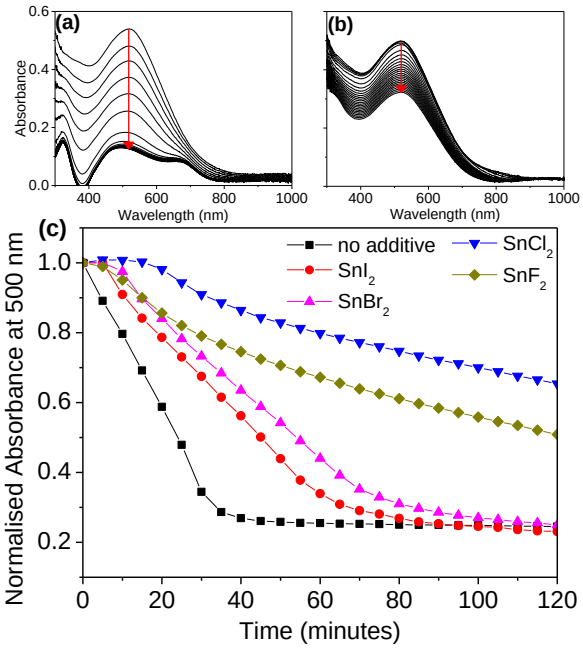

Figure 4.1: Evolution of electronic absorption spectrum of $CsSnI_3$ films with different tin halide additives over a period of 2 hours in ambient air for: **(a)** $CsSnI_3$; **(b)** $CsSnI_3$ + 10% $SnCl_2$; and **(c)** normalised absorbance at 500 nm for $CsSnI_3$ with 10 mol% of SnI_2, $SnBr_2$, $SnCl_2$ or SnF_2, and with no tin halide additive. In all cases the $CsSnI_3$ solution concentration was 8 wt% which resulted in a film thickness of $\sim$ 50 nm.

It is evident from Figure 4.1 (c) that of the four tin halides investigated $SnCl_2$ results in the highest film stability. Based on the time taken for the absorbance at 500 nm to reduce

by 30%, films with $SnCl_2$ are more stable by a factor of ~ 3.7 times as compared to the case with 10 mol% excess SnI_2, and a factor of ~ 6.7 times compared to $CsSnI_3$ films with no tin halide additive. The SEM images in Figure 4.2 shows that the former cannot be attributed to a difference in film porosity because films prepared with 10 mol% $SnCl_2$ have a comparable or higher pin-hole density than films prepared with 10 mol% excess SnI_2, $SnBr_2$ or SnF_2.

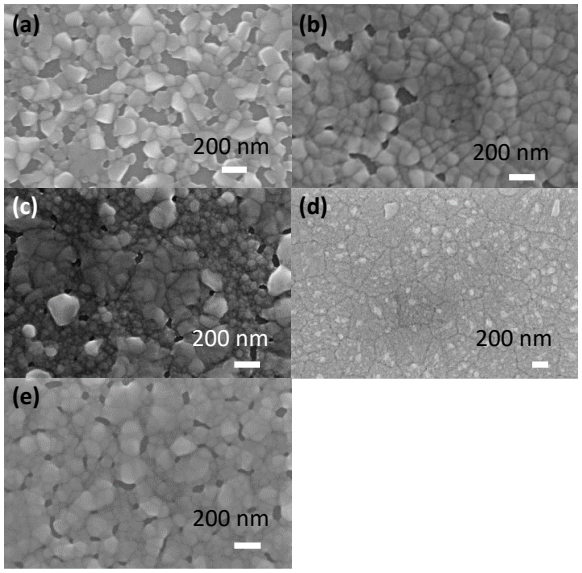

Figure 4.2: SEM images of $CsSnI_3$ with: **(a)** no tin halide additive, **(b)** 10 mol% added SnI_2, **(c)** 10 mol% added $SnBr_2$, **(d)** 10 mol% added SnF_2, **(e)** 10 mol% added $SnCl_2$.

This result indicates that the improvement in film stability upon addition of $SnCl_2$ is due to enhanced chemical stability towards oxidation in air, rather than the formation of a more compact film which could improve film stability by reducing the surface area of perovskite presented to the ambient atmosphere. Step height analysis of a scored $CsSnI_3$ + 10 mol% $SnCl_2$ film shown in Figure 4.3 shows that the film has a thickness of ~ 50 nm.

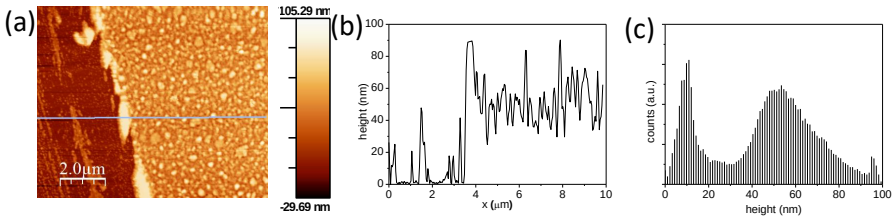

Figure 4.3: AFM stepheight image **(a)**, cross section **(b)** and histogram **(c)** of $CsSnI_3$ + 10 mol% $SnCl_2$ made from 8 wt% DMF solution.

Wide angle diffraction patterns confirming the formation of B-γ $CsSnI_3$ structure, both with and without tin halide additives, and degradation products, Cs_2SnI_6 and Y-$CsSnI_3$ structures are given in Figure 4.4 (a) - (c).

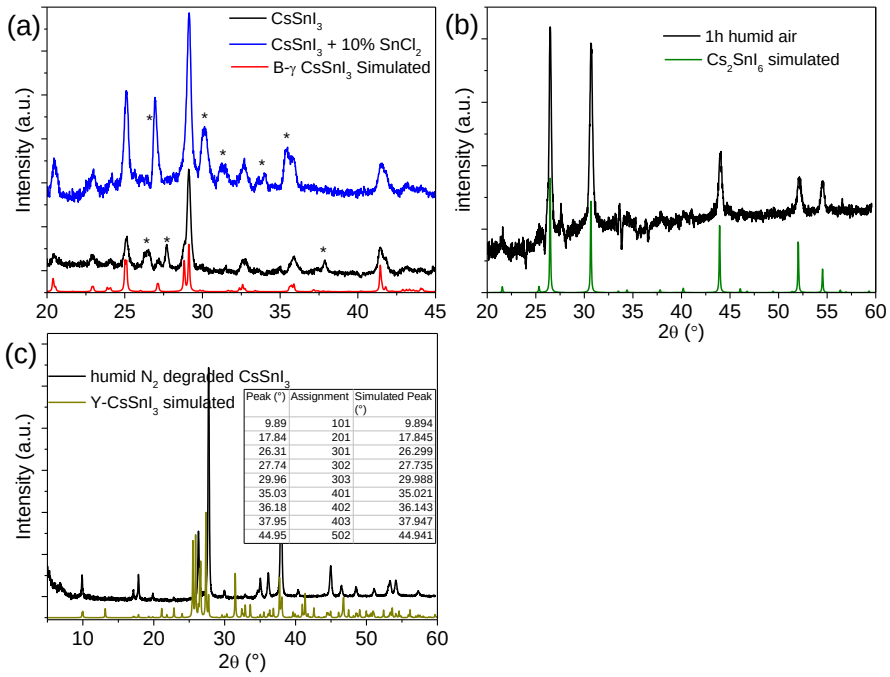

Figure 4.4: Wide angle XRD patterns of $CsSnI_3$ + 10 mol% $SnCl_2$ under flow of nitrogen **(a)** with no air or moisture exposure, **(b)** after humid air exposure, and **(c)** after humid nitrogen exposure, table of peak assignments for Y-$CsSnI_3$ inset. Simulated patterns generated using CIFs from refs. [5, 6]

Corroborating evidence for the large improvement in $CsSnI_3$ film stability when prepared with

10 mol% $SnCl_2$ is provided by the evolution of the XRD pattern of thin films with time exposed to ambient air (Figure 4.5). Figure 4.5 shows how the intensity of one of the most intense reflections; the (202) Bragg peak, in the B-γ $CsSnI_3$ diffraction pattern, disappears completely with time, and so this peak serves as a good probe for monitoring the oxidation of B-γ $CsSnI_3$ to Cs_2SnI_6 in air. It is evident from a comparison of Figures 4.5 (a) and (d) that addition of $SnCl_2$ dramatically improves film stability, since after 3 hours of air exposure this peak has $\sim 80\%$ of its starting intensity, whilst it has almost completely disappeared for the $CsSnI_3$ film prepared with no tin halide additive.

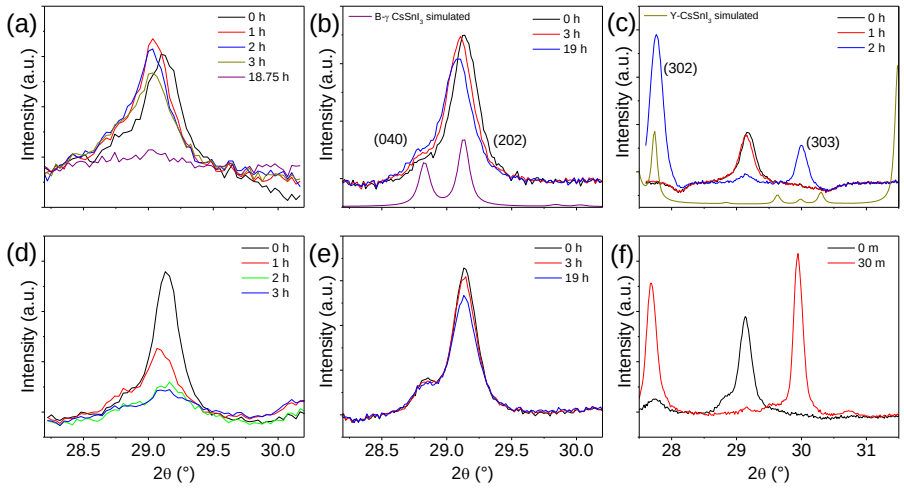

Figure 4.5: Upper: XRD patterns of thin films of $CsSnI_3$ prepared with 10 mol% $SnCl_2$ additive with exposure to; **(a)** 25% humid air, **(b)** dry air, and **(c)** humid nitrogen. Lower: XRD patterns of thin films of $CsSnI_3$ exposed to **(d)** 25% humid air, **(e)** dry air, and **(f)** humid nitrogen.

The evolution of the XRD patterns upon exposure to dry air and humid nitrogen also provides insight into the different roles of oxygen and water in the degradation of B-γ $CsSnI_3$ when exposed to ambient air. It is evident from Figures 4.5 (b) and 4.5 (e) that B-γ $CsSnI_3$ is stable in dry air, but converts to the yellow phase (Y-$CsSnI_3$) in a humid nitrogen atmosphere (Figure 4.5 (c) and 4.5 (f)). It is therefore only with the combined action of water and oxygen that

Cs_2SnI_6 is formed, which is in agreement with a study of bulk samples reported by Stoumpos *et al.*[7] Notably when Y-$CsSnI_3$ is formed it is also highly orientated, since only reflections from the $(h0l)$ planes are intense enough to be observed.

4.3 Elucidating the Structure of $CsSnI_3$:$SnCl_2$ films

The exceptional stability of $CsSnI_3$ films prepared with 10 mol% added $SnCl_2$ ($CsSnI_3$:$SnCl_2$) prompted further investigation into this specific system to determine the role of the $SnCl_2$. High resolution X-ray photoelectron spectroscopy (HRXPS) analysis reveals that there is only one Cl 2p environment in $CsSnI_3$ films prepared with 10 mol% $SnCl_2$, which has the same binding energy as for $SnCl_2$ (Figure 4.6), consistent with Cl not being incorporated into the perovskite structure. This suggests that the $SnCl_2$ is present as a thin film or layer of particles at the perovskite crystallite surfaces as schematically illustrated in Figure 4.7.

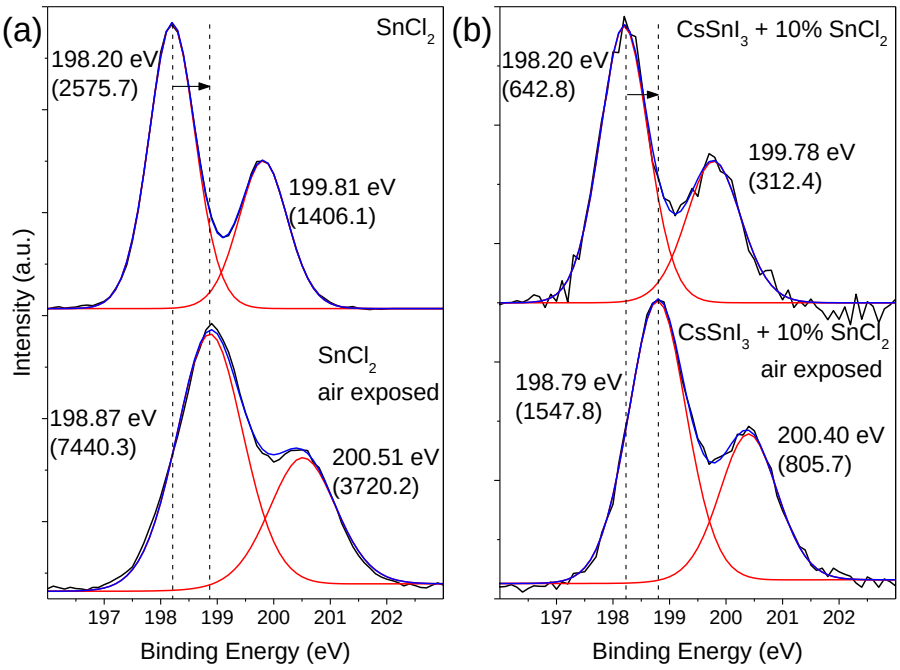

Figure 4.6: HRXPS spectra of Cl 2p environments in: **(a)** $SnCl_2$ with and without 1 hour of air exposure; **(b)** $CsSnI_3$ + 10 mol% $SnCl_2$ with and without 1 hour of air exposure. The measured spectra, peak deconvolution and the sum of the fitted peaks are given by black, red and blue lines respectively. Peak positions and intensities labelled on figures.

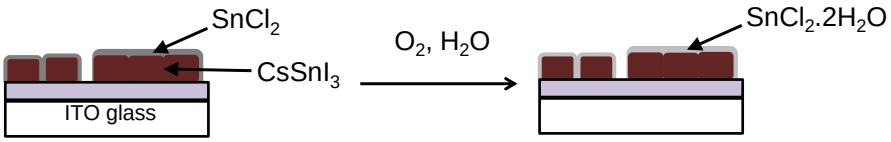

Figure 4.7: Diagram of structure of $CsSnI_3$:$SnCl_2$ film on ITO.

To confirm this hypothesis, the elemental composition of the surface of a compact film of $CsSnI_3$:$SnCl_2$ (Figure 4.8) and a thickness of $\sim$ 80 nm was probed using HRXPS for angles of photoelectron detection of 90° and 30°. Reducing the emission angle from 90° to 30° halves the sampling depth from $\sim$ 8 nm to $\sim$ 4 nm. For an angle of emission of 90° the Cl percentage composition is 36.4% (Table 4.1), which is several times higher than would be expected if Cl was evenly distributed throughout the thickness of the film.

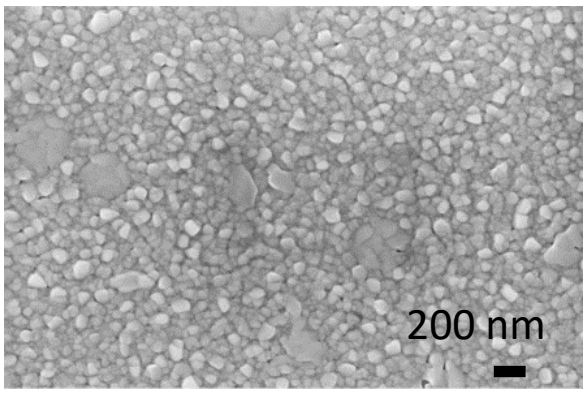

Figure 4.8: SEM image of a $CsSnI_3$ + 10 mol% $SnCl_2$ film made from 8 wt% DMF solution deposited on a gold substrate.

Table 4.1: Elemental ratios in a film of $CsSnI_3$ + 10 mol% added $SnCl_2$ measured using XPS with an incident angle of 90°or 30°.

Take off angle	%Sn	%Cs	%I	%Cl
90°	22.95	21.86	18.84	36.35
30°	23.75	18.08	15.25	42.91

When the angle of photoelectron detection is reduced to 30° the Cl atomic ratio increases to 42.9%, and the I atomic ratio decreases from 18.8% to 15.3% and the Cs atomic ratio decreases from 21.9% to 18.1%, which collectively is compelling evidence that the $SnCl_2$ is concentrated at the surface of the $CsSnI_3$ crystallites. Further direct evidence supporting this conclusion is provided by the results of an argon ion sputtering experiment on the film surface and analysing the elemental composition as a function of depth, since the atomic percentage Cl decreases rapidly as the surface is etched, whilst the I concentration increases and then saturates (Figure 4.9).

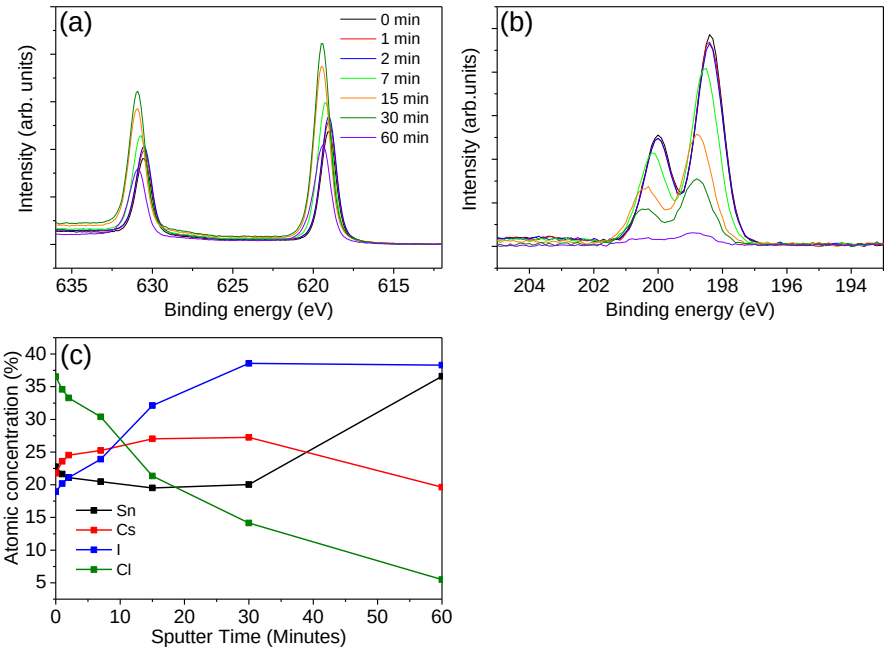

Figure 4.9: XPS spectra of $CsSnI_3$ + 10% $SnCl_2$ showing **(a)** I 3d, and **(b)** Cl 2p orbitals at different argon sputtering times. **(c)** Atomic concentrations of Sn, Cs, I, and Cl over argon sputtering time on the sample.

The conclusion that Cl is not incorporated into the $CsSnI_3$ lattice is also consistent with the observation that Cl does not displace I in methylammonium lead iodide perovskite but is located at the grain boundaries,[8] and that solid solutions of $CsSnI_{3-x}Cl_x$ are not formed from stoichiometric DMF solutions of the halide precursors.[9] The latter likely stems from the large difference in ionic radii between Cl and I (1.81 Å for Cl and 2.2 Å for I)[10], and/or the very different structures of $CsSnCl_3$ and $CsSnI_3$ at room temperature, which are monoclinic and orthorhombic respectively.[9] Additionally Peedikakkandy *et al.*[9] have shown that a processing temperature of 70 °C is needed to form $CsSnCl_3$ from DMF solutions, which may explain why there is no evidence for the presence of the $CsSnCl_3$ perovskite when processing at room temperature.

When films of $SnCl_2$ only, and $CsSnI_3$ with 10 mol% $SnCl_2$ are exposed to ambient air for one hour the Cl 2p peaks in both spectra shift to higher binding energies by the same amount

(Figure 4.6 (a) - lower and 4.6 (b) - lower), and the intensities of the two weak O1s peaks at 530.7 eV and 532.1 eV (Figure 4.10 (b) (ii)), assigned to SnO_2 [11] and H_2O, respectively, are increased by a factor of ~ 10. The insight as to the differing roles of water and oxygen provided by the XRD patterns, combined with the changes in the XPS spectra upon exposure to ambient air, are consistent with the $SnCl_2$ surface layer functioning as a desiccant which slows the oxidation of the underlying $CsSnI_3$ by H_2O, since $SnCl_2$ is known to form a stable hydrate ($SnCl_2 \cdot 2\,H_2O$) as well as oxidising to form SnO_2. As such, the susceptibility of $CsSnI_3$ towards oxidation in ambient air is not actually changed, rather the onset of oxidation is slowed by the sacrificial oxidation of the $SnCl_2$ at its surface. It is evident from Figures 4.10 (e), (f) and (g), that there are two Sn environments in $CsSnI_3$ without added $SnCl_2$, assigned to Sn^{2+} and Sn^{4+} states (Figure 4.10 (f) (ii)) for the low and high binding energy peaks respectively. The shoulder Sn peaks in the $CsSnI_3$:$SnCl_2$ are at significantly lower binding energies than the shoulder peaks in $CsSnI_3$. The shoulder peaks are assigned to Sn in the 2+ oxidation state as $SnCl_2$ because they match quite closely to the Sn3d peaks in $SnCl_2$, and it would be unlikely that a Sn^{4+} environment could be lower in binding energy than any Sn^{2+} environment. This is further evidence that $SnCl_2$ exists as a separate phase to $CsSnI_3$ rather than chloride being incorporated into the perovskite structure.

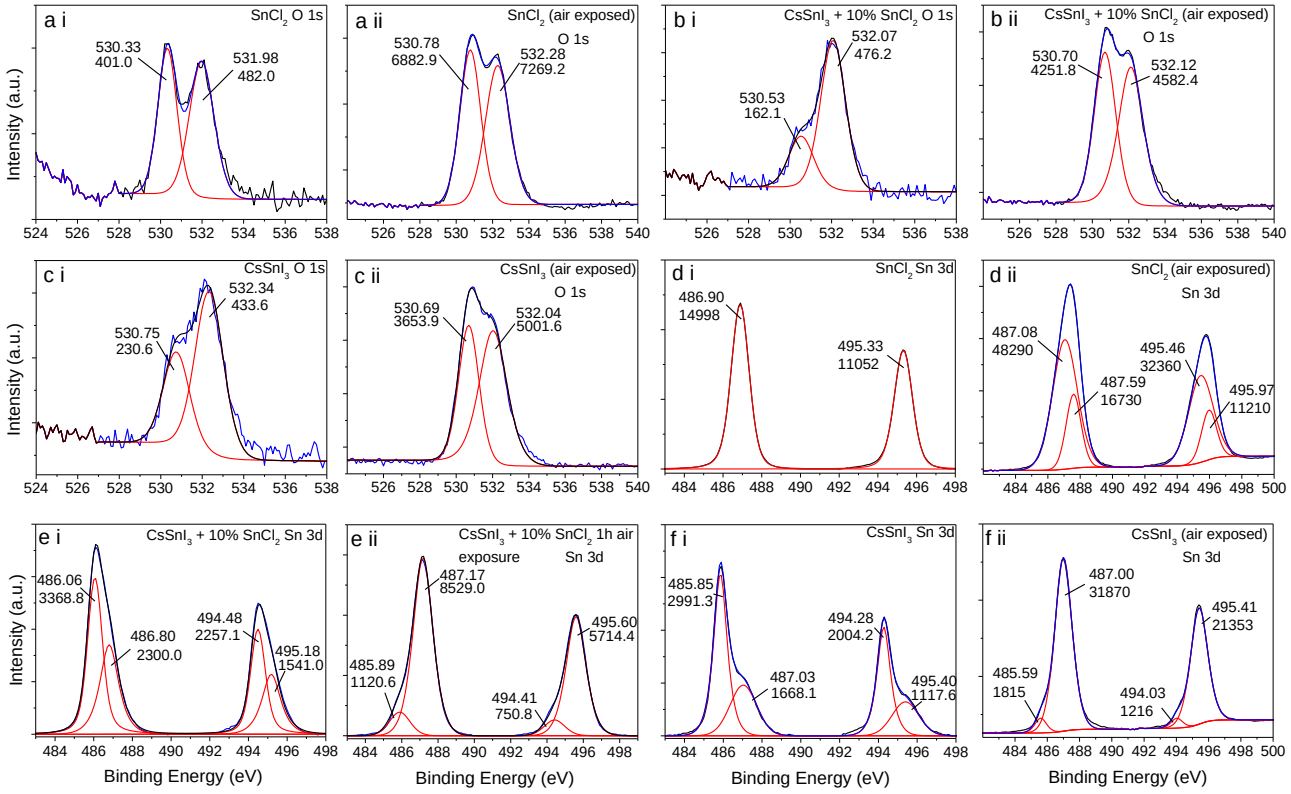

Figure 4.10: High resolution (HR) XPS spectra of: **(a)** $SnCl_2$ O 1s **(i)** with $\sim$ 1 min air exposure and ii after 1 hour air exposure.; **(b)** $CsSnI_3$ with 10 mol% $SnCl_2$ additive O 1s **(i)** with $\sim$ 1 min air exposure and **(ii)** after 1 hour air exposure.; **(c)** $CsSnI_3$ O 1s **(i)** with $\sim$ 1 min air exposure and **(ii)** after 1 hour air exposure.; **(d)** $SnCl_2$ Sn 3d **(i)** with $\sim$ 1 min air exposure and **(ii)** after 1 hour air exposure.; **(e)** $CsSnI_3$ + 10 mol% $SnCl_2$ Sn 3d **(i)** with $\sim$ 1 min air exposure and **(ii)** after 1 hour air exposure.; **(f)** $CsSnI_3$ Sn 3d **(i)** with $\sim$ 1 min air exposure and **(ii)** after 1 hour air exposure.

4.4 Device Studies

To test if the improvement in film stability towards air exposure translates into improved stability in PPVs, devices with a simplified architecture were fabricated, based on a planar heterojunction using $PC_{61}BM$ as the electron transport layer and $CsSnI_3$ as the light harvesting layer (Figure 4.11), the thicknesses were $\sim$ 50 nm for the $CsSnI_3$ and $\sim$ 70 nm thick for PCBM, giving a total bilayer thickness of $\sim$ 120 nm (Figures 4.3 and 4.12).

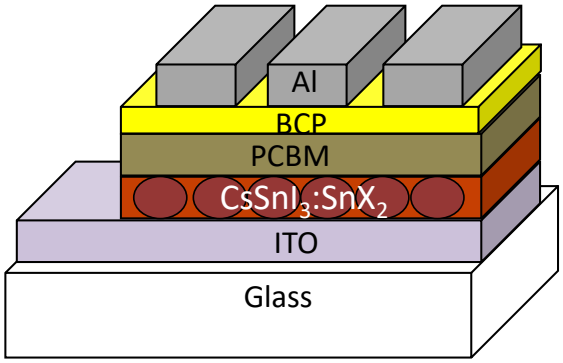

Figure 4.11: Diagram of primary device architecture used during this chapter.

This structure was chosen because it simplifies device fabrication and reduces the number of parallel degradation pathways that can complicate the interpretation of device stability studies. A simplified architecture is also attractive from a commercial perspective, since fabrication costs typically increase with increasing number of processing steps.[12] Of the four additives; $SnCl_2$, SnI_2, $SnBr_2$ and SnF_2, PPV devices using $SnBr_2$ and SnF_2 exhibited poor device performance with $\eta \leq 0.4\%$ (Table 4.2) and/or poor device yield and so were not investigated further. SnF_2 additive may have had poor solubility in the DMF solvent, and formed small isolated particles on the surface which could have affected their performance.

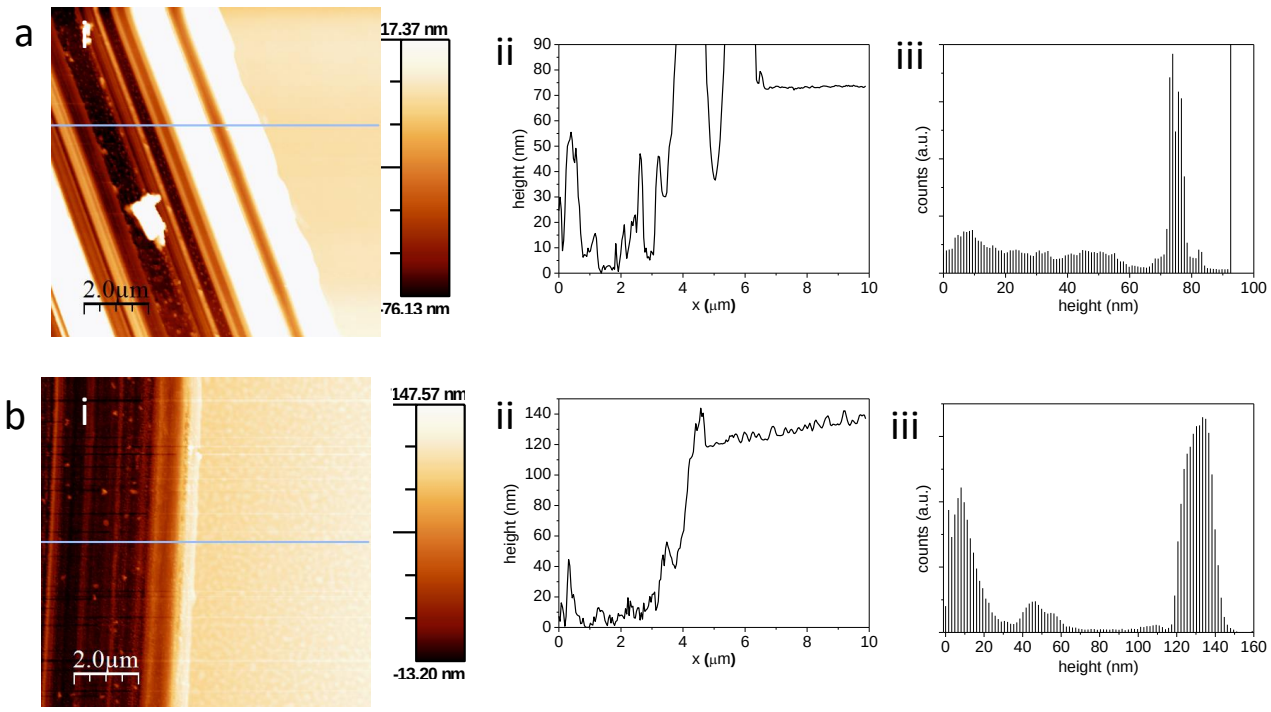

Figure 4.12: AFM (i) image, (ii) cross-section, and (iii) histogram of **(a)** a step edge of a PCBM film, and **(b)** a step edge of a $CsSnI_3$:$SnCl_2$| PCBM film.

Table 4.2: JV parameters (± one standard deviation) for devices with the structure: ITO glass| $CsSnI_3$ with either added $SnBr_2$ or SnF_2| $PC_{61}BM$| BCP| Al

Device	n	J_{sc} (mA/cm^2)	V_{oc} (V)	*FF*	η (%)	Champion η (%)
$CsSnI_3$ + 10% $SnBr_2$	12	2.32 ± 0.23	0.32 ± 0.04	0.38 ± 0.02	0.29 ± 0.05	0.35
$CsSnI_3$ + 10% SnF_2	4	6.23 ± 0.58	0.14 ± 0.01	0.42 ± 0.02	0.37 ± 0.03	0.40

4.4.1 Investigating $SnCl_2$ loading

Initially $SnCl_2$ loadings of 5, 10 and 15 mol% were investigated (Table 4.3 and Figure 4.13), and a loading of 10 mol% was found to give the highest yield of working devices combined with a narrow photocurrent spread. Consequently 10 mol% tin halide is the additive loading used

throughout this study, although it is evident from Table 4.3 and Figure 4.13 that there is scope for further optimisation of η for loadings in the range 10-15 mol%.

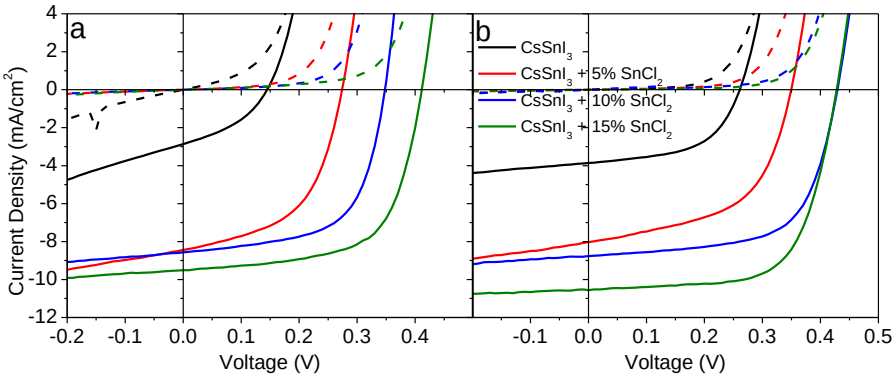

Figure 4.13: Representative JV plots for devices made using $CsSnI_3$ with the structure: ITO glass| $CsSnI_3$ + X mol% $SnCl_2$| $PC_{61}BM$| BCP| Al, with 0, 5, 10, or 15 mol% $SnCl_2$ additive tested **(a)** immediately after fabrication, and **(b)** after 3 weeks storage in a nitrogen glovebox. Full data set given in Table 4.3.

Table 4.3: Typical JV parameters (± one standard deviation) for devices with the structure: ITO glass| $CsSnI_3$ + X mol% $SnCl_2$| $PC_{61}BM$| BCP| Al where X = 0, 5, 10, or 15. Data in black - devices tested immediately after fabrication. Data in red - devices tested after storage in a nitrogen filled glove box for 3 weeks.

Device	n	J_{sc} (mA/cm^2)	V_{oc} (V)	*FF*	η (%)	Champion η (%)
$CsSnI_3$	26	3.41 ± 0.63	0.15 ± 0.03	0.38 ± 0.07	0.21 ± 0.12	0.45
	28	3.06 ± 0.59	0.21 ± 0.04	0.43 ± 0.07	0.30 ± 0.15	0.58
$CsSnI_3$ +	15	8.72 ± 0.52	0.27 ± 0.01	0.50 ± 0.05	1.18 ± 0.16	1.36
5 mol% $SnCl_2$	15	8.2 ± 1.0	0.33 ± 0.05	0.52 ± 0.07	1.48 ± 0.38	1.73
$CsSnI_3$ +	29	8.04 ± 0.68	0.35 ± 0.01	0.60 ± 0.06	1.71 ± 0.27	2.14
10 mol% $SnCl_2$	31	8.27 ± 0.78	0.41 ± 0.06	0.60 ± 0.11	2.08 ± 0.55	2.75
$CsSnI_3$ +	17	8.9 ± 1.2	0.40 ± 0.01	0.64 ± 0.02	2.29 ± 0.34	2.71
15 mol% $SnCl_2$	17	10.3 ± 1.3	0.42 ± 0.03	0.59 ± 0.07	2.55 ± 0.39	3.16

Importantly, the current-voltage characteristics of devices recorded in forward and reverse

sweep for a range of starting voltages and scan rates exhibit no significant hysteresis, and the performance is fractionally improved for slower scan rates; $\sim$ 45 mV s^{-1} (Figure 4.14). This could be because $CsSnI_3$ has a lower concentration of mobile iodide vacancy defects than $MAPbI_3$.[13] However, it has been shown using TOF-SIMS experiments that at high temperatures (> 60 °C) iodide vacancies can form in $CsSnI_3$.[14] Another possibility is that PCBM devices typically show less hysteresis than TiO_2 ETL devices because of a surface passivation effect which reduces capacitative trap state density.[15, 16]

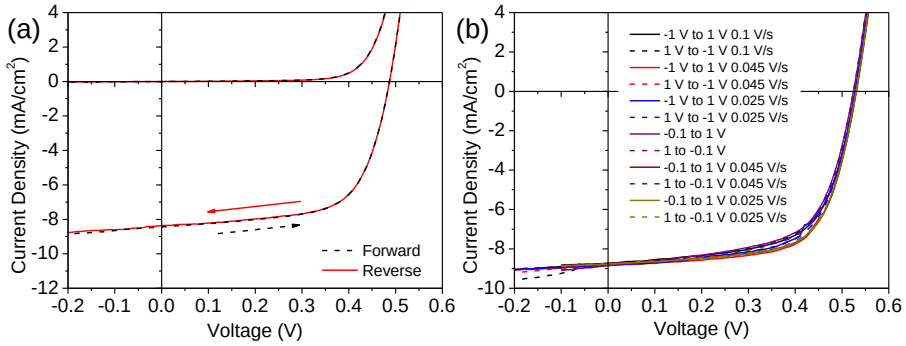

Figure 4.14: **(a)** JV plot of a device in the structure ITO| $CsSnI_3$ + 10 mol% $SnCl_2$| $PC_{61}BM$| BCP| Al, scanned in both forward (−1 V to +1 V) and reverse (+1 V to −1 V) directions at 0.1 V/s showing negligible hysteresis, and **(b)** JV plots of a device in the same structure with different scan speeds and direction.

4.4.2 Comparison of $SnCl_2$, SnI_2 and no additive

Immediately after fabrication devices with a $SnCl_2$ additive are 60-70% more efficient than those using SnI_2 and a factor of 4 times more efficient than those with no tin halide additive, due to higher J_{sc}, V_{oc} and *FF* (Table 4.4). However, when stored in a nitrogen filled glovebox (< 5 ppm O_2 and < 1 ppm H_2O) there are further large improvements in the η of devices with tin halide additives, on the time scale of weeks to several months (Figure 4.15, and Tables 4.4 and 4.5). Indeed the onset of significant improvements begins after only 1 week with

$\sim$ 10% improvement in V_{oc} and *FF* (Figure 4.16 (a)), although there is no change in either the electronic absorption spectrum or XRD pattern (peak intensity at 29.1° shows no trend over time) of the perovskite film (Figure 4.16 (b) and (c)), however, the XRD is difficult to interpret due to the change in intensity of background peaks. SEM images of several weeks old films of $CsSnI_3$ with different additives would be useful to see if morphology gradually changes over time. Notably this additional improvement is particularly pronounced for devices that have a low shunt resistance when tested immediately after fabrication, which is a useful self-healing mechanism for practical purposes (Figure 4.15 (b) and Tables 4.4 and 4.5).

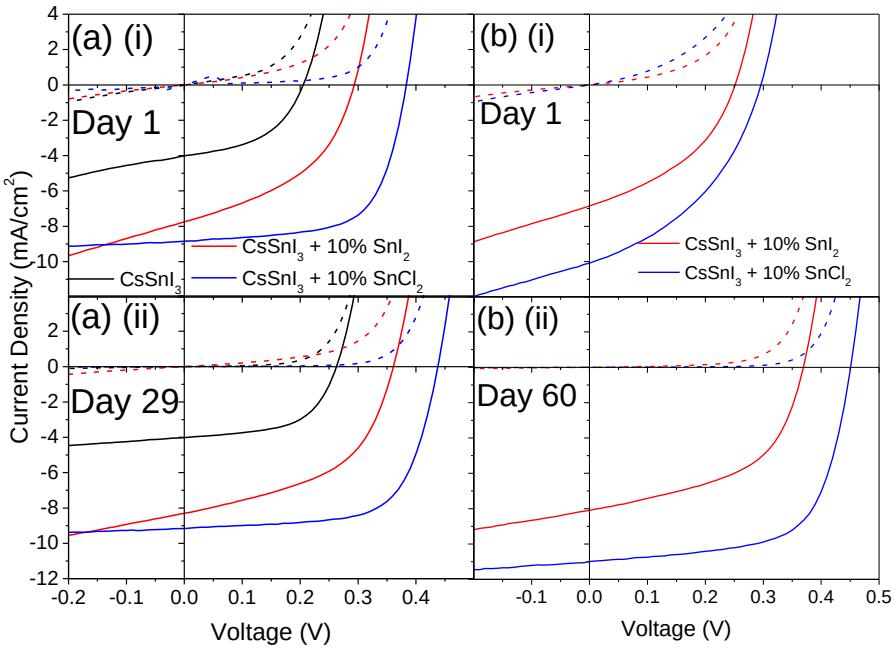

Figure 4.15: Current-voltage (JV) characteristics of representative PPVs with the structure: ITO| $CsSnI_3$| $PC_{61}BM$| BCP| Al using $CsSnI_3$ with 10 mol% $SnCl_2$, 10 mol% SnI_2 and with no additive as the light harvesting layer and $PC_{61}BM$ as the electron transport layer. Devices were tested immediately after fabrication (**a (i)** and **b(i)**) and after storage under nitrogen for an extended period (**a(ii)** and **b(ii)**). Representative data for two separate batches of devices are shown.

Table 4.4: JV parameters (± one standard deviation) for devices with the structure: ITO glass| $CsSnI_3$| $PC_{61}BM$| BCP| Al. Data in black - devices tested immediately after fabrication. Data in red - devices tested 28 days after fabrication after storage in a nitrogen filled glove box.

Device	n	J_{sc} (mA/cm^2)	V_{oc} (V)	*FF*	η (%)	Champion η (%)
$CsSnI_3$	16	3.74 ± 0.36	0.18 ± 0.06	0.43 ± 0.08	0.30 ± 0.13	0.49
	17	3.76 ± 0.34	0.20 ± 0.08	0.45 ± 0.13	0.38 ± 0.22	0.68
$CsSnI_3$ +	15	7.69 ± 0.54	0.28 ± 0.03	0.40 ± 0.09	0.87 ± 0.26	1.15
10 mol% SnI_2	16	8.44 ± 0.61	0.35 ± 0.02	0.49 ± 0.06	1.46 ± 0.26	1.73
$CsSnI_3$ +	14	8.58 ± 0.68	0.37 ± 0.01	0.63 ± 0.03	2.00 ± 0.21	2.23
10 mol% $SnCl_2$	14	8.72 ±0.67	0.44 ± 0.01	0.66 ± 0.02	2.53 ± 0.25	2.87

Table 4.5: JV parameters (± one standard deviation) for devices with the structure: ITO glass| $CsSnI_3$ with either added $SnCl_2$ or SnI_2| $PC_{61}BM$| BCP| Al. Both shortly after fabrication (black), and after 60 days storage under nitrogen.

Sample	n	J_{sc} (mA/cm^2)	V_{oc} (V)	*FF*	η (%)	Champion η (%)
$CsSnI_3$ +	15	6.80 ± 0.34	0.25 ± 0.02	0.41 ± 0.04	0.69 ± 0.12	0.88
10% SnI_2	11	8.05 ± 0.31	0.36 ± 0.01	0.51 ± 0.02	1.50 ± 0.12	1.72
$CsSnI_3$ +	16	9.82 ± 0.45	0.26 ± 0.05	0.42 ± 0.05	1.18 ± 0.37	1.72
10% $SnCl_2$	9	11.25 ± 0.83	0.40 ± 0.05	0.56 ± 0.10	2.54 ± 0.67	3.26

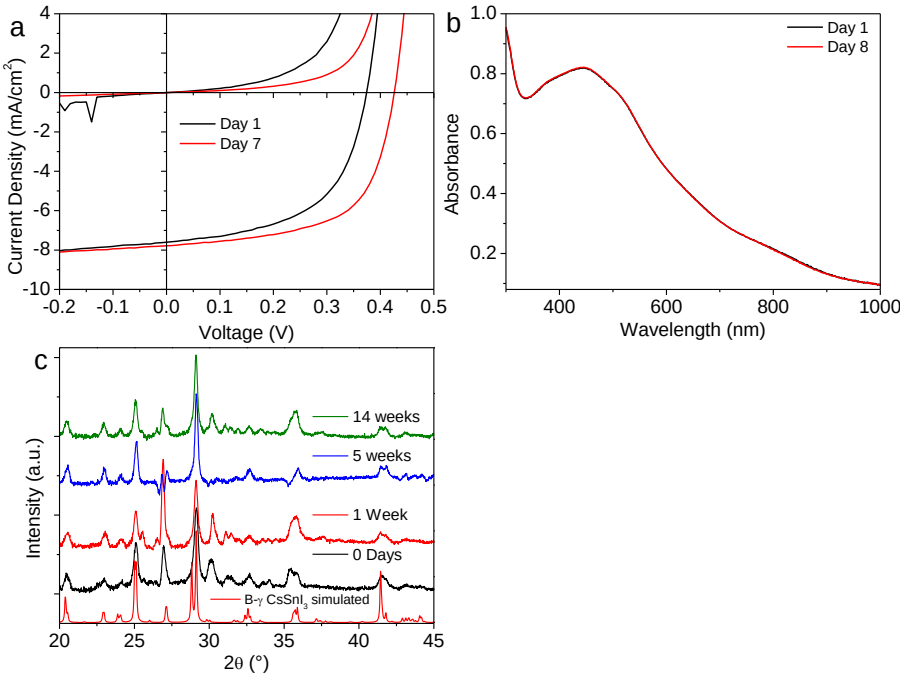

Figure 4.16: **(a)** JV plots of a device after shortly after fabrication and 6 days later, **(b)** UV/vis/NIR plots of an encapsulated film of $CsSnI_3$ + 10 mol% $SnCl_2$, shortly after fabrication and 7 days later, and **(c)** XRD patterns of films of $CsSnI_3$ + 10 mol% $SnCl_2$ shortly after fabrication and 7 days later.

4.4.3 Comparison of Different Concentrations

Notably the *FF* is very high for a tin perovskite based PV device, with a mean value of 0.63 and champion value of 0.69. This result is particularly impressive given that there is no HTL and the perovskite film has a high density of pinholes as is evident in Figure 4.2 (e). Furthermore, whilst $CsSnI_3$ films with 10 mol% $SnCl_2$ that are prepared from 8 wt% solution have a much greater density of pinholes than those prepared from 16 wt% solution (Figure 4.17), the device *FF* is comparable (Figure 4.18 and Table 4.6), which is consistent with the $SnCl_2$ preventing electrons moving from the $PC_{61}BM$ into the ITO electrode.

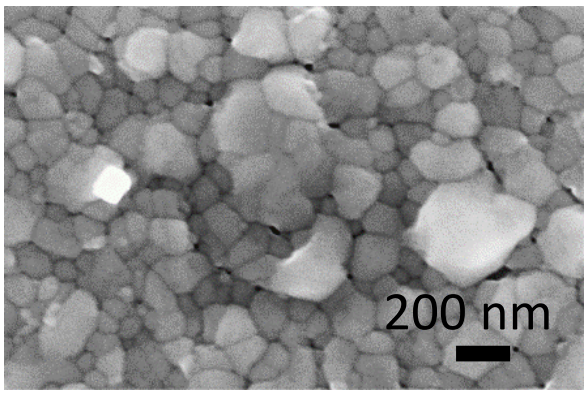

Figure 4.17: SEM image of $CsSnI_3$ + 10 mol% $SnCl_2$ made from 16 wt% DMF solution on ITO.

Table 4.6: Typical JV parameters (± one standard deviation) for devices with the structure: ITO glass| $CsSnI_3$ + 10 mol% $SnCl_2$| $PC_{61}BM$| BCP| Al. Films of $CsSnI_3$ + 10 mol% $SnCl_2$ where prepared using DMF solutions with concentrations 8, 16 and 20 wt%. Data in black - devices tested immediately after fabrication. Data in red - devices tested after 5 months storage in a nitrogen filled glove box.

Sample	n	J_{sc} (mA/cm^2)	V_{oc} (V)	*FF*	η (%)	Champion η (%)
8 wt%	10	8.89 ± 0.55	0.38 ± 0.01	0.53 ± 0.01	1.77± 0.20	2.06
	4	9.89 ± 0.55	0.50 ± 0.01	0.68 ± 0.01	3.35 ± 0.21	3.56
16 wt%	18	6.46 ± 0.86	0.36 ± 0.02	0.52 ± 0.07	1.21 ± 0.25	1.71
	10	9.1 ± 1.1	0.29 ± 0.04	0.58 ± 0.03	1.56 ± 0.45	2.52
20 wt%	11	6.11 ± 0.97	0.33 ± 0.02	0.49 ± 0.06	0.99 ± 0.26	1.29
	10	3.7 ± 1.0	0.21 ± 0.02	0.48 ± 0.03	0.38 ± 0.17	0.81

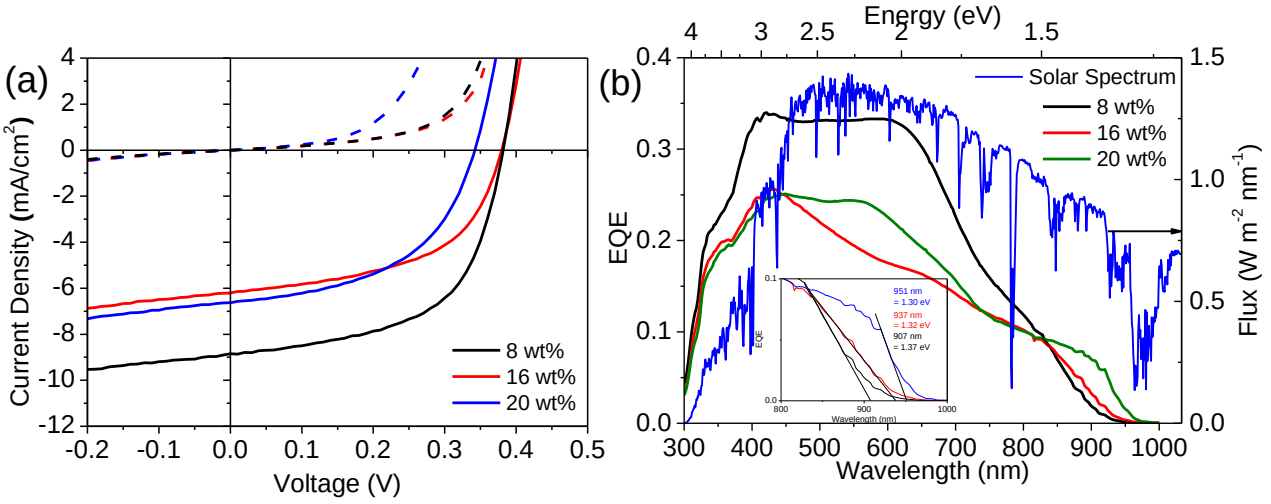

Figure 4.18: **(a)** Representative JV characteristics for devices with the structure: ITO glass| perovskite| $PC_{61}BM$| BCP| Al, using $CsSnI_3$ with 10 mol% $SnCl_2$ additive. Films prepared using 8, 16, and 20 wt% DMF solution. Full data set given in Table 4.6. **(b)** EQE of these devices with a zoom-in of low energy cut-off shown inset.

The devices made using 8 wt% perovskite solution performed better than those made using more concentrated solutions. Possible explanations are that the increased thickness, which also leads to increased surface roughness leading to a reduction in shunt resistance. Other explanations are that the increased device thickness leads to a reduction in the built in field across the device, leading to a drop in charge extraction, or that the defect density in the perovskite films is too high to allow high enough charge carrier diffusion lengths for thicker films. From the EQE shown in Figure 4.18 (b), the onset of absorption is red-shifted as the thickness of the perovskite layer increases; the onset of EQE signal changes from 1.37 eV for a film made from 8 wt% solution to 1.30 eV for a film made from 20 wt% solution, the onset of absorption also becomes more direct with higher concentrations. The origin of this could be related to quantum confinement effects; when crystal sizes are small enough to be comparable to double the exciton Bohr radius of the material, the band gap increases in size due to the reduction in molecular orbitals contributing to the energy bands of the material. Comparing

the SEM images of films of $CsSnI_3$:$SnCl_2$ made from 8 and 16 wt%, the mean crystal sizes are approximately 4400 nm^2 and 12000 nm^2, respectively. It has been shown that polycrystalline films of tin and lead halide perovskite have a higher energy electronic absorption onset than single crystals.[17, 18] However, it has been reported elsewhere that nanocrystals $\sim$ 10 nm across show little quantum confinement in PL spectra.[19] The change in band-gap could be attributed to optical interference, though this is less likely.[20]

4.5 Elucidating the Role of $SnCl_2$

The simplest possible explanation for the difference in device performance with and without $SnCl_2$ additive is that the $SnCl_2$ forms a thin ($>$ 1 nm) hole-selective layer at the ITO| $CsSnI_3$ interface. However, UPS measurements (Figure 4.19 (a) and (b)) show that the valence band of $SnCl_2$ is 6.6 $\pm$ 0.1 eV below the vacuum level, which is well below that measured for $CsSnI_3$ at 4.9 eV $\pm$ 0.1 eV (Figure 4.20), the latter being in very close agreement with that previously reported by Chung *et al.*[1] Consequently, a $SnCl_2$ layer at this interface having a thickness $>$ 1 nm would be expected to impede rather than facilitate hole-extraction, thereby degrading device fill-factor - which is not observed. Alternatively, it is possible that a layer of $SnCl_2$ with a thickness $\leq$ 1 nm is buried at the ITO| $CsSnI_3$ interface which, whilst sufficiently thin to be transparent to the flow of charge carriers, could perturb the interfacial energetics by modifying the surface potential at the ITO electrode. To explore this possibility, measurements of the work function of the ITO electrode were made using a Kelvin probe located in the same nitrogen filled glovebox, before and after deposition of $SnCl_2$ from a DMF solution having the same $SnCl_2$ loading as used to achieve 10 mol% $SnCl_2$ in a 8 wt% $CsSnI_3$ solution: 2.4 mg ml^{-1} $SnCl_2$. The work function of ITO treated with DMF only was measured to be 4.76 $\pm$ 0.06 eV. Following treatment with 2.4 mg ml^{-1} $SnCl_2$ solution the work function is essentially unchanged

at 4.72 eV ± 0.08 eV, which is a strong indication that the energetics for hole-extraction are neither improved nor degraded when $SnCl_2$ is added to the $CsSnI_3$ layer at the loading used.

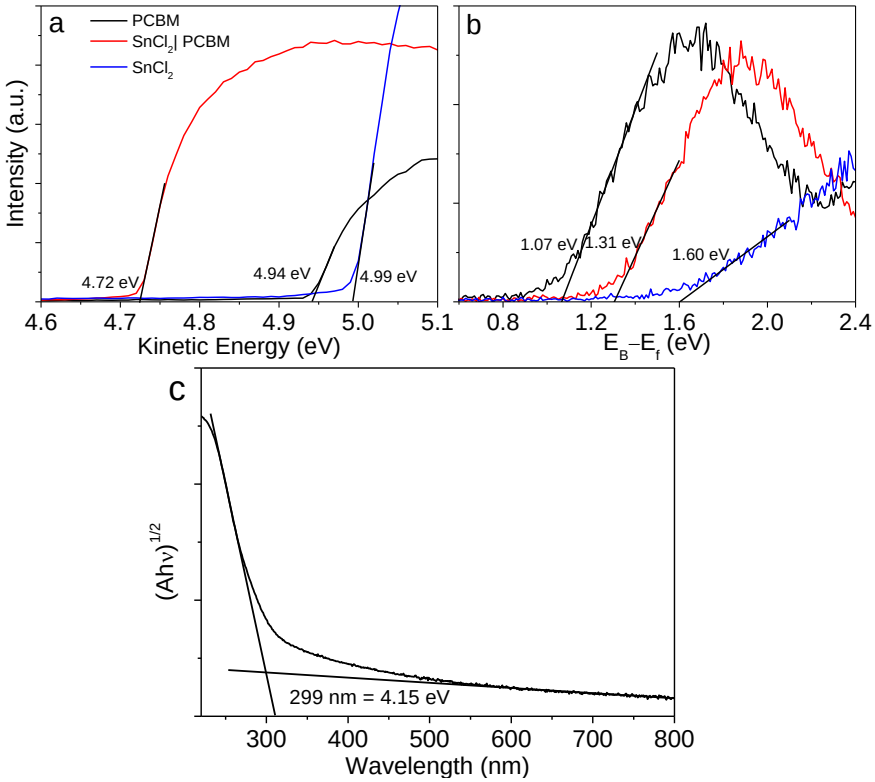

Figure 4.19: UPS spectra of $SnCl_2$, $PC_{61}BM$ ($\sim$ 40 nm) and bilayer $SnCl_2$ ($<$ 3 nm)| PCBM ($\sim$ 40 nm) films showing **(a)** the secondary electron cut-off and **(b)** the low binding energy edge. **(c)** The electronic absorption spectrum of a $SnCl_2$ film on quartz showing the indirect band-gap.

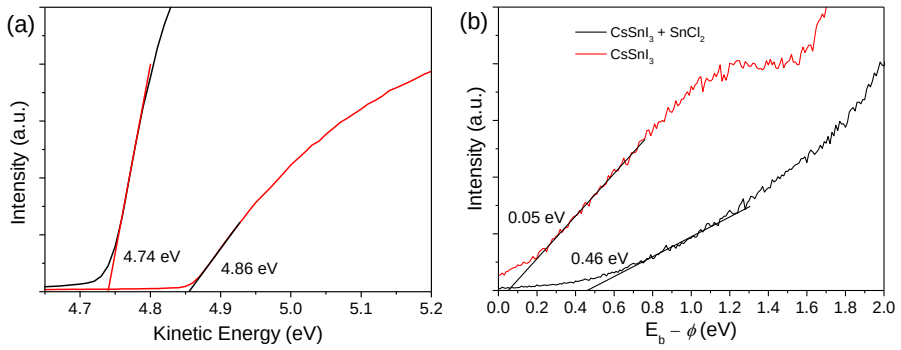

Figure 4.20: UPS of a film of $CsSnI_3$ with and without $SnCl_2$ on a gold substrate.

A more likely explanation for the improvement in device performance is that the excess $SnCl_2$ at the surface of the $CsSnI_3$ crystallites moderately *n*-dopes the fullerene layer, forming a Schottky barrier to the unwanted extraction of electrons from the fullerene into the ITO electrode at the site of pinholes in the perovskite film, thereby allowing the devices to function well without the need for a discrete HTL. This explanation may suggest that plain $CsSnI_3$ devices should not work at all because $PC_{61}BM$ contacting the hole-extracting electrode would cause a short-circuit, and so UPS measurements should be made on a film of $PC_{61}BM$ deposited on a thin $CsSnI_3$ film to test if there is an *n*-type doping interaction to a lesser extent. Alternatively, $PC_{61}BM$ in devices may be impacted by the built in field of the PV device, making electrons selectively extract towards the electron-extracting electrode, if there is an absence of mobile ions in the $PC_{61}BM$ or BCP layers screening the electric field of the Al electrode. The dark current-voltage characteristics re-plotted on a log-linear scale (Figure 4.21) validate this conclusion, since the current in reverse bias is dramatically reduced with the $SnCl_2$ additive; by ~ 10 times at a bias of -1 V. This interpretation requires that the $SnCl_2$ at least partially diffuses into the fullerene layer when the device is fabricated, and that there is an electron donating interaction from the $SnCl_2$ to the fullerene, giving rise to an *n*-type doping effect. To the author's knowledge such an interaction has not been reported before. To confirm this hypothesis, UPS measurements were performed on a ~ 40 nm thick $PC_{61}BM$ film spin cast onto a gold substrate pre-coated with a very thin (< 3 nm) film of $SnCl_2$. The results of these measurements are summarised in Figure 4.22, from which it is evident that the energy difference between the Fermi level and valence band edge increases by 240 meV when $SnCl_2$ is at the buried interface, consistent with *n*-type doping. It is not possible to know the dopant density very close to the interface and at the site of the pinholes in the $CsSnI_3$ film, although if the coverage of $SnCl_2$ over the surface of the $CsSnI_3$ crystallites is approximately even - as schematically depicted in Figure 4.7 - then the $SnCl_2$ dopant density will be highest at the site

of the pinholes in the perovskite film.

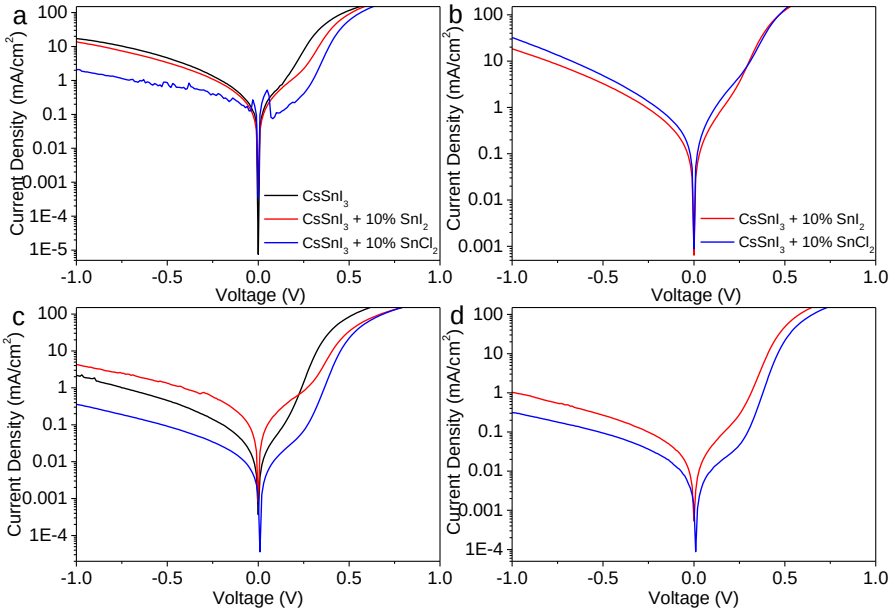

Figure 4.21: Absolute dark current plots on logarithmic scale of representative devices plotted in Figure 4.15.

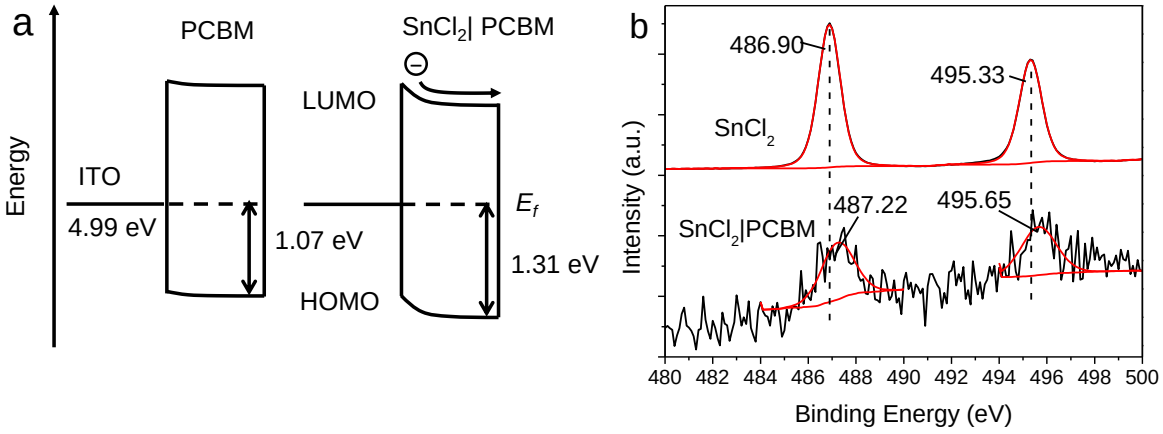

Figure 4.22: **(a)** Energy level diagram of an ITO| $PC_{61}BM$ interface with and without $SnCl_2$ derived from UPS data given in Figure 4.19; **(b)** HRXPS spectra of Sn 3d region of $SnCl_2$ the high kinetic energy cut-offs of $PC_{61}BM$, $SnCl_2$, and $SnCl_2$| $PC_{61}BM$.

Consequently, the barrier to hole-extraction from the fullerene layer at the site of pinholes is likely to be considerably larger. Corroborating evidence for n-type doping is provided by HRXPS of the same films, which shows that the binding energy of the Sn 3d orbitals in $SnCl_2$ is increased by 0.4-0.5 eV when incorporated in a $PC_{61}BM$ film, consistent with partial electron transfer from the $SnCl_2$ to the $PC_{61}BM$ (Figure 4.22). Based on a bandgap of 1.3 eV [5, 7] the energy of the conduction band edge of $CsSnI_3$ is 3.6 eV below the vacuum level, which is considerably shallower in energy than the LUMO of $PC_{61}BM$ at 3.78 eV [20] below the vacuum level, and so there is unlikely to be a barrier to electron extraction across this interface either with or without $SnCl_2$ doping of the $PC_{61}BM$ layer.

4.6 Device Stability Towards Air Ingress and Constant Illumination

By monitoring the JV characteristics of PPV devices with air exposure time, the devices in this HTL-free architecture and with $PC_{61}BM$ ETL were much more stable than those described in Chapter 3, which used CuI HTL and C_{60} ETL. Devices were left in air for 18 hours, and many had only degraded by less than 20% of initial η, by comparison, those studied in Chapter 3 had degraded by over 80% in 14 hours in the best case (Figures 3.23 and 4.23).

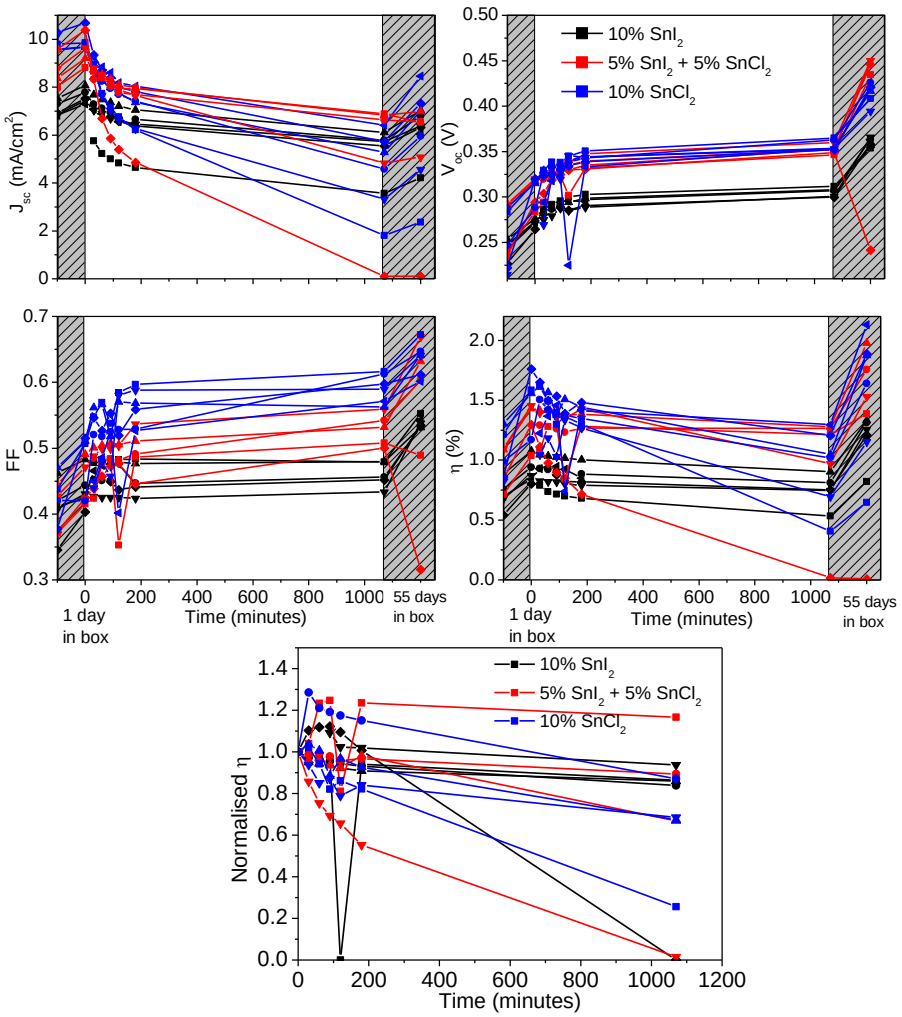

Figure 4.23: JV data of devices in the structure ITO| $CsSnI_3$:SnX_2| $PC_{61}BM$| BCP| Al, where SnX_2 is either 10 mol% added $SnCl_2$, 10 mol% added SnI_2, or 5 mol% added $SnCl_2$ and 5 mol% SnI_2 measured over time exposed to ambient air (not under constant illumination). JV measurements were made under nitrogen.

Figure 4.24 (a) - (d) shows the performance of $CsSnI_3$ based PPV devices without encapsulation and tested in ambient air at a humidity of $\sim$ 25% under constant 1 sun simulated solar illumination. After 45 minutes continuous illumination the device temperature stabilised at $\sim$ 50 °C.

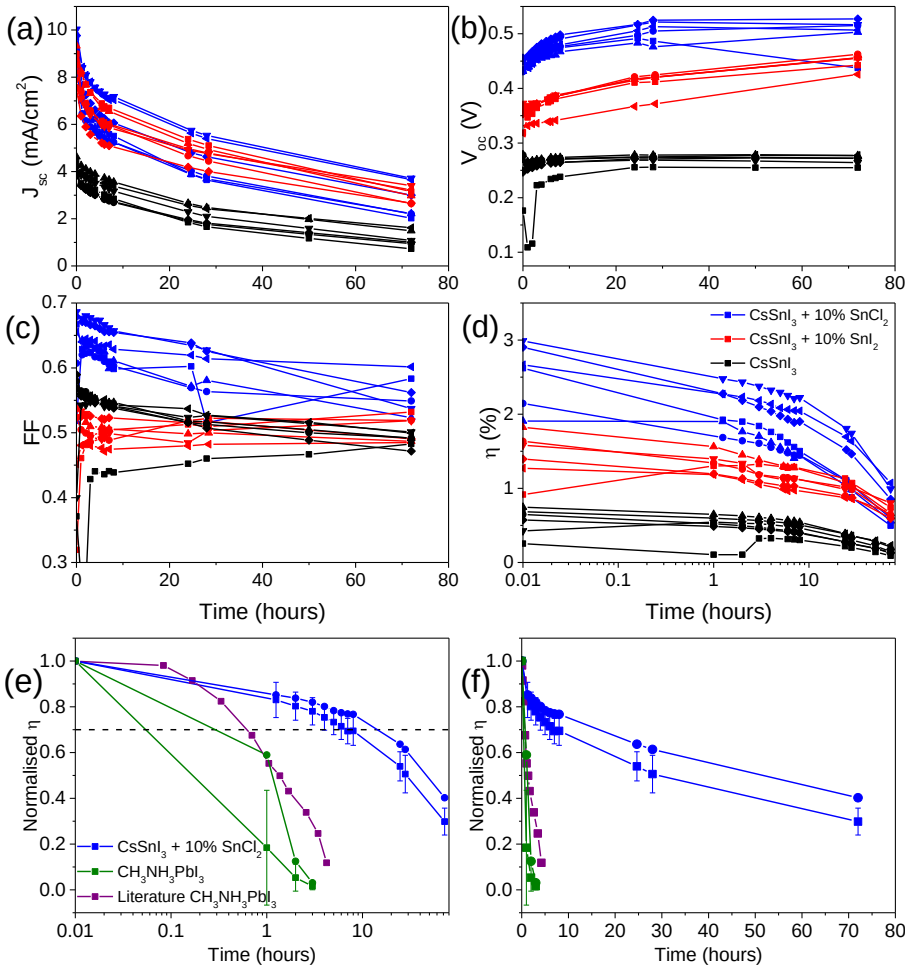

Figure 4.24: Evolution of **(a)** J_{sc}, **(b)** V_{oc}, **(c)** *FF*, and **(d)** η for a representative set of unencapsulated devices tested in air under continuous 1 sun simulated at $\sim$ 25% humidity. The devices have the structure: ITO glass| $CsSnI_3$ + 10 mol% X| $PC_{61}BM$| BCP| Al, where X = $SnCl_2$ (blue), SnI_2 (red) or no additive (black). Mean (squares) and champion (circles) normalised η, with time ploted **(e)** on a $\log_{10}$ scale, and **(f)** linearly, for PPV devices with the structure: ITO| $CsSnI_3$ + 10 mol% $SnCl_2$ (blue) or $CH_3NH_3PbI_3$ (green)| $PC_{61}BM$| BCP| Al at $\sim$ 25% humidity; or ITO| $CH_3NH_3PbI_3$| $PC_{61}BM$| Bis-C_{60}| Ag (purple) reported in ref. [12]. Error bars are $\pm$ 1 standard deviation.

To our knowledge the stability of these devices is the highest reported for any tin PPV to date: On average, η reduces to 70% of its starting value for unencapusulated devices only after $\sim$ 7 hours under continuous 1 sun illumination in ambient air, with the best performing devices

taking 16 hours (Figure 4.24 (e) and (f)). The improvement in stability reported herein is a factor of 20 greater than devices with the same architecture fabricated using $CH_3NH_3PbI_{3-x}Cl_x$ in place of $CsSnI_3$ fabricated in our laboratory, and 10 times more stable than reported independently by the group of Zhang *et al.*[12], also for the same device architecture (Figures 4.24 (e) and (f)). Crucially this exceptional stability for a tin-perovskite PV is common to devices with and without metal halide additive, consistent with the dispersing of the $SnCl_2$ into the PCBM layer, and so is tentatively attributed to the removal of the HTL or the use of $PC_{61}BM$ by comparison with the work of Chapter 3. Notably however, champion stability is exhibited only by devices with a tin halide additive: 11 hours with no additive; 16 hours with 10 mol% $SnCl_2$; and 22 hours for SnI_2. Using $SnCl_2$ as an additive offers the advantage of the highest η, due to reduced sensitivity of device parameters to pin-holes, without complicating the process of device fabrication.

It is evident from Figure 4.24 (a) - (d) that most of the degradation in device η is due to loss in J_{sc}, whilst *FF* is very stable and V_{oc} actually increasing by $\sim 10\%$ for all devices. The increase in V_{oc} can be attributed in part to the improved crystallisation in the fullerene layer that occurs when the device is subject to intense light for an extended period, which reduces the number of LUMO tail states that erode V_{oc} [21, 22] and/or partial oxidation of the electrode to form a very thin low work function aluminium oxide layer.[23] The improvement in V_{oc} may also be partially attributed to increasing of n-doping due to the migration of tin species into the $PC_{61}BM$, under the heat of the lamp, increasing current rectification, which might explain why the devices using $CsSnI_3$ with no additive show little change in V_{oc} under constant illumination. The good stability in device *FF* indicates that the series resistance in these devices does not change significantly as the light harvesting ability deteriorates. This observation is consistent with the fact that Cs_2SnI_6 is a weak absorber of light and has a high electron mobility[24, 25], and is compelling evidence that the barriers to electron transport

across the $CsSnI_3$| Cs_2SnI_6 and Cs_2SnI_6| $PC_{61}BM$ are small. That is, the Cs_2SnI_6 layer that forms at the $CsSnI_3$| fullerene interface as a result of air oxidation allows electron transport, whilst not significantly contributing to light harvesting.

4.6.1 Effect of PCBM on $CsSnI_3$:$SnCl_2$ Film Stability

The fact that devices with and without $SnCl_2$ have nearly comparable stability, in conjunction with evidence for *n*-type doping of the fullerene layer, indicates that in devices the $SnCl_2$ is no longer confined at the $CsSnI_3$ surface but is dispersed in the adjacent fullerene layer. Further evidence for this, and for a significant interaction between $SnCl_2$ and $PC_{61}BM$, is provided by the electronic absorption spectra shown in Figure 4.25. Figure 4.25 (a) shows how the absorbance of a $\sim$ 50 nm thick $CsSnI_3$ film prepared with 10 mol% $SnCl_2$ at a wavelength of 450 nm changes with time exposed to ambient air, with and without a $PC_{61}BM$ overlayer. It is evident that the $CsSnI_3$ with 10 mol% added $SnCl_2$ becomes less stable when buried beneath a layer of $PC_{61}BM$ which is consistent with partial removal of the $SnCl_2$ from the perovskite surface. Conversely, Figure 4.25 (b) shows that washing with chlorobenzene has no detrimental effect on the perovskite film stability, which together is compelling evidence for a strong interaction between $PC_{61}BM$ and $SnCl_2$. Notably, whilst the Al electrode is evidently able to slow the ingress of water and oxygen into the device sufficiently for a stability study on the time scale reported herein - consistent with lifetime studies of organic PV devices using a very similar ETL [26] – its long term barrier properties are limited.[26] Consequently, it is anticipated that further significant improvements in the stability of these tin perovskite PV devices can be achieved by using an electron extracting electrode with better long-term barrier properties towards ambient water and oxygen.

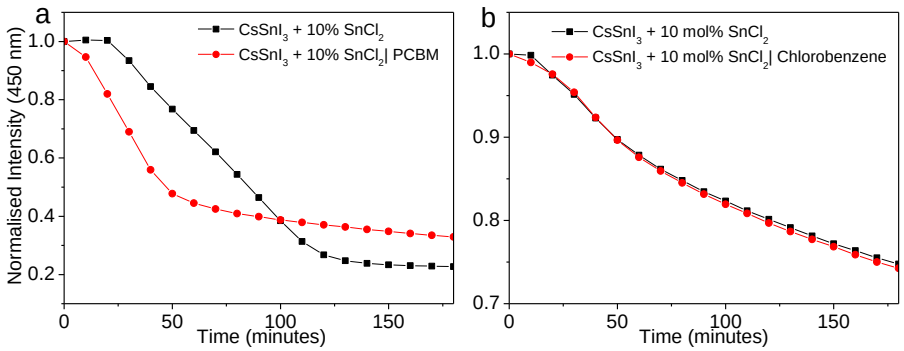

Figure 4.25: Normalised UV/vis/NIR absorption data of $CsSnI_3$ + 10 mol% $SnCl_2$ films **(a)** with and without a layer of $PC_{61}BM$ deposited on top, and **(b)** with and without having a chlorobenzene drop-cast on top.

Taken together, the aforementioned experiments provide compelling evidence that $SnCl_2$ is the best of the tin halides investigated for the current application. The reason for this is almost certainly a complex interplay between a number of factors including the following: (i) Firstly, Cl cannot easily displace I in $CsSnI_3$ perovskite, due to the size mismatch of the two halides, and so $SnCl_2$ is pushed to the surface of the crystallites, whilst still ensuring that the perovskite is formed in a tin-rich environment.; (ii) $SnCl_2$ is much more soluble in common solvents, including DMF, than SnF_2 due to its greater covalency, which is particularly important when processing films from solution at room temperature, as in our fabrication method.; (iii)The propensity for solid-state diffusion of tin chloride into fullerene is likely to be larger due to the smaller size and lower mass of chloride species compared to the iodide and bromide analogues. The ratio of Sn:I:Cl is not expected to have changed, but the excess Sn^{2+} ions in solution is assumed to allow the formation of $CsSnI_3$ with a lower vacancy defect density, followed by formation of $SnCl_2$ at the surface.

4.7 Comparison to $MAPbI_3$

PPV devices using $CH_3NH_3PbI_3$ devices performed better than the tin perovskite devices initially, but degraded over time after storage in the glovebox, particularly in terms of V_{oc} and *FF* (Figure 4.26 (a) and (b) and Table 4.7). This loss of V_{oc} and *FF* implies a loss of device integrity leading to an increase in leakage. However, from Figure 4.26 (c), the leakage current appears to decrease slightly as the absolute current density at -1 V becomes lower, on average, after 1 week storage. By inspecting the gradient of the dark JV plots at 1 V, some information can be obtained about the series resistance in the devices; there is a higher gradient for the devices on the first day than on the ninth day indicating the series resistance has increased, offering a plausible explanation for the drop in *FF*. However, an increase in series resistance should also lead to a drop in J_{sc} which increases in this time (Table 4.7).

Table 4.7: JV data of devices in the structure; ITO| $CsSnI_3$ + 10 mol% $SnCl_2$ or $CH_3NH_3PbI_3$| $PC_{61}BM$| BCP| Al, initially (black) and after 8 days (red).

Device	n	J_{sc} (mA/cm^2)	V_{oc} (V)	*FF*	η (%)	Champion η (%)
$CsSnI_3$ + $SnCl_2$	11	9.54 ± 0.89	0.37 ± 0.01	0.50 ± 0.07	1.77 ± 0.34	2.40
	15	8.97 ± 0.91	0.43 ± 0.01	0.51 ± 0.05	2.00 ± 0.38	2.68
$CH_3NH_3PbI_3$	18	11.25 ± 1.98	0.41 ± 0.04	0.50 ± 0.04	2.34 ± 0.58	3.39
	12	11.84 ± 2.19	0.29 ± 0.07	0.47 ± 0.03	1.71 ± 0.77	3.16

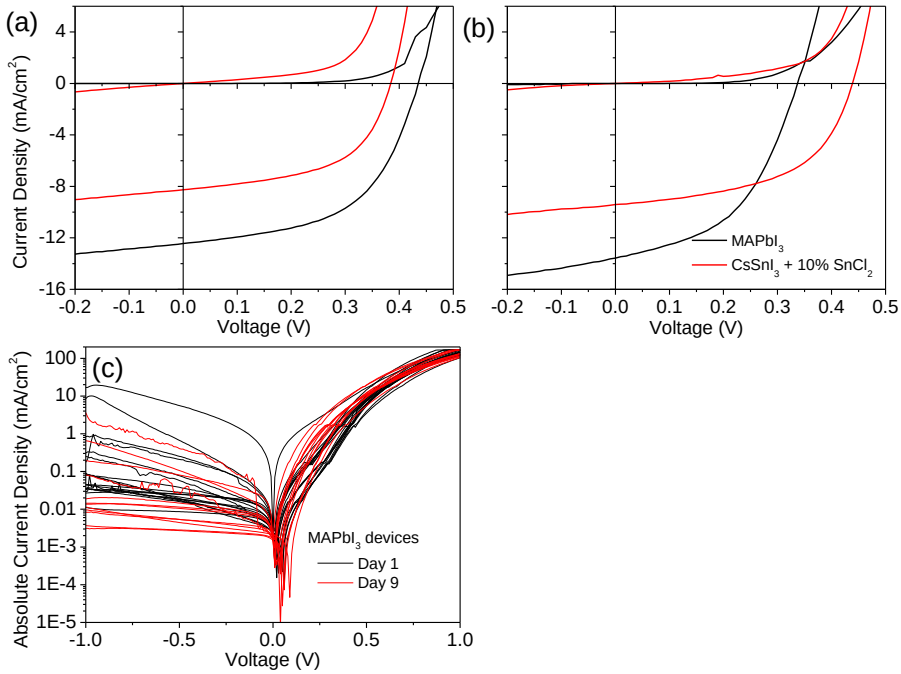

Figure 4.26: JV plots of representative devices with the structure ITO| Perovskite| $PC_{61}BM$| BCP| Al. Where the perovskite is either $CsSnI_3$ + 10 mol% added $Sncl_2$, or $CH_3NH_3PbI_3$, **(a)** shortly after fabrication and **(b)** after 8 days storage in the glove box. **(c)** Plots of absolute current density against voltage of $CH_3NH_3PbI_3$ devices in the dark both shortly after fabrication and after 8 days storage in the glove box.

Although there have been reports of lead perovskite devices being much more stable than those reported here, these were in different device architectures in which efforts were made to suppress oxygen infiltration by either improving the morphology of the film which is deposited on top of the perovskite, or by coating the perovskite in a barrier layer such as Al_2O_3.

4.8 Attempts to Improve V_{oc}

4.8.1 Use of $IC_{60}BA$

The V_{oc} can be increased by using $IC_{60}BA$ in place of $PC_{61}BM$ because $IC_{60}BA$ has a smaller electron affinity, more closely aligned to the CB edge of $CsSnI_3$ (Chapter 3 Figure 3.10). Although initial performance is low compared with the $PC_{61}BM$ devices, after 9 days the performance, particularly V_{oc}, substantially improves. V_{oc} increases to over 0.5 V, and a highest η of over 3.3% is achieved (Figure 4.27 and Table 4.8). However, *FF* is quite low in this architecture. The ICBA devices require a lower film thickness because of higher series resistance, and so it is more difficult to balance J_{sc} with V_{oc} and *FF*. In the absence of an HTL there is a lower shunt resistance, and so in order to increase the overall shunt resistance, thicker films of $IC_{60}BA$ are required in order to increase the *FF* and V_{oc} to levels at which the devices achieve good overall performance.

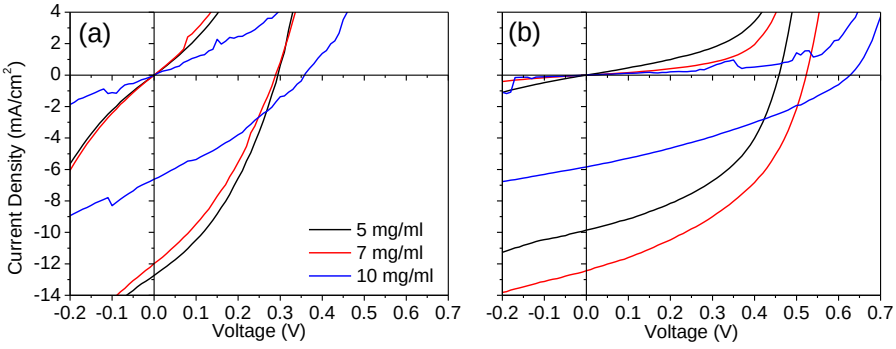

Figure 4.27: JV plots of representative devices in the structure ITO| $CsSnI_3$ + 10 mol% $SnCl_2$| $IC_{60}BA$| BCP| Al, using $IC_{60}BA$ from either 5, 7, or 10 mg/ml chlorobenzene solution. **(a)** Initially, and **(b)** after 9 days stored under nitrogen.

Table 4.8: JV data for devices in the structure ITO| $CsSnI_3$ + 10 mol% $SnCl_2$| $IC_{60}BA$| BCP| Al, using $IC_{60}BA$ from either 5, 7, or 10 mg/ml chlorobenzene solution, initially (black) and after 9 days storage in a nitrogen glove box (red).

Device	n	J_{sc} (mA/cm^2)	V_{oc} (V)	FF	η (%)	Champion η (%)
5 mg/ml	16	12.63 ± 0.52	0.25 ± 0.06	0.33 ± 0.03	1.04 ± 0.34	1.69
	14	10.22 ± 0.71	0.38 ± 0.12	0.39 ± 0.10	1.59 ± 0.66	0.35
7 mg/ml	13	11.42 ± 0.83	0.29 ± 0.04	0.33 ± 0.02	1.10 ± 0.26	1.58
	14	11.87 ± 0.57	0.52 ± 0.02	0.44 ± 0.03	2.69 ± 0.35	3.32
10 mg/ml	12	6.98 ± 0.55	0.31 ± 0.10	0.28 ± 0.04	0.64 ± 0.30	1.26
	15	6.28 ± 0.53	0.46 ± 0.16	0.34 ± 0.06	0.99 ± 0.35	1.59

4.8.2 Interaction Between Phthalocyanines and $CsSnI_3$

In an attempt to improve the V_{oc} of devices, metal phthalocyanines (Pc) were tried as the ETL in $CsSnI_3$ devices. This was due to their high LUMO level which may better align with the conduction band edge of $CsSnI_3$ than fullerenes; CuPc and ZnPc have electron affinities of $\sim$ 3.1 eV and $\sim$ 3.2 eV respectively[27], whereas $CsSnI_3$ has an electron affinity of $\sim$ 3.6 eV (Chapter 3). However, it was found that evaporating metal phthalocyanines resulted in a reaction between the perovskite and the phthalocyanine, causing the dark brown/red $CsSnI_3$ film to turn to a pale grey colour. JV characteristics and EQE response showed that there was no current signal from the perovskite, only from metal phthalocyanine (Figure 4.28).

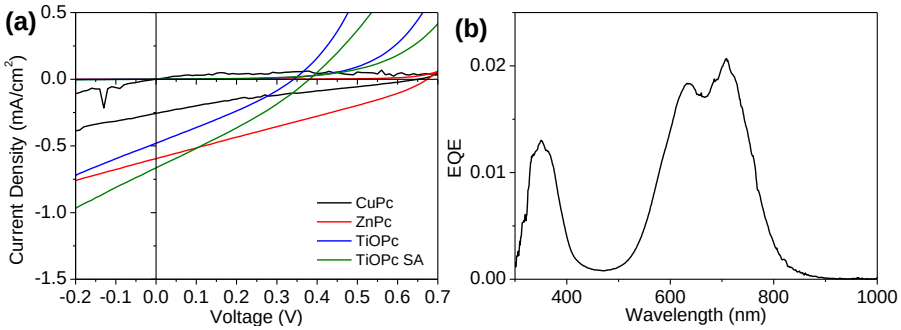

Figure 4.28: **(a)** JV plots of devices in the structure ITO| $CsSnI_3$ + 10 mol% $SnCl_2$| MPc| BCP| Al, where M is Cu, Zn or TiO (solvent annealed or not). **(b)** EQE of a device fabricated in the structure ITO| $CsSnI_3$| ZnPc| BCP| Al.

The two most likely results of the reaction are that the phthalocyanine ligands bind to tin atoms from the $CsSnI_3$, and thus cause the perovskite structure to break down, or the metals in the phthalocyanines may be involved in a redox reaction with the tin, causing the Sn^{2+} to oxidise to Sn^{4+}. The latter is less likely because Cu^{2+}, Zn^{2+} and Ti^{4+} are stable oxidation states. The fact that there is some reaction occurring at all is surprising because metal phthalocyanine dyes are known to be very stable; CuPc is used on the £5 note.

4.8.3 DMSO Processing

DMSO is an alternative solvent for perovskite processing to DMF. It is less toxic, has a higher boiling point and binds more easily to metals. Spin casting a perovskite solution from DMSO results in a film of the solute mixed with DMSO. The DMSO can be driven off by heating the films at 60 °C (Figure 4.29 (a) and (b)) or by spin casting a solvent which will precipitate the perovskite and wash away the DMSO. The latter method has been reported using toluene and chlorobenzene for lead perovskites.[28] However, toluene and chlorobenzene did not wash away the DMSO from the $CsSnI_3$:DMSO film. Isopropanol worked for this purpose, however, did not produce high quality films; films were made up of large isolated crystals because the isopropanol

partially dissolved the perovskite film (Figure 4.29 (c)). The use of DMSO has produced films with large crystals, but still with a large pinhole density which has reduced their effectiveness in devices.

Unlike with DMF processed films, the morphologies of DMSO processed films are substantially different when using $CsSnI_3$ with 10 mol% added SnI_2 or $SnCl_2$. The $CsSnI_3$ films with added $SnCl_2$ have very large crystals which are grouped together in islands, between which there is a lot of space, whereas the $CsSnI_3$ with added SnI_2 film is made up of smaller crystals which are all packed together with a large number of pinholes roughly uniformly distributed across the film (Figure 4.29 (a) and (b)).

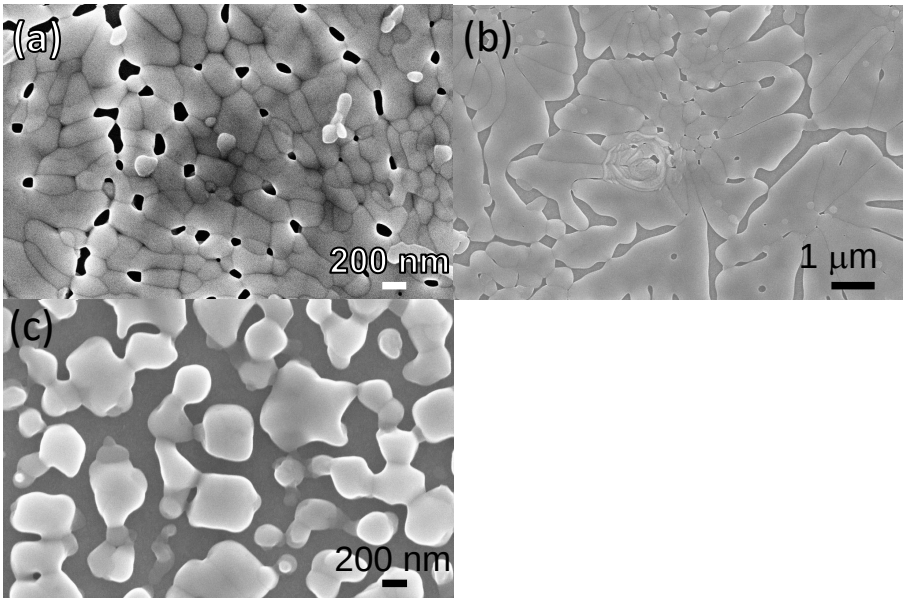

Figure 4.29: SEM images of $CsSnI_3$ with 10 mol% added **(a)** SnI_2 and **(b)** $SnCl_2$ processed from 20 wt% DMSO solution, films were dried at 60 °C, and **(c)** $CsSnI_3$ with 10 mol% added $SnCl_2$ processed from 20 wt% DMSO solution dried using isopropanol.

Devices made using DMSO processed perovskite have lower performance than those made using DMF solution, particularly in terms of J_{sc} (Figure 4.30 and Table 4.9). This is likely a result of the rough films and low coverage of the perovskite films processed from DMSO.

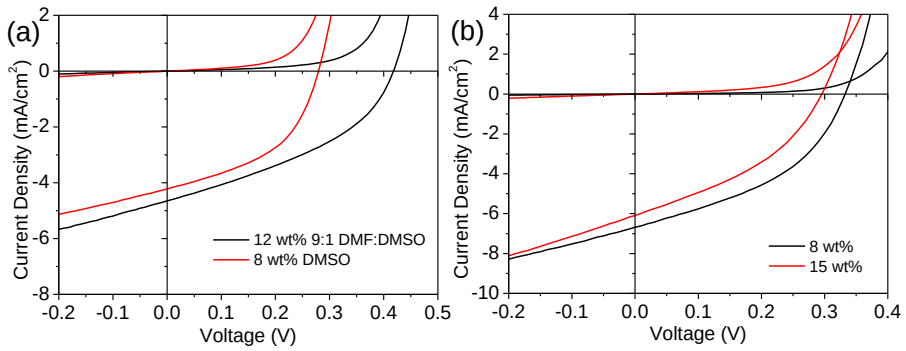

Figure 4.30: JV plots of the best performing devices made in the structure **(a)** ITO| $CsSnI_3$ + 10 mol% SnI_2| $PC_{61}BM$| BCP| Al, where the perovskite is processed from either 12 wt% of 9:1 DMF:DMSO solution, or 8 wt% DMSO solution, and **(b)** ITO| $CsSnI_3$ + 10 mol% SnI_2| C_{60}| BCP| Al, where the perovskite is processed from either 8 or 15 wt% DMSO solution.

Table 4.9: JV data of devices in the structure ITO| $CsSnI_3$ + 10 mol% SnI_2| $PC_{61}BM$ or C_{60}| BCP| Al, where the perovskite is processed from either 8, 15 or 20 wt% DMSO solution.

Device	n	J_{sc} (mA/cm^2)	V_{oc} (V)	*FF*	η (%)	Champion η (%)
8 wt% C_{60}	14	6.76 ± 0.42	0.32 ± 0.02	0.41 ± 0.04	0.88 ± 0.12	1.00
15 wt% C_{60}	12	6.08 ± 0.66	0.29 ± 0.02	0.37 ± 0.02	0.64 ± 0.07	0.71
20 wt% C_{60}	12	4.68 ± 0.33	0.11 ± 0.03	0.29 ± 0.01	0.16 ± 0.05	0.28
8 wt% PCBM	14	4.04 ± 0.36	0.19 ± 0.07	0.34 ± 0.08	0.28 ± 0.15	0.55
12 wt% (9:1 DMF: DMSO) PCBM	5	5.0 ± 1.8	0.32 ± 0.10	0.34 ± 0.04	0.49 ± 0.20	0.76

4.9 Use of C_{60}

Replacing $PC_{61}BM$ with C_{60} gives the same trend in device performance when using $CsSnI_3$ with no additive, 10 mol% added SnI_2 or 10 mol% added $SnCl_2$. However, after leaving in the glovebox for several days there is no improvement in device performance, and a slight degradation (Figure 4.31 and Table 4.10). This may be because the C_{60} is highly symmetric and deposited by thermal evaporation which may cause it to adopt a high degree of crystallinity

which does not improve with time, and therefore, there is no observable improvement in V_{oc} and *FF* with reduction in tail states. Evidence for this is that the V_{oc} of the $CsSnI_3$ with added $SnCl_2$ devices are initially quite high at over 0.4 V. This is expected when compared to the maximum V_{oc} achieved using PCBM which is 0.5 V (Table 4.6).[29] It would be useful to compare the device performance and evolution with time with that of evaporated $PC_{61}BM$ to see if evaporated $PC_{61}BM$ devices improve over time.

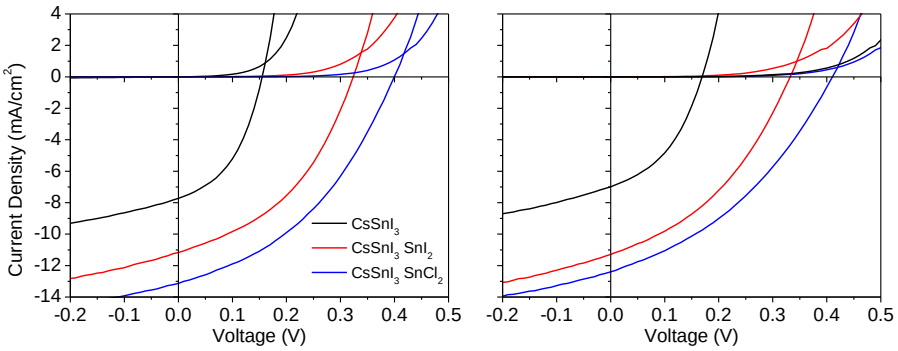

Figure 4.31: JV plots of representative devices in the structure ITO| $CsSnI_3$ with no additive, 10 mol% added SnI_2, or 10 mol% $SnCl_2$| C_{60}| BCP| Al. Initially (black) and after 5 days storage in the glovebox (red).

Table 4.10: JV data for devices made in the structure ITO| $CsSnI_3$ with no additive, 10 mol% added SnI_2, or 10 mol% $SnCl_2$| C_{60}| BCP| Al. Initially (black) and after 5 days storage in the glovebox (red).

Device	n	J_{sc} (mA/cm^2)	V_{oc} (V)	*FF*	η (%)	Champion η (%)
$CsSnI_3$	18	7.61 ± 0.55	0.16 ± 0.01	0.43 ± 0.01	0.52 ± 0.05	0.60
	16	7.37 ± 0.48	0.16 ± 0.02	0.39 ± 0.04	0.45 ± 0.08	0.56
$CsSnI_3$ + SnI_2	17	11.03 ± 0.17	0.31 ± 0.02	0.42 ± 0.01	1.43 ± 0.10	1.53
	17	11.22 ± 0.18	0.30 ± 0.04	0.38 ± 0.02	1.32 ± 0.21	1.56
$CsSnI_3$ + $SnCl_2$	16	12.88 ± 0.58	0.40 ± 0.02	0.41 ± 0.01	2.09 ± 0.12	2.28
	16	12.38 ± 0.37	0.40 ± 0.02	0.38 ± 0.01	1.88 ± 0.12	2.07

The devices incorporating $CsSnI_3$ + 10 mol% $SnCl_2$ behave differently from those with $CsSnI_3$ with added SnI_2 or no additive when measured under constant illumination in the air. From Figure 4.32, the $CsSnI_3$ with added $SnCl_2$ appears to slowly degrade over the course of 8 hours and then suddenly begins to degrade much faster.

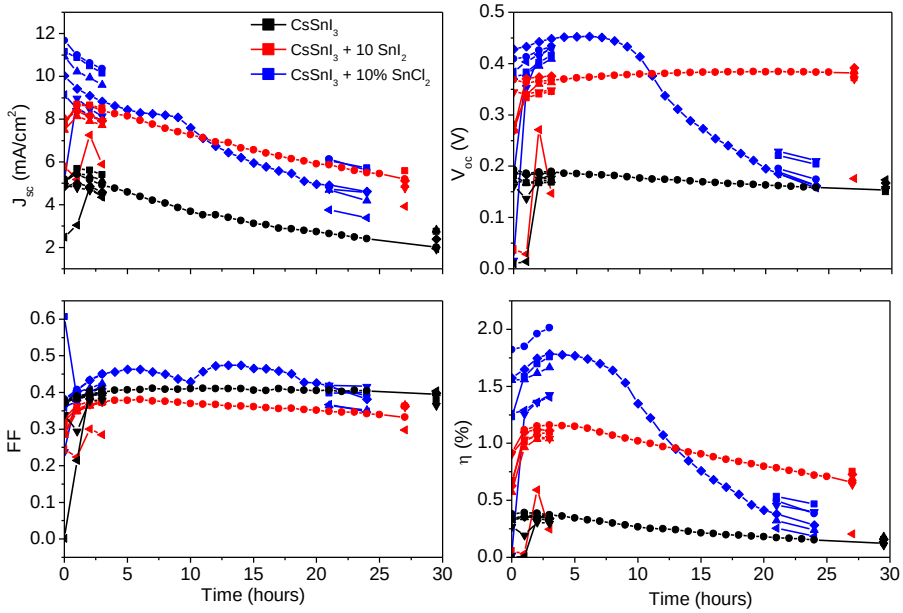

Figure 4.32: JV data over time of devices over time in air and under constant illumination at a humidity of $\sim$ 35% for devices in the structure ITO| $CsSnI_3$ + 10% $SnCl_2$, SnI_2 or no additive| C_{60}| BCP| Al.

One possible explanation for this is that perovskite degradation in the air causes the reduction in current, while the energy from the lamp causes diffusion of tin chloride species into the C_{60} layer, thereby increasing the extent of n-type doping, increasing the V_{oc} and FF, but with too much infiltration of tin chloride, the doping at the perovskite| C_{60} interface becomes too great, creating a tunnelling junction which reduces the rectification at the ITO| C_{60} interface at the pinholes. This effect is also observed under constant illumination under a nitrogen atmosphere (Figure 4.33). However, it is not observed consistently, indicating there are some other variables which causes this effect.

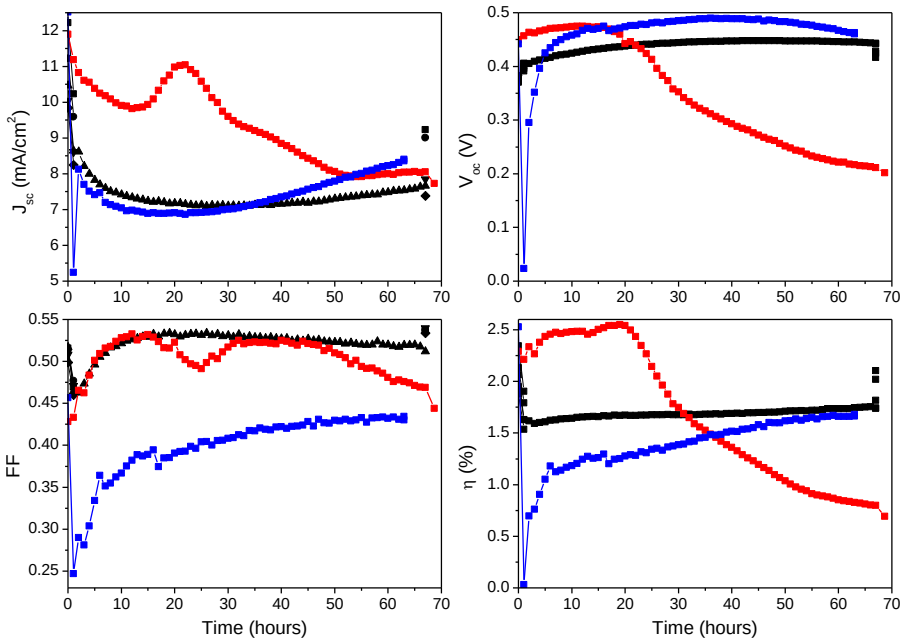

Figure 4.33: Plots of JV parameters over time of different devices in the structure ITO| $CsSnI_3$ + 10 mol% $SnCl_2$| C_{60}| BCP| Al, from three different slides in two different batches under constant illumination in a nitrogen atmosphere.

Annealing devices on a hotplate or using the solar simulator after depositing C_{60} but before depositing the BCP and top electrode improves the V_{oc} and *FF*, but reduces the current in devices. The initial hypothesis was that the thermal energy would help to rearrange the C_{60} molecules to make the film more uniform, thereby increasing shunt resistance of device, but AFM shows that there is no significant difference in roughness between a light annealed and non-annealed sample (Figure 4.34, Table 4.11).

Table 4.11: Device data for ITO| $CsSnI_3$ + 10 mol% $SnCl_2$| C_{60} (light annealed)| BCP| Al devices.

n	J_{sc} mA/cm^2	V_{oc} (V)	*FF*	η (%)	Champion η (%)
15	10.45 ± 1.01	0.42 ± 0.01	0.50 ± 0.01	2.21 ± 0.22	2.55

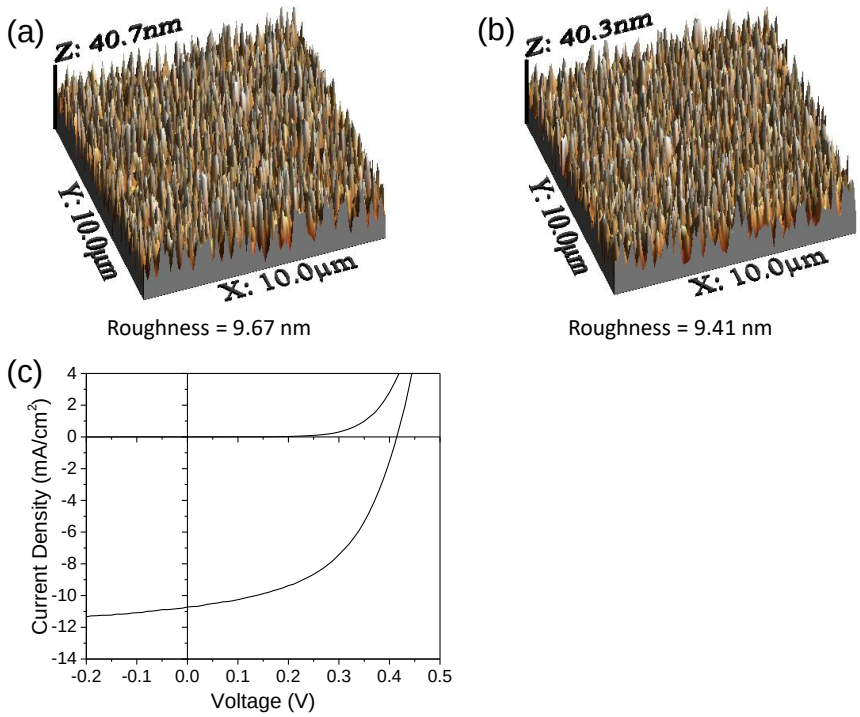

Figure 4.34: AFM images with RMS roughness values of **(a)** a light annealed and **(b)** non-annealed film of C_{60} deposited on $CsSnI_3$:$SnCl_2$. **(c)** Representative JV plot of a $CsSnI_3$:$SnCl_2$ device with C_{60} ETL light annealed after C_{60} deposition.

Because there is not a significant difference in morphology with and without annealing, the difference in device performance could be partially explained by diffusion of Sn species into the fullerene causing n-type doping, thereby improving the difference in E_f values between the ETL and light harvester, increasing the voltage, and reducing reverse current flow (see Figures 4.19 and 4.22). Additionally, it may be that the annealing step increases the crystallinity of the fullerene layer without affecting the morphology, this would have the effect of reducing the tail states in the LUMO of the fullerene, thereby increasing the difference between.[21] However, the reason for the drop in J_{sc} is not easily explained.

4.10 Conclusions

$SnCl_2$ leads to an improvement in the film stability and device performance of $CsSnI_3$ devices, with the best η of over 3.5%. However, it does not improve the stability of devices. We show evidence that the $SnCl_2$ *n*-dopes $PC_{61}BM$, increasing the energy difference between the Fermi level of the PCBM and the $CsSnI_3$ and gives rise to a Schottky contact, thereby improving the V_{oc} and *FF* of devices. Using UV/vis/NIR we show evidence that the PCBM interacts with the $SnCl_2$, reducing the stability of the perovskite films. Devices without an HTL are much more stable than those with an HTL, and improve over time when stored under nitrogen. These devices are also quite stable toward constant illumination in the air, degrading to 40% η only after 3 days.

References

[1] I. Chung, B. Lee, J. He, R. P. H. Chang, and M. G. Kanatzidis, "All-solid-state dye-sensitized solar cells with high efficiency.," *Nature*, vol. 485, pp. 486–489, 2012.

[2] M. H. Kumar, S. Dharani, W. L. Leong, P. P. Boix, R. R. Prabhakar, T. Baikie, C. Shi, H. Ding, R. Ramesh, M. Asta, M. Graetzel, S. G. Mhaisalkar, and N. Mathews, "Lead-free halide perovskite solar cells with high photocurrents realized through vacancy modulation," *Adv. Mater.*, vol. 26, pp. 7122–7127, 2014.

[3] K. P. Marshall, R. I. Walton, and R. A. Hatton, "Tin perovskite/fullerene planar layer photovoltaics: Improving the efficiency and stability of lead-free devices," *J. Mater. Chem. A*, vol. 3, pp. 11 631–11 640, 2015.

[4] J. Zhang, C. Yu, L. Wang, Y. Li, Y. Ren, and K. Shum, "Energy barrier at the N719-dye/$CsSnI_3$ interface for photogenerated holes in dye-sensitized solar cells.," *Sci. Rep.*, vol. 4, p. 6954, 2014.

[5] I. Chung, J.-H. Song, J. Im, J. Androulakis, C. D. Malliakas, H. Li, A. J. Freeman, J. T. Kenney, and M. G. Kanatzidis, "$CsSnI_3$: Semiconductor or metal? High electrical conductivity and strong near-infrared photoluminescence from a single material. High hole mobility and phase-transitions.," *J. Am. Chem. Soc.*, vol. 134, pp. 8579–8587, 2012.

[6] W. Werker, "Die kristallstruktur des Rb_2SnI_6 und Cs_2SnI_6," *Recl. des Trav. Chim. des Pays-Bas*, vol. 58, pp. 257–258, 1939.

[7] C. C. Stoumpos, C. D. Malliakas, and M. G. Kanatzidis, "Semiconducting tin and lead iodide perovskites with organic cations: phase transitions, high mobilities, and near-infrared photoluminescent properties.," *Inorg. Chem.*, vol. 52, pp. 9019–9038, 2013.

[8] B. Yang, J. Keum, O. S. Ovchinnikova, A. Belianinov, S. Chen, M.-H. Du, I. N. Ivanov, C. M. Rouleau, D. B. Geohegan, and K. Xiao, "Deciphering halogen competition in organometallic halide perovskite growth," *J. Am. Chem. Soc.*, vol. 138, pp. 5028–5035, 2016.

[9] L. Peedikakkandy and P. Bhargava, "Composition dependent optical, structural and photoluminescence characteristics of cesium tin halide perovskites," *RSC Adv.*, vol. 6, pp. 19 857–19 860, 2016.

[10] R. D. Shannon, "Revised effective ionic radii and systematic studies of interatomic distances in halides and chalcogenides," *Acta Crystallogr. Sect. A Found. Adv.*, vol. A32, pp. 751–767, 1976.

[11] P. R. Moses, L. M. Wier, J. C. Lennox, H. O. Finklea, J. R. Lenhard, and R. W. Murray, "X-ray photoelectron spectroscopy of alkylamine-silanes," *Anal. Chem.*, vol. 50, pp. 576–585, 1978.

[12] Y. Zhang, X. Hu, L. Chen, Z. Huang, Q. Fu, Y. Liu, L. Zhang, and Y. Chen, "Flexible, hole transporting layer-free and stable $CH_3NH_3PbI_3$/ $PC_{61}BM$ planar heterojunction perovskite solar cells," *Org. Electron.*, vol. 30, pp. 281–288, 2016.

[13] P. Xu, S. Chen, H.-J. Xiang, X.-G. Gong, and S.-H. Wei, "Influence of defects and synthesis conditions on the photovoltaic performance of perovskite semiconductor $CsSnI_3$," *Chem. Mater.*, vol. 26, pp. 6068–6072, 2014.

[14] G. Rajendra Kumar, H.-J. Kim, S. Karupannan, and K. Prabakar, "Interplay between Iodide and Tin Vacancies in $CsSnI_3$ Perovskite Solar Cells," *J. Phys. Chem. C*, vol. 121, pp. 16 447–16 453, 2017.

[15] Y. Shao, Z. Xiao, C. Bi, Y. Yuan, and J. Huang, "Origin and elimination of photocurrent hysteresis by fullerene passivation in $CH_3NH_3PbI_3$ planar heterojunction solar cells," *Nat. Commun.*, vol. 5, pp. 1–7, 2014.

[16] B. Chen, M. Yang, S. Priya, and K. Zhu, "Origin of J-V hysteresis in perovskite solar cells," *J. Phys. Chem. Lett.*, vol. 7, pp. 905–917, 2016.

[17] B. Wu, Y. Zhou, G. Xing, Q. Xu, H. F. Garces, A. Solanki, T. W. Goh, N. P. Padture, and T. C. Sum, "Long minority-carrier diffusion length and low surface-recombination velocity in inorganic lead-free $CsSnI_3$ perovskite crystal for solar cells," *Adv. Funct. Mater.*, vol. 27, 2017.

[18] J. Huang, Y. Shao, and Q. Dong, *Organometal Trihalide Perovskite Single Crystals: A Next Wave of Materials for 25% Efficiency Photovoltaics and Applications Beyond?* 2015.

[19] T. C. Jellicoe, J. M. Richter, H. F. Glass, M. Tabachnyk, R. Brady, S. E. Dutton, A. Rao, R. H. Friend, D. Credgington, N. C. Greenham, and M. L. Böhm, "Synthesis and optical properties of lead-free cesium tin halide perovskite nanocrystals," *J. Am. Chem. Soc.*, vol. 138, pp. 2941–2944, 2016.

[20] M. S. Tyler, I. M. Nadeem, and R. A. Hatton, "An electrode design rule for high performance top-illuminated organic photovoltaics," *Mater. Horiz.*, vol. 3, pp. 348–354, 2016.

[21] Y. Shao, Y. Yuan, and J. Huang, "Correlation of energy disorder and open-circuit voltage in hybrid perovskite solar cells," *Nat. Energy*, vol. 1, p. 15 001, 2016.

[22] Y. Yan, "Perovskite solar cells: High voltage from ordered fullerenes," *Nat. Energy*, vol. 1, p. 15 007, 2016.

[23] N. Karst and J. C. Bernède, "On the improvement of the open circuit voltage of plastic solar cells by the presence of a thin aluminium oxide layer at the interface organic/aluminium," *Phys. Stat. Sol. (a)*, vol. 203, R70–R72, 2006.

[24] B. Lee, C. C. Stoumpos, N. Zhou, F. Hao, C. Malliakas, C.-y. Yeh, T. J. Marks, M. G. Kanatzidis, and R. P. H. Chang, "Air-stable molecular semiconducting iodosalts for solar cell applications: Cs_2SnI_6 as a hole conductor," *J. Am. Chem. Soc.*, vol. 136, pp. 15 379–15 385, 2014.

[25] B. Saparov, J.-P. Sun, W. Meng, Z. Xiao, H.-S. Duan, O. Gunawan, D. Shin, I. G. Hill, Y. Yan, and D. B. Mitzi, "Thin-film deposition and characterization of a Sn-deficient perovskite derivative Cs_2SnI_6," *Chem. Mater.*, vol. 28, pp. 2315–2322, 2016.

[26] T. S. Glen, N. W. Scarratt, H. Yi, A. Iraqi, T. Wang, J. Kingsley, A. R. Buckley, D. G. Lidzey, and A. M. Donald, "Dependence on material choice of degradation of organic solar cells following exposure to humid air," *J. Polym. Sci. Part B Polym. Phys.*, vol. 54, pp. 216–224, 2016.

[27] H. Yoshida, "Measuring the electron affinity of organic solids: An indispensable new tool for organic electronics," *Anal. Bioanal. Chem.*, vol. 406, pp. 2231–2237, 2014.

[28] N. J. Jeon, J. H. Noh, Y. C. Kim, W. S. Yang, S. Ryu, and S. I. Seok, "Solvent engineering for high-performance inorganic-organic hybrid perovskite solar cells.," *Nat. Mater.*, vol. 13, pp. 897–903, 2014.

[29] H. Derouiche, "The effect of energy levels of the electron acceptor materials on organic photovoltaic cells," *Smart Grid Renew. Energy*, vol. 2, pp. 278–281, 2011.

Chapter 5

Elucidating the role of the hole-extracting electrode on the stability and efficiency of inverted $CsSnI_3/C_{60}$ perovskite photovoltaics

5.1 Introduction

The stability of lead PPVs is known to depend strongly on the choice of materials used for the extraction of holes from the perovskite layer, particularly in inverted device architectures where the choice of materials not only ensures optimal interfacial energy level alignment for selective extraction of holes but is also a key determinant of perovskite film morphology.[1–3] This chapter reports the results of a study focused on how the stability of inverted $CsSnI_3$ based PV devices with the structure: hole-extracting window electrode| $CsSnI_3$:$SnCl_2$| C_{60}| bathocuproine (BCP)| Al depends on the choice of hole-extracting substrate. The hole-extracting electrode materials compared are: (i) ITO coated glass, which is a widely used transparent electrode and

is sufficiently smooth to be used in simple bilayer PPV device architecture without an additional layer to smooth the electrode surface. This system serves as the benchmark against which the others are compared.; (ii) ITO| CuI, because CuI has recently been used for both Pb [4, 5] and Sn [6] based PPVs, and is reported to be a very stable hole transport layer (HTL) for Pb PPV applications.[5, 7].; (iii) ITO| PEDOT:PSS, because it is the most widely used HTL used in Pb PPV research in which a fullerene electron-transport layer is used.[8–10] Due to the very high doping level, PEDOT:PSS can be regarded as a synthetic metal.; (iv) An optically thin (8 nm thick) Au electrode, because Au is widely used in PPV research [11, 12] due to its high stability and in this context serves as a chemically stable and structurally well-defined model electrode. At the time of writing, the stability of Sn PPVs towards complex test conditions (i.e. constant 1 sun illumination, moisture, elevated temperature) has been sparsely reported, and to the author's knowledge this is the first report comparing the stability of inverted Sn PPV with the choice of hole-extracting electrode/HTL.

5.2 Probing the Effect of the Bottom Contact on Perovskite Film Stability and Structure

The perovskite B-γ $CsSnI_3$ is known to degrade in ambient air in a two stage process; firstly into the one dimensional yellow phase of $CsSnI_3$ (Y-$CsSnI_3$), with the same chemical composition, upon reaction with moisture, and then into the zero-dimensional Sn(IV) salt Cs_2SnI_6 upon reaction with oxygen and water,[13–15] the latter of which has an absorption coefficient across the visible spectrum $\sim$ 10 times smaller than that of B-γ $CsSnI_3$.[16] Exploiting the large reduction in absorption strength upon oxidation to Cs_2SnI_6, the evolution of the absorption spectrum of thin films of $CsSnI_3$ supported on the different substrates was used to follow the oxidation of $CsSnI_3$ films in air (Figure 5.1).

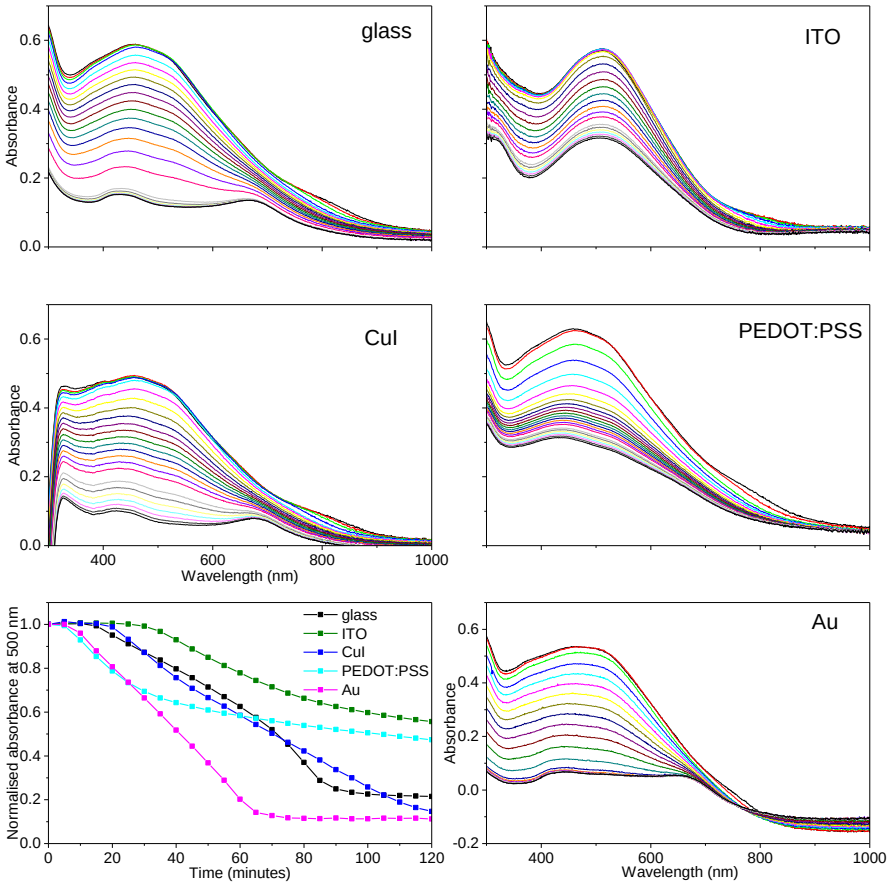

Figure 5.1: UV/Vis/NIR spectra measured as a function of time exposed to ambient air for thin films of $CsSnI_3$ + 10 mol% $SnCl_2$ deposited on glass, ITO, CuI, PEDOT:PSS, or Au. Measurements made on the same day, throughout which the relative humidity was 38%.

It is evident from Figure 5.1 that the stability of $CsSnI_3$:$SnCl_2$ films decreases in the order ITO glass > glass ~ CuI/ITO glass > PEDOT:PSS/ITO glass > Au. Au appears to be the least stable film, but the interpretation is complicated by the optical effects, which cause absorbance at long wavelength to be below 0 compared with the Au film reference. Whilst glass is not suitable as an electrode in its own right, it is a simple transparent reference substrate against which the optical properties of the perovskite films on the other more complex substrates can be compared. The spectrum of $CsSnI_3$:$SnCl_2$ on ITO includes a broad local minimum at ~ 400 nm that is not a feature of $CsSnI_3$ films on all of the other substrates (Figure 5.1). Optical modelling reveals that this feature results from an optical interference effect (Figure 5.2), rather

than from a difference in electronic structure.

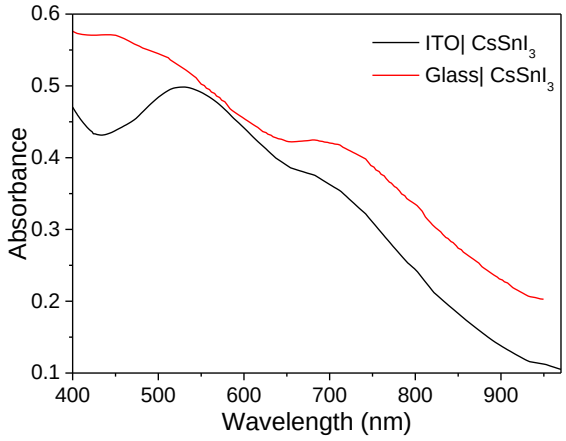

Figure 5.2: Optical simulation using the Essential MacLeod simulation package, showing the difference in absorbance for a 50 nm $CsSnI_3$ film on glass and ITO coated glass assuming an ITO thickness of 140 nm and $CsSnI_3$ film with an idealised uniform slab-like structure.

The stability of $CsSnI_3$:$SnCl_2$ films supported on different HTL/electrodes towards air-oxidation is inevitably a complex function of: (i) the intrinsic stability of the perovskite film (which strongly depends on its morphology, including the crystallite size and orientation); (ii) the density of pinholes and fissures in the film, which determines the surface area of film exposed to the environment and therefore its susceptibility to oxidation; (iii) the intrinsic stability of the underlying substrate material(s) towards oxidation in air; (iv) and the intrinsic stability of the interfaces between the films, the relative importance of which are not easily disentangled. It is however evident from Figures 5.1 and 5.3 that for perovskite films on ITO glass, glass, CuI and PEDOT:PSS the decrease in perovskite film stability correlates with a decrease in the perovskite coverage of the underlying substrate: excluding the perovskite film on Au, the film on ITO glass is the most compact with a significant number density of pin-holes with diameter 15 - 25 nm.

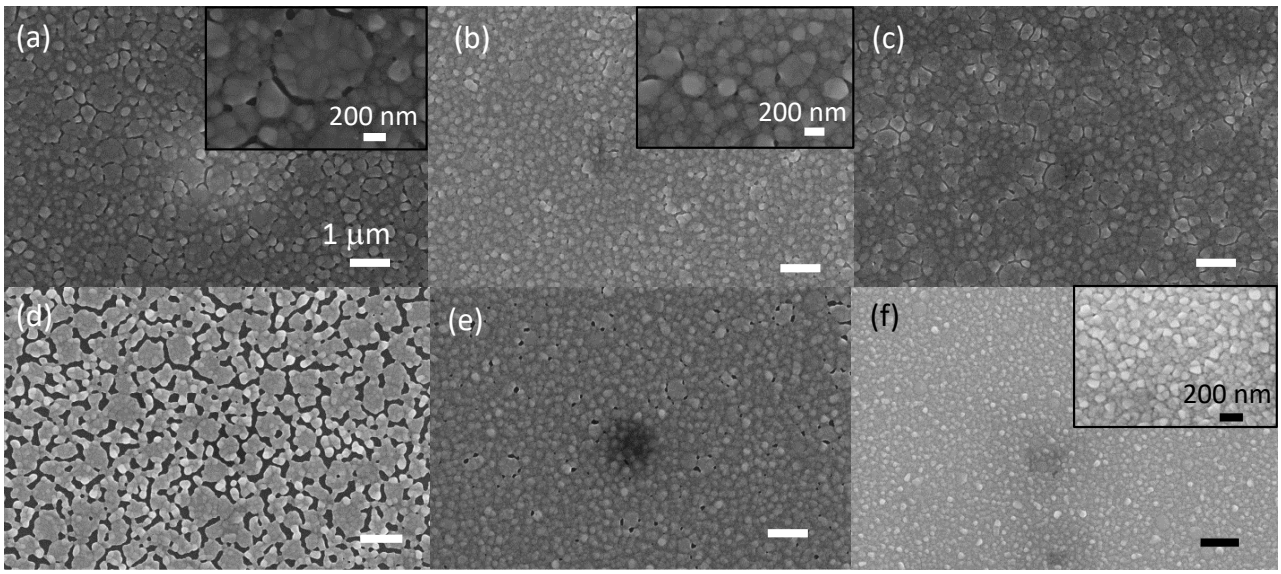

Figure 5.3: SEM images of $CsSnI_3$ + 10 mol% $SnCl_2$ deposited on top of **(a)** glass, **(b)** ITO, **(c)** CuI, **(d)** PEDOT:PSS (low coverage section), **(e)** PEDOT:PSS (high coverage area), **(f)** Au. The scale bar (b)-(f) is equal to 1 µm.

On CuI the perovskite film has a high density of elongated fissures along grain boundaries, while on the PEDOT:PSS substrate the perovskite film is non-uniform with some regions being densely packed with a pinhole density and pin-hole size comparable to that on ITO glass (Figure 5.3 (e)), and others having a high density of large fissures (Figure 5.3 (d)). The decrease in stability with reduced perovskite coverage of the underlying substrate can be rationalised in terms of the greater surface area of the perovskite film presented to the oxidising environment. The stability of the underlying substrate towards ambient air may also play a role given that PEDOT:PSS is known to be hygroscopic [17] and the first stage of $CsSnI_3$ film oxidation (i.e. conversion of B-γ $CsSnI_3$ to Y-$CsSnI_3$) results from the interaction with water[15]. The stability of $CsSnI_3$:$SnCl_2$ film on Au does not follow this trend because it is the least stable towards air-oxidation whilst also has the most compact and uniform film morphology with a relatively low density of very small (13 -17 nm) pinholes. Given that the Au electrode is stable in ambient air[11], the poor stability of the $CsSnI_3$:$SnCl_2$ film on Au most likely stems from instability in the

perovskite film itself. Close inspection of the SEM images in Figures 5.3 (b) and (f) reveals that $CsSnI_3$:$SnCl_2$ films on Au have the smallest and most uniform crystallite sizes; $\sim$ 2200 nm^2 vs $\sim$ 4900 nm^2 on ITO glass, and so it is likely that the higher density of grain boundaries enables more rapid water and oxygen penetration into the film, giving rise to increased instability despite the high film coverage of the underlying substrate, as previously been reported for lead halide perovskites.[18] Collectively these observations show that the stability of $CsSnI_3$ films towards air oxidation depends not only on the density of microscopic pin-holes and fissures but also on the density of grain boundaries between $CsSnI_3$ crystallites, with highest stability offered by perovskite films that are compact and comprise larger crystallites.

XRD was used to confirm that the B-γ phase of $CsSnI_3$ was formed on all of the substrates, and to investigate the possibility that the stability of the perovskite films depends on the orientation of the crystallites making up the film, since different crystal faces would be expected to have different reactivity towards water and oxygen due to the different arrangement and density of atoms presented to the atmosphere (Figure 5.4).

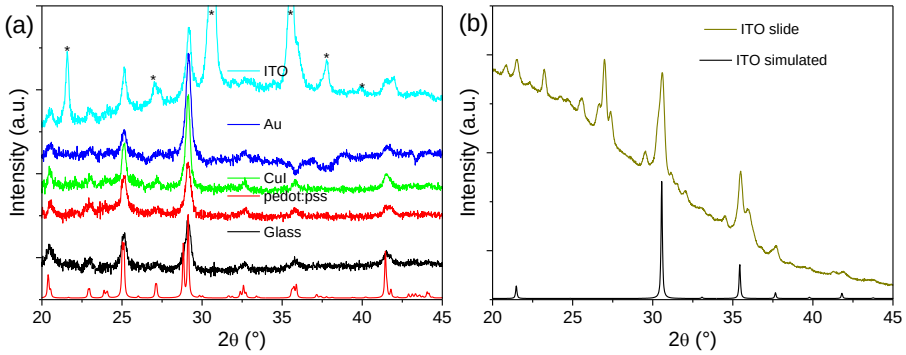

Figure 5.4: **(a)** XRD patterns of $CsSnI_3$:$SnCl_2$ films spin-coated from 8 wt% solution onto either ITO, Au, CuI, PEDOT:PSS, or glass substrates. * denotes ITO background peaks. **(b)** XRD pattern of an ITO glass slide with a simulated ITO slide shown (calculated using a CIF from ref. [19]).

The XRD patterns shown in Figure 5.4 confirm the presence of only B-γ $CsSnI_3$, and indicate

that there is a preferred orientation for crystallites on CuI and Au, because the intensity of the reflection at $\sim 29°$ (202 and 040) is greatly increased as compared to that at $\sim 25°$ (220 and 022). However, the large differences in preferred crystallite orientation do not correlate with film stability towards oxidation in air, since films on CuI and Au have very similar preferred orientation, but very different stability in air (Figure 5.1).

Solution processed CuI has been reported to be an effective as an HTL in lead PPVs prepared using DMF as the solvent for perovskite deposition.[5, 20] However, whilst the SEM image in Figure 5.3 (c) shows that $CsSnI_3$ films on CuI have high coverage of the underlying substrate, the XRD pattern; Figure 5.5, shows complete disappearance of the intense CuI (111) peak when a $CsSnI_3$ film is deposited on top of a CuI film by spin coating, indicating the ~ 40 nm CuI film is dissolved and displaced by the $CsSnI_3$ solution during the spin coating process. XPS revealed the presence of some Cu in a $CsSnI_3$:$SnCl_2$ film deposited on top of CuI (Figure 5.6) and a Cs:Cu ratio of 2.12:1.

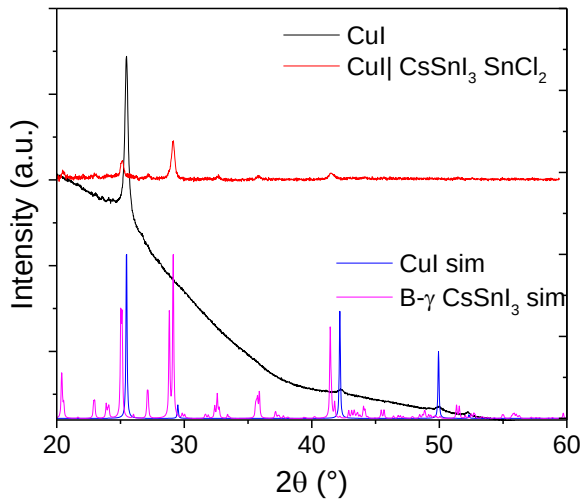

Figure 5.5: XRD pattern of $CsSnI_3$ on a glass| CuI substrate, and a film of CuI on glass. Simulated patterns of $CsSnI_3$ and CuI (calculated using CIFs from refs. [13] and [21], respectively) also shown.

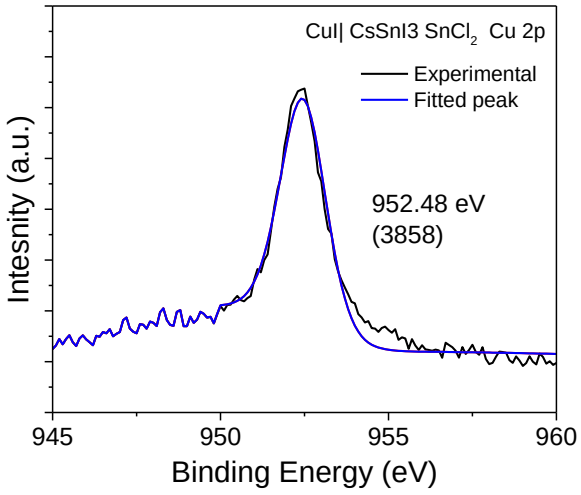

Figure 5.6: XPS of Cu $2p_{1/2}$ environment of a film of $CsSnI_3$:$SnCl_2$ deposited on top of a film of CuI. The $2p_{3/2}$ environment is not shown because it overlaps with I 3p peaks.

This conclusion is supported by the absorption spectrum of the perovskite film deposited on CuI (Figure 5.7), which shows only a small perturbation of shape of the $CsSnI_3$:$SnCl_2$ spectrum at wavelengths below $\sim$ 350 nm, which corresponds to the onset of strong absorption in CuI.

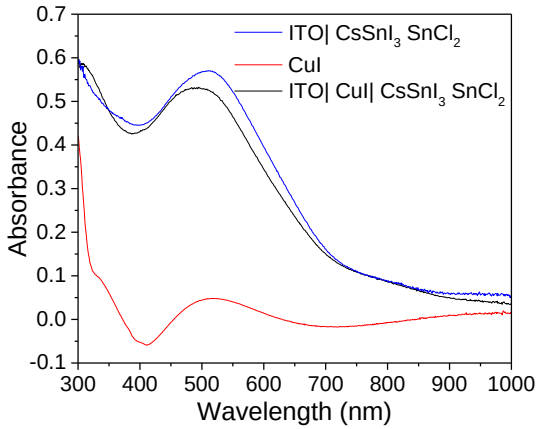

Figure 5.7: Electronic absorption spectra of a $CsSnI_3$:$SnCl_2$ (10 mol%) film supported on ITO glass (blue); a $\sim$ 40 nm CuI film on ITO glass (red); a $CsSnI_3$:$SnCl_2$ film on CuI coated ITO glass (black). In all cases ITO glass was used as the background. The apparent negative absorbance in some parts of the CuI spectrum is attributed to the CuI film functioning as an anti-reflective layer over particular wavelength ranges.

Additionally, cross-sectional AFM image analysis of CuI| $CsSnI_3$:$SnCl_2$ films; Figure 5.8, shows that the measured thickness of the film is 35 - 40 nm, which is only half the combined thickness of separate CuI and perovskite overlayer. Energy-dispersive X-ray analysis of the films (Figure 5.9 and Table 5.1) also shows that Cu is barely detectable in CuI| $CsSnI_3$:$SnCl_2$ films supported on ITO glass, whilst the indium signal from the underlying ITO substrate is very intense.

Table 5.1: Average atomic composition of five EDX scans of a film of $CsSnI_3$:$SnCl_2$ deposited onto a $\sim$ 40 nm thick CuI film supported on an ITO glass substrate.

Element	Cs	Sn	I	Cl	In
Atom %	3.8	13.9	9.8	0.4	72.1

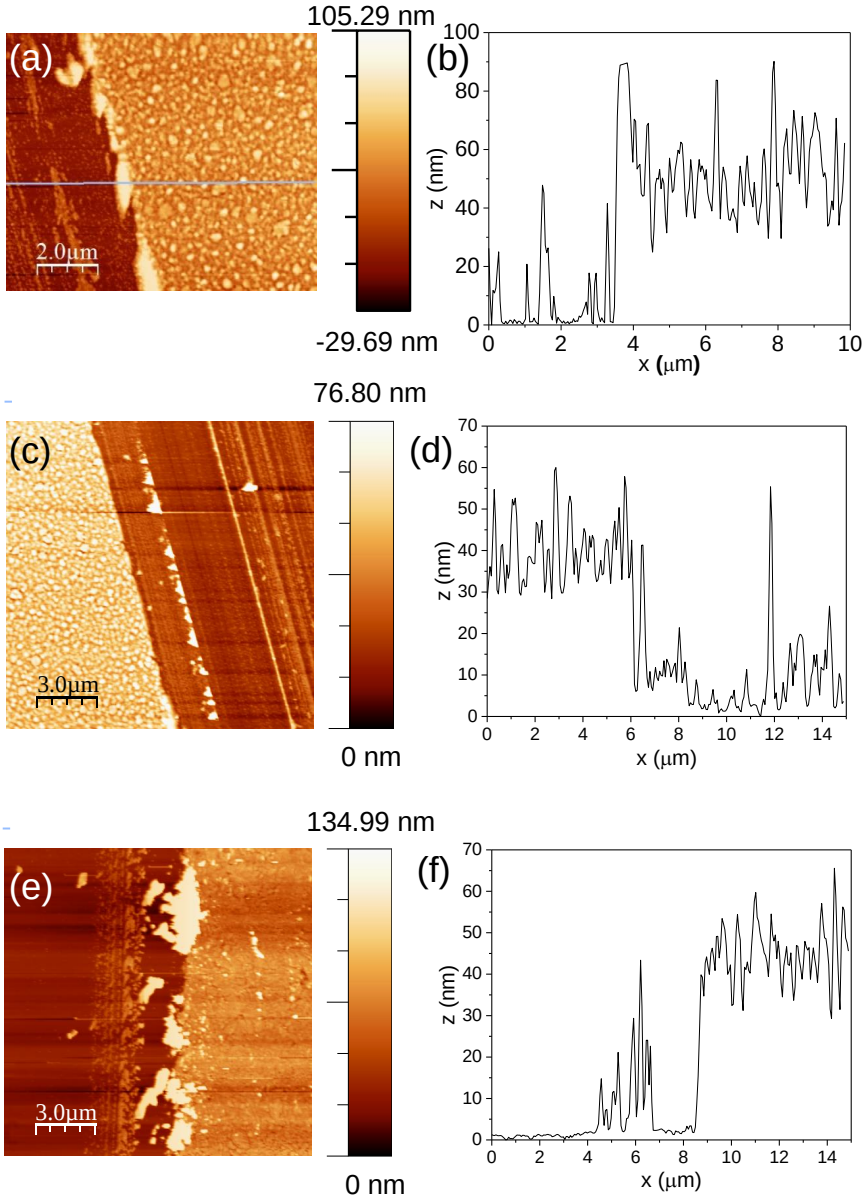

Figure 5.8: **(a)** AFM image and **(b)** AFM cross section of a film of $CsSnI_3$:$SnCl_2$ spin-cast on glass, **(c)** AFM image and **(d)** AFM cross section of a film of $CsSnI_3$:$SnCl_2$ deposited on top of a film of CuI on glass. **(e)** AFM image and **(f)** AFM cross section of a film of CuI deposited on glass.

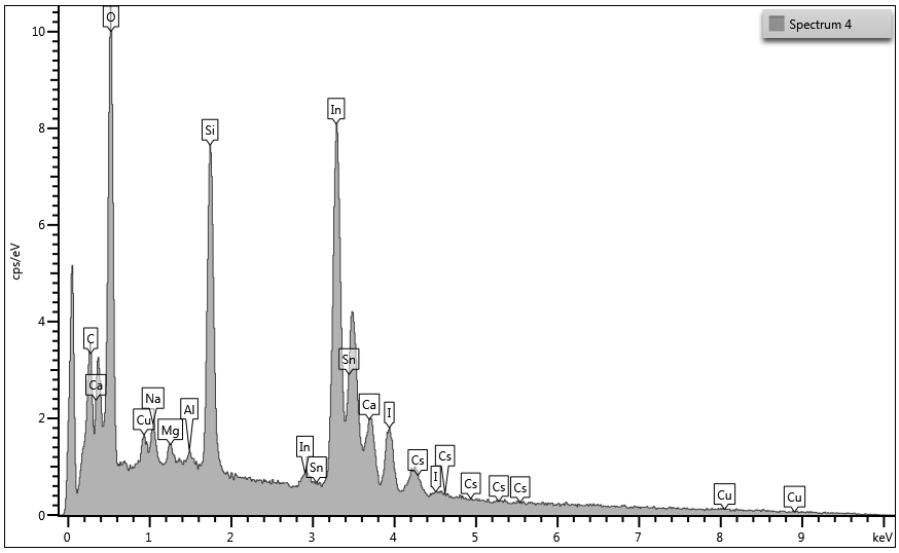

Figure 5.9: Energy-dispersive X-ray spectrum of a film of $CsSnI_3$:$SnCl_2$ deposited onto a 40 nm thick CuI film supported on an ITO glass substrate.

AFM imaging and electronic absorption spectroscopy of CuI films before and after spin casting DMF, Figure 5.10 (a) - (c), reveals that CuI films are partially soluble in DMF, which would be expected to give rise to a complex interpenetrating interface between the CuI and perovskite overlayer, with a significant amount of CuI remaining at the interface between the ITO glass and the perovskite film. However, the weight of experimental evidence is consistent with almost complete displacement of the $\sim$ 40 nm CuI film to form a perovskite film with comparable crystallinity and film coverage to that achieved on ITO glass without Cu, which is unexpected given the very rapid speed of the perovskite film formation during spin coating process. It is known that CuI is soluble in concentrated aqueous solutions of iodide ion,[22] and so it is plausible that in this case the iodide concentration in the DMF solution used to prepare the perovskite films is sufficiently high to make the solution a very powerful solvent for CuI, which together with the tendency of $CsSnI_3$ to crystallise very rapidly from DMF[23], results in the near complete displacement of the CuI film, rendering CuI unsuitable as an HTL in inverted $CsSnI_3$ PV devices.

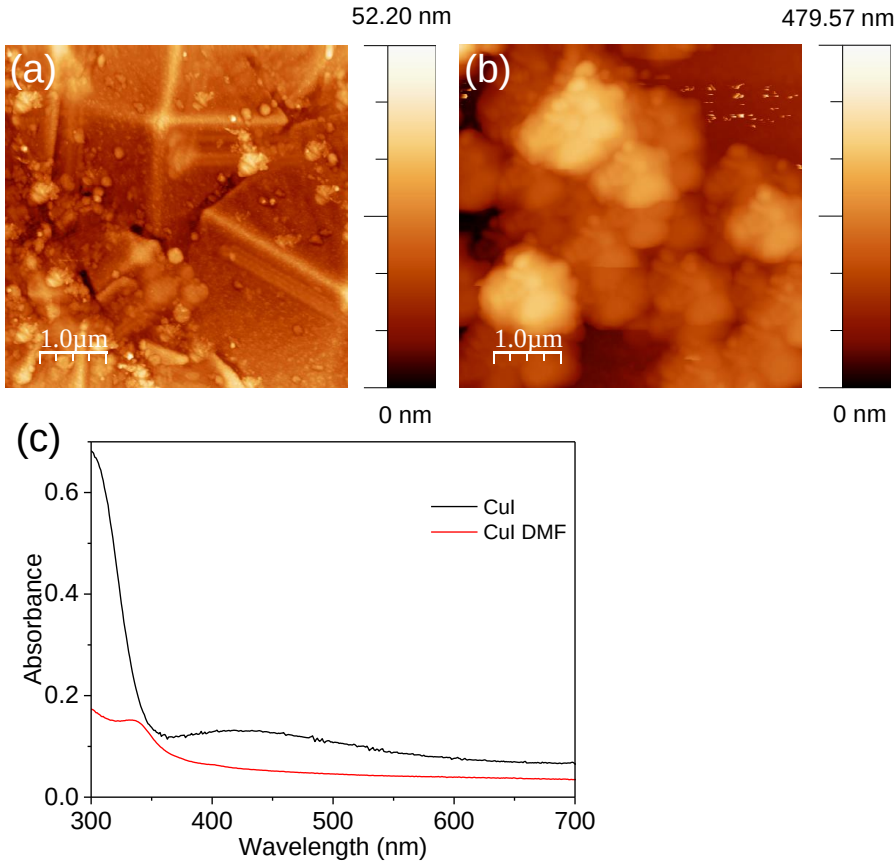

Figure 5.10: AFM images of CuI deposited on glass **(a)** before and **(b)** after spin-casting DMF on top of the film: **(c)** UV/vis/NIR spectra of films of CuI with (red) and without (black) DMF spin-casted on top.

Linking to Chapter 3, similar experiments would be useful in determining if evaporated CuI films are eroded by perovskite deposition from DMF.

5.3 Photovoltaic Device Studies

5.3.1 Initial Device Performance

Device studies were performed to compare the different bottom contacts using the structure shown in Figure 5.11 (a). Figure 5.12 and Tables 5.2 and 5.3 show that devices using an ITO electrode with either no HTL, or CuI HTL exhibit the best initial average performance, whereas

those using PEDOT:PSS give higher V_{oc} in conjunction with lower J_{sc} values. C_{60} was chosen as the ETL because it is evaporated and gives better reproducibility and device yield than solution processed $PC_{61}BM$.

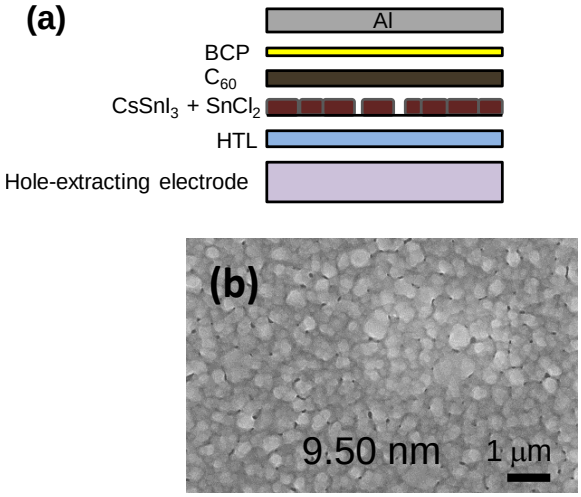

Figure 5.11: **(a)** Schematic diagram of the model device architecture used in this study, including $CsSnI_3$ with pinholes. **(b)** SEM image of the surface morphology C_{60} deposited by vacuum evaporation onto a $\sim$ 50 nm thick $CsSnI_3$ film supported on ITO glass. The root-mean-square surface roughness (SR) (measured using atomic force microscopy) is given on the image.

Table 5.2: JV data for devices with the structure; (ITO| CuI), (ITO| PEDOT:PSS), or ITO only| $CsSnI_3$ + 10 mol% $SnCl_2$| C_{60}| BCP| Al. $\pm$ 1 SD.

Device	n	J_{sc} (mA/cm^2)	V_{oc} (V)	*FF*	η (%)	Champion η (%)
ITO	18	12.63 $\pm$ 1.09	0.27 $\pm$ 0.05	0.45 $\pm$ 0.03	1.54 $\pm$ 0.33	2.15
CuI	18	11.77 $\pm$ 1.21	0.34 $\pm$ 0.03	0.49 $\pm$ 0.02	1.95 $\pm$ 0.28	2.38
PEDOT:PSS	18	8.00 $\pm$ 0.81	0.46 $\pm$ 0.01	0.46 $\pm$ 0.03	1.72 $\pm$ 0.22	2.05

Table 5.3: JV data for PPV devices with the structure; (ITO| CuI), ITO or Au| $CsSnI_3$ + 10 mol% $SnCl_2$| C_{60}| BCP| Al

Sample	n	J_{sc} (mA/cm^2)	V_{oc} (V)	*FF*	η (%)	Champion η (%)
ITO	15	12.46 ± 0.52	0.36 ± 0.01	0.48 ± 0.04	2.12 ± 0.19	2.27
Au	12	4.58 ± 0.29	0.29 ± 0.02	0.51 ± 0.06	0.69 ± 0.11	0.79
ITO| CuI	13	11.12 ± 1.03	0.34 ± 0.02	0.46 ± 0.03	1.78 ± 0.32	2.41

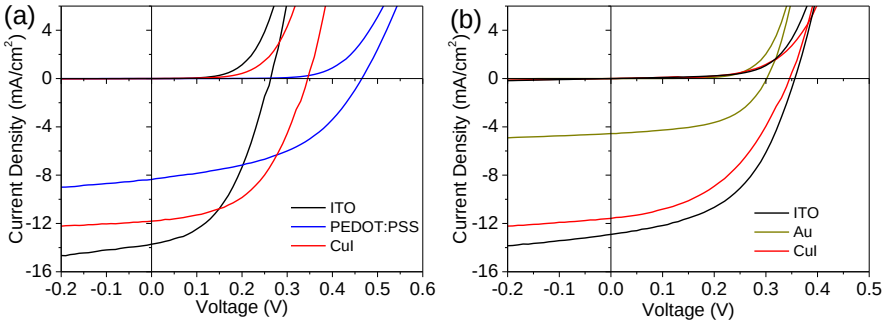

Figure 5.12: Representative JV plots of devices in the structure **(a)** (ITO| CuI), (ITO| PEDOT:PSS), or ITO only| $CsSnI_3$ + 10 mol% $SnCl_2$| C_{60}| BCP| Al, and **(b)** the same structure, except for hole extracting electrodes consisting of ITO| CuI, ITO only, or Au only.

The series resistance in devices can be estimated from the inverse of the gradient of JV characteristics under illumination at the open-circuit condition. From this it was found that devices using a PEDOT:PSS HTL had $\sim$ 2.4 times higher series resistance than HTL free devices on ITO, and devices fabricated on Au have $\sim$ 1.7 times higher series resistance (Figure 5.13). This large difference in series resistance offers a plausible explanation as to why PEDOT:PSS devices have substantially lower currents than HTL free devices. Au devices have lower current in part due to higher series resistance and in part due to the lower transparency of Au compared with ITO. The differences in J_{sc} between devices made using different bottom contacts is discussed later.

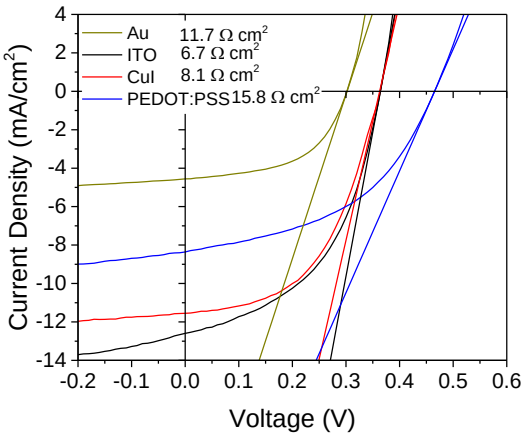

Figure 5.13: Dark current JV plots of $CsSnI_3$: $SnCl_2$| C_{60} based devices with ITO, ITO| CuI, ITO| PEDOT:PSS, or Au hole-extracting bottom contacts.

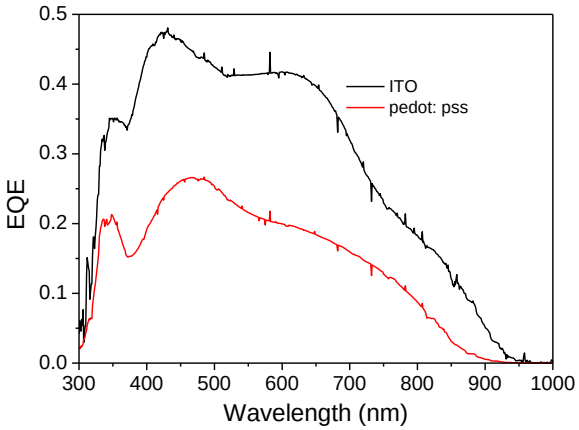

Figure 5.14: EQE spectra of devices in the structure ITO| PEDOT:PSS or no HTL| $CsSnI_3$:$SnCl_2$|C_{60}| BCP| Al.

5.3.2 Hysteresis

Unlike PV devices made using a $PC_{61}BM$ ETL, devices using a C_{60} ETL exhibited significant hysteresis (Figure 5.15). The biggest difference between C_{60} films and $PC_{61}BM$ films is the surface roughness. Hysteresis can be caused by a build up of charges associated with mobile ions and capacitative charge traps,[24, 25] or ferroelectric effects [26]. The reason for the hysteresis in this case is uncertain and would require further experiments, such as the use

of evaporated $PC_{61}BM$ in devices. It is plausible that because the evaporated C_{60} does not conformally cover the surface of the perovskite film as effectively as the $PC_{61}BM$ processed from solution, there is a greater density of non-passivated surface trap states which are known to give rise to hysteresis.[25, 27]

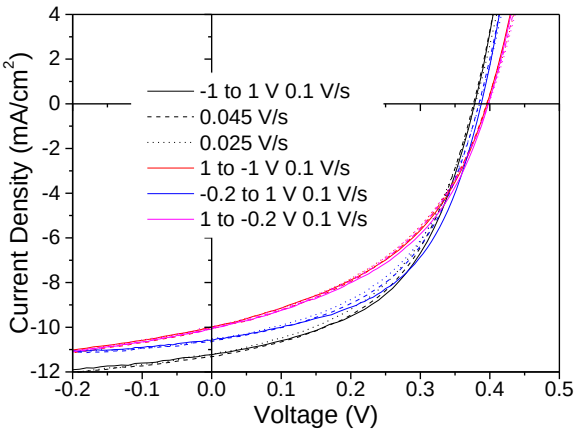

Figure 5.15: Current density - voltage plot of an ITO| $CsSnI_3$:$SnCl_2$| C_{60}| BCP| Al devices with different scan parameters.

5.3.3 Stability

Stability studies under 1 sun continuous illumination in ambient air without device encapsulation were performed on PV devices identical in every respect, except in the choice of hole-extracting electrode and/or HTL, as schematically illustrated in Figure 5.11.

Ingress of ambient air into a PV device is inevitable even with encapsulation (given sufficient time) and so testing in air under constant illumination is a test condition of practical relevance. However, the degradation mechanisms under such complex conditions are inevitably multi-faceted, with a number of parallel mechanisms operating over different time scales.[28] For this reason the device structure used to investigate the correlation between device stability and the choice of hole-extracting substrate is based on a simple discrete layer architecture.

It is evident from Figures 5.4 and 5.16 that there is no strong correlation between the preferred crystallite orientation and device stability towards oxidation, since the rate of reduction in absolute efficiency of devices using Au and ITO electrodes is similar, even though a preferred crystallite orientation is much more evident for $CsSnI_3$ films on Au. Consequently,

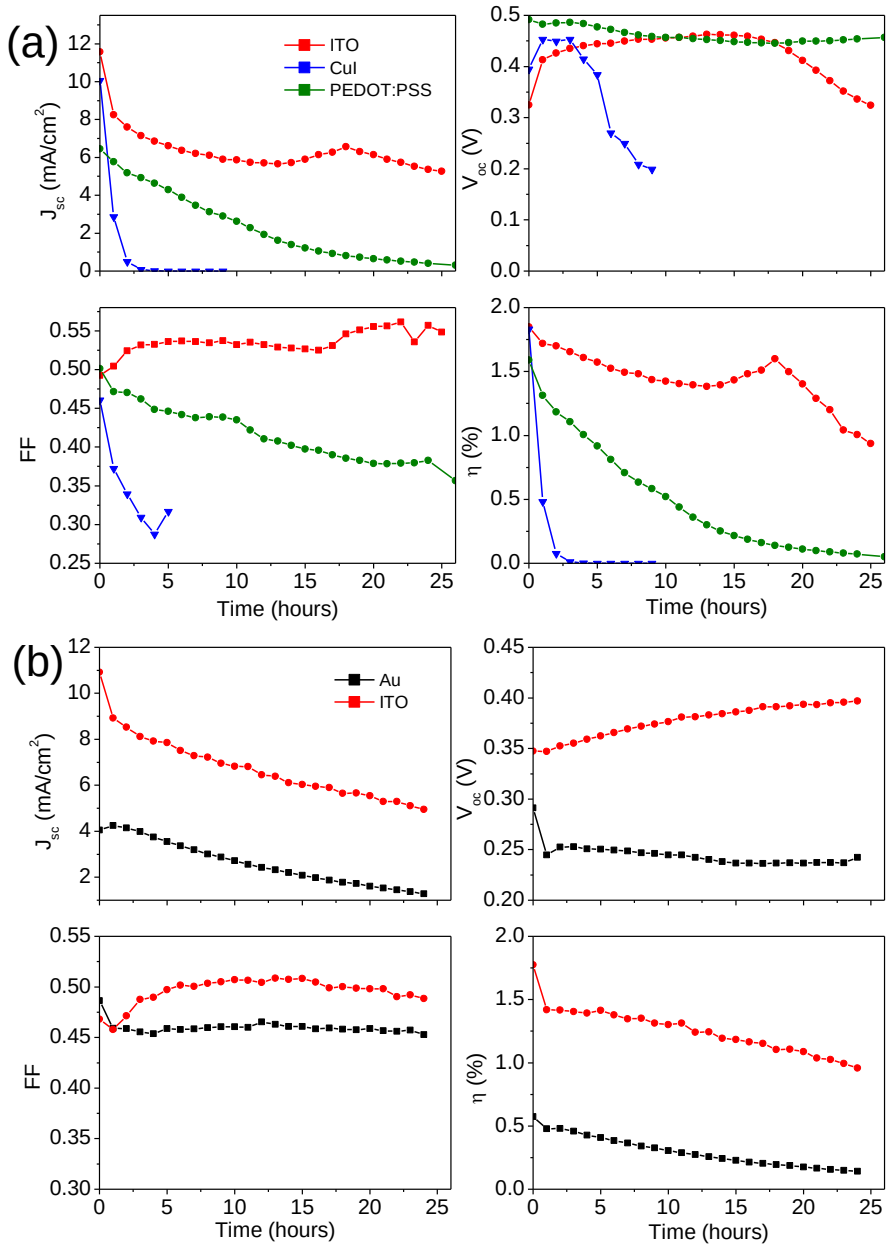

Figure 5.16: JV parameters over time exposed to ambient air under constant illumination of devices with bottom contacts **(a)** ITO, PEDOT:PSS, and CuI and **(b)** ITO, and Au, with the rest of the device in the structure $CsSnI_3$:$SnCl_2$| C_{60}| BCP| Al.

whilst crystallite orientation may play some role in determining $CsSnI_3$ film stability towards air-oxidation, it is much less important than the role of pinholes and grain boundaries between crystallites. For the champion device using ITO only the hole-extracting electrode the efficiency degrades to 70% of its initial value only after $\sim$ 20 hours which is comparable to the highest reported for unencapsulated Sn PPV devices tested under constant illumination in ambient air. [15, 29–33].

The primary reason for the deterioration in efficiency of devices using ITO (only) or Au as the hole extracting electrode over the first 24 hours testing in air is the $\sim$ 50% loss in J_{sc}, which almost certainly results from several parallel processes, some of which may be unrelated to the $CsSnI_3$ layer. For example, it is known that exposure of C_{60} to ambient air deteriorates its conductivity due to doping by H_2O and O_2 which trap electrons.[34, 35] BCP is also known to crystallise when exposed to air (a process that will be accelerated by the elevated temperature under the solar simulator, $\sim$ 50 °C) forming electron trap states at the interface between crystallites.[36, 37] Air ingress into the device through pin-holes in the Al electrode is also known to result in the formation of an insulating Al_2O_3 layer at the BCP| Al interface.[38, 39] Any of these processes can explain the increase in device series resistance, which is evident from the decrease in gradient of the JV characteristic where it crosses the voltage axis: Figure 5.17.

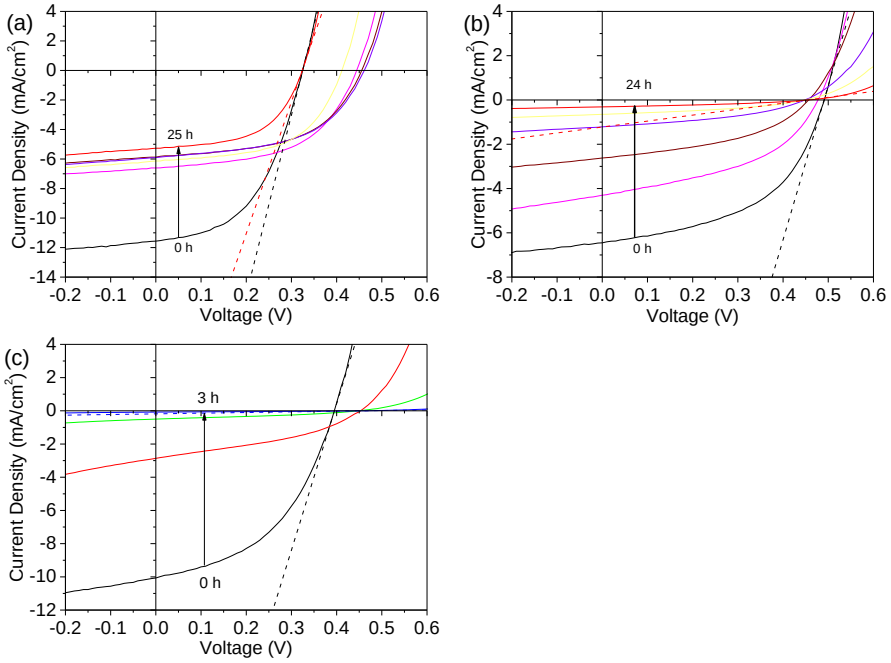

Figure 5.17: JV plots of devices over time exposed to constant illumination in air. Devices had the architecture $CsSnI_3$:$SnCl_2$| C_{60}| BCP| Al on **(a)** ITO, **(b)** ITO| PEDOT:PSS, and **(c)** ITO| CuI substrates. Tangents of first and last scans at V_{oc} are shown as dotted lines.

Figure 5.18 shows JV data for PV devices with identical structure as a function of time under constant illumination in air and in a nitrogen glovebox for devices using an ITO only hole-extracting bottom electrode, which shows that there is a significant increase in J_{sc} degradation for devices in the air. However, there is also a significant degradation for devices tested in the glovebox, which shows that some of the degradation mechanisms do not involve O_2 and H_2O.

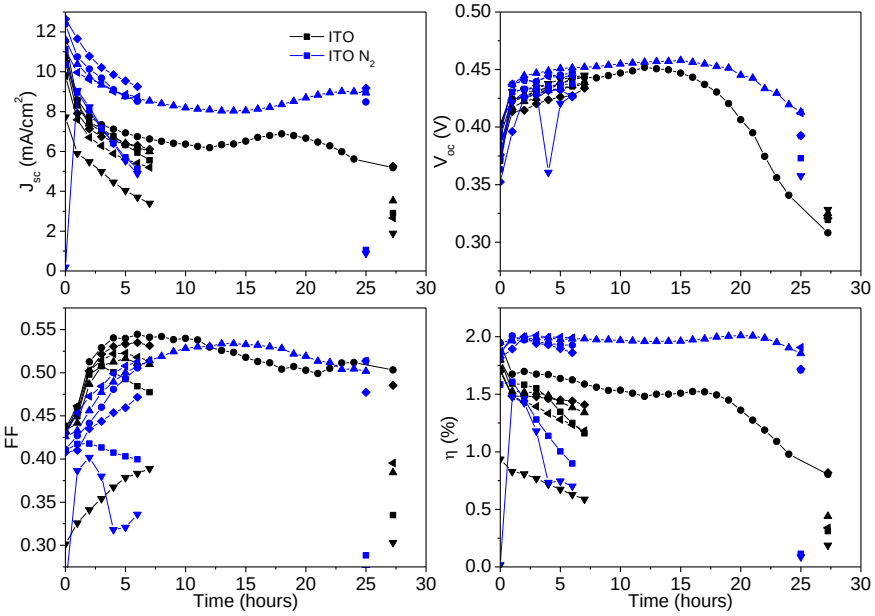

Figure 5.18: JV data from devices with time exposed to constant illumination, either in air (black) or under N_2 atmosphere (blue) for devices using an ITO substrate, with a C_{60} ETL. Different symbols represent different pixels on the same slide.

Assuming the efficiency of hole-extraction across the buried interface between the ITO (or Au) electrode and perovskite remains unchanged, any reduction in the efficiency of electron extraction to the external circuit as a result of any of the aforementioned degradation processes would be expected to increase recombination losses in the perovskite layer, offering a plausible explanation for the observed decline in J_{sc}[40]. However, air ingress into the device would also be expected result in oxidation of the $CsSnI_3$ to form Cs_2SnI_6,[15] resulting in two additional mechanisms for J_{sc} degradation: (i) Cs_2SnI_6 is a semiconductor with an absorption coefficient across the visible spectrum $\sim 10\times$ smaller than that of B-$\gamma CsSnI_3$, and so the transformation of $CsSnI_3$ into Cs_2SnI_6 would reduce the light harvesting capability of the device, thereby reducing J_{sc}.; (ii) The work function and energy of the valence band edge of Cs_2SnI_6 (prepared by air oxidation of $CsSnI_3$) was measured using ultra-violet photo-electron spectroscopy (UPS) as part

of this study with special care to remove adsorbed water and carbon contaminants; Figure 5.19, are 5.1 eV and 5.83 eV below the vacuum level, respectively.

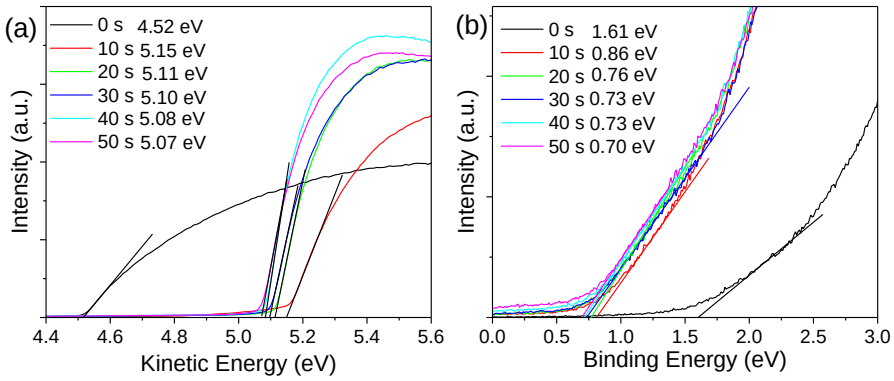

Figure 5.19: UPS of a film of Cs_2SnI_6 (supported on Au) formed by air oxidation of $CsSnI_3$. **(a)** The secondary electron cut off region, **(b)** and the valance band edge cut-off. The sample was Ar^+ ion etched for 0 to 50 s, in 10 sec steps to remove surface contaminants and adsorbed water. For t = 20, 30 and 40 seconds sputtering the data sets converge to the same value (within error) giving a valence band edge energy for Cs_2SnI_6 as 5.83 eV $\pm$ 0.05 eV below the vacuum level and work function of 5.1 eV.

Given that the band gap of Cs_2SnI_6 has been reported to be between 1.3 eV [16, 41] and 1.6 eV [42], the conduction band edge in Cs_2SnI_6 is estimated to be in the range 4.2 - 4.5 eV below the vacuum level (Figure 5.20). Whilst both of these limits are well below the energy of the conduction band edge in $CsSnI_3$; 3.6 eV [15], and the lowest unoccupied molecular orbital energy of C_{60}; 4.0 eV [43], at the real interface between $CsSnI_3$ and Cs_2SnI_6 electron transfer from the $CsSnI_3$ into Cs_2SnI_6 would be expected to occur, driven by the differences in Fermi level energy, which would reduce the barrier to electron transport across this interface possibly to < 0.1 eV. There is also a large degree of uncertainty as to the extent of charge transfer at the Cs_2SnI_6| C_{60} interface, which will depend on the local $SnCl_2$ doping level in the C_{60} layer.

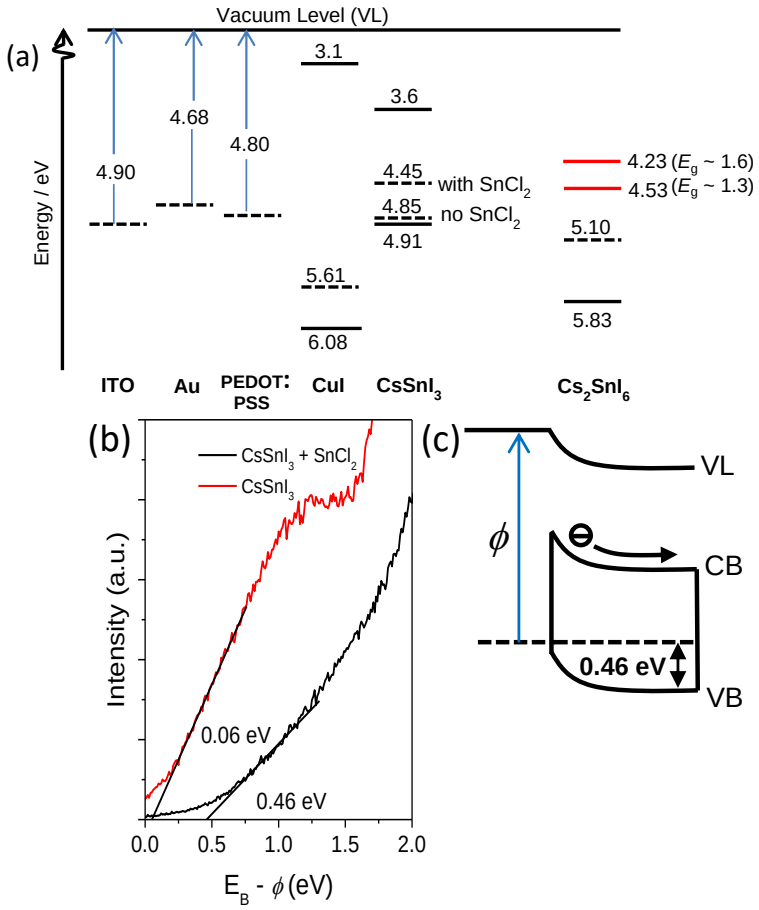

Figure 5.20: Schematic energy level diagram summarising the energy of the VB edge with respect to the VL, the work function (ϕ) and E_f (dotted line) for each material used in this study. (b) UPS of $CsSnI_3$ and $CsSnI_3$: $SnCl_2$ at VB band edge. The small signal above E_f (i.e. $E_B - \phi > 0$ eV) results from $\sim 1\%$ of the incident UV photons from the UV lamp having energy > 21.22 eV. (c) Energy level diagram depicting the Schottky contact between the $CsSnI_3$:$SnCl_2$ and the ITO electrode.

Consequently it is not possible to know with a high degree of accuracy the extent to which the formation of Cs_2SnI_6 at the interface between $CsSnI_3$ and C_{60} would impede the flow of electrons to the external circuit, giving rise to an increase in device series resistance. However, it can be concluded that a Cs_2SnI_6 layer formed at the $CsSnI_3$| C_{60} interface due to air ingress into the device would serve as reservoir of trapped electrons occupying energy states with energies

in the band gap of the $CsSnI_3$, the presence of which would be expected to erode J_{sc} due to increased recombination loses.

To determine the extent of formation of Cs_2SnI_6 in an actual device, devices with a cell area of $\sim$ 74 mm^2 were fabricated and tested under continuous 1 sun simulated illumination for 24 hours: Figure 5.21. The evolution of V_{oc}, FF and J_{sc} of these larger cell area devices is comparable to that for much smaller area (6 mm^2) devices shown in Figure 5.16, and is discussed in detail in the next part of this chapter. Following device stability testing the C_{60}, BCP and Al layers were removed by peeling off the Al electrode using tape followed by repeated washing with chlorobenzene, and the absorption spectrum of the remaining $CsSnI_3$ measured to determine the extent of film oxidation: Figure 5.21 (e). Most strikingly, the rate of degradation of light absorption by the perovskite film after 24 hours testing is much slower than the rate of degradation in J_{sc}: after 24 hours J_{sc} has decreased by $\sim$ 75% ($\sim$ 50% in 6 mm^2 devices) whilst the absorption intensity (at 500 nm) is reduced only by 0-11% over the same time period (Figure 5.21). Quantification of the reduction in absorption intensity with a higher degree of certainty is not possible because the variation in absorbance for $CsSnI_3$ films prepared in the same way is comparable to the reduction in absorbance intensity for films in devices after 24 hours testing (Figure 5.21 (f)).

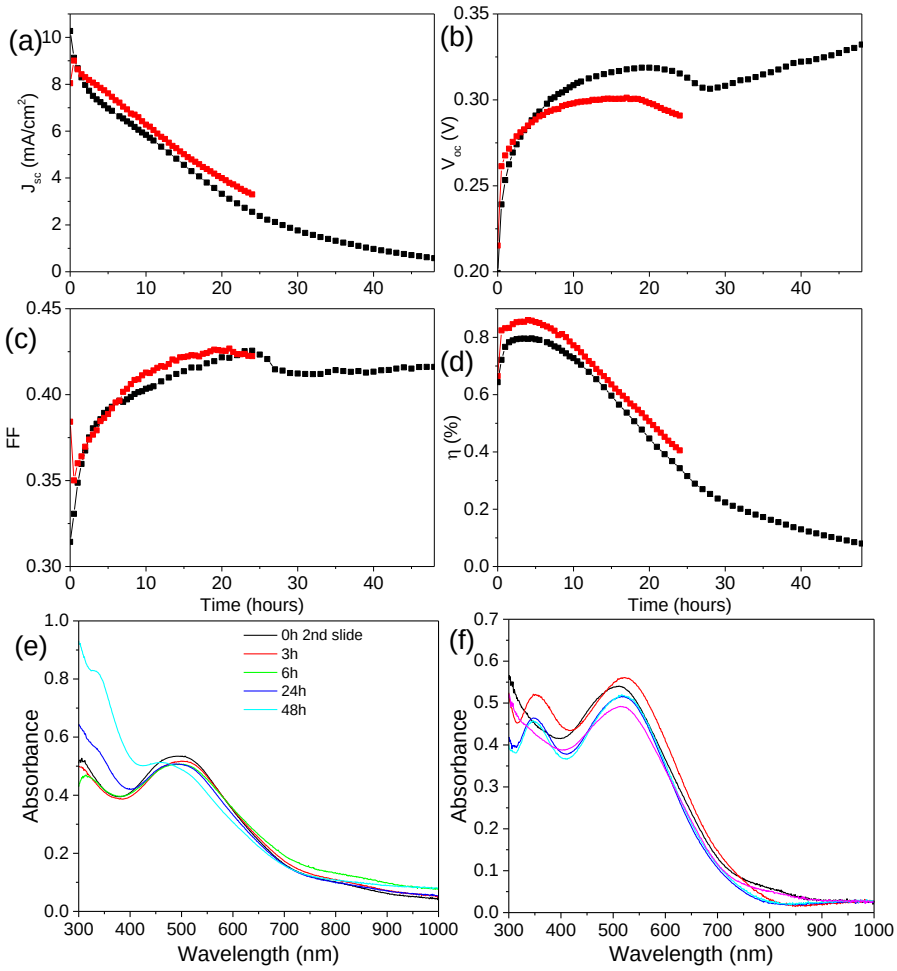

Figure 5.21: Plots of **(a)** J_{sc}, **(b)** V_{oc}, **(c)** *FF*, and **(d)** η of two devices in the structure; ITO| $CsSnI_3$:$SnCl_2$| C_{60}| BCP| Al, with a device area of 74 mm^2, over time exposed to air under constant illumination. RH $\sim$ 35%. **(e)** UV/vis/NIR spectra of devices exposed to air under constant illumination with the top electrode peeled off using tape, and then washed in chlorobenzene. **(f)** UV/vis/NIR spectra of different films of $CsSnI_3$:$SnCl_2$ spin-cast on ITO.

5.4 Probing the Electronic Structure of Devices and Interfaces

High resolution XPS analysis of the perovskite film following removal of the C_{60}, BCP and Al layers after 24 hours continuous illumination testing gives the thickness of the Cs_2SnI_6 layer to be $\sim$ 3% (or $\sim$ 1.6 nm) (Figure 5.22 (a)).

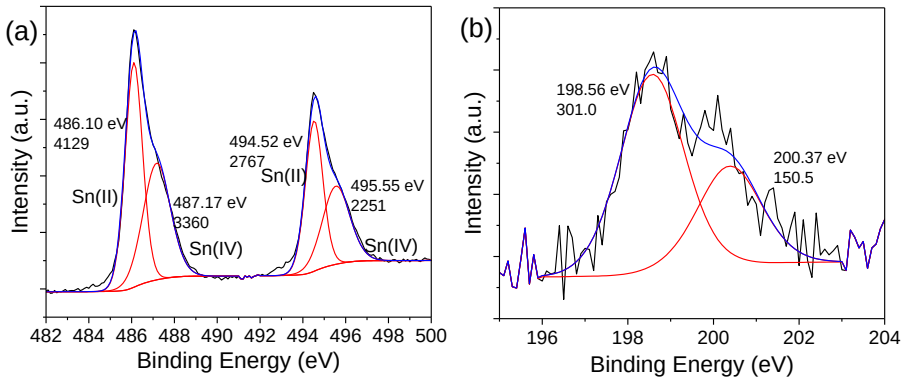

Figure 5.22: XPS of **(a)** the Sn 3d and **(b)** the Cl 2p environment of a device exposed to air under constant illumination for 24 hours. After illumination the device was transferred to a nitrogen glove-box, and the top electrode was peeled off using conductive carbon tape and then it was washed by immersing in anhydrous chlorobenzene three times. Peak positions and intensities are shown on the figures.

Assuming that the Sn^{4+} material is a thin layer on top of a substrate of $CsSnI_3$, the thickness of this layer was estimated to be 1.6 nm using equations described in the literature; Cumpson *et al.* described a graphical method called a Thickogram for calculating film thickness,[44] and by estimating an inelastic mean free path (IMFP) value using the equation derived by Tanuma *et al.*[45] Whilst there is uncertainty associated with this value, due to the presence of a small but significant Cl 2p peak in the XPS (Figure 5.22 (b)) which indicates the presence of residual $SnCl_2$, it is well within the range determined from the electron absorption spectroscopy. This finding indicates that the large deterioration in J_{sc} - which is the primary reason for the degradation in device efficiency - does not primarily result from a reduction in the light absorption capability of the perovskite film due to oxidation of the $CsSnI_3$ layer, which is expected to form Cs_2SnI_6 which has a much lower lying conduction band edge [16, 41, 42] than $CsSnI_3$ and C_{60} [43], and so forms a potential well in which electrons become trapped (Figure 5.23). Indeed, for a tin perovskite PV such a low level of perovskite oxidation after 24 hours

continuous illumination in air without encapsulation is remarkable.

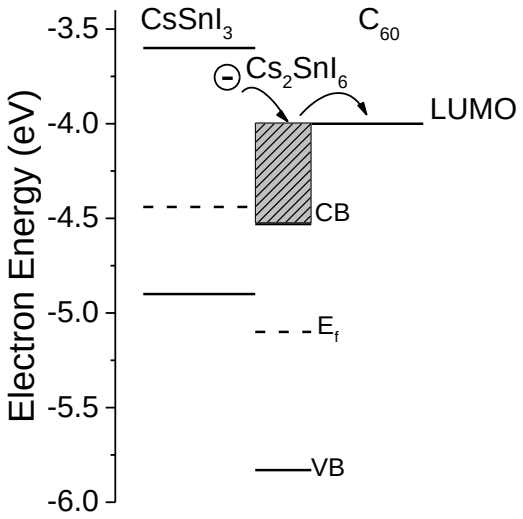

Figure 5.23: Zero-field energy level diagram depicting electronic barrier created by trap state reservoir when Cs_2SnI_6 forms at the $CsSnI_3$| C_{60} interface.

The most striking conclusion from a comparison of the device performance (Figure 5.16) is that devices with an Au or ITO electrode without an HTL have superior stability to those using the archetypal HTL layer PEDOT:PSS. The high stability of devices using the Au electrode is also counter to that expected on the basis that the $CsSnI_3$ film stability measurements (Figure 5.1). To rationalise the latter, it is necessary to take into account not only the intrinsic stability of each semiconductor layer making up the device, but also their combined morphology, since the morphology and uniformity of the Al top electrode is strongly dependant on that of the underlying materials. Since the Al electrode is the primary barrier to the ingress of water and oxygen in these devices,[39, 46] any fine gaps or pinholes in the Al electrode resulting from the high surface roughness of the semiconductor layers onto which it is deposited will have a major adverse effect on device stability.[47, 48] In this study all of the organic semiconductor layers were thermally evaporated to guarantee a high degree of control and reproducibility over deposited film thickness. However, unlike solution processed organic semiconductors, evaporated

organic semiconductor layers tend to have a morphology very similar to that of the substrate onto which they are deposited, and so the pinholes in the $CsSnI_3$:$SnCl_2$ film are also present in the C_{60} over-layer (Figure 5.24). Consequently, organic semiconductor films vacuum deposited onto a very uniform and compact perovskite film, such as that formed on Au (Figure 5.3 (f)), can be expected to have a reduced number of defects in the C_{60}, BCP and Al layers that may allow H_2O and O_2 ingress into the device.

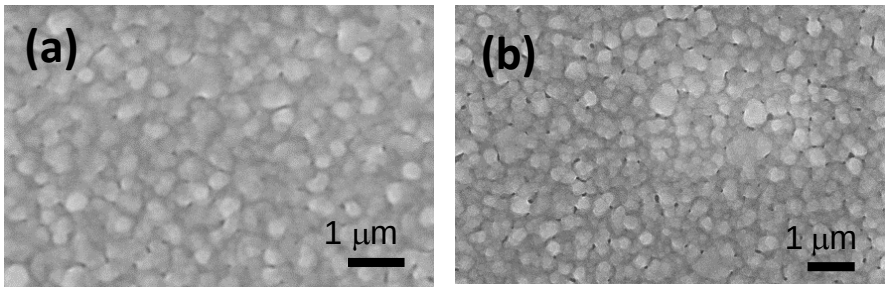

Figure 5.24: SEM images of **(a)** $PC_{61}BM$ and **(b)** C_{60} (40 nm), deposited on top of ITO| $CsSnI_3$ + 10% $SnCl_2$ substrates.

The simplest explanation for the reduced stability using ITO glass| PEDOT:PSS electrode is that the low surface coverage (in many areas) and its well-known hygroscopic properties.[49] The latter is particularly problematic for $CsSnI_3$ because it is known to degrade in the presence of water to form Y-$CsSnI_3$, or Cs_2SnI_6 when oxygen is also present.[13, 14] However, it is also notable that the rate of degradation in efficiency is much more pronounced than on ITO, because the *FF* and V_{oc} do not initially improve, as is observed to be the case for devices using ITO without a PEDOT:PSS layer. The initial improvement in these parameters for devices using ITO without an HTL occurs over several hours under constant illumination and is similar to that previously reported to occur after a period of extended storage in a nitrogen filled glovebox for devices using $PC_{61}BM$ in place of evaporated C_{60}.[15] This improvement in devices using $PC_{61}BM$ ETL was shown to result from *n*-type doping of the $PC_{61}BM$ by the

$SnCl_2$, which results in the formation of a Schottky barrier to parasitic electron extraction by the ITO electrode at the site of small pinholes in the perovskite film.[15] Direct evidence for an *n*-type doping interaction between C_{60} and $SnCl_2$ is provided by high resolution XPS (Figures 5.25 and 5.26), which shows that the binding energies of the Cl 2p electrons in $SnCl_2$ incorporated into a C_{60} film are 198.81 - 199.1 eV ($2p_{3/2}$) and 200.5 - 200.8 eV ($2p_{1/2}$), which are $\sim$ 0.6 eV higher than that of $SnCl_2$; 198.2 eV and 199.8 eV respectively[15].

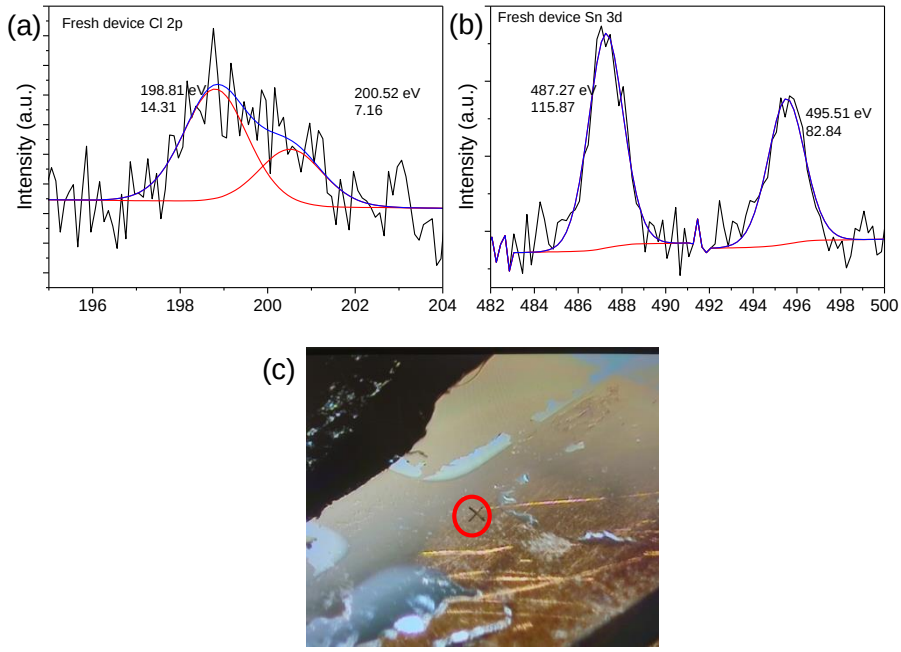

Figure 5.25: High resolution XPS of the **(a)** Cl 2p and **(b)** Sn 3d regions at the point marked in the photograph; **(c)**. The photograph shows the surface of device with the structure ITO| $CsSnI_3$:$SnCl_2$| C_{60}| BCP| Al, in which the BCP| Al and part of the C_{60} layer has been removed using carbon tape to expose the interfacial region between the perovskite film and C_{60}. Peak position and area are shown on the graphs.

This large chemical shift to higher binding energy is consistent with partial electron transfer from the $SnCl_2$ into the C_{60}, similar to that reported to occur between $SnCl_2$ and PCBM[15]. It is reasonable to expect that diffusion of $SnCl_2$ into C_{60} is accelerated by the inevitable heating that occurs under the solar simulator lamp: After 45 minutes exposure to one sun simulated

solar illumination devices stabilise at a temperature of $\sim$ 50 °C, and so the C_{60} film at the site of pin-holes in the $CsSnI_3$ film takes time to be optimally doped with $SnCl_2$.

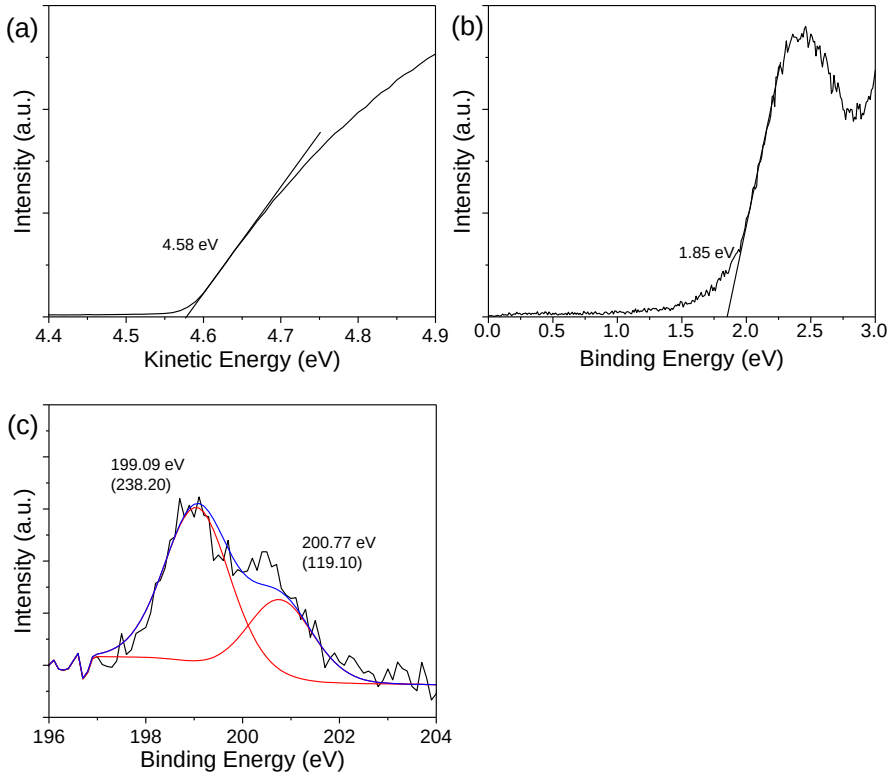

Figure 5.26: UPS of a film of C_{60} prepared from 5 mg/ml chlorobenzene solution with 0.5 mg/ml $SnCl_2$ showing **(a)** the secondary and **(b)** the primary cut-offs. **(c)** Cl 2p XPS of the same film.

The dark current-voltage characteristics of the same devices before and after five hours continuous illumination plotted on a log-linear scale (Figure 5.27) validate the conclusion that a barrier to parasitic electron extraction forms at the ITO electrode, since the dark current in reverse bias (-1 V) is dramatically reduced by 3 orders of magnitude after 5 hours. Within the framework of this model the lack of improvement in V_{oc} and FF for devices using PEDOT:PSS can be understood in terms of the very large size of the holes in $CsSnI_3$:$SnCl_2$ layer on PEDOT:PSS (Figure 5.3 (d) and (e)), because the $SnCl_2$ concentration in the C_{60} film at the site of these large holes is unlikely to be as high as at the site of the much smaller pinholes in

the $CsSnI_3$:$SnCl_2$ layer on ITO (Figure 5.3 (b)) where $SnCl_2$ on the side walls of the $CsSnI_3$ crystallites will also be a significant source of $SnCl_2$. Conversely, the absence of any improvement in V_{oc} and *FF* for devices using an Au hole-extracting electrode can be explained by the very compact, almost pin-hole free morphology of the perovskite film on Au (Figure 5.3 (f)), which means that the aforementioned mechanism of improvement in *FF* and V_{oc} would be less operative. In terms of fullerene crystallinity improving with time, which was suggested as one reason for the improvement in device performance over time in Chapter 4, it is unlikely for the $CsSnI_3$:$SnCl_2$ morphology to affect this.

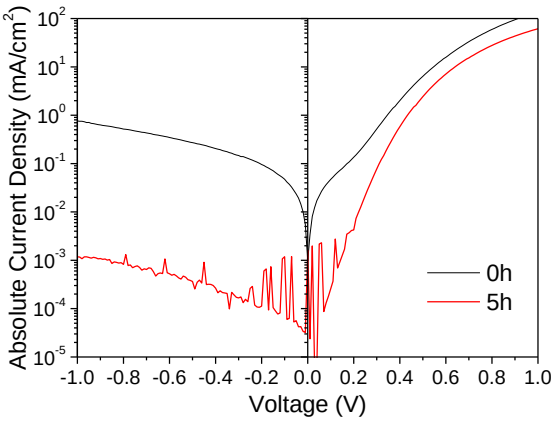

Figure 5.27: Representative log-linear dark current-voltage characteristic of the ITO| $CsSnI_3$:$SnCl_2$| C_{60}| BCP| Al photovoltaic devices. These data shows that the current in reverse bias is dramatically reduced after the device has been subjected to constant 1 sun solar illumination for 5 hours in air, which corresponds to the point at which the improvement in device fill-factor has saturated.

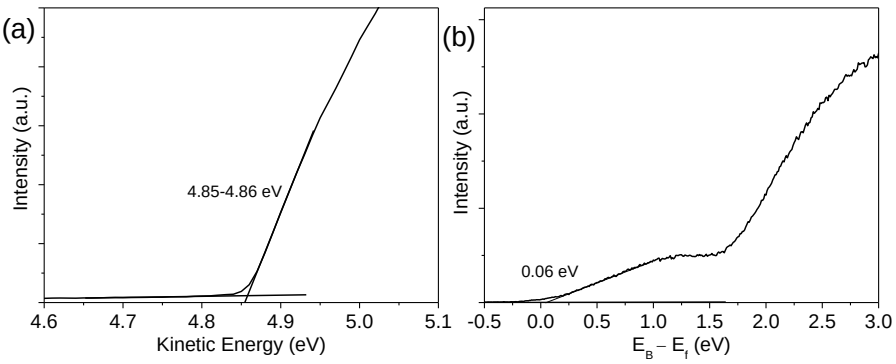

Figure 5.28: UPS of **(a)** the secondary electron cut-off and **(b)** the valence band cut-off of $CsSnI_3$ on Au without exposure to the ambient environment.

CuI has been proposed as an attractive alternative to PEDOT:PSS for lead perovskite PV devices due to its wide band gap, and ease with which it can be solution processed to form thin films and high stability.[4, 5, 7] However, it is evident from Figure 5.16 devices using CuI as the HTL are in fact very unstable, exhibiting a rapid deterioration in FF and J_{sc} when tested under continuous illumination. This instability is attributed to the previously discussed disordered nature and very low thickness of the CuI layer at the ITO| perovskite interface after perovskite deposition. Measurement of the work function and energy of the valence band edge with respect the vacuum level (Figures 5.28 and 5.29) schematically shown in Figure 5.20, reveals that, whilst the VB in $CsSnI_3$ should be closely aligned with the VB in CuI once thermodynamic equilibrium is established, holes could become trapped in the potential well at the interface (Figure 5.30) which would be expected to reduce J_{sc} by reducing the built-in electric field.

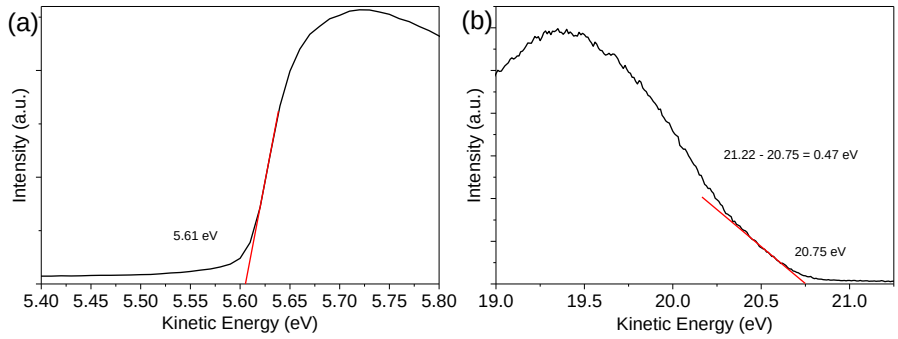

Figure 5.29: UPS of **(a)** secondary electron cut-off and **(b)** valence band cut-off of CuI on ITO without exposure to the ambient environment.

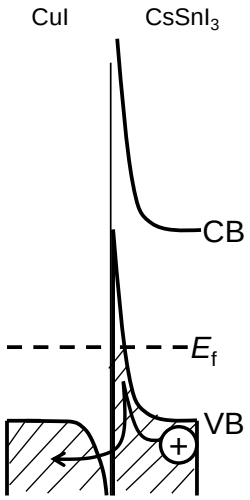

Figure 5.30: Energy level diagram depicting the interface between CuI and $CsSnI_3$ at thermodynamic equilibrium.

However, the J_{sc} is in fact comparable to that using ITO with no HTL, which is consistent with the finding that the CuI layer is almost completely displaced by the perovskite film during $CsSnI_3$ film deposition.

Analysis of the valence band (VB) edge region in the UPS (Figure 5.20 (b)) shows that the difference in energy between the E_f and the VB in $CsSnI_3$ is increased by ~ 0.4 eV when $CsSnI_3$ is synthesised in the presence of 10 mol% $SnCl_2$. This large shift in the E_f away from VB confirms that $SnCl_2$ serves to reduce the density of Sn vacancy defects, which are known

to be the primary source of background carrier density in $CsSnI_3$.[50]

It can be surmised from Figure 5.20 that there should be no barrier to the extraction of photo-generated holes using ITO, Au or ITO— PEDOT:PSS since the ϕ of $CsSnI_3$:$SnCl_2$ is smaller than all of the hole-extraction electrodes/HTL materials investigated, and the valance band edge in $CsSnI_3$:$SnCl_2$ is lower in energy than the E_f in ITO, Au or PEDOT:PSS/ITO. Consequently, the energetics upon contact formation should facilitate hole-extraction, as schematically illustrated in Figure 5.20 (c). Notably, however, devices using ITO| PEDOT:PSS initially exhibit approximately half the J_{sc} of those using ITO only. Optical modelling of the optical field distribution in the PEDOT:PSS shows that this large difference in J_{sc} cannot be attributed to a difference in light intensity in the $CsSnI_3$ layer, which is comparable for devices with and without PEDOT:PSS (Figure 5.31 (a) and (b)). The difference in J_{sc} can however be explained in terms of the difference in the ϕ of the PEDOT:PSS and ITO glass, because the former is ~ 0.1 eV smaller than that of ITO. Whilst the absolute magnitude of this difference it relatively small, it is significant compared to the difference in energy between the E_f in $CsSnI_3$:$SnCl_2$ and the hole-extracting electrode E_f (0.35 - 0.45 eV), which would result in a narrower depletion region in the $CsSnI_3$ when using PEDOT:PSS as the electrode. It is over the depletion region, which forms when a Schottky junction forms at the $CsSnI_3$| hole-extracting electrode interface, that photo-generated electrons and holes are most efficiently separated in a perovskite PV device[51], and so reducing the width of the depletion region would be expected to reduce J_{sc} – as is observed to be the case. This rationale also offers an explanation for the low J_{sc} in devices using an optically thin Au electrode, which have a J_{sc} only one third of that achieved using an ITO electrode, even though the far-field transparency of the Au electrode is approximately two thirds that of ITO glass.[11] Again, optical modelling confirms that the low J_{sc} cannot be explained in terms of the lower transparency of the Au electrode alone (Figure 5.31 (a) and (c)). However, the ϕ of the Au electrode is significantly smaller than that of ITO

or PEDOT:PSS electrode, which would reduce the depletion width between the $CsSnI_3$ and the hole-extracting contact, and thus the perovskite thickness over which photo-generated charge carriers are efficiency separated. This hypothesis would require additional data using numerous hole-extracting contacts with different work functions and correlating them with the J_{sc} values of the resulting PPV devices.

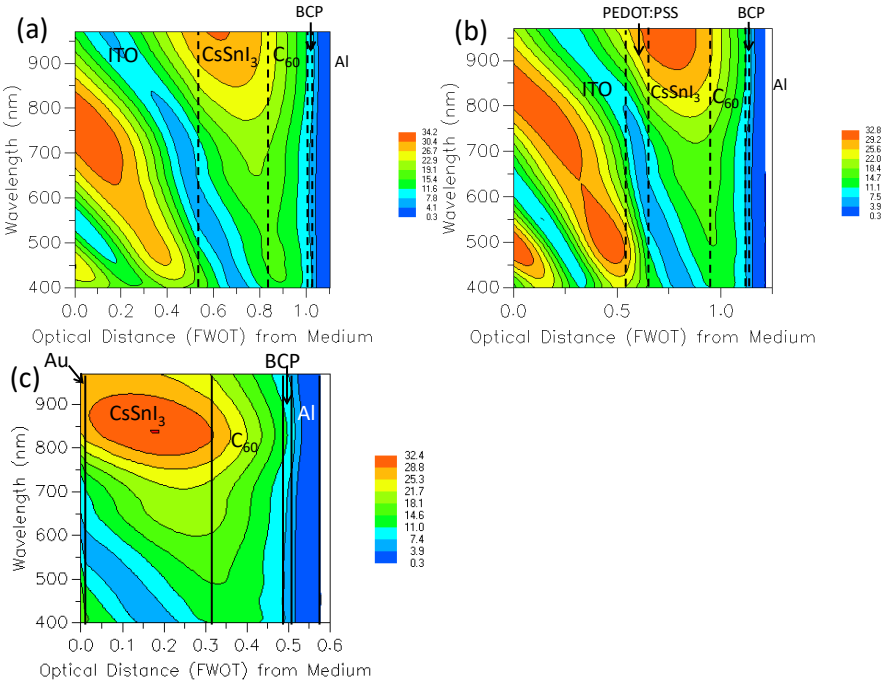

Figure 5.31: Simulation of light intensity plotted against wavelength and position in devices using **(a)** ITO, **(b)** ITO| PEDOT:PSS, or **(c)** Au substrates.

5.5 Conclusion

The key findings of the study presented in this chapter are:

(1) Using five different types of substrate it is shown that the stability of thin films of B-γ $CsSnI_3$ perovskite towards oxidation in air depends strongly not only on the density of microscopic pinholes and fissures, but also on the density of grain boundaries between $CsSnI_3$ crystallites, with best stability offered by films that are compact and comprise of larger cry-

stallites. X-ray diffraction measurements performed on perovskite films prepared in the same way as for PV devices, show that the stability of $CsSnI_3$ films towards oxidation in air is not strongly dependent on preferred orientation of the $CsSnI_3$ crystallites.

(2) We have shown that CuI is unsuitable as the HTL in $CsSnI_3$ inverted PV when using DMF as the solvent, because it is almost completely displaced by the $CsSnI_3$ precursor solution during the spin coating process and its large ionisation potential is poorly matched to the valance band edge of $CsSnI_3$. It is likely that a similar problem will arise if DMF is substituted by another polar solvent.

(3) It is shown that unencapsulated PV devices based on an inverted bilayer device architecture using ITO or semi-transparent Au, as the hole-extracting electrode without an HTL are more stable than those using the archetypal HTL PEDOT:PSS when tested under 1 sun constant simulated illumination in ambient air. This difference is attributed to the inferior film forming properties of $CsSnI_3$ on PEDOT:PSS combined with its well-known hygroscopic nature. Whilst chemical modification of PEDOT:PSS to rectify the problem of film uniformity may be possible, the hygroscopic nature is a particular problem for $CsSnI_3$ based PVs because H_2O in known to initiate oxidation of $CsSnI_3$, and so hygroscopic materials immediately adjacent to $CsSnI_3$ should be avoided.

(4) PV devices using ITO only as the hole-extracting electrode exhibit the highest stability, with 30% reduction in efficiency only after $\sim$ 20 hours testing in air for the champion device, which is very high for an unencapsulated tin perovskite PV device tested in air. However, devices using a model semi-transparent 8 nm gold window electrode also exhibit good stability, which indicates that this simplification in device structure could be generalised to other stable hole-extracting electrodes.

(5) The reason for the deterioration in devices using ITO, Au and PEDOT:PSS with time is primarily degradation in J_{sc}. However, analysis of the composition of the upper surface

of the $CsSnI_3$ layer recovered from devices tested in ambient air for 24 hours without device encapsulation, reveals that $\leq 11\%$ of the $CsSnI_3$ film has oxidised to Cs_2SnI_6. Consequently, the deterioration in device efficiency over this time frame does not primarily result from a reduction in the light absorption capability of the perovskite film due to oxidation of the $CsSnI_3$ layer.

(6) Finally, the results of the photoelectron spectroscopy study have shown (for the first time) that when $CsSnI_3$ is synthesised in the presence of $SnCl_2$ as a source of excess Sn the work function of the perovskite is reduced from ~ 4.85 eV to ~ 4.45 eV, which is consistent with a reduction in the density of Sn vacancy defects in the perovskite. Notably, this reduction in work function ensures that the work function of $CsSnI_3$ is smaller than most hole-extracting electrode materials used in perovskite and organic PV research, and so in most instances a Schottky contact will be formed that would operate to selectively block the unwanted extraction of electrons. This, combined with the added complexity in fabrication and potential for additional degradation pathways that comes with the inclusion of an HTL into the device architecture, brings into question the rationale for the inclusion of an HTL in this type of device.

References

[1] Y. Zhang, X. Hu, L. Chen, Z. Huang, Q. Fu, Y. Liu, L. Zhang, and Y. Chen, "Flexible, hole transporting layer-free and stable $CH_3NH_3PbI_3$/ $PC_{61}BM$ planar heterojunction perovskite solar cells," *Org. Electron.*, vol. 30, pp. 281–288, 2016.

[2] A. Mei, X. Li, L. Liu, Z. Ku, T. Liu, Y. Rong, M. Xu, M. Hu, J. Chen, Y. Yang, M. Grätzel, and H. Han, "A hole-conductor–free, fully printable mesoscopic perovskite solar cell with high stability," *Science*, vol. 345, pp. 295–298, 2014.

[3] L. Meng, J. You, T.-F. Guo, and Y. Yang, "Recent advances in the inverted planar structure of perovskite solar cells," *Acc. Chem. Res.*, vol. 49, pp. 155–165, 2016.

[4] P. Qin, S. Tanaka, S. Ito, N. Tetreault, K. Manabe, H. Nishino, M. K. Nazeeruddin, and M. Grätzel, "Inorganic hole conductor-based lead halide perovskite solar cells with 12.4% conversion efficiency," *Nat. Commun.*, vol. 5, p. 3834, 2014.

[5] W. Sun, S. Ye, H. Rao, Y. Li, Z. Liu, L. Xiao, Z. Chen, Z. Bian, and C. Huang, "Room-temperature and solution-processed copper iodide as hole transport layer for inverted planar perovskite solar cells," *Nanoscale*, vol. 8, pp. 15 954–15 960, 2016.

[6] K. P. Marshall, R. I. Walton, and R. A. Hatton, "Tin perovskite/fullerene planar layer photovoltaics: Improving the efficiency and stability of lead-free devices," *J. Mater. Chem. A*, vol. 3, pp. 11 631–11 640, 2015.

[7] J. A. Christians, R. C. M. Fung, and P. V. Kamat, "An inorganic hole conductor for organo-lead halide perovskite solar cells. Improved hole conductivity with copper iodide.," *J. Am. Chem. Soc.*, vol. 136, pp. 758–764, 2014.

[8] H.-B. Kim, H. Choi, J. Jeong, S. Kim, B. Walker, S. Song, and J. Y. Kim, "Mixed solvents for the optimization of morphology in solution-processed, inverted-type perovskite/fullerene hybrid solar cells.," *Nanoscale*, vol. 6, pp. 6679–6683, 2014.

[9] X. Bao, Y. Wang, Q. Zhu, N. Wang, D. Zhu, J. Wang, A. Yang, and R. Yang, "Efficient planar perovskite solar cells with large fill factor and excellent stability," *J. Power Sources*, vol. 297, pp. 53–58, 2015.

[10] J.-Y. Jeng, Y.-F. Chiang, M.-H. Lee, S.-R. Peng, T.-F. Guo, P. Chen, and T.-C. Wen, "$CH_3NH_3PbI_3$ perovskite/fullerene planar-heterojunction hybrid solar cells.," *Adv. Mater.*, vol. 25, pp. 3727–3732, 2013.

[11] H. M. Stec, R. J. Williams, T. S. Jones, and R. A. Hatton, "Ultrathin transparent Au electrodes for organic photovoltaics fabricated using a mixed mono-molecular nucleation layer," *Adv. Funct. Mater.*, vol. 21, pp. 1709–1716, 2011.

[12] H. M. Stec and R. A. Hatton, "Widely applicable coinage metal window electrodes on flexible polyester substrates applied to organic photovoltaics.," *ACS Appl. Mater. Interfaces*, vol. 4, pp. 6013–6020, 2012.

[13] I. Chung, J.-H. Song, J. Im, J. Androulakis, C. D. Malliakas, H. Li, A. J. Freeman, J. T. Kenney, and M. G. Kanatzidis, "$CsSnI_3$: Semiconductor or metal? High electrical conductivity and strong near-infrared photoluminescence from a single material. High hole mobility and phase-transitions.," *J. Am. Chem. Soc.*, vol. 134, pp. 8579–8587, 2012.

[14] C. C. Stoumpos, C. D. Malliakas, and M. G. Kanatzidis, "Semiconducting tin and lead iodide perovskites with organic cations: phase transitions, high mobilities, and near-infrared photoluminescent properties.," *Inorg. Chem.*, vol. 52, pp. 9019–9038, 2013.

[15] K. P. Marshall, M. Walker, R. I. Walton, and R. A. Hatton, "Enhanced stability and efficiency in hole-transport-layer-free $CsSnI_3$ perovskite photovoltaics," *Nat. Energy*, vol. 1, p. 16 178, 2016.

[16] J. Zhang, C. Yu, L. Wang, Y. Li, Y. Ren, and K. Shum, "Energy barrier at the N719-dye/$CsSnI_3$ interface for photogenerated holes in dye-sensitized solar cells.," *Sci. Rep.*, vol. 4, p. 6954, 2014.

[17] J. Zhou, D. H. Anjum, L. Chen, X. Xu, I. A. Ventura, L. Jiang, and G. Lubineau, "The temperature-dependent microstructure of PEDOT/PSS films: insights from morphological, mechanical and electrical analyses," *J. Mater. Chem. C*, vol. 2, pp. 9903–9910, 2014.

[18] A. M. A. Leguy, Y. Hu, M. Campoy-Quiles, M. I. Alonso, O. J. Weber, P. Azarhoosh, M. van Schilfgaarde, M. T. Weller, T. Bein, J. Nelson, P. Docampo, and P. R. F. Barnes, "Reversible hydration of $CH_3NH_3PbI_3$ in films, single crystals, and solar cells," *Chem. Mater.*, vol. 27, pp. 3397–3407, 2015.

[19] N. Nadaud, N. Lequeux, M. Nanot, J. Jovenstitut, and T. Roisnel, "Structural studies of tin-doped indium oxide (ITO) and $In_4Sn_3O_{12}$," *J. Solid State Chem.*, vol. 135, pp. 140–148, 1998.

[20] W.-Y. Chen, L.-L. Deng, S.-M. Dai, X. Wang, C.-B. Tian, X.-X. Zhan, S.-Y. Xie, R.-B. Huang, and L. Zheng, "Low-cost solution-processed copper iodide as an alternative to PEDOT: PSS hole transport layer for efficient and stable inverted planar heterojunction perovskite solar cells," *J. Mater. Chem. A*, vol. 3, pp. 19 353–19 359, 2015.

[21] D. A. Keen and S. Hull, "The high-temperature structural behaviour of copper(I) iodide," *J. Phys. Condens. Matter*, vol. 7, pp. 5793–5804, 1995.

[22] G. B. Kauffman, L. Y. Fang, N. Viswanathan, and G. Townsend, "Purification of copper(I) iodide," *Inorg. Synth.*, vol. 22, pp. 101–103, 2006.

[23] F. Hao, C. C. Stoumpos, P. Guo, N. Zhou, T. J. Marks, R. P. H. Chang, and M. G. Kanatzidis, "Solvent-mediated crystallization of $CH_3NH_3SnI_3$ films for heterojunction depleted perovskite solar cells," *J. Am. Chem. Soc.*, vol. 137, pp. 11 445–11 452, 2015.

[24] S. V. Reenen, M. Kemerink, and H. J. Snaith, "Modeling anomalous hysteresis in perovskite solar cells," *J. Phys. Chem. Lett.*, vol. 6, pp. 3808–3814, 2015.

[25] B. Chen, M. Yang, S. Priya, and K. Zhu, "Origin of J-V hysteresis in perovskite solar cells," *J. Phys. Chem. Lett.*, vol. 7, pp. 905–917, 2016.

[26] J. Wei, Y. Zhao, H. Li, G. Li, J. Pan, D. Xu, Q. Zhao, and D. Yu, "Hysteresis analysis based on the ferroelectric effect in hybrid perovskite solar cells," *J. Phys. Chem. Lett.*, vol. 5, pp. 3937–3945, 2014.

[27] Y. Shao, Z. Xiao, C. Bi, Y. Yuan, and J. Huang, "Origin and elimination of photocurrent hysteresis by fullerene passivation in $CH_3NH_3PbI_3$ planar heterojunction solar cells," *Nat. Commun.*, vol. 5, pp. 1–7, 2014.

[28] T. A. Berhe, W.-N. Su, C.-H. Chen, C.-J. Pan, J.-H. Cheng, H.-M. Chen, M.-C. Tsai, L.-Y. Chen, A. A. Dubale, and B.-J. Hwang, "Organometal halide perovskite solar cells: degradation and stability," *Energy Environ. Sci.*, vol. 9, pp. 323–356, 2016.

[29] N. K. Noel, S. D. Stranks, A. Abate, C. Wehrenfennig, S. Guarnera, A.-A. Haghighirad, A. Sadhanala, G. E. Eperon, S. K. Pathak, M. B. Johnston, A. Petrozza, L. M. Herz, and H. J. Snaith, "Lead-free organic-inorganic tin halide perovskites for photovoltaic applications," *Energy Environ. Sci.*, vol. 7, pp. 3061–3068, 2014.

[30] F. Hao, C. C. Stoumpos, D. H. Cao, R. P. H. Chang, and M. G. Kanatzidis, "Lead-free solid-state organic–inorganic halide perovskite solar cells," *Nat. Photonics*, vol. 8, pp. 489–494, 2014.

[31] S. Gupta, T. Bendikov, G. Hodes, and D. Cahen, "$CsSnBr_3$, a lead-free halide perovskite for long-term solar cell application: insights on SnF_2 addition," *ACS Energy Lett.*, vol. 1, pp. 1028–1033, 2016.

[32] D. Moghe, L. Wang, C. J. Traverse, A. Redoute, M. Sponseller, P. R. Brown, V. Bulović, and R. R. Lunt, "All vapor-deposited lead-free doped CsSnBr3 planar solar cells," *Nano Energy*, vol. 28, pp. 469–474, 2016.

[33] W. Liao, D. Zhao, Y. Yu, C. R. Grice, C. Wang, A. J. Cimaroli, P. Schulz, W. Meng, K. Zhu, R. G. Xiong, and Y. Yan, "Lead-free inverted planar formamidinium tin triiodide perovskite solar cells achieving power conversion efficiencies up to 6.22%," *Adv. Mater.*, vol. 28, pp. 9333–9340, 2016.

[34] Q. Bao, X. Liu, S. Braun, and M. Fahlman, "Oxygen- and water-based degradation in [6,6]-phenyl-C_{61}-butyric acid methyl ester (PCBM) films," *Adv. Energy Mater.*, vol. 4, p. 1 301 272, 2014.

[35] Q. D. Yang, T.-W. Ng, M.-F. Lo, F. Y. Wang, N. B. Wong, and C.-S. Lee, "Effect of water and oxygen on the electronic structure of the organic photovoltaic," *J. Phys. Chem. C*, vol. 116, pp. 10 982–10 985, 2012.

[36] P. Peumans, A. Yakimov, and S. R. Forrest, "Small molecular weight organic thin-film photodetectors and solar cells," *J. Appl. Phys.*, vol. 93, pp. 3693–3723, 2003.

[37] Z. R. Hong, Z. H. Huang, and X. T. Zeng, "Utilization of copper phthalocyanine and bathocuproine as an electron transport layer in photovoltaic cells with copper phthalocyanine/buckminsterfullerene heterojunctions: Thickness effects on photovoltaic performances," *Thin Solid Films*, vol. 515, pp. 3019–3023, 2007.

[38] A. Guerrero, P. P. Boix, L. F. Marchesi, T. Ripolles-Sanchis, E. C. Pereira, and G. Garcia-Belmonte, "Oxygen doping-induced photogeneration loss in P3HT:PCBM solar cells," *Sol. Energy Mater. Sol. Cells*, vol. 100, pp. 185–191, 2012.

[39] T. Glen, N. Scarratt, H. Yi, A. Iraqi, T. Wang, J. Kingsley, A. Buckley, D. Lidzey, and A. Donald, "Grain size dependence of degradation of aluminium/calcium cathodes in organic solar cells following exposure to humid air," *Sol. Energy Mater. Sol. Cells*, vol. 140, pp. 25–32, 2015.

[40] C. M. Proctor, J. A. Love, and T. Q. Nguyen, "Mobility guidelines for high fill factor solution-processed small molecule solar cells," *Adv. Mater.*, vol. 26, pp. 5957–5961, 2014.

[41] B. Lee, C. C. Stoumpos, N. Zhou, F. Hao, C. Malliakas, C.-y. Yeh, T. J. Marks, M. G. Kanatzidis, and R. P. H. Chang, "Air-stable molecular semiconducting iodosalts for solar cell applications: Cs_2SnI_6 as a hole conductor," *J. Am. Chem. Soc.*, vol. 136, pp. 15 379–15 385, 2014.

[42] B. Saparov, J.-P. Sun, W. Meng, Z. Xiao, H.-S. Duan, O. Gunawan, D. Shin, I. G. Hill, Y. Yan, and D. B. Mitzi, "Thin-film deposition and characterization of a Sn-deficient perovskite derivative Cs_2SnI_6," *Chem. Mater.*, vol. 28, pp. 2315–2322, 2016.

[43] H. Yoshida, "Measuring the electron affinity of organic solids: An indispensable new tool for organic electronics," *Anal. Bioanal. Chem.*, vol. 406, pp. 2231–2237, 2014.

[44] P. J. Cumpson and P. C. Zalm, "Thickogram: A method for easy film thickness measurement in XPS," *Surf. Interface Anal.*, vol. 29, pp. 403–406, 2000.

[45] S. Tanuma, C. J. Powell, and D. R. Penn, "Calculation of electron inelastic mean free paths (IMFPs) VII. Reliability of the TPP-2M IMFP predictive equation," *Surf. Interface Anal.*, vol. 35, pp. 268–275, 2003.

[46] T. S. Glen, N. W. Scarratt, H. Yi, A. Iraqi, T. Wang, J. Kingsley, A. R. Buckley, D. G. Lidzey, and A. M. Donald, "Dependence on material choice of degradation of organic solar cells following exposure to humid air," *J. Polym. Sci. Part B Polym. Phys.*, vol. 54, pp. 216–224, 2016.

[47] W. Nie, H. Tsai, R. Asadpour, A. J. Neukirch, G. Gupta, J. J. Crochet, M. Chhowalla, S. Tretiak, M. A. Alam, and H.-l. Wang, "High-efficiency solution-processed perovskite solar cells with millimeter-scale grains," *Science*, vol. 347, pp. 522–525, 2015.

[48] M.-C. Jung, S. R. Raga, L. K. Ono, and Y. Qi, "Substantial improvement of perovskite solar cells stability by pinhole-free hole transport layer with doping engineering," *Sci. Rep.*, vol. 5, p. 9863, 2015.

[49] M. P. de Jong, L. J. van Ijzendoorn, and M. J. A. de Voigt, "Stability of the interface between indium-tin-oxide and poly(3,4-ethylenedioxythiophene)/ poly(styrenesulfonate) in polymer light-emitting diodes," *Appl. Phys. Lett.*, vol. 77, pp. 2255–2257, 2000.

[50] P. Xu, S. Chen, H.-J. Xiang, X.-G. Gong, and S.-H. Wei, "Influence of defects and synthesis conditions on the photovoltaic performance of perovskite semiconductor $CsSnI_3$," *Chem. Mater.*, vol. 26, pp. 6068–6072, 2014.

[51] S. Aharon, S. Gamliel, B. El Cohen, and L. Etgar, "Depletion region effect of highly efficient hole conductor free $CH_3NH_3PbI_3$ perovskite solar cells," *Phys. Chem. Chem. Phys.*, vol. 16, pp. 10 512–10 518, 2014.

Chapter 6

A and B-site Substitution in $CsSnI_3$

6.1 Background

The optoelectronic properties of tin and lead halide perovskites are highly tunable, since by changing the elements occupying different sites of the perovskite lattice the energy of the valence and conduction band edges, E_g and the stability towards oxidation can all be tuned. In this chapter the findings of experiments investigating the use of Sr B-site substitution, and $CH_3NH_3^+$ and Rb^+ A-site substitution are reported. $CH_3NH_3^+$ has been used as an A-site cation extensively for lead halide perovskite and in a few reports relating to tin halide perovskites.[1–3] For lead-halide PPVs the use of mixed A-site cations has been widely studied, most notably in the context of formamidinium methylammonium lead halide perovskites,[4, 5] and the triple cation system $Cs_{1-x-y}(FA)_x(MA)_yPbI_3$.[6] There has also been some interest in mixed Sn-Pb perovskites due to the reduction in E_g that the inclusion of Sn imparts without compromising V_{oc} too much.[7, 8] Previous computational study has predicted that Rb substitution into $CsSnI_3$ would lead to ferroelectric properties which, it was proposed, could enable more efficient extraction of charge carriers in PPVs.[9]

6.2 Sr and CH_3NH_3 Substitution

The instability of $CsSnI_3$ towards oxidation in air results from oxidation of Sn^{2+} to Sn^{4+}, and so substituting some of the tin with a metal in a 2+ oxidation state, and with no higher oxidation states offers a means of improving the stability towards oxidation of $CsSnI_3$. The approach investigated was to replace some of the Sn^{2+} with Sr^{2+} to slow tin oxidation due to the presence of atoms in the corner sharing BX_6 octahedral lattice which cannot easily be oxidised, which should slow the bond breaking which occurs during the oxidation of the perovskite. Sr^{2+} has a similar ionic radius to Sn^{2+} (1.18 Å for Sr^{2+} [10] compared with 1.10 Å for Sn^{2+} [11]), and $CsSrI_3$ fits the tolerance factor for 3D perovskite ($t = 0.854$), and Sr halide perovskite, $CsSrCl_3$ has been reported to exist [12]. Figure 6.1 (a) shows a SEM image of a film of $CsSnI_3$ with added SrI_2 which has large gaps in the film. Unlike the $CsSnI_3$ with added tin halide, the film does not form immediately after spin casting, and takes several seconds to darken to the dark colour indicative of 3D perovskite.

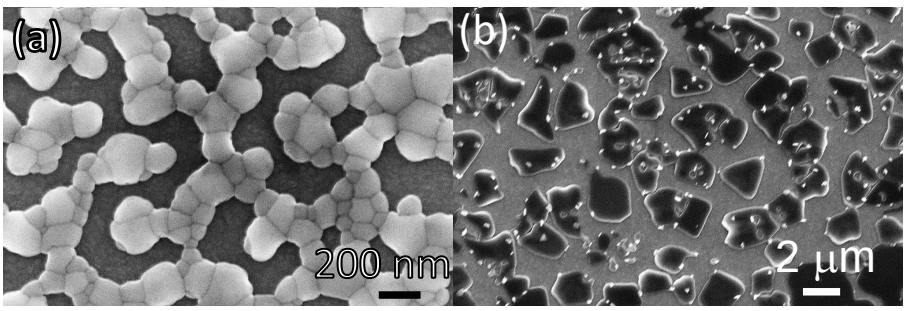

Figure 6.1: SEM images of **(a)** $CsSnI_3$ + 10 mol% added SrI_2 and **(b)** $CH_3NH_3SnI_3$. Both films were prepared from 8 wt% DMF solutions

The evolution of the electronic absorption spectra for $CsSnI_3$ prepared with SrI_2; Figure 6.2, shows the reduced stability as compared to that prepared with added SnI_2. The evolution of the absorbance spectra of $CsSnI_3$ + 10 mol% SrI_2 with air exposure is unusual in that the absorption at long wavelengths appears to increase in intensity, leading to a flattening of the

spectra (Figure 6.2 (a), (b) and (d)). It is tentatively suggested that this is due to a light scattering effect given the large size of the crystallites (Figure 6.1 (a)).

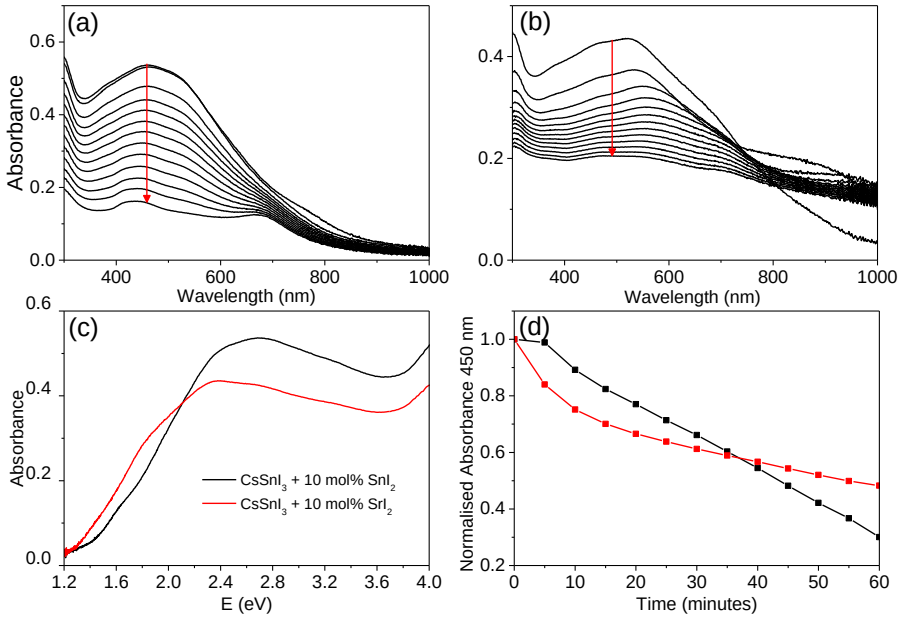

Figure 6.2: UV/Vis/NIR spectra recorded every 5 minutes for 1 hour after bringing into ambient air for films of **(a)** $CsSnI_3$ + 10 mol% SnI_2 and **(b)** $CsSnI_3$ + 10 mol% SrI_2. **(c)** UV/Vis/NIR spectra at time 0 of $CsSnI_3$ + 10 mol% added SnI_2 or SrI_2. **(d)** Normalised absorbance of $CsSnI_3$ with added SnI_2 or SrI_2 over time.

For PPV devices with the structure; ITO| CuSCN| $CsSnI_3$| $PC_{61}BM$| BCP| Al, those using $CsSnI_3$ with added SrI_2 performed poorly, generating very little current (Figure 6.3). This, combined with the reduced stability compared to $CsSnI_3$, did not bode well for utility in PPV devices so this material was not explored further.

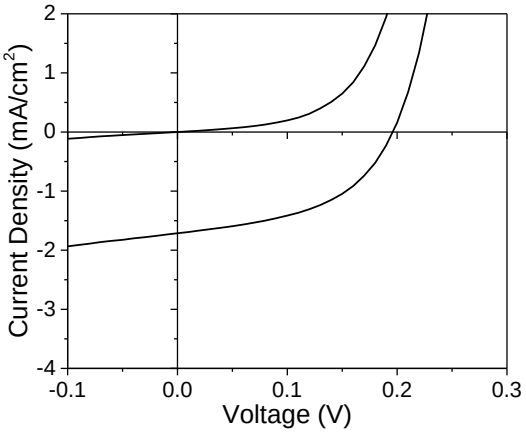

Figure 6.3: JV characteristic of champion PV device with the architecture; ITO| CuSCN| $CsSnI_3$ + 10 mol% SrI_2| $PC_{61}BM$| BCP| Al.

The use of $CH_3NH_3^+$ as the A-site cation is another simple way to modify the perovskite; $CH_3NH_3PbI_3$ is commonly used and $CH_3NH_3SnI_3$ has been demonstrated in PV devices in conjunction with mesoporous TiO_2 ETL.[1–3, 13] $CH_3NH_3^+$ is a larger cation than Cs^+, and gives a higher tolerance factor and a cubic perovskite structure for $ASnI_3$ (i.e. a lower degree of octahedral tilting).[14] When processed from DMF solution, films of $CH_3NH_3SnI_3$ would not crystallise without post-deposition annealing. Using a mixed solvent of DMF and DMSO, perovskite films could be made to form without annealing. However, in both cases, the perovskite films were not uniform and were made up of large isolated crystals when deposited directly onto ITO (Figure 6.1 (b)). $CH_3NH_3SnI_3$ has not been reported in planar architecture, which may be because it is much better suited to mesoporous architecture where there is a large surface area scaffold onto which the perovskite film can form a continuous film.[15, 16]

6.3 Rb A-site substitution

$RbSnI_3$ has a tolerance factor of 0.840 which is in the range of tolerance factors for which 3D perovskite structures have been reported; 0.813 - 1.1, but is just outside the range for which

perovskite formation is likely; 0.85 - 1.1 (Equation 1.6).[11] Computational simulations have predicted that $RbSnI_3$ should have a wider E_g than $CsSnI_3$,[9] and it has also been shown experimentally that a reduction in the size of the A-site cation (e.g. from $CH_3NH_3^+$ to Cs^+) increases the E_g in both tin and lead halide perovskites.[17] The increase in E_g is due to a reduction in orbital overlap caused by increased octahedral tilting. However, to date, $RbSnI_3$ has only been reported in the yellow phase [18] and not the 3D perovskite phase needed for utility in PV devices.

6.3.1 Thin Film Characterisation

The XRD patterns shown in Figure 6.4 indicate that films prepared from room temperature DMF solutions of RbI, CsI and SnI_2 with high RbI: CsI ratios make films with a crystal structure similar to that of Y-$CsSnI_3$. However, when the solution is made with 10 mol% or 20 mol% substitution of CsI with RbI, the structure is more like that of B-γ $CsSnI_3$.

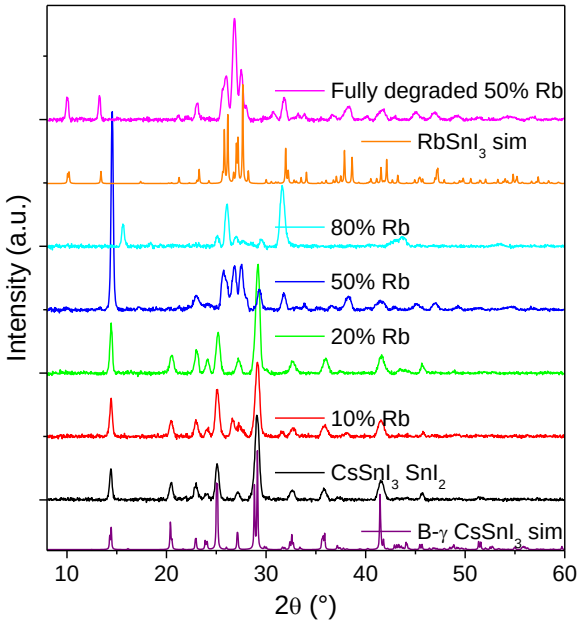

Figure 6.4: XRD patterns of $Cs_{1-x}Rb_xSnI_3$ + 10 mol% SnI_2, where $x = 0$, 0.1, 0.2, 0.5 or 0.8. Two patterns of 50% Rb substituted samples are shown, one which had degraded during the scan, and one which had fully degraded before before the scan began. Simulated B-γ $CsSnI_3$ [19] and yellow phase $RbSnI_3$ [18] are also plotted.

Fitting the lattice parameters shows that there is no significant difference in lattice parameters between $CsSnI_3$:SnI_2 and $Cs_{0.8}Rb_{0.2}SnI_3$:SnI_2 since the calculated cell volumes based on the measured XRD patterns are 936.6 ± 1.0 Å^3 for $CsSnI_3$:SnI_2 and 935.1 ± 1.4 Å^3 for $Cs_{0.8}Rb_{0.2}SnI_3$:SnI_2. Jung *et al.*[20] predicted only a very small difference in lattice parameters between 3D perovskite phases of $CsSnI_3$ and $RbSnI_3$, giving rise to a 5% reduction in unit cell volume, but with a much higher degree of octahedral tilting in the latter. Consequently, a significant shift in XRD peak positions when changing the Cs:Rb ratio from 1:0 to 1:1 would not be expected.[20] A simulation of an XRD pattern based on a crystallographic information file (CIF) in which 20% of the Cs atoms in B-γ $CsSnI_3$ are substituted with Rb shows that there should, however, be some difference in the peak intensities: Figure 6.5. The simulation shows that the (101) and (020) reflections should increase in intensity relative to the (202) and (040)

reflections when Cs is partially replaced with Rb (Figure 6.5). Comparing the measured patterns of $Cs_{1-x}Rb_xSnI_3$:SnI_2 (Figure 6.5), there is no significant trend in the relative ratios of the (101) and (020):(202) and (040) intensities, although both samples incorporating Rb do have higher relative intensities for the (101) and (020) peaks compared with (202). Additionally, the $Cs_{0.5}Rb_{0.5}SnI_3$:SnI_2 sample has a very intense peak at 14.5°, assigned to (101) and (020) Miller planes for perovskite material, before the sample degraded later in the measurement. By comparison, the fully degraded $Cs_{0.5}Rb_{0.5}SnI_3$:SnI_2 sample has peaks at 10.0° and 13.3°, which is characteristic of the yellow phase (Figure 6.4).

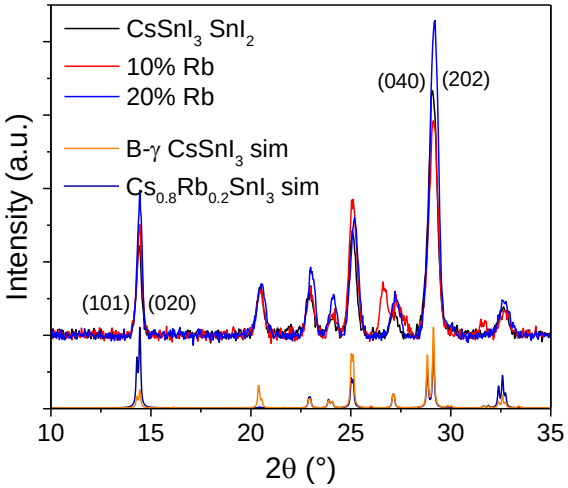

Figure 6.5: XRD patterns of $Cs_{1-x}Rb_xSnI_3$:SnI_2 where $x = 0$, 0.1, or 0.2, with simulated patterns of B-γ $CsSnI_3$ and of $CsSnI_3$ in which 20% of Cs atoms are replaced by Rb.

6.3.2 Stability of $Cs_{1-x}Rb_xSnI_3$:SnI_2 Thin Films

Electronic absorption spectroscopy was used to probe the stability of $Cs_{1-x}Rb_xSnI_3$:SnI_2 perovskite films with different proportions of Rb incorporated into the perovskite lattice. It is evident from Figure 6.6 that partial substitution of Cs with Rb reduces the stability significantly, since there is a much faster evolution of the absorbance spectra with time for films with higher Rb content. For 50% Rb substitution, the perovskite film had completely degraded after

10 minutes. The colour change during this degradation process is consistent with formation of the orthorhombic yellow phase. Additionally, the absorbance spectrum of the fully degraded $x = 0.5$ material (after 25 minutes) (Figure 6.6 (f)) is different from that of the degradation products of B-γ $CsSnI_3$ (as shown in earlier chapters), consistent with the fact that the yellow phase is the only reported structure of $RbSnI_3$,[18] and so a mixed Cs:Rb A-site cation would be expected to more stable in the yellow phase than a fully Cs A-site, assuming Vegard-like behaviour of tolerance factor. Due to this instability and the time taken to prepare and collect XRD patterns with good signal-to-noise, measurements of the crystal structure using XRD proved difficult for films with high Rb content, and so an XRD measurement of the perovskite with 50% Rb substitution was not achieved. The reduction in stability upon partial substitution of Cs with Rb is likely a result of the increased octahedral tilting which increases the strain due to electron repulsion,[20] reducing the stability of the black phase perovskite compared with the yellow phase material, leading to faster formation of the yellow phase upon exposure to moisture in ambient air (the conversion of B-γ $CsSnI_3$ to Y-$CsSnI_3$ under humid atmosphere was demonstrated in Chapter 4). Although the XRD data provides no direct evidence for the incorporation of Rb into the perovskite lattice, the decrease in E_g determined by the electronic absorption spectroscopy (Figure 6.6) does provide convincing evidence for Rb incorporation.

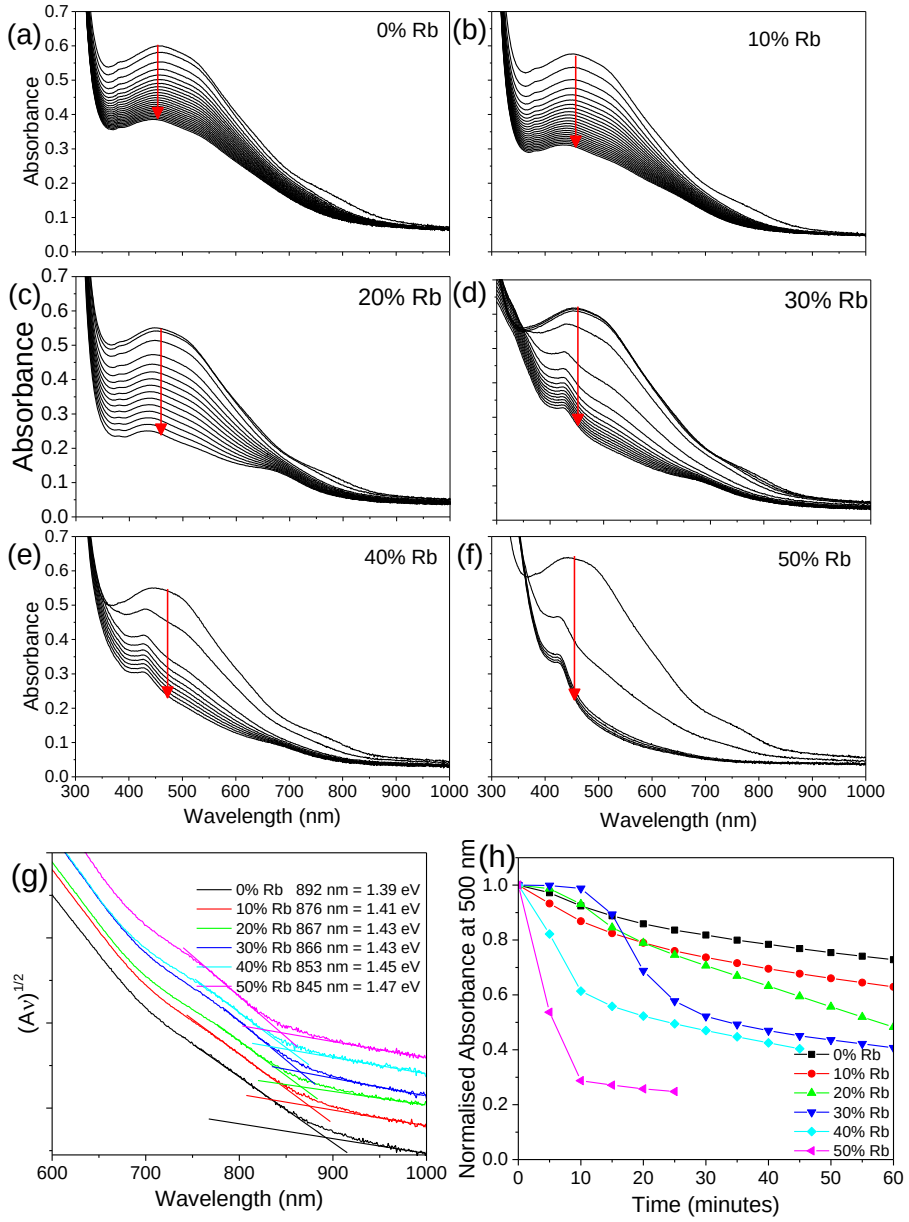

Figure 6.6: **(a)**, **(b)**, **(c)**, **(d)**, **(e)**, and **(f)** UV/vis/NIR spectra over time in air of $Cs_{1-x}Rb_xSnI_3$:SnI_2, where $x = 0$, 0.1, 0.2, 0.3, 0.4, and 0.5 respectively. **(g)** $(Ah\nu)^{1/2}$ plotted against wavelength for all films at $t = 0$. **(h)** Normalised absorption over time at 500 nm.

The SEM images in Figure 6.7 reveal that there is a high pinhole density in the $Cs_{1-x}Rb_xSnI_3$:SnI_2 film on ITO as compared to the film without Rb substitution ($\sim$ 6% vs. $\sim$ 1.6% pinhole coverage for 20% and 0% Rb samples, respectively), which could be another source of instability

towards oxidation, since pinholes increase the surface area to volume ratio, thereby increasing the amount of material exposed to water in ambient air. Notably solutions of partially Rb substituted tin halide perovskite precursors were also less stable than those using only Cs cations, with the partial Rb substituted solutions often turning from yellow to orange only after several days stored in a nitrogen filled glovebox.

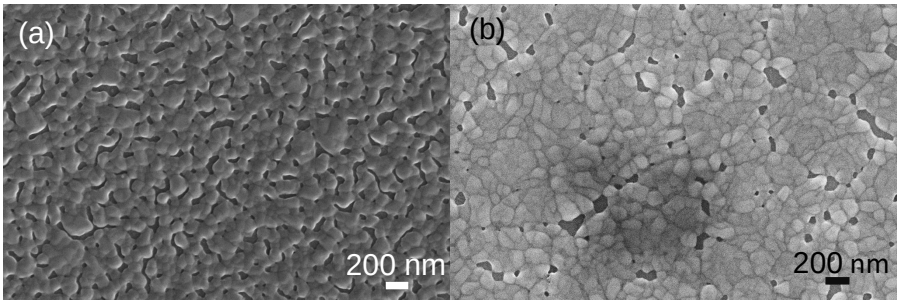

Figure 6.7: SEM image of a film of **(a)** $Cs_{0.8}Rb_{0.2}SnI_3$:SnI_2 and **(b)** $CsSnI_3$:SnI_2 on an ITO glass substrates.

6.3.3 Photovoltaic Devices

Model PPV devices were fabricated with the structure; ITO| $Cs_{1-x}Rb_xSnI_3$:SnI_2| C_{60}| BCP| Al, where $x = 0$, 0.2, or 0.5. The JV characteristics in the dark and under 1 sun simulated illumination; Figure 6.8 and Table 6.1, show a large increase in device V_{oc} as the Rb content is increased from 0% to 20% and then to 50% Cs substitution by Rb. However, the increasing Rb content also correlates with a decrease in J_{sc} with no significant change in *FF*. A Rb content corresponding to $x = 0.2$ yielded PPV devices with the highest η of the three Rb loadings tested.

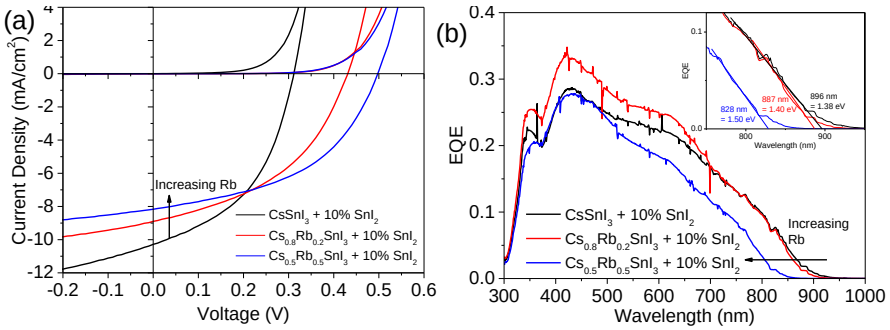

Figure 6.8: **(a)** Representative JV characteristics for devices made using $CsSnI_3$ + 10 mol% SnI_2 with 0, 20%, and 50% Cs substituted with Rb. **(b)** Corresponding EQE spectra with inset showing the zoom in of the low energy onset of absorption.

Table 6.1: Summary of JV characteristics of PV devices made using $CsSnI_3$ + 10 mol% SnI_2 with 0, 20% or 50% Cs substituted for Rb, and a C_{60} ETL.

Sample	n	J_{sc} (mA/cm^2)	V_{oc} (V)	FF	η (%)	Champion η(%)
$CsSnI_3$:SnI_2	18	9.84 ± 0.67	0.31 ± 0.01	0.46 ± 0.02	1.37 ± 0.14	1.55
$Cs_{0.8}Rb_{0.2}SnI_3$:SnI_2	17	8.79 ± 0.25	0.43 ± 0.02	0.45 ± 0.01	1.70 ± 0.09	1.84
$Cs_{0.5}Rb_{0.5}SnI_3$:SnI_2	18	8.11 ± 0.53	0.48 ± 0.04	0.46 ± 0.05	1.81 ± 0.30	2.25

The UPS measurements shown in Figure 6.9 show that partial Rb substitution lowers the energy of VB edge with respect to the vacuum level, which offers a plausible explanation for the increase in V_{oc} because the maximum V_{oc} is, to a first approximation, expected to scale with the energy difference between the VB edge in the perovskite and the LUMO level of the fullerene ETL. The VB edge of $Cs_{0.8}Rb_{0.2}SnI_3$ + 10 mol% SnI_2 is 0.15 eV lower than that of $CsSnI_3$:SnI_2, and the VB edge of $Cs_{0.5}Rb_{0.5}SnI_3$ + 10 mol% SnI_2 is 0.28 eV lower (Figures 6.9 and 6.10). Notably it is not possible to precisely know the magnitude of the I_p in each case because the excess SnI_2, which is needed to minimise the Sn vacancy defect density, is likely accumulated at the perovskite film surface (as has been shown to be the case for $SnCl_2$), modifying the surface potential contribution to the I_p. Although the absolute values cannot be precisely determined,

the relative values can be, because it is reasonable to assume that the excess SnI_2 is distributed in the same way in the perovskite film, and so there will be very similar perturbation of the surface potential contribution to the I_p measurement. The magnitude and direction of the change in I_p is of the same order as the difference in device V_{oc}: Champion V_{oc} values are 0.32 V, 0.45 V, and 0.53 V for $x = 0$, 0.2 and 0.5, respectively.

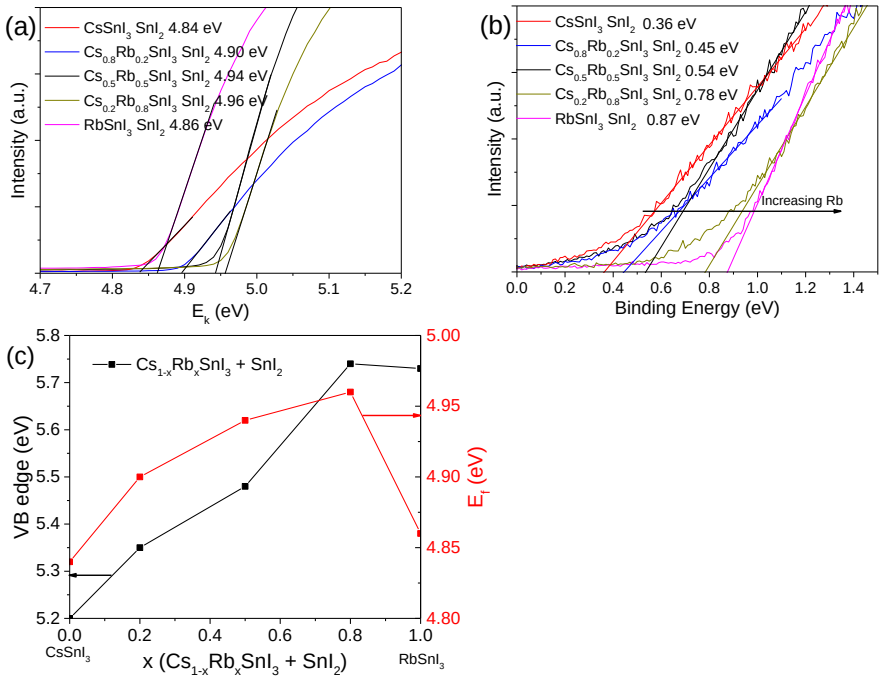

Figure 6.9: UPS spectra of $Cs_{1-x}Rb_xSnI_3$ + 10 mol% SnI_2 where x=0, 0.2, 0.5, 0.8 and 1, showing **(a)** the low kinetic energy edge and **(b)** the high kinetic energy edge. **(c)** Plot of the VB edge and E_f against Rb composition. The error on the low kinetic energy edge is ±0.01 eV. The error on the high kinetic energy edge is ±0.05 eV. Arrow added to **(b)** to indicate the direction corresponding to Rb content.

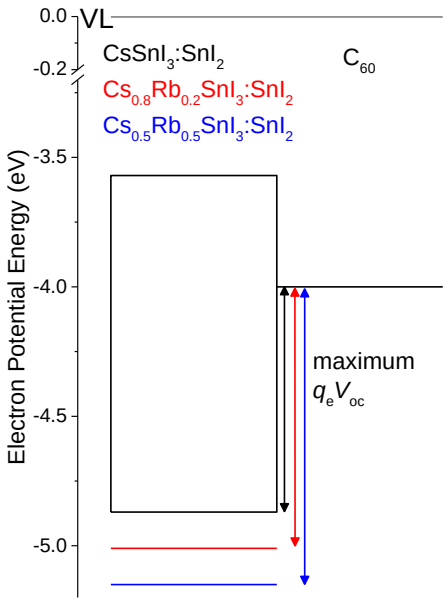

Figure 6.10: Schematic energy level diagram depicting the VB edges of $Cs_{1-x}Rb_xSnI_3$:SnI_2 for $x = 0$, 0.2 and 0.5, the CB edge for $x = 0$, and the LUMO position of C_{60}.

As discussed previously, the smaller size of Rb compared with Cs is expected to increase tilting of the SnI_6 octahedra, which reduces Sn-I orbital overlap, leading to a larger E_g.[9, 21, 22] The reason for the decrease in J_{sc} for devices with 20% Rb substitution compared with 0% Rb devices is not clear, since it cannot be explained in terms of a decrease in light absorbance due to increased E_g because the EQE shown in Figure 6.8 (b) shows that the blue shift in absorbance onset between $CsSnI_3$:SnI_2 and $Cs_{0.8}Rb_{0.2}SnI_3$:SnI_2 is too small to explain this the difference in J_{sc}: 1.38 eV for $CsSnI_3$:SnI_2 and 1.40 for $Cs_{0.8}Rb_{0.2}SnI_3$:SnI_2.

In Chapter 4 $SnCl_2$ was shown to be much more effective than SnI_2 as a source of excess Sn for $CsSnI_3$ PPV devices, and so it was also tested for use in the partially Rb substituted perovskite devices in conjunction with a $PC_{61}BM$ ETL. However, it should be noted that adding an extra element increases the complexity of the material system, as it adds the possibility of the formation of phase-separated $Cs_yRb_{1-y}SnI_{3-x}Cl_x$ and/or $RbSnCl_3$ ($t = 0.858$). It is evident from Figure 6.11 that the $x = 0.2$ substituted sample was best performing in all four device

parameters, with a significant decrease in J_{sc} for $x = 0.5$.

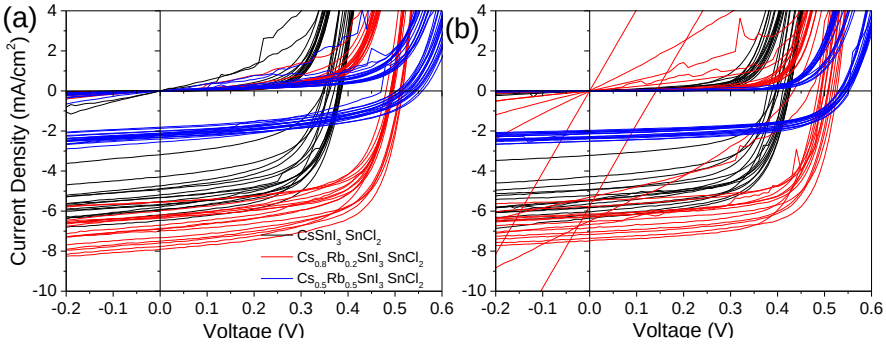

Figure 6.11: JV characteristics of devices in the structure ITO| $Cs_{1-x}Rb_xSnI_3$ + 10 mol% $SnCl_2$| $PC_{61}BM$| BCP| Al, where $x = 0$, 0.2 or 0.5, tested under 1 sun simulated solar illumination and in the dark **(a)** immediately after fabrication, and **(b)** after 12 days storage in the glove box.

Notably perovskite films made with a Rb content corresponding to $x = 0.5$ were lighter and orange in colour, as compared with the dark red/brown of the films prepared with 0% and 20% Rb substitution (Figure 6.11 and Table 6.2). The EQE spectra in Figure 6.12 show that there is very little difference in E_g for $x = 0$ and $x = 0.2$ (1.34 eV and 1.37 eV respectively), and the onset of absorbance for $x = 0.5$ is much higher at $\sim$ 1.45 eV. These differences are consistent with the UV/vis/NIR absorbance data shown in Figure 6.6.

Table 6.2: JV characteristics of PPV devices in the structure ITO| $Cs_{1-x}Rb_xSnI_3$ + 10 mol% $SnCl_2$| $PC_{61}BM$| BCP| Al, where $x = 0$, 0.2, or 0.5, immediately after fabricating (black), after 5 days (red) and 12 days (blue) storage in an N_2 filled glovebox.

Sample	n	J_{sc} (mA/cm^2)	V_{oc} (V)	FF	η (%)	Champion η (%)
$CsSnI_3$:$SnCl_2$	16	5.32 ± 0.78	0.37 ± 0.01	0.57 ± 0.04	1.14 ± 0.24	1.50
	15	5.30 ± 0.79	0.41 ± 0.02	0.61 ± 0.02	1.33 ± 0.26	1.67
	14	5.33 ± 0.97	0.44 ± 0.01	0.62 ± 0.03	1.46 ± 0.34	1.98
$Cs_{0.8}Rb_{0.2}SnI_3$:$SnCl_2$	17	6.71 ± 0.71	0.50 ± 0.01	0.61 ± 0.03	2.05 ± 0.26	2.58
	16	6.42 ± 0.63	0.48 ± 0.09	0.60 ± 0.14	1.93 ± 0.64	2.64
	16	6.75 ± 0.68	0.48 ± 0.02	0.67 ± 0.02	2.19 ± 0.20	2.45
$Cs_{0.5}Rb_{0.5}SnI_3$:$SnCl_2$	18	2.18 ± 0.17	0.53 ± 0.02	0.44 ± 0.03	0.50 ± 0.07	0.63
	16	2.22 ± 0.17	0.54 ± 0.01	0.58 ± 0.01	0.70 ± 0.06	0.79
	17	2.31 ± 0.17	0.53 ± 0.01	0.60 ± 0.02	0.74 ± 0.07	0.90

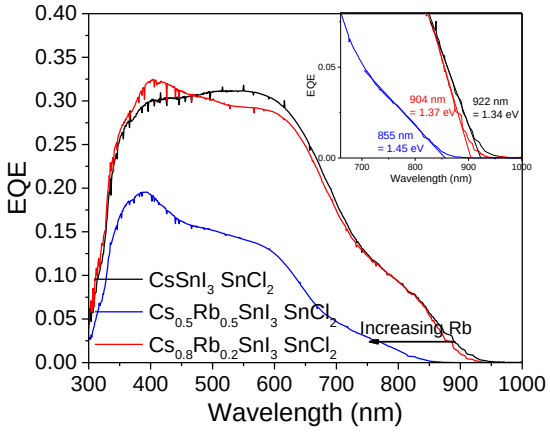

Figure 6.12: EQE spectra for PV devices with the structure; ITO| $Cs_{1-x}Rb_xSnI_3$ + 10 mol% $SnCl_2$| $PC_{61}BM$| BCP| Al, where $x = 0$, 0.2 or 0.5. **Inset**: zoom in of low energy cut-off from where E_g is estimated.

Thin films of $Cs_{1-x}Rb_xSnI_3$:SnI_2 were prepared with Rb content $x = 0$, 0.2, 0.5, 0.8 and 1. The films with $x = 0$, 0.2 and 0.5 formed dark coloured films typical of tin halide perovskite. However for $x = 0.8$ and 1, the films were orange/yellow in colour, which indicates that they did not form 3D perovskite phases.

XPS analysis of the films with different Rb loadings was performed to explore differences in chemical structures. Importantly, the films were transferred to the instrument via an air tight transfer arm which attaches directly to the instrument. The XPS Sn $3d_{5/2}$ and $3d_{3/2}$ peaks show a shift to higher binding energies as Cs is replaced by Rb in $Cs_{1-x}Rb_xSnI_3$:SnI_2 from 486.09 eV and 494.50 eV for $x = 0$ to 486.32 eV and 494.72 eV for $x = 1$ (Figure 6.13). This is likely due to the change in Sn-I-Sn bond angles of the corner sharing SnI_6 octahedra which results from the inclusion of Rb, and, coupled with the fact that there is no significant change in the full-width-at-half-maximum of the peaks, which only varies between 0.84 to 0.88 eV for the different samples, implies that Rb is being incorporated into the structure, and does not exist as a separate RbI phase.

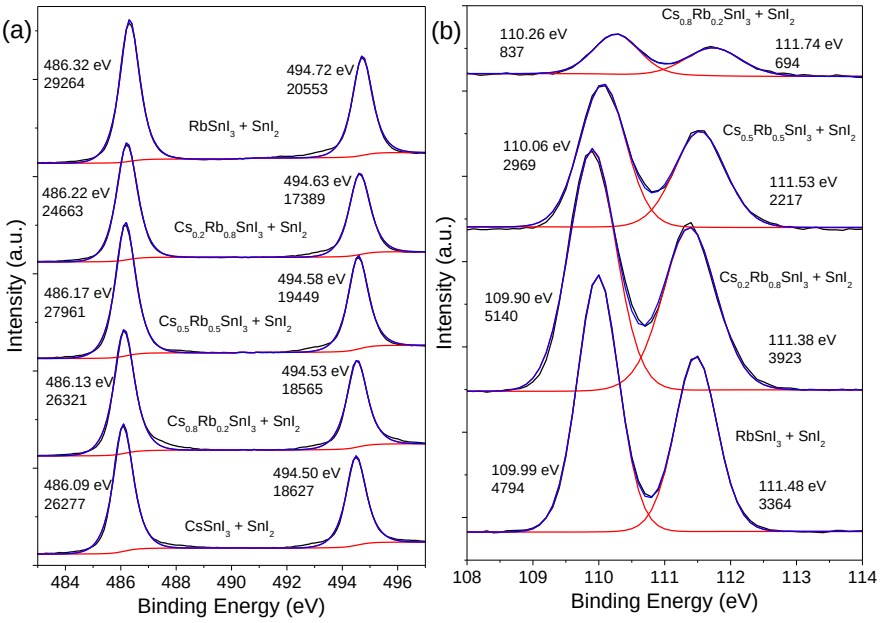

Figure 6.13: XPS spectra of $Cs_{1-x}Rb_xSnI_3$ + 10 mol% SnI_2 where x=0, 0.2, 0.5, 0.8, and 1, showing **(a)** Sn 3d and **(b)** Rb 3d.

The XPS peak intensities can be used to estimate the elemental ratios. This is done using the relative sensitivity factors (RSF) using the formula;

$$\text{atomic ratio} = \frac{\text{intensity}}{\text{RSF}} \tag{6.1}$$

The calculated ratios of Cs:Rb are in close agreement with the ratios used to make the solutions (Table 6.3). These were calculated using the RSFs and the total area of the Cs 3d peaks (40.22) and the Rb 3d peaks (4.21) (i.e. $3d_{5/2}$ + $3d_{3/2}$).

Table 6.3: Cs:Rb ratios measured using XPS for the materials $Cs_{1-x}Rb_xSnI_3$:SnI_2, where $x = 0.2$, 0.5 or 0.8.

Sample	Cs	Rb
$Cs_{0.8}Rb_{0.2}SnI_3$:SnI_2	80.1	19.9
$Cs_{0.5}Rb_{0.5}SnI_3$:SnI_2	43.5	56.5
$Cs_{0.2}Rb_{0.8}SnI_3$:SnI_2	15.0	85.0

6.4 Conclusions

In summary Sr was studied as a partial B-site substitute in $CsSnI_3$ with the aim of stabilising the 3D perovskite towards oxidation by incorporating an element in the 2+ oxidation state that has no higher states. $CsSnI_3$ films incorporating SrI_2 did show higher absorption in the NIR region, but exhibited reduced stability and did not function well in as a light harvester in PV devices. $CH_3NH_3^+$ was also tested as an A-site cation, but the perovskite did not form uniform films. Rb was explored for partial A-site substitution. It was found to form dark, highly absorbing films up to 50% Rb substitution, although increasing the Rb content reduced

film stability. In devices with added SnI_2 and $SnCl_2$, the use of 20% Rb substitution gave higher performance than the 0% and 50% substituted materials, partly due to a lower VB edge leading to a higher V_{oc}, while not affecting the J_{sc} to the same extent. Electronic absorption spectra show a gradual increase in E_g with increasing Rb substitution, and XPS showed a gradual shift in Sn 3d peak position to higher binding energy with increased Rb content, consistent with A-site substitution, rather than phase separation of RbI mixed with $CsSnI_3$ and SnI_2.

6.5 Future Work

It is evident from the results presented in this chapter that there is further scope for investigating the $Cs_{1-x}Rb_xSnI_3$ system. Improved XRD characterisation would be useful for the unstable compounds, which would require fast sample placement and high N_2 pressure to displace as much of the oxygen and water as possible before beginning the scan. Further evidence for the incorporation of Rb into the perovskite lattice is also needed. One such experiment would be to measure the XPS of RbI to see if there is a significant change in the Rb 3d binding energies when Rb is incorporated into the perovskite lattice because high resolution XPS data for RbI is not available in the literature. Computational modelling to predict the change in electronic structure as a function of Rb incorporation would also help to give further insight into the experimental observations. It would also be interesting to investigate the effect of incorporating Br into the partially Rb substituted perovskite because the smaller halide may allow for larger Rb incorporation by reducing distortion of the perovskite structure.

Two of the most important factors in determining PPV device η are film uniformity and crystallite size. In the literature there are several procedures which have been described in order to achieve this for lead perovskite PVs which has resulted in large improvements in device η. Controlling the rate of crystal growth is important in this regard, because larger crystals are

typically grown by slowing crystal formation, although, this needs to be balanced with the number of nucleation sites, which needs to be large enough to ensure high uniformity and low pinhole density. Further work could involve the use of thicker films with post-deposition thermal and solvent annealing, and further exploration of the use of DMSO and solvent mixtures containing DMSO.

References

[1] F. Hao, C. C. Stoumpos, D. H. Cao, R. P. H. Chang, and M. G. Kanatzidis, "Lead-free solid-state organic–inorganic halide perovskite solar cells," *Nat. Photonics*, vol. 8, pp. 489–494, 2014.

[2] N. K. Noel, S. D. Stranks, A. Abate, C. Wehrenfennig, S. Guarnera, A.-A. Haghighirad, A. Sadhanala, G. E. Eperon, S. K. Pathak, M. B. Johnston, A. Petrozza, L. M. Herz, and H. J. Snaith, "Lead-free organic-inorganic tin halide perovskites for photovoltaic applications," *Energy Environ. Sci.*, vol. 7, pp. 3061–3068, 2014.

[3] T. Yokoyama, D. H. Cao, C. C. Stoumpos, T.-B. Song, Y. Sato, S. Aramaki, and M. G. Kanatzidis, "Overcoming short-circuit in lead-free $CH_3NH_3SnI_3$ perovskite solar cells via kinetically controlled gas-solid reaction film fabrication process," *J. Phys. Chem. Lett.*, vol. 7, pp. 776–782, 2016.

[4] N. Pellet, P. Gao, G. Gregori, T.-Y. Yang, M. K. Nazeeruddin, J. Maier, and M. Grätzel, "Mixed-organic-cation perovskite photovoltaics for enhanced solar-light harvesting.," *Angew. Chem. Int. Ed. Engl.*, vol. 53, pp. 3151–3157, 2014.

[5] T. Jesper Jacobsson, J.-P. Correa-Baena, M. Pazoki, M. Saliba, K. Schenk, M. Grätzel, and A. Hagfeldt, "Exploration of the compositional space for mixed lead halogen perovskites for high efficiency solar cells," *Energy Environ. Sci.*, vol. 9, pp. 1706–1724, 2016.

[6] M. Saliba, T. Matsui, J.-Y. Seo, K. Domanski, J.-P. Correa-Baena, N. Mohammad K., S. M. Zakeeruddin, W. Tress, A. Abate, A. Hagfeldt, and M. Grätzel, "Cesium-containing triple cation perovskite solar cells: Improved stability, reproducibility and high efficiency," *Energy Environ. Sci.*, vol. 9, pp. 1989–1997, 2016.

[7] F. Hao, C. C. Stoumpos, R. P. H. Chang, and M. G. Kanatzidis, "Anomalous band gap behavior in mixed Sn and Pb perovskites enables broadening of absorption spectrum in solar cells," *J. Am. Chem. Soc.*, vol. 136, pp. 8094–8099, 2014.

[8] Y. Ogomi, A. Morita, S. Tsukamoto, T. Saitho, N. Fujikawa, Q. Shen, T. Toyoda, K. Yoshino, S. S. Pandey, and S. Hayase, "$CH_3NH_3Sn_xPb_{(1-x)}I_3$ perovskite solar cells covering up to 1060 nm," *J. Phys. Chem. Lett.*, vol. 5, pp. 1004–1011, 2014.

[9] G. Gou, J. Young, X. Liu, and J. M. Rondinelli, "Interplay of cation ordering and ferroelectricity in perovskite tin iodides: Designing a polar halide perovskite for photovoltaic applications," *Inorg. Chem.*, vol. 56, pp. 26–32, 2017.

[10] R. D. Shannon, "Revised effective ionic radii and systematic studies of interatomic distances in halides and chalcogenides," *Acta Crystallogr. Sect. A Found. Adv.*, vol. A32, pp. 751–767, 1976.

[11] C. Li, X. Lu, W. Ding, L. Feng, Y. Gao, and Z. Guo, "Formability of ABX_3 (X = F, Cl, Br, I) halide perovskites.," *Acta Crystallogr. B.*, vol. 64, pp. 702–707, 2008.

[12] M. A. Macdonald, E. N. Mel'chakov, I. H. Munro, P. A. Rodnyi, and A. S. Voloshinovsky, "Radiative core-valence transitions in CsMgCl3 and CsSrCl3," *J. Lumin.*, vol. 65, pp. 19–23, 1995.

[13] F. Hao, C. C. Stoumpos, P. Guo, N. Zhou, T. J. Marks, R. P. H. Chang, and M. G. Kanatzidis, "Solvent-mediated crystallization of $CH_3NH_3SnI_3$ films for heterojunction depleted perovskite solar cells," *J. Am. Chem. Soc.*, vol. 137, pp. 11 445–11 452, 2015.

[14] Y. Dang, Y. Zhou, X. Liu, D. Ju, S. Xia, H. Xia, and X. Tao, "Formation of hybrid perovskite tin iodide single crystals by top-seeded solution growth," *Angew. Chemie - Int. Ed.*, vol. 55, pp. 3447–3450, 2016.

[15] V. Gonzalez-Pedro, E. J. Juarez-Perez, W.-S. Arsyad, E. M. Barea, F. Fabregat-Santiago, I. Mora-Sero, and J. Bisquert, "General working principles of $CH_3NH_3PbX_3$ perovskite solar cells," *Nano Lett.*, vol. 14, pp. 888–893, 2014.

[16] D. Ramirez, M. A. M. Escobar, J. F. Montoya, and F. Jaramillo, "Understanding the role of the mesoporous layer in the thermal crystallization of a meso-superstructured perovskite solar cell," *J. Phys. Chem. C*, vol. 120, pp. 8559–8567, 2016.

[17] P. P. Boix, S. Agarwala, T. M. Koh, N. Mathews, and S. G. Mhaisalkar, "Perovskite solar cells: Beyond methylammonium lead iodide," *J. Phys. Chem. Lett.*, vol. 6, pp. 898–907, 2015.

[18] G. Thiele and B. R. Serr, "Crystal structure of rubidium triiodostannate(II), $RbSnI_3$," *Zeitschrift für Krist.*, vol. 210, p. 64, 1995.

[19] I. Chung, J.-H. Song, J. Im, J. Androulakis, C. D. Malliakas, H. Li, A. J. Freeman, J. T. Kenney, and M. G. Kanatzidis, "$CsSnI_3$: Semiconductor or metal? High electrical conductivity and strong near-infrared photoluminescence from a single material. High hole mobility and phase-transitions.," *J. Am. Chem. Soc.*, vol. 134, pp. 8579–8587, 2012.

[20] Y. K. Jung, J. H. Lee, A. Walsh, and A. Soon, "Influence of Rb/Cs cation-exchange on inorganic Sn halide perovskites: From chemical structure to physical properties," *Chem. Mater.*, vol. 29, pp. 3181–3188, 2017.

[21] M. R. Filip, G. E. Eperon, H. J. Snaith, and F. Giustino, "Steric engineering of metal-halide perovskites with tunable optical band gaps," *Nat. Commun.*, vol. 5, p. 5757, 2014.

[22] M. R. Linaburg, E. T. McClure, J. D. Majher, and P. M. Woodward, "$Cs_{1-x}Rb_xPbCl_3$ and $Cs_{1-x}Rb_xPbBr_3$ solid solutions: Understanding octahedral tilting in lead halide perovskites," *Chem. Mater.*, vol. 29, pp. 3507–3514, 2017.